

# **Elastic Flow Instabilities of Non-Newtonian Fluids in Shear Flows**

**Dissertation  
zur Erlangung des Grades  
des Doktors der Naturwissenschaften  
der Naturwissenschaftlich-Technischen Fakultät II  
– Physik und Mechatronik –  
der Universität des Saarlandes**



**von**

**Christof Schäfer**

**Saarbrücken  
2013**



**Tag des Kolloquiums: 09.05.2014**

**Dekan: Univ.-Prof. Dr. Christian Wagner**

**Mitglieder des**

**Prüfungsausschusses: Univ.-Prof. Dr. Andreas Schütze (Vorsitz)  
Univ.-Prof. Dr. Christian Wagner (Gutachter)  
Univ.-Prof. Dr. Manfred Lücke (Gutachter)  
Prof. Dr. Sandra Lerouge (Gutachterin)  
Dr. Andreas Tschöpe (Akad. Mitarbeiter)**



---

# Abstract / Kurzdarstellung

## Abstract

The present work deals with the investigation of flow phenomena of non-Newtonian, viscoelastic fluids and particularly with the emergence of elastic flow instabilities and their underlying mechanism. It is mainly focused on the experimental and theoretical investigation of the viscoelastic Taylor-Couette flow for which previous approaches exhibited some unanswered questions and apparent discrepancies to theoretical predictions. The present study is based on experiments in different Taylor-Couette cells using various polymer solutions with diverse rheological properties. Here, the various cells differ from each other just by their characteristic curvature. The objective is the experimental verification of the universal criterion which predicts the onset of elastic instability of a viscoelastic flow with curved streamlines. Based on a customized, constitutive model which is able to describe the explicit shear rheology of the used polymer solutions, linear stability analysis is performed with aiming at an interpretation of the experimental findings. A supplementary study is presented which addresses the possible degradation of the polymer solutions during the Taylor-Couette measurements. Its results are essential to provide a consistent interpretation of the Taylor-Couette measurements. The findings of further studies on elastic flow phenomena are summarized by means of appended reprints of recently published or submitted papers.

## Kurzdarstellung

Die vorliegende Arbeit befasst sich mit verschiedenen Strömungsphänomenen nicht-Newtonscher, viskoelastischer Flüssigkeiten, insbesondere mit elastischen Strömungsinstabilitäten und deren zugrundeliegendem Mechanismus. Der Fokus liegt hierbei auf der experimentellen wie theoretischen Untersuchung des viskoelastischen Taylor-Couette-Flusses, dessen bisherige Behandlung offene Fragen und Unstimmigkeiten gegenüber theoretischen Vorhersagen aufweist. Grundlage unserer Studie bilden Experimente mit mehreren Polymerflüssigkeiten unterschiedlicher rheologischer Eigenschaften in verschiedenen Taylor-Couette-Geometrien, die sich in ihrem Krümmungsparameter unterscheiden. Zielsetzung ist insbesondere die experimentelle Verifizierung eines universellen Kriteriums, das die lineare elastische Instabilität einer viskoelastischen Strömung mit gekrümmten Stromlinien vorhersagt. Basierend auf einem angepassten, konstitutiven Flüssigkeitsmodell, welches die Scherrheologie der verwendeten Flüssigkeiten zu erfassen vermag, wird mit Hilfe einer linearen Stabilitätsanalyse versucht, die experimentellen Ergebnisse nachzuvollziehen. Ergänzend dazu werden die Ergebnisse einer Studie vorgestellt, die die Degradation der Polymerflüssigkeiten im Verlauf der Taylor-Couette Messungen zum Gegenstand hat. Erst diese lassen eine stimmige Interpretation der vorherigen Resultate zu. Die Ergebnisse weiterer Studien elastischer Strömungsphänomene sind in Form angefügter Publikationen zusammengefasst.

---

# Contents

<b>Abstract / Kurzdarstellung</b>	<b>v</b>
<b>Contents</b>	<b>vi</b>
<b>Nomenclature</b>	<b>ix</b>
<b>1 Preface</b>	<b>1</b>
<b>I Introduction</b>	<b>3</b>
<b>2 Fundamental physics of (non-)Newtonian fluid flow</b>	<b>5</b>
2.1 Newtonian vs. non-Newtonian fluid flow . . . . .	5
2.2 Linear viscoelasticity . . . . .	7
2.3 Constitutive modeling . . . . .	8
2.4 Hydrodynamic flow instabilities . . . . .	16
<b>3 Rheometric toolkit</b>	<b>23</b>
3.1 Rotational steady shear rheometry . . . . .	23
3.2 Relaxation after cessation of steady shear stress . . . . .	27
3.3 Small amplitude oscillatory rheometry (SAOR) . . . . .	31
3.4 Capillary breakup extensional rheometry (CaBER) . . . . .	34
<b>II Study of viscoelastic Taylor-Couette flow [Sch13]</b>	<b>39</b>
<b>4 Introduction</b>	<b>41</b>
4.1 Basic literature and milestones . . . . .	42
4.2 Scientific relevance and perspective of the present study . . . . .	43
4.3 The Taylor-Couette flow of an Oldroyd-B fluid... reloaded . . . . .	45
<b>5 Fluid samples</b>	<b>51</b>
5.1 Preparation of polymer solutions . . . . .	51
5.2 Rheometric properties of polymer solutions . . . . .	52
5.3 Summing up the rheometry . . . . .	62
<b>6 The Taylor-Couette setup</b>	<b>65</b>
<b>7 Taylor-Couette measurements</b>	<b>69</b>

7.1	Integral stress measurements . . . . .	69
7.2	Flow visualization . . . . .	70
7.3	Interpretation of Taylor-Couette data . . . . .	71
<b>8</b>	<b>Pakdel-McKinley criterion for finite gap</b>	<b>79</b>
<b>9</b>	<b>Linear stability analysis</b>	<b>85</b>
9.1	Solving the Taylor-Couette base problem for the non-isothermal hybrid model	85
9.2	Perturbation functions . . . . .	87
9.3	Generalized eigenvalue problem & instability criterion . . . . .	91
9.4	LSA of the Maxwell and Oldroyd-B fluid - Consistency check . . . . .	93
9.5	LSA of the isothermal hybrid model . . . . .	98
9.6	LSA of the non-isothermal hybrid model . . . . .	100
9.7	LSA vs. geometrical transition . . . . .	104
<b>10</b>	<b>Degradation of polymer solutions</b>	<b>107</b>
10.1	Historical synopsis . . . . .	107
10.2	Experimental degradation study . . . . .	109
10.3	Interpretation of degradation data . . . . .	116
<b>11</b>	<b>Summary</b>	<b>119</b>
<b>12</b>	<b>Conclusion</b>	<b>123</b>
<b>III</b>	<b>Appendices</b>	<b>125</b>
<b>A</b>	<b>Rheometric data</b>	<b>127</b>
A.1	The P150 <sub>G80</sub> polymer solution . . . . .	128
A.2	The P1200 <sub>G80</sub> polymer solution . . . . .	132
A.3	The P500 <sub>S58</sub> polymer solution . . . . .	136
A.4	The P80 <sub>S64</sub> polymer solution . . . . .	140
A.5	The P150 <sub>S65.6</sub> polymer solution . . . . .	144
<b>B</b>	<b>Mathematics</b>	<b>147</b>
B.1	Pseudospectral Chebyshev collocation method . . . . .	147
<b>C</b>	<b>Publications</b>	<b>153</b>
C.1	Serpentine channels: micro-rheometers for fluid relaxation times [Zil14] . . . . .	153
C.2	Elasto-inertial turbulence [Sam13] . . . . .	162
C.3	Rheology of human blood plasma [Bru13] . . . . .	174
	<b>List of Figures</b>	<b>180</b>
	<b>List of Tables</b>	<b>184</b>
	<b>Bibliography</b>	<b>185</b>



---

## Nomenclature

$G^{M,J}$	relaxation modulus of the Maxwell/Jeffreys model
$[\eta]$	intrinsic viscosity
$\alpha$	parameter of the PTT model
$\beta$	viscosity ratio $\eta_s/\eta$
$\beta_r$	ratio $\beta^U/\beta^P$
$\chi$	minimum positive, real-valued solution of the cubic equation $K(S)$
$\Delta E$	activation energy
$\delta$	delta-distribution
$\dot{\gamma}$	shear rate, rate-of-shear tensor
$\epsilon$	cone angle of the cone-and-plate geometry
$\eta$	(total) viscosity
$\eta^*$	complex viscosity
$\eta^P$	polymer contribution of the sPTT component to the viscosity
$\eta^U$	polymer contribution of the UCM component to the viscosity
$\eta_{sp}$	specific viscosity = $(\eta - \eta_s)/\eta_s$
$\eta_p$	polymer contribution to the viscosity
$\eta_s$	solvent viscosity
$\frac{D}{Dt}$	material derivative = $\frac{\partial}{\partial t} + \mathbf{v} \cdot \nabla$
$\Gamma$	aspect ratio (height/gap) of a Taylor-Couette cell
$\Im(\mu)$	imaginary part of a complex number $\mu$
$\kappa$	thermal conductivity
$\lambda$	relaxation time
$\lambda^P$	relaxation time of sPTT-component
$\lambda^U$	relaxation time of UCM-component
$\lambda_L$	Lamé's first parameter
$\lambda_r$	ratio of relaxation times $\lambda^U/\lambda^P$
$\langle R^2 \rangle$	mean-square end-to-end length of polymer molecules
$\mathcal{H}$	Heaviside function
$\mathcal{L}$	characteristic length
$\mathcal{M}$	torque
$\mathcal{R}$	characteristic radius of curvature
$\mathcal{T}$	characteristic stress
$\mathcal{U}$	characteristic velocity
$\mu$	(complex) eigenvalue
$\nabla_{\mathbf{v}}$	velocity gradient tensor
$\nabla$	Nabla, vector differential operator

$\nabla \mathbf{v}^\dagger$	transposed velocity gradient tensor
$\nu$	normalized (dimensionless) activation energy
$\Omega$	rotational velocity
$\omega$	angular frequency
$\phi$	polar angle
$\Psi$	temperature perturbation field
$\Psi_1$	first normal stress coefficient
$\Re$	real part of a complex number
$\rho$	mass density
$\square$	upper convected time derivative of $\square$
$\tau_{ij}$	components of the stress tensor
$\text{tr}(\square)$	trace of a tensor $\square$
$\Theta$	normalized (dimensionless) temperature
$\theta$	azimuthal angle
$\underline{T}$	stress tensor of Taylor-Couette base flow
$\underline{\delta}$	unity tensor
$\underline{\sigma}$	stress perturbation tensor
$\underline{\tau}$	stress tensor
$\varepsilon$	relative (dimensionless) gap width of the Taylor-Couette geometry
$\vartheta$	temperature
<b>F</b>	spring force vector
<b>Q</b>	polymer end-to-end vector
<b>u</b>	velocity perturbation vector
<b>w</b>	eigenvectors of generalized eigenvalue problem
<b>f</b>	force field vector (per unity mass)
<b>r</b>	position vector
<b>v</b>	velocity vector
$\xi$	drag coefficient
$\zeta$	parameter of the PTT model
$Br$	Brinkman number
$c$	polymer concentration
$c^*$	overlap concentration
$c^{***}$	corrected overlap concentration according to the approach by Solomon-Ciuta
$c^{**}$	corrected overlap concentration
$c_p$	specific heat capacity
$d$	gap width of the Taylor-Couette or plane Couette cell
$De$	Deborah number
$F$	force
$F_z$	normal force in the cone-and-plate rheometer
$G$	elastic (shear) modulus
$G'$	storage modulus
$G''$	loss modulus
$H$	spring constant
$h$	CaBER filament width
$K$	cubic equation giving the rheometric scaling of elastic instability of an Oldroyd-B fluid
$k_B$	Boltzmann's constant
$k_H$	Huggins coefficient
$k_z$	axial wavenumber
$L$	effective height of the inner cylinders of the Taylor-Couette cells

---

$L'$	space between the end face of the inner cylinder and the bottom of the outer beaker of the Taylor-Couette cells
$M$	critical Pakdel-McKinley (in)stability threshold
$m$	azimuthal wavenumber
$M_w$	weight-averaged molecular weight
$n$	number density of polymer chains or index
$N_A$	Avogadro constant
$N_{1,2}$	first/second normal stress differences
$Na$	Nahme number
$P$	pressure field of Taylor-Couette base flow
$Pe$	Péclet number
$Pr$	Prandtl number
$q$	pressure perturbation field
$R$	radius
$r$	radial coordinate
$R^2$	coefficient of determination
$Re$	Reynolds number
$S$	ratio of solvent to polymer viscosity
$t$	time
$T_n$	Chebyshev polynomial of the first kind of order $n$
$V_\theta$	azimuthal velocity field of Taylor-Couette base flow
$V_x$	upper plate velocity in simple unidirectional shear experiment
$Wi$	Weissenberg number
$x_k^{GL}$	Gauss-Lobatto points
$Z$	rescaled (dimensionless) temperature at the inner cylinder of the Taylor-Couette cell
$z$	relative axial position in the annular gap of the Taylor-Couette cell



---

## Preface

*“Everything is in a state of flux”* - πάντα ρεῖ (panta rhei). This is the famous aphorism of the greek philosopher Simplicius (~ 490-560) which inspired the designation “Rheology” coined by Eugene C. Bingham and Marcus Reiner in 1928 in the course of the re-establishment of the branch of physics dealing with the mechanics of continua [Pet67, Rei64]. Even if the originally underlying notion is philosophical rather than physical, it grasps the fundamental idea of rheology as the study of flow of any kind of matter and, in particular, without the restriction to “simple” fluids. Of course, the term “simple fluid” requires an explicit definition and it will be given in the scope of this work. At this point, we make do with a rather cursory and phenomenological distinction between a fluid that behaves water-like, called Newtonian, and a fluid that behaves in a different manner, i.e. non-Newtonian. But what is “different” in this context?

Indeed, non-Newtonian fluids exhibit multifaceted flow phenomena and they are literally omnipresent. We are surrounded by them in our everyday life: the ketchup, toothpaste or hair gel which all do not flow out of their bottles when just tilted until they are forced to do so by gently shaking or squeezing. The yeast dough in the stirrer which climbs up the stirring rod counter-intuitively and in contrast to how water would behave in the same situation, namely partially depleting the rod. The wet paint at the wall which remains there in a thin layer unlike pure water even if it behaves water-like when processed with the brush. Or even the versatile blood in our veins which “adapts” to the various conditions in the tiniest or biggest blood vessels, maintaining the life-sustaining transport of oxygen and plenty of biological compounds. This listing could be continued ad infinitum, in particular, when adding those fluids which appear to behave Newtonian but which reveal non-Newtonian flow properties when being thoroughly examined such as blood plasma [Bru13]. In this context, it strongly depends on “how” the fluids are handled, i.e. deformed (squeezed, shaken, stretched). It may be even crucial to know the complete history of the treatment in order to suggest the present state of a non-Newtonian fluid at hand.

In most of the commercial products listed above, the individual non-Newtonian flow characteristics are particularly desired and they are often tailor-made by the addition of small amounts of additives such as polymers or beads. As a consequence, the need for an extensive knowledge about how to establish the desired non-Newtonian fluid properties opened up a huge commercial market which stimulated thorough, fundamental research on non-Newtonian fluid dynamics. Today, looking back at more than sixty years of extensive research, the knowledge about the features of a non-Newtonian fluid flow is broad. Nevertheless, there are still unanswered questions which have to be addressed and which will engage scientists in the future.

The present work comprises the investigation of diverse flow phenomena of non-Newtonian

fluids with the focus on flow instabilities induced or influenced by elasticity, i.e. the transition from a state of laminar flow to the regime of more complex, non-laminar or even turbulent flow.

## Outline

**Part I** provides the **mathematical framework** for the investigations presented subsequently. It involves the **modeling of Newtonian and non-Newtonian fluid** flow, starting with the most simple relations in simple shear flow and extending to the formulation of the constitutive equations for arbitrary flow conditions. In doing so, the rheological terminology is introduced and non-Newtonian fluids are categorized. In the context of elastic flow instabilities, whose fundamental mechanism is elucidated, the **conception of linear stability analysis** is presented. Furthermore, the extensive **rheometric toolkit** is described from an experimental as well as a theoretical point of view and its handling is exemplified by means of a viscoelastic sample fluid.

**Part II** is the most extensive and outstanding part of the present work and deals with the study of various non-Newtonian, viscoelastic flow problems. The **non-inertial, viscoelastic Taylor-Couette flow**, i.e. the annular flow in the gap between two concentric, rotating cylinders, makes the main contribution. The focus is on the elastic instability of its laminar base flow and it is investigated in great detail by means of experimental, theoretical and numerical methods. Its experimental treatment is based on various polymer solutions which were thoroughly characterized prior to the main measurements in a set of various customized Taylor-Couette cells. The onset of elastic instability is analyzed with explicit focus on the **scaling with the characteristic (radius of) curvature** of the system. Based on an adequate constitutive model, **extensive linear stability analysis** supplements the experimental approach and the results are contrasted to the **theoretical predictions of a simple stability criterion by Pakdel and McKinley**. An additional study focuses on the **impact of polymer degradation** which has to be incorporated in a consistent interpretation of the overall findings.

**Part III** appends a collection of the **explicit rheometric measurements** of all polymer solutions investigated in the scope of the Taylor-Couette study. Furthermore, the mathematical framework is complemented by the introduction of the **Chebyshev collocation method** which underlays the numerical treatment of the linear stability analysis.

By reference of three appended publications, the author's contribution to the investigation of further viscoelastic flow problems is highlighted. It comprises the **viscoelastic flow in a serpentine channel**, the **elasto-inertial turbulence in pipe flow** as well as the **viscoelastic flow of human blood plasma** and it involves the **thorough rheological characterization** of the respective working fluids by steady shear and normal stress as well as extensional rheometry.

# **Part I**

## **Introduction**





stress components  $\tau_{ij}$ . In total, there are six shearing and three normal stress components, which build up the (deviatoric) stress tensor  $\underline{\tau} = (\tau_{ij})$ . From simple considerations of the stress components acting on a fluid element (cf. figure 2.1, right),  $\underline{\tau}$  has to be symmetric, i.e.  $\underline{\tau} = \underline{\tau}^\dagger$ , and for incompressible fluids  $\underline{\tau}$  is also tracefree, i.e.  $\sum_i \tau_{ii} = 0$ . This finally gives only three independent off-diagonal shear components and two normal stress differences of the diagonal elements

$$\tau_{xy} = \tau_{yx} , \quad (2.2)$$

$$\tau_{xz} = \tau_{zx} , \quad (2.3)$$

$$\tau_{yz} = \tau_{zy} , \quad (2.4)$$

$$N_1 = \tau_{xx} - \tau_{yy} , \quad (2.5)$$

$$N_2 = \tau_{zz} - \tau_{yy} . \quad (2.6)$$

For a simple Newtonian flow, the stress tensor  $\underline{\tau}$  is linearly related to the *rate-of-strain tensor*

$$\underline{\dot{\gamma}} = \nabla \mathbf{v} + \nabla \mathbf{v}^\dagger \quad (2.7)$$

and the constant of proportionality is the shear viscosity  $\eta$ , i.e.

$$\underline{\tau} = \eta (\nabla \mathbf{v} + \nabla \mathbf{v}^\dagger) = \eta \underline{\dot{\gamma}} . \quad (2.8)$$

Furthermore, in simple shear flow, the normal stress components  $\tau_{ii}$  of a Newtonian fluid all equal zero, and so do the normal stress differences. The deviation from this for non-Newtonian fluid, i.e. a non-zero (elastic) first normal-stress difference  $N_1 \neq 0$ , will be of fundamental importance in the further elaboration of non-Newtonian flow phenomena and we will revisit this point later on.

The most simple way to think of a deviation from the Newtonian characteristics of simple shear flow is a non-linear relation between the shear stress  $\tau = \tau_{xy}$  and the shear rate  $\dot{\gamma} = \dot{\gamma}_{xy}$ , i.e. their ratio at the observation time  $t$  may be a function of the current shear rate at time  $t$  and the shear stress history  $\tau(t')$ ,  $t' \leq t$ ,

$$\frac{\tau}{\dot{\gamma}}(\dot{\gamma}, t) = f(\dot{\gamma}, \tau(t')) . \quad (2.9)$$

According to the properties of  $f$ , which is also known as the *apparent shear viscosity*, a categorization of non-Newtonian materials into three categories can be performed [Chh10]: For *purely viscous* (or *generalized Newtonian*) fluids, only the current value of the shear stress at the time of observation determines the shear rate. The respective flow is time-independent and the fluid may e.g. show a shear-thinning ( $\partial_{\dot{\gamma}} f < 0$ ), shear-thickening ( $\partial_{\dot{\gamma}} f > 0$ ) or yield-stress behavior ( $\dot{\gamma} \equiv 0$  for  $0 < \tau < \tau_{\text{yield}}$ ). If the relation between shear stress and shear rate depends also on the stress history or the duration of the shear process, the fluids are called *time-dependent*. A prominent example is the thixotropic fluid, whose apparent viscosity drops when kept shearing at a constant shear rate. Everyday representatives are, e.g., tooth paste, ketchup or paints, where thixotropy contributes to the demanded specific functionality. Finally, *viscoelastic* systems combine fluid-like (viscous) and solid-like (elastic) properties. For example, a so called Boger fluid [Bog85] shows a constant shear viscosity, but the normal stress components are no longer zero and differ from each other, giving a first normal-stress difference, which depends on the shear rate.

The last point clearly shows that it is by far not sufficient to solely focus on single derived quantities such as the apparent viscosity in order to properly characterize a fluid at hand.

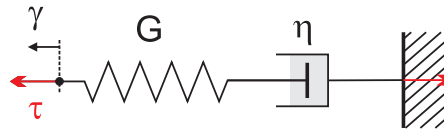


**Figure 2.2:** Sketch of a Maxwell element, a serial connection of an elastic spring and a viscous dashpot, characterized by the elastic modulus  $G$  and viscosity  $\eta$ , respectively.

A thorough description of a fluid has to take into account a complete investigation of the stress tensor by means of the measurement of viscous and potential elastic flow properties. In chapter 3 we will present different experimental methods which allow to extract the respective information. But first, we have to get a deeper understanding in the modeling of non-Newtonian fluid flow, which is essential to relate macroscopic quantities (as the flow curve  $\tau/\dot{\gamma}$ ) to the explicit properties of the flow. In the following, we will particularly focus on polymer solutions, which are well-known to exhibit viscoelastic flow behavior and which we thoroughly investigated in our experiments.

## 2.2 Linear viscoelasticity

In simple (unidirectional) shear flow, the shear stress in a Newtonian fluid is proportional to the shear rate, i.e.  $\tau_{xy} = \eta \dot{\gamma}_{xy}$ . In contrast, when replacing the Newtonian fluid by an elastic (Hookean) solid, for small displacements the shear stress is proportional to the shear component of the strain tensor, i.e.  $\tau_{xy} = G \gamma_{xy}$  with the elastic (shear) modulus  $G$ . With the objective of combining the ideas of viscosity and elasticity into a single constitutive equation, that describes the various effects of viscoelastic materials, early attempts were based on the use of mechanical analogues which involve combinations of two mechanical components: elastic (Hookean) springs and viscous dashpots [Bir84, Par11].

### 2.2.1 The Maxwell model

Accordingly, the most simple mechanical “spring-and-dashpot” model is given by a serial connection of a single spring and a single dashpot (cf. figure 2.2). The total strain rate according to this so-called *Maxwell element* is given by the summation of the contributions of the single components, i.e.

$$\dot{\gamma}_{xy} = \frac{\dot{\tau}_{xy}}{G} + \frac{\tau_{xy}}{\eta} . \quad (2.10)$$

It yields a linear relation between the shear stress and shear rate and it can be transformed to the form

$$\tau_{xy} + \lambda \dot{\tau}_{xy} = \eta \dot{\gamma}_{xy} \quad (2.11)$$

with a characteristic time constant  $\lambda = \eta/G$ . For steady-state motions, the shear is time-independent and the model reduces to the Newtonian shear flow equation. For sudden changes of the stress, its temporal derivative dominates the equation and the equation simplifies to Hooke’s law. In the generalized tensorial form, the *Maxwell model* is given by

$$\underline{\tau} + \lambda \dot{\underline{\tau}} = \eta \dot{\underline{\gamma}} . \quad (2.12)$$

Equation (2.12) can be transformed to an explicit equation for the stress. It is [Bir84]

$$\underline{\tau}(t) = \int_{-\infty}^t \left( \frac{\eta}{\lambda} e^{-\frac{t-t'}{\lambda}} \right) \dot{\underline{\gamma}}(t') dt' = \int_{-\infty}^t G^M(t-t') \dot{\underline{\gamma}}(t') dt' . \quad (2.13)$$

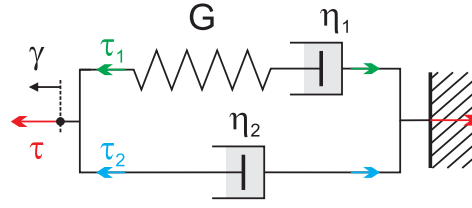


**Figure 2.3:** Sketch of a Jeffreys element, a parallel connection of a Maxwell element and a dashpot. It is characterized by an elastic modulus  $G$  and viscosities  $\eta_1, \eta_2$ .

Obviously, the stress at time  $t$  not only depends on the rate of strain at that time  $t$ , but on its complete history before. The contribution of  $\dot{\gamma}(t')$  is weighted by the so called relaxation modulus of the Maxwell model  $G^M(t - t')$  which exponentially decays with the time constant  $\lambda$ . Accordingly,  $\lambda$  has got the meaning of a relaxation time. Virtually, the system remembers what it has experienced in the past, but with kind of a “fading memory”.

## 2.2.2 The Jeffreys model

By adding a second dashpot in parallel to the Maxwell element, one gets a slightly more complicated, but still linear viscoelastic model. In the parallel connection, the stresses of each element add up to make the total stress. Thus, we have the relations

$$\underline{\tau} = \underline{\tau}_1 + \underline{\tau}_2, \quad (2.14)$$

$$\underline{\tau}_1 + \lambda \dot{\underline{\tau}}_1 = \eta_1 \dot{\underline{\gamma}}, \quad (2.15)$$

$$\underline{\tau}_2 = \eta_2 \dot{\underline{\gamma}}, \quad (2.16)$$

and one easily finds the constitutive equation of the *Jeffreys model*

$$\underline{\tau} + \lambda \dot{\underline{\tau}} = \eta \dot{\underline{\gamma}} + \eta_2 \lambda \ddot{\underline{\gamma}} \quad (2.17)$$

with the relaxation time  $\lambda = \eta_1/G$  and the total viscosity  $\eta = \eta_1 + \eta_2$ . According to (2.14) and with the relaxation modulus of the Maxwell model (2.13), the stress functions adds up to

$$\underline{\tau}(t) = \int_{-\infty}^t \left( \frac{\eta_1}{\lambda} e^{-\frac{t-t'}{\lambda}} + \delta(t-t')\eta_2 \right) \dot{\underline{\gamma}}(t') dt' = \int_{-\infty}^t G^J(t-t') \dot{\underline{\gamma}}(t') dt' \quad (2.18)$$

with the Dirac delta  $\delta(t-t')$ <sup>1</sup>. The Jeffreys model combines stresses of a Newtonian and Maxwellian component and we will show in the following, that this is the basis for well-established, nonlinear viscoelastic models.

## 2.3 Constitutive modeling

The simplicity of the previous modeling of a viscoelastic fluid in terms of the material function  $G(t-t')$ , associated with a linear relationship between the stress tensor and the rate-of-strain tensor, stems from the restriction to small displacements which leads to a linear velocity profile in the associated (unidirectional shear) experiment. Though, in the most general case where only the boundary conditions of the flow problem are predefined, the fundamental equations of motion and continuity have to be involved in the calculation of the explicit velocity profile which finally has to be mapped to the stress tensor. For Newtonian fluids, this leads to the so called *Navier-Stokes equations* which are introduced first in this section. They

<sup>1</sup>Here we use the definition of the Dirac delta according to  $\int_a^b f(x)\delta(x-x_0)dx = f(x_0)$  for  $a < x_0 < b$ .

are the basis for the following constitutive modeling of a viscoelastic fluid which involves the supplementation of a quasi-linear constitutive equation for the polymer stress tensor which adds up to the viscous stress tensor. For the quasi-linear *Oldroyd-B model*, this constitutive equation turns out to emerge from the linear viscoelastic Jeffreys model by replacing the time derivatives by the so-called *upper convected (Oldroyd) derivative*. The latter is required to provide invariance of the constitutive equations with respect to a rigid body rotation. Finally, the *PTT model* is presented as an extension of the Oldroyd-B model.

### 2.3.1 The Navier-Stokes equations

In the first half of the 19th century, the physicists Claude L. M. H. Navier and George G. Stokes independently developed the fundamental equation of momentum that constitutes the flow of a viscous, generally compressible fluid exposed to external forces. It can be derived from Newton's law of motion applied to a fluid element [Lor94]. With the fluid's mass density  $\rho$ , pressure gradient  $\nabla p$  and external force field  $\rho \mathbf{f}$  (which in general are all dependent of time and space), it is given by<sup>2</sup>

$$\frac{\partial(\rho \mathbf{v})}{\partial t} + \nabla \cdot (\rho \mathbf{v} \otimes \mathbf{v}) = -\nabla p + \nabla \cdot \underline{\boldsymbol{\tau}} + \rho \mathbf{f} . \quad (2.19)$$

The viscous stress tensor

$$\underline{\boldsymbol{\tau}} = \lambda_L (\nabla \cdot \mathbf{v}) \underline{\boldsymbol{\delta}} + \eta (\nabla \mathbf{v} + \nabla \mathbf{v}^\dagger) \quad (2.20)$$

is assumed to be composed of two contributions: the first one is given by the product of Lamé's first parameter  $\lambda_L$  and the divergence of the velocity field  $\nabla \cdot \mathbf{v}$  ( $\underline{\boldsymbol{\delta}}$  is the unity tensor) while the second contribution is the product of the rate-of-strain tensor  $\nabla \mathbf{v} + \nabla \mathbf{v}^\dagger$  and the dynamic viscosity  $\eta$  (Lamé's second parameter); cf. equation (2.8). Using the identities

$$\nabla \cdot (\nabla \mathbf{v} + \nabla \mathbf{v}^\dagger) = (\nabla \cdot \nabla) \mathbf{v} + \nabla (\nabla \cdot \mathbf{v}) , \quad (2.21)$$

$$\frac{\partial(\rho \mathbf{v})}{\partial t} + \nabla \cdot (\rho \mathbf{v} \otimes \mathbf{v}) = \left( \frac{\partial \rho}{\partial t} + \nabla \cdot (\rho \mathbf{v}) \right) \mathbf{v} + \rho \left( \frac{\partial \mathbf{v}}{\partial t} + \mathbf{v} \cdot \nabla \mathbf{v} \right) \quad (2.22)$$

with the Laplacian  $\nabla \cdot \nabla = \sum_i \frac{\partial^2}{\partial x_i^2}$ , the momentum equation can be written in the form

$$\left( \frac{\partial \rho}{\partial t} + \nabla \cdot (\rho \mathbf{v}) \right) \mathbf{v} + \rho \left( \frac{\partial \mathbf{v}}{\partial t} + \mathbf{v} \cdot \nabla \mathbf{v} \right) = -\nabla p + \eta (\nabla \cdot \nabla) \mathbf{v} + (\lambda_L + \eta) \nabla (\nabla \cdot \mathbf{v}) + \rho \mathbf{f} . \quad (2.23)$$

The first bracket on the left hand side is zero as it reflects the formulation of the continuity equation

$$\frac{\partial \rho}{\partial t} + \nabla \cdot (\rho \mathbf{v}) = \frac{\partial \rho}{\partial t} + \nabla \rho \cdot \mathbf{v} + \rho (\nabla \cdot \mathbf{v}) = 0 \quad (2.24)$$

which supplements the equation of momentum. Based on the reasonable approximation of incompressibility, it further simplifies to the common relation of vanishing divergence of the velocity field

$$\nabla \cdot \mathbf{v} = 0 . \quad (2.25)$$

Consequently, the *Navier-Stokes equations*

$$\rho \left( \frac{\partial \mathbf{v}}{\partial t} + \mathbf{v} \cdot \nabla \mathbf{v} \right) = -\nabla p + \eta (\nabla \cdot \nabla) \mathbf{v} , \quad (2.26)$$

$$\nabla \cdot \mathbf{v} = 0 \quad (2.27)$$

<sup>2</sup>The dyadic product  $\mathbf{a} \otimes \mathbf{b} \in \mathbb{R}^{n \times n}$ ,  $n \in \mathbb{N}$  of vectors  $\mathbf{a}, \mathbf{b} \in \mathbb{R}^n$  is defined as  $(\mathbf{a} \otimes \mathbf{b})_{ij} = a_i b_j$ ,  $i, j = 1, 2, \dots, n$ .

give a set of nonlinear partial differential equations for the velocity field  $\mathbf{v}(\mathbf{r}, t)$  of an incompressible, isothermal, viscous fluid in the absence of outer forces, supplemented by boundary conditions. As it gives a more transparent view to the basic assumption (2.20), we prefer the formulation

$$\rho \left( \frac{\partial \mathbf{v}}{\partial t} + \mathbf{v} \cdot \nabla \mathbf{v} \right) = -\nabla p + \nabla \cdot \underline{\tau}, \quad (2.28)$$

$$\underline{\tau} = \eta (\nabla \mathbf{v} + \nabla \mathbf{v}^\dagger), \quad (2.29)$$

$$\nabla \cdot \mathbf{v} = 0 \quad (2.30)$$

and we will refer to these equations as the (dimensional) Navier-Stokes equations in the following.

### Non-dimensionalization of constitutive equations

For a deeper insight into the system's intrinsic properties, it is useful to remove all the physical units from the constitutive equations. This can be achieved by introducing dimensionless quantities which give a measure of the original variables relative to respective quantities that are characteristic for the system. Therefore, we introduce a minimum set consisting of a characteristic length  $\mathcal{L}$  and velocity  $\mathcal{U}$  and we substitute all the variables by the product of the corresponding dimensionless variable (symbolized with a tilde) and some combination of the characteristic numbers and system parameters ( $\eta$  and  $\rho$ ) via

$$\mathbf{r} = \mathcal{L} \tilde{\mathbf{r}}, \quad \mathbf{v} = \mathcal{U} \tilde{\mathbf{v}}, \quad t = \frac{\mathcal{L}}{\mathcal{U}} \tilde{t}, \quad p = \eta \frac{\mathcal{U}}{\mathcal{L}} \tilde{p}, \quad \underline{\tau} = \eta \frac{\mathcal{U}}{\mathcal{L}} \tilde{\underline{\tau}}. \quad (2.31)$$

Hence the Navier-Stokes equations (2.28)–(2.30) can be rewritten in the dimensionless form (tildes are omitted)

$$Re \left( \frac{\partial \mathbf{v}}{\partial t} + \mathbf{v} \cdot \nabla \mathbf{v} \right) = -\nabla p + \nabla \cdot \underline{\tau}, \quad (2.32)$$

$$\underline{\tau} = \nabla \mathbf{v} + \nabla \mathbf{v}^\dagger, \quad (2.33)$$

$$\nabla \cdot \mathbf{v} = 0 \quad (2.34)$$

with the dimensionless *Reynolds number*

$$Re = \frac{\rho \mathcal{U} \mathcal{L}}{\eta}. \quad (2.35)$$

It is the ratio of inertial forces to viscous forces or the ratio of convection to diffusion rates of momentum, respectively. The use of dimensionless numbers as motivated above allows to compare the flow of different fluids in different flow situations. As long as the dimensionless Reynolds number is the same for the different situations, the solution of the Navier-Stokes equation by means of the dimensionless variables are identical. And so are all the respective features which are embedded in the mathematical characteristics of the constitutive equations.

It should be emphasized that the practical way of non-dimensionalization is arbitrary with respect to the choice of characteristic quantities. Of course, as long as the derived non-dimensional equations are exactly (analytically) solved, the results translated to real coordinates are identical regardless of the (arbitrary) set of characteristic quantities. However, this does not hold when the calculus is simplified by dropping single terms, e.g., in the approximation of negligible inertia  $Re = 0$ . And even if the calculus is solely limited by its numerical accuracy, the choice of characteristic quantities has to be appropriate in order to guarantee the convergence of numerical methods (ideally all the non-dimensional variables should be of order  $\mathcal{O}(1)$ ).

### 2.3.2 The elastic dumbbell (Oldroyd-B) model

As already illustrated in section 2.1, simple and complex fluids differ from each other fundamentally. It is the fundamental assumption of proportionality between the rate-of-strain tensor and the (viscous) stress tensor (cf. (2.20)) that leads to the formulation of the Navier-Stokes equations (2.32)–(2.34) and that governs the flow of any simple Newtonian fluid which is characterized by a constant viscosity. For polymer solutions, this simple relation between internal stresses and the local strain rate does not hold. Viscous stresses are superposed by elastic stresses which do not vanish instantly when the load ceases but which decay on a given time scale, defining a characteristic relaxation time. Hence the actual state of internal stresses directly depends on the past flow history, which gives rise to strongly non-Newtonian rheology and flow phenomena.

In order to understand these specific features, one has to find an expression for the polymer contribution to the total stress tensor by means of appropriate models of the fluids elasticity and its coupling to the surrounding fluid.

A rather simple mechanical approach which maps microscopic properties of a polymer (or its model) to macroscopic flow properties and which highlights the essential ingredients of effective model building, is given by the so-called *dumbbell models* (in the following we refer to explanations given in [Bir87]). They are based on the idea of interpreting the flexible polymer chains as entropic springs which tend to maintain a state of highest entropy by coiling up instead of being elongated. In this picture, a linear polymer is idealized by an elastic dumbbell, which is solely build up of two point masses connected by an elastic spring.

In the following, we assume the spring to be Hookean, i.e. the relation between the bead separation, given by the end-to-end vector  $\mathbf{Q}$  and the connector force  $\mathbf{F}^{(c)}$  is proportional

$$\mathbf{F}^{(c)} = H\mathbf{Q} \quad (2.36)$$

giving a characteristic spring constant  $H$ . The stretching of the spring is not restricted by any maximum separation of the beads. Furthermore each bead  $i$  only interacts with the surrounding fluid by a hydrodynamic drag force according to the Stokes' law

$$\mathbf{F}_i^{(h)} = -\xi(\mathbf{v}_i - \mathbf{v}_s(\mathbf{r}_i)) \quad (2.37)$$

with drag coefficient  $\xi$  and velocity of the respective bead  $\mathbf{v}_i$  relative to the velocity of the surrounding solvent  $\mathbf{v}_s(\mathbf{r}_i)$  at position  $\mathbf{r}_i$ . No direct or hydrodynamic interaction among the dumbbells themselves is considered. Consequently, this most simple dumbbell models is only applicable to describe very low concentrated (dilute) polymeric solutions. Finally, Brownian motion of the beads is considered.

Accounting for the superposed forces acting on the beads, combined with appropriate averaging<sup>3</sup> over all the dumbbells of number density  $n$  leads to two alternative relations for the polymer stress tensor

$$-\underline{\tau} = -nH \langle \mathbf{Q} \cdot \mathbf{Q} \rangle + nk_B \vartheta \underline{\delta}, \quad (2.38)$$

$$-\underline{\tau} = \frac{n\xi}{4} \langle \mathbf{Q} \cdot \overset{\nabla}{\mathbf{Q}} \rangle. \quad (2.39)$$

The use of the upper convected time derivative

$$\overset{\nabla}{\square} = \frac{\partial \square}{\partial t} + \mathbf{v} \cdot \nabla \square - (\nabla \mathbf{v}^\dagger \cdot \square + \square \cdot \nabla \mathbf{v}) = \frac{D \square}{Dt} - (\nabla \mathbf{v}^\dagger \cdot \square + \square \cdot \nabla \mathbf{v}) \quad (2.40)$$

<sup>3</sup>The phase-space average  $\langle f(\mathbf{Q}) \rangle$  is calculated with respect to the configuration-space distribution of the dumbbells  $\Xi(\mathbf{Q}, t)$  via  $\langle f(\mathbf{Q}) \rangle = \int f(\mathbf{Q}) \Xi(\mathbf{Q}, t) d\mathbf{Q}$ .

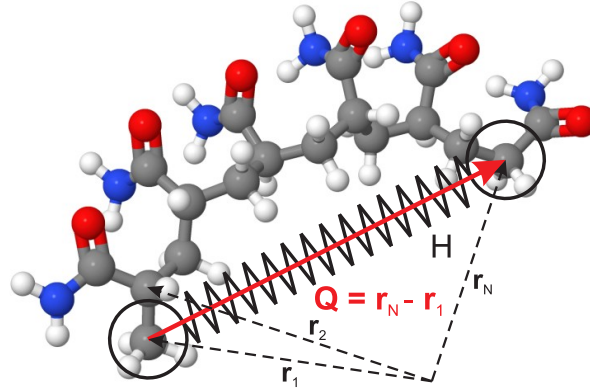


**Figure 2.4:** In the elastic dumbbell model, the polymer is represented by an elastic spring connecting two massless beads. The length of the elastic spring (with spring constant  $H$ ) is equal to the end-to-end vector  $\mathbf{Q} = \mathbf{r}_N - \mathbf{r}_1$  of the polymer backbone. Loading the spring means changing the conformation of the polymer.

allows for the independence of the equations of any coordinate system, which is convected and deformed with the fluid. In particular, the coordinate system is invariant with respect to a rigid body rotation that does not lead to any deformation. The convected time derivative includes the material derivative

$$\frac{D}{Dt} = \frac{\partial}{\partial t} + \mathbf{v} \cdot \nabla. \quad (2.41)$$

The stress equations (2.38) and (2.39) can be combined to

$$-\underline{\tau} = \frac{\xi}{4H} \left( \frac{\nabla}{\underline{\tau}} + nk_B\vartheta \frac{\nabla}{\underline{\delta}} \right), \quad (2.42)$$

and with the convected derivative of the unity tensor  $\frac{\nabla}{\underline{\delta}} = -(\nabla\mathbf{v} + \nabla\mathbf{v}^\dagger)$  and the time constant for the Hookean dumbbells

$$\lambda = \frac{\xi}{4H} \quad (2.43)$$

the constitutive equation for the polymeric stress tensor is given by

$$\underline{\tau} + \lambda \frac{\nabla}{\underline{\tau}} = nk_B\vartheta \lambda (\nabla\mathbf{v} + \nabla\mathbf{v}^\dagger). \quad (2.44)$$

It is worth mentioning that this corresponds to the respective stress equation (2.15) of the Jeffreys model by replacing the time derivative by the upper convected derivative and identifying the polymer viscosity

$$\eta_p = nk_B\vartheta \lambda. \quad (2.45)$$

Again, we can eliminate the units by using a set of characteristic quantities. In contrast to the previous choice for the rescaling of the Navier-Stokes equation, we now use a characteristic stress proportional to the polymer viscosity  $\mathcal{T} = \eta_p \mathcal{U} / \mathcal{L}$  and together with the numbers in (2.31) we obtain the dimensionless constitutive equation for the polymer stress tensor  $\underline{\tau}$  based on the linear elastic dumbbell model

$$\underline{\tau} + Wi \frac{\nabla}{\underline{\tau}} = \nabla\mathbf{v} + \nabla\mathbf{v}^\dagger. \quad (2.46)$$

This equation for the polymer stress tensor supplements the Navier-Stokes equations. The stress tensor in (2.32) has to be replaced by the sum of the viscous and polymer stress tensor.

With that we finally end up with the prominent *Oldroyd-B model* in dimensionless form

$$Re \left( \frac{\partial \mathbf{v}}{\partial t} + \mathbf{v} \cdot \nabla \mathbf{v} \right) = -\nabla p + (1 - \beta) \nabla \cdot (\underline{\tau}_s + \underline{\tau}), \quad (2.47)$$

$$\underline{\tau}_s = \frac{\beta}{1 - \beta} (\nabla \mathbf{v} + \nabla \mathbf{v}^\dagger), \quad (2.48)$$

$$\underline{\tau} + Wi \frac{\nabla}{\mathcal{L}} \underline{\tau} = \nabla \mathbf{v} + \nabla \mathbf{v}^\dagger, \quad (2.49)$$

$$\nabla \cdot \mathbf{v} = 0. \quad (2.50)$$

Aside from the Reynolds number  $Re$  another two parameters appear in the set of equations: the relative viscosity  $\beta = \eta_s/\eta = \eta_s/(\eta_s + \eta_p)$  as well as the so-called *Weissenberg number*

$$Wi = \lambda \frac{\mathcal{U}}{\mathcal{L}}. \quad (2.51)$$

It is the product of the characteristic time constant  $\lambda$  associated with the properties of the Hookean dumbbell and a characteristic rate of deformation  $\mathcal{U}/\mathcal{L}$ . The Weissenberg number  $Wi$  plays a fundamental role in the scope of this work and we will go into more detail with it later on (see section 2.4).

### 2.3.3 The Phan-Thien/Tanner (PTT) model

As will be presented later, the Oldroyd-B model suffers from the essential disability to describe the feature of shear thinning, which is a fundamental rheological property of many polymer solutions and melts. The so-called PTT-model overcomes this shortcoming. It has been derived by Nhan Phan-Thien and Roger I. Tanner from a network theory for polymeric fluids and considers the movement of junctions of polymer molecules which are created and destroyed by given rates and which can slip relative to the total motion of the fluid [Pha77, Pal05, Bir87]. Thus, in contrast to the Oldroyd-B model for dilute solutions, it is based on the explicit interaction of polymer chains. Accounting for a single polymeric fluid component with a single characteristic time constant  $\lambda$  and (zero-shear) viscosity  $\eta_p$ , which is diluted in a Newtonian solvent  $\eta_s$ , the governing equations are given in dimensionless form (using the same characteristic quantities as before, tildes are omitted) by

$$Re \left( \frac{\partial \mathbf{v}}{\partial t} + \mathbf{v} \cdot \nabla \mathbf{v} \right) = -\nabla p + (1 - \beta) \nabla \cdot (\underline{\tau}_s + \underline{\tau}), \quad (2.52)$$

$$\underline{\tau}_s = \frac{\beta}{1 - \beta} \dot{\underline{\gamma}}, \quad (2.53)$$

$$Wi \left( \frac{\nabla}{\mathcal{L}} + \frac{\zeta}{2} [\dot{\underline{\gamma}} \cdot \underline{\tau} + \underline{\tau} \cdot \dot{\underline{\gamma}}] \right) + f(\alpha; \underline{\tau}) \underline{\tau} = \dot{\underline{\gamma}}, \quad (2.54)$$

$$\nabla \cdot \mathbf{v} = 0, \quad (2.55)$$

with constant parameters  $\alpha, \zeta$ , the dimensionless rate-of-strain tensor  $\dot{\underline{\gamma}} = \nabla \mathbf{v} + \nabla \mathbf{v}^\dagger$  and  $f(\alpha; \underline{\tau})$  being a function of the trace of the polymeric stress tensor  $\underline{\tau}$ , i.e.  $\text{tr}(\underline{\tau}) = \sum_i \tau_{ii}$ . It can take either a linear or exponential form [Pal05, Bir87]

$$f(\alpha; \underline{\tau}) = 1 + \alpha Wi \text{tr}(\underline{\tau}), \quad (2.56)$$

$$f(\alpha; \underline{\tau}) = e^{\alpha Wi \text{tr}(\underline{\tau})}. \quad (2.57)$$

We will use the linear form throughout the presented work and with the special choice  $\xi = 0$  we refer to it as the simple PTT-model (sPTT). This model has been analytically analyzed in detail elsewhere (cf., e.g., [Mir05]), however without including a solvent contribution to

the stress tensor. With the inclusion of the latter, the analytical study is much more difficult even for the most simple flow situations. The sPTT-model incorporates all the features of the Oldroyd-B model which is included in the special case  $\alpha = 0$ , i.e. neglecting any (slipping) interaction of the dumbbells.

### 2.3.4 A non-isothermal two-component hybrid model

So far, we have presented two models based on rather simple interpretations of the polymer chains diluted in a Newtonian solvent. Despite their simplicity they turn out to reproduce fairly well most of the main rheological features of polymer solutions. The simplicity of these models originates in some approximations. One of them is the reduction to a single characteristic time constant given by a single spring constant in the modeling of Hookean dumbbells. This is a rather strong limitation as literally every polymer solution has to be described by some distribution of relaxation times which can be experimentally shown by chromatographic methods [Che70, Gra67]. But even though the theoretical analysis of respective models gives a more exact description of real fluids, their practical application with regard to the interpretation of experimental rheometry is limited.

Nevertheless, as they provide different rheological features, a linear combination of two single components, one of them Oldroyd-B (UCM) and the other one sPTT, with respective sets of parameters  $(\lambda^U, \eta^U)$  and  $(\lambda^P, \eta^P, \alpha)$ , gives a very useful hybrid model which allows to describe the rheology of our investigated solutions while both individual models fail to do it properly when applied separately. In dimensionless formulation, the constitutive equations for our hybrid model are given by

$$Re \left( \frac{\partial \mathbf{v}}{\partial t} + \mathbf{v} \cdot \nabla \mathbf{v} \right) = -\nabla p + \beta^P \nabla \cdot (\underline{\boldsymbol{\tau}}_s + \underline{\boldsymbol{\tau}}^P + \underline{\boldsymbol{\tau}}^U) , \quad (2.58)$$

$$\underline{\boldsymbol{\tau}}_s = \frac{\beta}{\beta^P} (\nabla \mathbf{v} + \nabla \mathbf{v}^\dagger) , \quad (2.59)$$

$$\underline{\boldsymbol{\tau}}^P [1 + \alpha Wi \operatorname{tr}(\underline{\boldsymbol{\tau}}^P)] + Wi \underline{\boldsymbol{\tau}}^P = \nabla \mathbf{v} + \nabla \mathbf{v}^\dagger , \quad (2.60)$$

$$\underline{\boldsymbol{\tau}}^U + \frac{\lambda^U}{\lambda^P} Wi \underline{\boldsymbol{\tau}}^U = \frac{\beta^U}{\beta^P} (\nabla \mathbf{v} + \nabla \mathbf{v}^\dagger) . \quad (2.61)$$

Here, all the stresses are non-dimensionalized by the characteristic stress  $\mathcal{T} = \eta^P \mathcal{U} / \mathcal{L}$  and the Weissenberg number is defined via the characteristic time of the sPTT component  $Wi = \lambda^P \mathcal{U} / \mathcal{L}$ . The Reynolds number  $Re = \rho \nu \mathcal{L} / \eta$  is calculated using the total (zero-shear) viscosity  $\eta = \eta_s + \eta^P + \eta^U$ .

As a second extension, we cancel the limitation of constant temperature and allow for non-isothermal fluid properties. The temperature function<sup>4</sup>  $\vartheta(\mathbf{r}, t)$  is constituted by the (dimensional) energy equation<sup>5</sup>

$$\rho c_p \frac{\partial \vartheta}{\partial t} = \kappa \Delta \vartheta + \eta (\nabla \mathbf{v} + \nabla \mathbf{v}^\dagger) : \nabla \mathbf{v} \quad (2.62)$$

which supplements the constitutive equations of our hybrid model. The heat capacity  $c_p$  and the thermal conductivity  $\kappa$  add to the set of fluid parameters. They are assumed to be constant and not a function of the temperature itself. The coupling of the energy equation

<sup>4</sup>For the rest of this section, all temperatures are given in Kelvins (K).

<sup>5</sup>For  $A, B \in \mathbb{R}^{n \times n}$  we defined the double sum  $A : B = \sum_{i,j=1}^n a_{ij} b_{ji}$ .

to the flow field is established by the temperature dependence of the fluid parameters, namely the viscosities  $\eta = \eta(\vartheta)$  and the relaxation times  $\lambda = \lambda(\vartheta)$  (the density is assumed to be constant). Thereby, we make two basic assumptions, which we then interpret by means of the dumbbell model: the first one is that the fluid's viscosity obeys the Arrhenius equation

$$\eta(\vartheta) = \eta(\vartheta_0) e^{\nu \left( \frac{\vartheta_0}{\vartheta} - 1 \right)} \quad (2.63)$$

with a reference temperature  $\vartheta_0$  and the normalized activation energy  $\nu = \Delta E / k_B \vartheta_0 > 0$ . The above is a well-established model to describe the mobility of molecules as a process which is activated by temperature. In section 9.6, we will show that equation (2.63) describes fairly well the viscosity of our investigated fluids within a temperature range relevant for our measurements. The second assumption concerns the dynamics of the polymer chains in terms of their entropic harmonic potential: the Hookean spring constant  $H$  is assumed to be proportional to the temperature, i.e.  $H \propto \vartheta$ . This can be motivated as follows: increasing the temperature increases the kinetic energy of the atoms of the polymer chains which consequently cover a larger region of the configuration space. Stretching the polymer chains from this state of increased entropy corresponds to a higher loss in entropy and thus in a higher value of the spring constant. Naturally, this affects the relaxation time according to equation (2.43).

When incorporating all these assumptions in the derivation of the non-isothermal constitutive model, we finally end up with the following set of dimensionless equations for the non-isothermal flow of a dilute, 2-component polymer solution

$$Re \left( \frac{\partial \mathbf{v}}{\partial t} + \mathbf{v} \cdot \nabla \mathbf{v} \right) = -\nabla p + f(\Theta) \left[ \beta \left( \Delta \mathbf{v} - \frac{\nu}{\Theta^2} \nabla \Theta \{ \nabla \mathbf{v} + \nabla \mathbf{v}^\dagger \} \right) + \beta^P \nabla \cdot \underline{\mathcal{T}}^{P+U} \right], \quad (2.64)$$

$$\underline{\mathcal{T}}^P \left[ 1 + \alpha \frac{Wi}{\Theta} \text{tr}(\underline{\mathcal{T}}^P) \right] + f(\Theta) \frac{Wi}{\Theta} \left( \underline{\mathcal{T}}^P - \frac{1}{\Theta} \frac{D\Theta}{Dt} \underline{\mathcal{T}}^P \right) = f(\Theta) (\nabla \mathbf{v} + \nabla \mathbf{v}^\dagger), \quad (2.65)$$

$$\underline{\mathcal{T}}^U + f(\Theta) \frac{\lambda^U Wi}{\lambda^P \Theta} \left( \underline{\mathcal{T}}^U - \frac{1}{\Theta} \frac{D\Theta}{Dt} \underline{\mathcal{T}}^U \right) = f(\Theta) \frac{\beta^U}{\beta^P} (\nabla \mathbf{v} + \nabla \mathbf{v}^\dagger), \quad (2.66)$$

$$\nabla \cdot \mathbf{v} = 0, \quad (2.67)$$

$$Pe \frac{D\Theta}{Dt} = \nabla \cdot \nabla \Theta + \beta Na (\nabla \mathbf{v} + \nabla \mathbf{v}^\dagger) : \nabla \mathbf{v} + \beta^P Na \underline{\mathcal{T}}^{P+U} : \nabla \mathbf{v} \quad (2.68)$$

with

$$f(\Theta) = e^{\nu \left( \frac{1}{\Theta} - 1 \right)}. \quad (2.69)$$

Aside from the continuity equation, all the equations depend on the dimensionless temperature  $\Theta := \vartheta / \vartheta_0$ . Thus, the energy equation is coupled to the momentum equation and the constitutive equations of the Oldroyd-B and sPTT component. Two more dimensionless groups appear in the energy equation, namely the *Péclet number*  $Pe$  and the *Nahme number*  $Na$ . The former

$$Pe = \frac{c_p \rho \mathcal{U} \mathcal{L}}{\kappa} \quad (2.70)$$

compares the rate of advection to the rate of diffusion of heat. It is related to the *Prandtl number*

$$Pr = \frac{Pe}{Re} = \frac{c_p \eta}{\kappa} \quad (2.71)$$

which is the ratio of viscous to thermal diffusion rates and consequently is governed by the fluid properties only. The *Nahme number*

$$Na = \frac{\eta \mathcal{U}^2}{\kappa \vartheta_0} \quad (2.72)$$

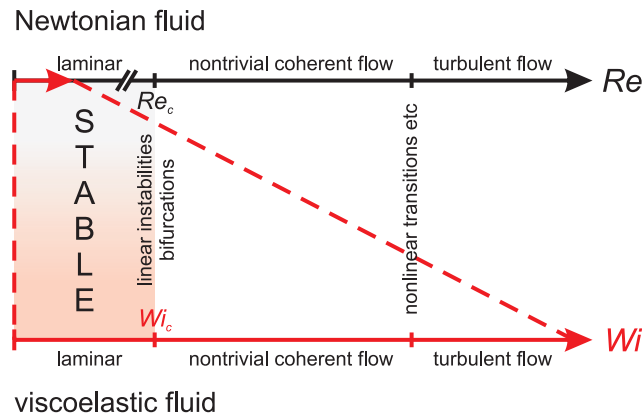


**Figure 2.5:** Sketch of the simplified flow scenario of a Newtonian and viscoelastic fluid. Adopted from Morozov *et al.* [Mor07].

gives a measure of the importance of viscous heating. It is related to the more prominent *Brinkman number*  $Br$  which gives the ratio of heat dissipated by viscous friction  $\eta\mathcal{U}^2$  and the heat conducted through the fluid due to a temperature difference  $\kappa\Delta\vartheta$ .

## 2.4 Hydrodynamic flow instabilities

*“When the state of things is such that an infinitely small variation of the present state will alter only by an infinitely small quantity the state at some future time, the condition of the system, whether at rest or in motion, is said to be stable; but when an infinitely small variation in the present state may bring about a finite difference in the state of the system in a finite time, the condition of the system is said to be unstable.”* [Cam82, Dra02].

This is how James Clerk Maxwell formulated the concept of stability of a state of a physical system in his essay on determinism and free will in 1872. As we will see in this section, this concept of “small variations” is strongly related to the concept of a linear stability analysis, which is rather a mathematical than a physical approach. In the following a more physical description of hydrodynamic (in)stability based on the constitutive models of (non-)Newtonian fluids is presented. Here, the Weissenberg number  $Wi$  will play a fundamental role.

### 2.4.1 Inertial vs. elastic flow instabilities and the physical meaning of the Weissenberg number

In section 2.3 we presented different constitutive models, which describe the flow of a simple or viscoelastic fluid. We have chosen the dimensionless form as it provides the possibility to compare different flow situations by simply asking for the dimensionless numbers. In the isothermal case, it is the Reynolds number  $Re$  and the Weissenberg number  $Wi$  that control the flow state of Newtonian and viscoelastic fluids. Figure 2.5 sketches the typical flow scenarios [Mor07].

At low Reynolds numbers, i.e. when viscous forces are dominant compared to inertial forces, the (non-inertial) Newtonian flow (*top axis*) is laminar and stable. This is related to the fact that the Reynolds number in (2.32) gives the weight of the non-linear term  $\mathbf{v} \cdot \nabla \mathbf{v}$  of the velocity field. With increasing  $Re$ , inertial forces become more and more important and so does the contribution of the non-linear term in the Navier-Stokes equation. At some critical value  $Re_c$ , the initially stable flow becomes unstable and more complicated flow patterns

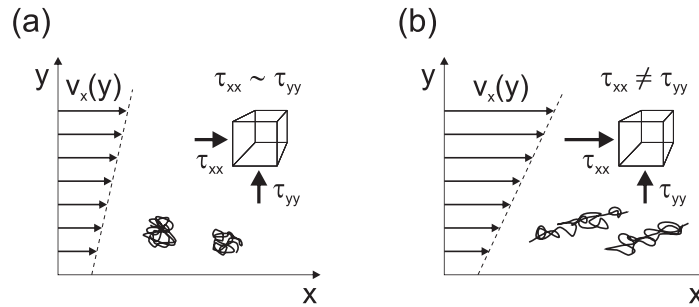


**Figure 2.6:** Sketch of the conformation of polymer chains under the influence of shear gradients of different strength. In the style of Morozov *et al.* [Mor07].

appear, which finally develop to turbulence when increasing the Reynolds number further. The exact value of  $Re_c$ , giving the onset of inertial instability, as well as the specific features of the nontrivial flow depend on the flow problem at hand that is characterized, e.g., by the explicit flow geometry and associated boundary conditions.

From a general point of view, this simplified Newtonian flow map can be adopted to the flow of a viscoelastic fluid (*bottom axis* in figure 2.5). While it is inertia which renders the flow of a Newtonian flow unstable, it is the impact of elasticity which maps to the different viscoelastic flow states. This impact is captured by the Weissenberg number. In analogy to the Reynolds number, it weights the nonlinear convected time derivative of the polymer stress tensor in the constitutive equations, e.g., (2.60) or (2.61).

The meaning of the Weissenberg number  $Wi = \lambda U / \mathcal{L}$  (or sometimes  $Wi = \lambda \dot{\gamma}$ ) as the indicator of elasticity becomes obvious when recalling its original definition by K. Weissenberg as the so-called “recoverable strain” which is the amount of strain that recovers after the release of the forces applied to a fluid at ground-state, bringing it to some energized state [Wei47]. White [Whi64] analyzed the steady shear flow of a second-order fluid and identified the recoverable strain with the dimensionless group  $\lambda U / \mathcal{L}$  which he consequently called the Weissenberg number. In the context of this analysis, the Weissenberg number can further be written as the ratio of the difference of normal stresses  $N_1 = \tau_{xx} - \tau_{yy}$  (called the first normal stress difference) and the shear stress  $\tau_{xy}$  associated with the polymers, i.e.

$$Wi = \frac{\tau_{p,xx} - \tau_{p,yy}}{2\tau_{p,xy}}. \quad (2.73)$$

Here, the flow is oriented in  $x$ -direction while the  $y$ -direction corresponds to the direction of the velocity variation (perpendicular to  $x$ ). The interplay between normal and shear stresses can be illustrated by figure 2.6, which sketches the conformation of polymer chains affected by a shear flow. At low shear rates (figure 2.6(a)), the polymer chains are hardly affected by the shear flow and the normal stresses are essentially isotropic, as there is no effective stretching of the polymers. When increasing the shear rate, the polymer chains are gradually stretched in the shear flow and the fluid becomes anisotropic, as the normal stress pointing along the streamlines is higher than in the direction perpendicular to the flow direction (figure 2.6(b)). Thus, the recoverable strain  $Wi$  “coordinates (...) the rheological states with respect to similitude in anisotropy in the sheared states” in an analogous way as does “the Reynolds number (...) with respect to similitude in the relative proportions of the forces of inertia and of internal friction” (citation of K. Weissenberg’s talk at the First International Rheological Congress in 1948, reprinted in [Whi64]).

The so-called *Weissenberg effect* - also known as *rod climbing effect* - impressively illustrates

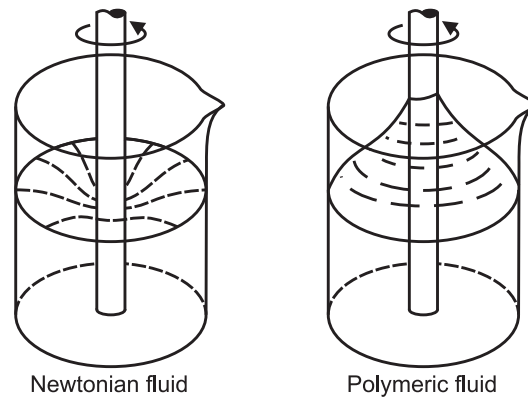


**Figure 2.7:** Sketch of the rod climbing effect of a viscoelastic (polymeric) fluid (*right*), contrasted by the partial depletion by a Newtonian fluid (*left*). In the style of Bird *et al.* [Bir84].

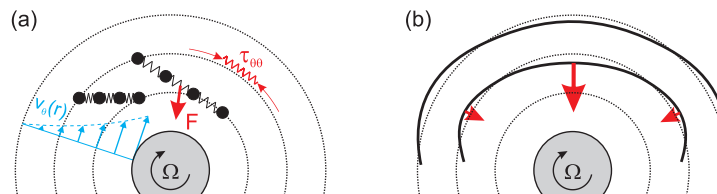


**Figure 2.8:** (a) Sketch of a polymer chain which is affected by shear forces and consequently pulled towards the rotating cylinder. (b) Linear instability: above the critical Weissenberg number, small perturbations to the flow will be amplified.

the impact of a non-zero normal stress difference [Bir84] (cf. figure 2.7) on the flow state of a viscoelastic fluid on a macroscopic scale. It describes the ascent of a viscoelastic fluid along an axially rotating cylindrical rod which is immersed into the fluid. This phenomenon is even observable at vanishing angular velocities far below the onset of inertially driven secondary flow. Obviously, the purely azimuthal, laminar shear flow at small shear rates is superposed by secondary flow, which is oriented towards the inner cylinder and which forces the fluid to climb up the rotating rod. In view of the scenario described before, this is obviously a manifestation of the elastic normal stress effect which couples to the curvilinear flow geometry at hand. Figure 2.8(a) sketches an explanation for the observation by means of a dumbbell representation of a polymer chain [Pak96]: when the Weissenberg number exceeds some critical Weissenberg number  $Wi_c$ , the shearing motion stretches the polymer chain non-uniformly and the normal stress acting along the streamlines  $\tau_{\theta\theta}$  (“hoop stress”) is amplified. This additional hoop stress translates to a radial force, which couples to the flow field by generating a radial velocity field towards the center of the system, that has to be compensated according to the continuity equation: the flow is pushed upwards. When  $Wi$  is slightly below the critical number  $Wi_c$ , any tiny perturbation of the flow lines (cf. figure 2.8(b)) will trigger the stress effect and causes secondary flow: the system is linearly unstable. Of course, the presented scenario is a very simplified approach and as the dependency on the given flow problem is crucial, it can only give a taste of the underlying mechanisms, which govern the flow of a viscoelastic fluid. Nevertheless, the presented normal stress effect in combination with a curvature of streamlines seems to be the main ingredient in the general recipe of elastic instability [Mor07].

### 2.4.2 Stability criterion by P. Pakdel and G. H. McKinley

In agreement with our final remark about the main ingredients of elastic instability in the previous section, P. Pakdel and G. H. McKinley were able to show that many of the explicit criteria for the onset of purely elastic instability in various curvilinear flow problems which are based on an interplay between curvature of streamlines and normal stress effect can be consistently formulated by a single, dimensionless criterion [McK96, Pak96, Mor07] of the form

$$\left[ \frac{\lambda \mathcal{U}}{\mathcal{R}} \frac{\tau_{11}}{\eta \dot{\gamma}} \right]^{0.5} \geq M. \quad (2.74)$$

Accordingly, this so-called *Pakdel-McKinley criterion* incorporates a characteristic radius of curvature  $\mathcal{R}$  and elastic normal stress  $\tau_{11}$  in the streamwise direction. They compete with the characteristic polymer relaxation length  $\lambda \mathcal{U}$  and the shear stress  $\tau_{12} = \eta \dot{\gamma}$ , respectively. The ratio  $\lambda \mathcal{U} / \mathcal{R}$  can be interpreted as a dimensionless measure of the (relative) distance over which disturbances to the base stress and velocity fields are advected compared to the local radius of curvature of the flow [McK96]. In other words, the ratio gives a measure of how much the stretched polymers can “feel” the curvature. This first geometrical term couples to the second rheological term which gives a measure of how much the elastic normal stress is extenuated by viscous drag. If the criterion is met at any point in the flow, i.e. when the left hand side of (2.74) exceeds the characteristic positive constant  $M$ , then tiny perturbations superposed to flow will be amplified and advected to other, initially stable regions in the flow which are consequently affected and which act as new sources of perturbations.

### 2.4.3 Linear stability analysis

In the previous sections, we motivated the onset of elastic instability by a rather cursory, but physical consideration of the nonlinear terms in the constitutive equations, which contribute to the equations via the Weissenberg number  $Wi$ . It can be reduced to a relation of the dynamical influence of viscoelastic normal stresses (taking into account the normal and the shear stress components  $\tau_{11}$ ,  $\tau_{22}$  and  $\tau_{12}$ ) which couple to the kinematic curvature of the streamlines [McK96]. Evaluating this procedure by facing the complexity of the strongly nonlinear constitutive equations presented above exhibiting a nonlinear coupling between the stress tensor  $\underline{\tau}$  and the velocity field  $\mathbf{v}$ , one can hardly imagine (or expect) to end up with a reasonable estimate of the exact transition point to elastic instability. However, from a mathematical point of view, one can approach the problem of the stability of a given flow state by applying well-established methods from stability theory by analyzing the explicit set of the constitutive, differential equations. This section gives only a short introduction to the topic of linear stability analysis, focusing on the aspects which are relevant for our study.

A given set of all incorporated flow variables

$$\mathbf{x}^B(\mathbf{r}, t) = \left( \tau_{ij}^B(\mathbf{r}, t), \mathbf{v}^B(\mathbf{r}, t), p^B(\mathbf{r}, t) \right) \quad (2.75)$$

which solve the complete mathematical set of constitutive equations including the corresponding boundary conditions, represents a physical flow state of the given fluid at any time  $t$  and position  $\mathbf{r}$  based on the underlying model. Let's identify this given solution of our constitutive model as the flow state, whose stability we want to analyze, and let's call it the base flow. Adapting to Maxwell's formulation of the stability of a physical state [Cam82, Dra02], we ask about the future impact of a small variation to this flow state given by a set of perturbation functions

$$\delta \mathbf{x}(\mathbf{r}, t) = \left( \delta \tau_{ij}(\mathbf{r}, t), \delta \mathbf{v}(\mathbf{r}, t), \delta p(\mathbf{r}, t) \right) \quad (2.76)$$

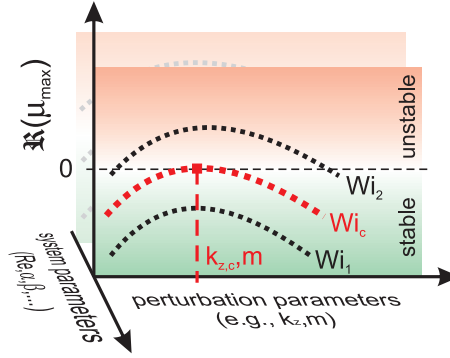


**Figure 2.9:** Schematic of the spectrum of eigenvalues  $\{\Re(\mu_{\max}(k_z, m))\}$  (real parts), which depends on all the parameters of the system such as the Reynolds number  $Re$ , shear thinning parameter  $\alpha$  or viscosity ratios  $\beta$ , and in particular on the Weissenberg number  $Wi$  and the characteristics of the perturbation (e.g., in Taylor-Couette flow the axial and azimuthal wavenumber  $k_z$  and  $m$ , respectively).

which superposes on the flow state  $\mathbf{x}^B(\mathbf{r}, t)$ . Thus, we have to analyze the temporal evolution of the perturbed state

$$\mathbf{x}(\mathbf{r}, t) = \mathbf{x}^B(\mathbf{r}, t) + \delta\mathbf{x}(\mathbf{r}, t) . \quad (2.77)$$

With the assumption of particularly small variation  $\delta\mathbf{x}$ , it is reasonable to simplify the nonlinear constitutive model by a linearization in the neighborhood of the base flow at hand. This is the general idea of a linear stability analysis. Let's representatively face a nonlinear system of differential equations in the explicit form

$$\dot{\mathbf{x}}(\mathbf{r}, t) = \mathcal{F}\{\mathbf{x}(\mathbf{r}, t)\} \quad (2.78)$$

with a nonlinear operator  $\mathcal{F}$ . With  $\mathbf{x}(\mathbf{r}, t)$  being the perturbed state according to (2.77), (2.78) can be linearized:

$$\dot{\mathbf{x}}^B(\mathbf{r}, t) + \dot{\delta\mathbf{x}}(\mathbf{r}, t) = \mathcal{F}\{\mathbf{x}^B(\mathbf{r}, t) + \delta\mathbf{x}(\mathbf{r}, t)\} = \mathcal{F}\{\mathbf{x}^B(\mathbf{r}, t)\} + A\delta\mathbf{x}(\mathbf{r}, t) + \mathcal{O}(\delta\mathbf{x}^2) \quad (2.79)$$

with the linear map  $A$  representing the linearization of  $\mathcal{F}$  in the neighborhood of the base flow  $\mathbf{x}^B(\mathbf{r}, t)$ . The latter solves the nonlinear system, i.e.  $\dot{\mathbf{x}}^B(\mathbf{r}, t) = \mathcal{F}\{\mathbf{x}^B(\mathbf{r}, t)\}$ , and thus, in first order approximation, the perturbed flow state is governed by the equation

$$\dot{\delta\mathbf{x}}(\mathbf{r}, t) \doteq A\delta\mathbf{x}(\mathbf{r}, t) . \quad (2.80)$$

With the common separation ansatz  $\delta\mathbf{x}(\mathbf{r}, t) = \delta\mathbf{x}(\mathbf{r}) \cdot y(t) = \delta\mathbf{x}(\mathbf{r})e^{\mu t}$ , this leads to a simple eigenvalue problem

$$\mu\delta\mathbf{x}(\mathbf{r}) = A\delta\mathbf{x}(\mathbf{r}) \quad (2.81)$$

for  $A$ . The corresponding eigenvectors give the different perturbation modes that the system is prone to and the respective eigenvalues  $\mu_i$  provide information on their stability. The base flow  $\delta\mathbf{x}(\mathbf{r}, t)$  is (linearly) stable, if all the eigenvalues  $\mu_i$  are smaller than zero in which case any perturbation mode exponentially decays. In contrast, if any eigenvalue  $\mu_i$  is greater than zero, the respective eigenvector (which refers to a special perturbation mode) will grow exponentially, and the flow is (linearly) unstable.

As we will demonstrate in the explicit analysis of the viscoelastic Taylor-Couette flow (cf. section 9), the starting point of the analysis is more complicated than assumed in (2.78). Namely, not only the perturbation functions  $\delta\mathbf{x}$  and their temporal derivatives but also their partial derivatives with respect to the spatial coordinates enter into the calculation. Furthermore, the system of differential equations becomes a coupled one and in general

an explicit analytical solution cannot be formulated. To cope with this additional degree of difficulty, one has to switch to numerical methods which provide an approximated and discretized solution of the problem leading to a generalized eigenvalue problem

$$\mu B \delta \tilde{\mathbf{x}}(r_i) = A \delta \tilde{\mathbf{x}}(r_i) \quad (2.82)$$

associated with a special set of discrete positions  $r_i$  within the flow. It is obvious that the eigenvalues  $\mu_j$  and eigenvectors  $\delta \tilde{\mathbf{x}}_j$  depend on all the system's parameters incorporated in  $A$  and  $B$ . It involves the Reynolds number  $Re$ , shear thinning parameter  $\alpha$  or viscosity ratios  $\beta$ . Referring to our viscoelastic flow problems, e.g., in the case of Taylor-Couette flow, and addressing the question of elastic instability, we are particularly interested in the impact of the Weissenberg number  $Wi$  (control parameter) on the spectrum of eigenvalues  $\mu(k_z, m)$  associated with predefined perturbation modes characterized by the azimuthal and axial wave numbers  $m$  and  $k_z$ , respectively. More precisely, when searching for the critical onset  $Wi_c$  of elastic linear Taylor-Couette instability, we have to increase  $Wi$  and to find the value  $Wi_c$  where the real part (in general, the eigenvalues are complex) of the spectrum of maximum eigenvalues  $\Re(\mu_{\max}(k_z, m))$  involves a positive value for the first time (cf. figure 2.9). Accordingly, we refer to the associated eigenvector as the first (or most) unstable perturbation mode. A more detailed description of the explicit numerical toolkit is presented in appendix B.1.



---

## Rheometric toolkit

From a theoretical point of view, we are now able to predict the rheology of a viscoelastic fluid by means of either linear or nonlinear constitutive equations. Depending on the explicit choice of the model, different fluid parameters are involved.

In principle, the analysis can be done for arbitrary flow situations and by supplementing the respective boundary conditions to the constitutive equations, the explicit flow field adapts to the problem. For special implementations of fluid flow which make use of symmetries, the given set of constitutive equations reduces to rather simple expressions for the stress components as functions of the incorporated flow parameters and the corresponding flow profiles turn out to be trivial. Consequently, these flows allow us to extract the fluid parameters in a rather convenient and simple way and such type of flows are called *rheometric*.

In this chapter, we present a selection of simple flow experiments which allow us to easily extract the characteristic fluid parameters of a set of polymer solutions that have been examined in our experiments. In doing so, we have to adapt the constitutive models to the given flow experiments and to fit the models to the experimental data. As a representative example for the different experiments, the corresponding data of a viscoelastic polymer solution (P600<sub>G80</sub>, cf. table 5.1 for a listing of the investigated solutions) are presented and discussed.

### 3.1 Rotational steady shear rheometry

#### 3.1.1 Methodology

One of the most simple and well-established flow experiments, which is commonly used to extract the fluid parameters of Newtonian as well as non-Newtonian fluids, is the rotational steady shear experiment. Figure 3.1 sketches a common realization of it, using a combination of a circular bottom plate and a coaxially arranged upper cone. We refer to it as the cone-and-plate setup. A sample of the test fluid is placed in the gap between the two geometries and the upper cone is axially rotated with a steady angular velocity. In order to minimize additional stress contributions, the amount of fluid has to be properly dimensioned so that the liquid-air interface is neither convex nor concave but flat. In our experiments, we commonly use a cone with an angle of  $\epsilon = 1^\circ$  or  $2^\circ$  and radius  $R = 30$  mm, while the radius of the bottom plate is  $R' = 30.5$  mm. The cone-and-plate geometry is embedded in a commercial rotational rheometer Haake MARS II (Thermo Fisher Scientific, Karlsruhe, Germany). While the bottom plate is fixed, the angular motion  $\Omega$  of the cone is performed by a DC motor mounted on a vertical positioning stage. Different operation modes are available, including a control of angular velocity (constant rate, CR) or torque (constant stress, CS). The applied

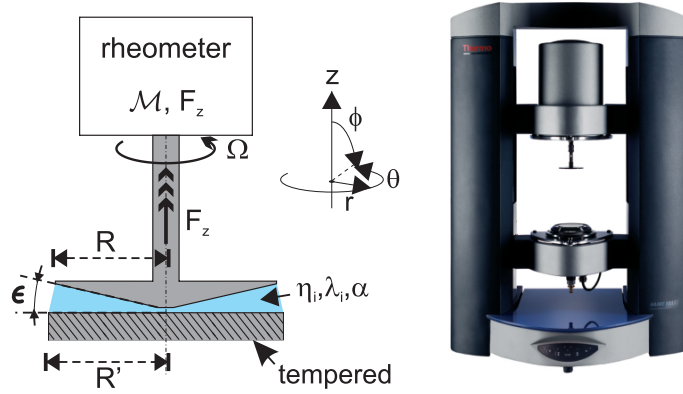


**Figure 3.1:** *Left:* Sketch of the cone-and-plate setup. *Right:* Photograph of a commercial Haake MARS rotational shear rheometer (courtesy of Thermo Fisher Scientific, Karlsruhe, Germany).

motor current is translated to the equivalent of the torque  $\mathcal{M}$  while inertial contributions due to the momentum of inertia of the rotating geometry and the motor as well as bearing forces are automatically accounted for. Reliable data can be acquired above a minimum torque of  $\mathcal{M}_{\min} \approx 2 \mu\text{Nm}$ . A strain gauge simultaneously measures the axial force  $F_z$  on the rotating cone down to values of  $F_{z,\min} \approx 10 \text{ mN}$ . Above this limit, the instrumental resolution is given with 1 mN. The mount of the bottom plate can be tempered by use of a closed-cycle thermostat and the desired temperature can be sustained during the operation with a precision of  $\pm 0.05^\circ\text{C}$  (as observed during the measurements). Allowing for potential temperature offsets of the sensors, the total accuracy of the temperature is supposed to be  $\pm 0.5^\circ\text{C}$ .

### 3.1.2 Rheometric output

In the case of small cone angles  $\epsilon$  (or  $\phi$  close to  $\pi/2$ ), the shear component of the rate-of-strain tensor ( $\phi\theta$ -component) in spherical coordinates is approximately constant in the laminar fluid flow in the gap [Bir84]

$$\dot{\gamma}_{\phi\theta}(r) = \frac{\sin \phi}{r} \frac{\partial}{\partial \phi} \left( \frac{v_\theta}{\sin \phi} \right) \doteq \frac{\Omega}{\epsilon} = \dot{\gamma}. \quad (3.1)$$

Hence, it is a good approximation of the unidirectional shear or plane-Couette experiment (cf. figure 2.1) with the favorable realization of a virtually infinite (closed-cycle) flow. Consequently, the respective shear stress component is constant and it can be easily calculated from the integral torque  $\mathcal{M}$  which acts on the cone at a constant rate of rotation. It is

$$\tau_{\phi\theta} = \frac{3\mathcal{M}}{2\pi R^3}. \quad (3.2)$$

Additionally, the axial normal force  $F_z$  can be translated to the first normal stress difference  $N_1$  by

$$N_1 = \frac{2(F_z - F_z^{\text{in}})}{\pi R^2}. \quad (3.3)$$

Here, one has to correct for inertial effects which cause an additional contribution to the axial force  $F_z^{\text{in}}$  which is directed in the opposite direction to  $F_z$ . It can be approximated by measuring the normal force data of the Newtonian solvent of the respective polymer solution.

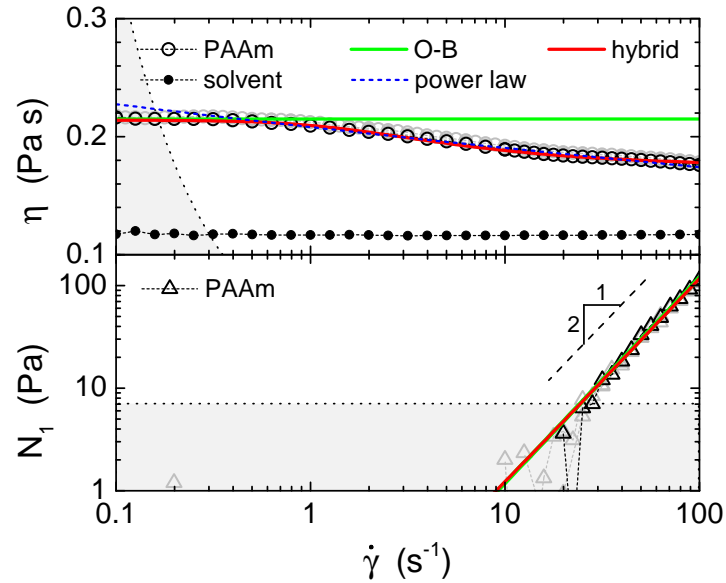


**Figure 3.2:** *Top:* Representative flow curve  $\eta(\dot{\gamma})$  of a polymer solution (P600<sub>G80</sub>, cf. table 5.1; open circles) and the corresponding solvent (filled dots), measured at  $\vartheta = 10^\circ\text{C}$ . *Bottom:* Corresponding data of first normal stress difference  $N_1(\dot{\gamma})$  (triangles). A cone-and-plate C60/2° setup has been used. Different models (colored lines) have been adapted to the data.

To conclude, the rotational rheometer equipped with a cone-and-plate setup and operated in steady shear mode provides steady shear stress and normal stress data, both depending on the shear rate  $\dot{\gamma}$  under control. In a standard scanning protocol, also called shear rate sweep measurement, in which the shear rate is stepwise increased according to a predefined schedule, the acquired data can be summarized by a presentation of the apparent viscosity  $\tau_{\phi\theta}(\dot{\gamma})/\dot{\gamma}$  (also called the flow curve) and the first normal stress difference  $N_1(\dot{\gamma})$ . In case of laminar (viscometric) flow, the first gives the apparent viscosity  $\eta(\dot{\gamma}) = \tau_{\phi\theta}(\dot{\gamma})/\dot{\gamma}$  (cf. equation (2.9)).

### 3.1.3 Representative data

Figure 3.2 shows representative data of a viscoelastic P600<sub>G80</sub> solution (circles and triangles). The sample consists of 600 ppm (parts per million, w/w) of polyacrylamide (molecular weight  $M_w = (5-6) \times 10^6$  Da) dissolved in an aqueous 80% glycerol solution. More information about the synthesis of the sample can be found in section 6. The viscosity data for the corresponding solvent (filled dots) are added. The measurements were performed in the C60/2° cone-and-plate setup at temperature  $\vartheta = 10^\circ\text{C}$  and the shear rate was increased stepwise, ranging from  $0.1\text{ s}^{-1}$  up to  $100\text{ s}^{-1}$  by waiting for 15 s at each step. The region beyond the working range of the rheometer (as outlined above) is highlighted in gray and consequently, data points within this region are not reliable. As expected, the viscosity of the Newtonian fluid is constant and gives  $\eta_s = (119 \pm 2)$  mPa s. In contrast, the flow curve of the polymer solution exhibits a non-Newtonian behavior in terms of shear thinning, i.e. the apparent viscosity  $\eta(\dot{\gamma})$  decreases with increasing shear rate. Furthermore, the first normal stress data shows an approximately quadratic growth with the shear rate.

### 3.1.4 Evaluation of rheometric data

In order to interpret the results of the steady shear experiment by means of the apparent viscosity and normal stress data in terms of the viscoelastic fluid properties, we adapt our 2-component Oldroyd-B/sPTT hybrid model to the explicit flow geometry. As motivated above, for small cone angles, the circular cone-and-plate flow exhibits a homogeneous shear rate. Thus, the flow can approximately be described by the plane-Couette flow, thereby simplifying the analytical calculus. After some straightforward calculus, we can extract the expressions for the steady state shear and normal stress components as functions of the shear rate  $\dot{\gamma}_{xy} =: \dot{\gamma}$

$$\tau_{xy}^s = \eta_s \dot{\gamma} \quad , \quad \tau_{xy}^P + 2\alpha \left( \frac{\lambda^P}{\eta^P} \right)^2 (\tau_{xy}^P)^3 = \eta^P \dot{\gamma} \quad , \quad \tau_{xy}^U = \eta^U \dot{\gamma} \quad (3.4)$$

$$\tau_{yy}^P = 2 \frac{\lambda^P}{\eta^P} (\tau_{xy}^P)^2 \quad , \quad \tau_{yy}^U = 2\eta^U \lambda^U \dot{\gamma}^2 \quad , \quad (3.5)$$

$$\tau_{xx}^P = \tau_{xx}^U = 0 \quad . \quad (3.6)$$

After solving the cubic equation (3.4) for the stress component  $\tau_{xy}^P$  we end up with the following expressions for the apparent viscosity and first normal stress difference:

$$\eta(\dot{\gamma}) = \frac{\sum \tau_{xy}(\dot{\gamma})}{\dot{\gamma}} = \eta_s + \eta^U + \frac{\tau_{xy}^P(\dot{\gamma}; \lambda^P, \eta^P, \alpha)}{\dot{\gamma}} \quad , \quad (3.7)$$

$$N_1(\dot{\gamma}) = \sum \tau_{yy}(\dot{\gamma}) = 2\eta^U \lambda^U \dot{\gamma}^2 + 2 \frac{\lambda^P}{\eta^P} (\tau_{xy}^P(\dot{\gamma}; \lambda^P, \eta^P, \alpha))^2 \quad . \quad (3.8)$$

In figure 3.2, adaptations of both the hybrid model (red curves) and the Oldroyd-B ( $\tau^P = 0$ , green curves) model are shown. Here, the data of the apparent viscosity and first normal stress difference are simultaneously fitted with a joint set of rheological parameters  $(\eta_s, \eta^U, \lambda^U, \eta^P, \lambda^P, \alpha)$ . As the Oldroyd-B model lacks the feature of shear thinning, it fails to reproduce the shape of the flow curve while the normal stress data is matched. In contrast, our hybrid model describes fairly well not only the normal stress data, but also the apparent viscosity. Table 3.1 lists the respective parameters of the best model fit. The data correspond to the evaluation of multiple independent measurements, giving values  $\bar{x} \pm \delta x$  of the respective parameters by means of the arithmetic mean values  $\bar{x} = N^{-1} \sum_{i=1}^N x_i$  and the unbiased sample variance  $\delta x^2 = (N-1)^{-1} \sum_{i=1}^N (x_i - \bar{x})^2$ . In fitting the model to the set of data, we use an iterative least-squares fitting method, performed by a commercial data analysis software (Origin 8.6 by OriginLab). We do not use absolute but relative errors, accounting for the fact that in the relevant region, the absolute values of the normal stresses are several magnitudes larger than the viscosity data and consequently, the latter would be neglected in the sum of absolute quadratic errors (the corresponding weighting method is proposed elsewhere [Mac94, Bir87]). The fitting routine turns out to be rather fragile, i.e. an initialization with reasonable starting parameters is important to obtain reliable fitting results in terms of minimum standard errors of the fitting parameters. We assume the viscosity  $\eta_s$  of the Newtonian contribution to be represented by the viscosity of the solvent, in the present case  $\eta_s = 119$  mPa s. Even if it is not fixed,  $\eta_s$  is not changed during the iterations. This is due to the additional contribution of the UCM component which gives another constant offset to the viscosity. While the parameters  $\eta^P$  and  $\eta^U$  are reproducibly estimated, giving small standard deviations, the uncertainty in the estimation of  $\lambda^P$  is rather high. This can be explained as follows: The additional sPTT component only significantly contributes to the shear stress component in order to account for the shear thinning of the viscosity data. Hereby, the zero-shear viscosity  $\eta^P$  as well as the thinning parameter  $\alpha$  are adjusted independently. As the normal stress data is already described by the UCM component (the normal stress

$\eta_s$ (mPa s)	$\eta^U$ (mPa s)	$\eta^P$ (mPa s)	$\lambda^U$ (ms)	$\lambda^P$ (ms)	$\alpha(\lambda^P)^2$ (s <sup>2</sup> )
119 ± 2	57 ± 1	40 ± 1	99 ± 5	23 ± 39	0.066 ± 0.014

**Table 3.1:** Fit parameters of the P600<sub>G80</sub> solution based on the 2-component hybrid model. The values  $\bar{x} \pm \delta x$  are given by the mean  $\bar{x} = N^{-1} \sum_{i=1}^N x_i$  and corresponding variance  $\delta x^2 = (N - 1)^{-1} \sum_{i=1}^N (x_i - \bar{x})^2$  calculated from sets of independent measurements.

basically scales quadratically with the shear rate), there is only a very weak contribution of the sPTT component in terms of the relaxation time  $\lambda^P$  (at given parameters  $\alpha$  and  $\eta^P$  from the viscosity data). Thus, it is the product  $\alpha(\lambda^P)^2$  which is adjusted predominantly via the adaption of the model to the viscosity data, giving reasonable error margins.

## 3.2 Relaxation after cessation of steady shear stress

### 3.2.1 Methodology

A different way to extract quantitative informations about the properties of viscoelastic fluid flow has been presented by Baravian *et al.* [Bar98]. In their experiments they made use of the instrumental inertia of the rheometric device (involving a coaxial cylindrical geometry) and its coupling to the fluid's elasticity to analyze the nonlinear behavior of a yield stress fluid. The system's response to a sudden cessation of the applied steady shear stress resulted in free oscillations of the cylinder and the oscillating movement has been analyzed based on a linear Kelvin-Voigt model. It turned out to be governed by one particular relaxation time of the fluid's relaxation spectrum.

Adapting to this method, we analyzed our polymer solutions by use of our rotational shear setup in stress-controlled mode (CS) as presented in section 3.1. First, we applied a constant shear stress  $\tau_0$  to the system, waiting for steady state, i.e. a constant shear rate  $\dot{\gamma}$ . Subsequently, the system's response to the sudden cessation of the shear stress  $\tau_0(1 - \mathcal{H}(t - t_0))$  has been recorded in terms of the shear movement  $\dot{\gamma}(t)$  of the cone ( $\epsilon = 2^\circ$ ,  $R = 30$  mm). The initial shear stress  $\tau_0$  has been varied in the range of two order of magnitudes. Figure 3.3 shows a sketch of the experiment.

### 3.2.2 Representative data

Figure 3.4 shows representative data for the P600<sub>G80</sub> solution. The shear rate  $\dot{\gamma}(t)$ , normalized by the initial shear rate in the steady state  $\dot{\gamma}_0 = \dot{\gamma}(\tau_0)$ , is plotted against the time  $t$  after cessation of shear stress. The relaxation curves are shown for five different initial stresses ranging from  $\tau_0 = 0.1$  Pa to  $\tau_0 = 10$  Pa which correspond to initial shear rates between  $\dot{\gamma}_0 = 0.47$  s<sup>-1</sup> and  $\dot{\gamma}_0 = 55.25$  s<sup>-1</sup>. Thus, all initial flow states  $\dot{\gamma}(\tau_0)$  can be found in the steady shear flow curves (cf. section 3.1).

All curves show a common behavior: after switching off the shear stress, the rotation of the cone slows down, i.e. the shear rate decreases. The higher the initial shear stress  $\tau_0$ , the longer takes it for the cone to slow down. After about 0.3 s to 0.4 s, the curves show a kink which is followed by a single oscillation which finally relaxes to the state of rest ( $\dot{\gamma}(t \rightarrow \infty) = 0$ ). This oscillation is connected to a reversal of the direction of rotation and it suggests the picture of an damped, elastic recoil.

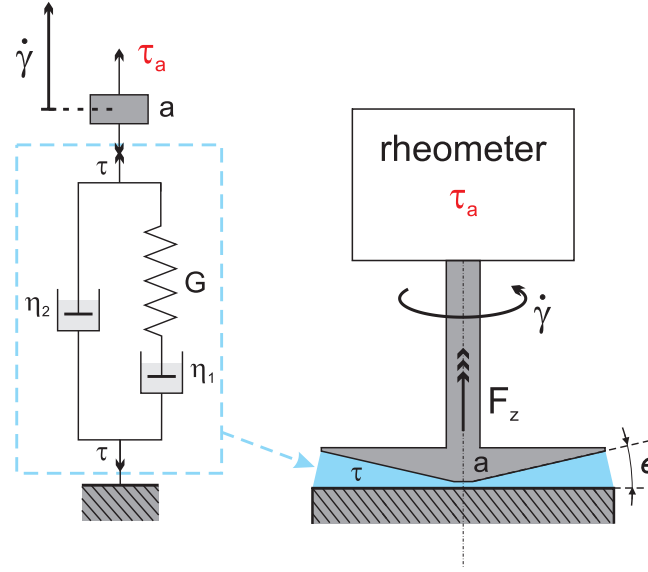


**Figure 3.3:** Schematic representation of the Jeffreys model adapted to the experimental setup.

### 3.2.3 Evaluation of rheometric data

Following the approach in [Bar98], we now want to analyze the stress relaxation data by means of a linear viscoelastic model, namely the Jeffreys model introduced in section 2.2.2. When accelerating the cone, the rheometer has to compensate for the inertia of the rotating device. Here, the stress  $\tau_a$  applied to the cone depends on the shear stress exerted to the fluid via

$$\frac{\tau_a(t) - \tau(t)}{a} = \ddot{\gamma}(t) \quad (3.9)$$

with  $a = 3\alpha J/2\pi R^3$  giving a measure of the momentum of inertia  $J$ . Vice versa, if the fluid exerts a stress on the cone, its movement is governed by its momentum of inertia. Combining (3.9) with the constitutive equation (2.17) and applying the special form of the applied stress

$$\tau_a(t) = \tau_0(1 - \mathcal{H}(t - t_0)) \quad , \quad \dot{\tau}_a(t) = -\tau_0\delta(t - t_0) \quad (3.10)$$

leads to

$$\ddot{\gamma}(t) + \underbrace{\frac{a + \lambda\eta_2}{\lambda a}}_{=:2A} \dot{\gamma}(t) + \underbrace{\frac{\eta_1 + \eta_2}{\lambda a}}_{=:B^2} \gamma(t) = \underbrace{\frac{\tau_0}{\lambda a}}_{=:C} [1 - \mathcal{H}(t - t_0) - \lambda\delta(t - t_0)] \quad (3.11)$$

Equation (3.11) corresponds to the differential equation of the forced damped harmonic oscillator. Its general response  $x(t) := \dot{\gamma}(t)$  is known to be either overdamped ( $A > B$ ), underdamped ( $A < B$ ) or critically damped ( $A = B$ ), depending on the system's parameters. The experimental data suggest an underdamped situation but close to the critical damping as only one oscillation can be observed. The general solution of the underdamped, forced harmonic oscillator can be derived via Laplace transform and one gets

$$\begin{aligned} \dot{\gamma}(t) = & \frac{C}{B^2} + \frac{e^{-Ax}(\dot{\gamma}_0 B^2 - C)}{B^2 \sqrt{D}} \left[ A \sin(\sqrt{D}t) + \sqrt{D} \cos(\sqrt{D}t) \right] \\ & + \mathcal{H}(t - t_0) \frac{C e^{-A(t-t_0)}}{B^2 \sqrt{D}} \left[ (A - \lambda B^2) \sin(\sqrt{D}(t - t_0)) + \sqrt{D} \cos(\sqrt{D}(t - t_0)) \right] \\ & - \mathcal{H}(t - t_0) \frac{C}{B^2} \end{aligned} \quad (3.12)$$

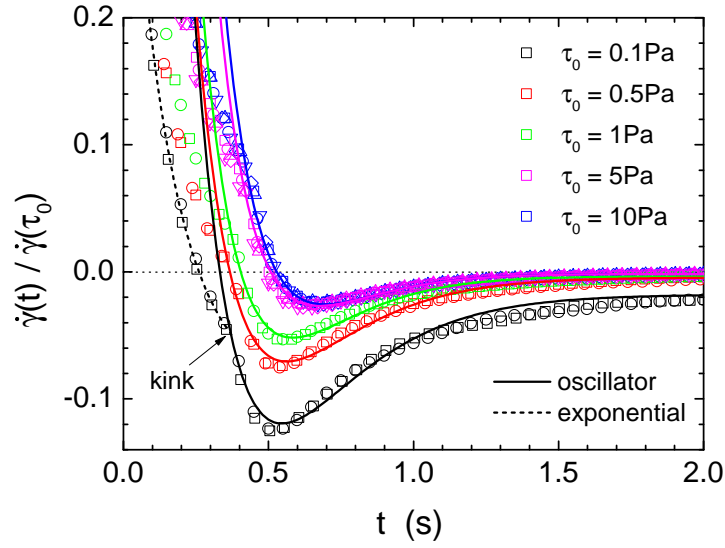


**Figure 3.4:** Representative data of the shear rate  $\dot{\gamma}(t)$  during the stress relaxation after the cessation of steady shear. The data is normalized for the initial shear rate, given by  $\dot{\gamma}_0 = \dot{\gamma}(\tau_0)$ . Different curves correspond to different initial shear stresses  $\tau_0$ .

with the substitutions  $A, B, C$  as highlighted above,  $D = B^2 - A^2$  and the implemented boundary conditions  $\dot{\gamma}(0) = \dot{\gamma}_0, \ddot{\gamma}(0) = 0$ . Here we accounted for an arbitrary instant of time  $t_0 \geq 0$  at which the stress is switched off. In the steady state ( $t < t_0$ ), the shear rate is constant  $\dot{\gamma}_0$  and the shear stress is accordingly given by  $\tau(t < t_0) = \tau_s(t < t_0) = \tau_0 = (\eta_1 + \eta_2)\dot{\gamma}_0$ . This last relation corresponds to  $C = \dot{\gamma}_0 B^2$  and equation (3.12) simplifies to

$$\dot{\gamma}(t) = \begin{cases} \dot{\gamma}_0 & , t < t_0 \\ \dot{\gamma}_0 e^{-A(t-t_0)} \left[ \frac{A-\lambda B^2}{\sqrt{D}} \sin(\sqrt{D}(t-t_0)) + \cos(\sqrt{D}(t-t_0)) \right] & , t \geq t_0 \end{cases} \quad (3.13)$$

In order to extract the relaxation time from an adaption of (3.13) to the experimental data, we have to estimate the rescaled momentum of inertia  $a$  as well as the viscosity  $\eta_2$ . According to the results of the steady shear measurements, we assume  $\eta_2$  to be the solvent viscosity  $\eta_2 = \eta_s = 119$  mPa s. The parameter  $a$  can be extracted by additional relaxation measurements with three different Newtonian fluids. The results are presented in figure 3.5 in terms of the averaged data of multiple independent measurements. Clearly, the different fluids describe the same exponential law as the rescaled curves collapse to a master curve (apart from deviations at very low shear rates which are assumed to be due to a resolution problem). This is consistent with the theoretical prediction obtained from the solution of the differential equation (3.11) for Newtonian fluids

$$\dot{\gamma}(t) = \dot{\gamma}_0 \left[ 1 - \left( 1 - e^{-\frac{\eta_2}{a}(t-t_0)} \right) \mathcal{H}(t-t_0) \right]. \quad (3.14)$$

Accordingly, the rescaled momentum of inertia  $a$  of the rotating device can be estimated by  $a = (16.4 \pm 0.1)$  mPa s<sup>2</sup>. Even if this value is somewhat higher than estimated from simple geometrical considerations ( $a_{\text{geom}} \approx 9.6$  mPa s<sup>2</sup>) involving the inertia of the cone as well as the inertia of the revolving fluid, the extracted value seems to be a reasonable measure of the system's momentum of inertia. Finally, with the estimates of  $a$  and  $\eta_2$ , we can extract the relaxation time  $\lambda$  as well as the viscosity  $\eta_1$  from an adaption of (3.13) to the experimental relaxation data. In figure 3.4, the respective curves are added (solid lines). Here, we have

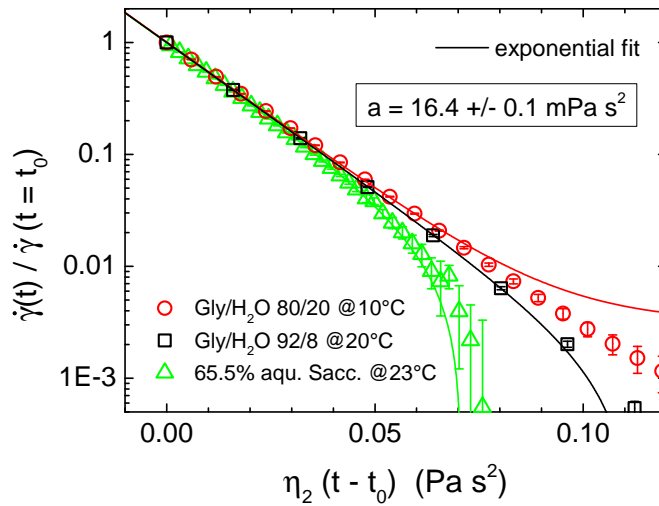


**Figure 3.5:** Relaxation of the shear rate of different Newtonian fluids after cessation of steady shear stress. Based on equation (3.14) one can estimate the rescaled momentum of inertia  $a$  of the moving device to  $a = (16.4 \pm 0.1)$  mPa s<sup>2</sup>.

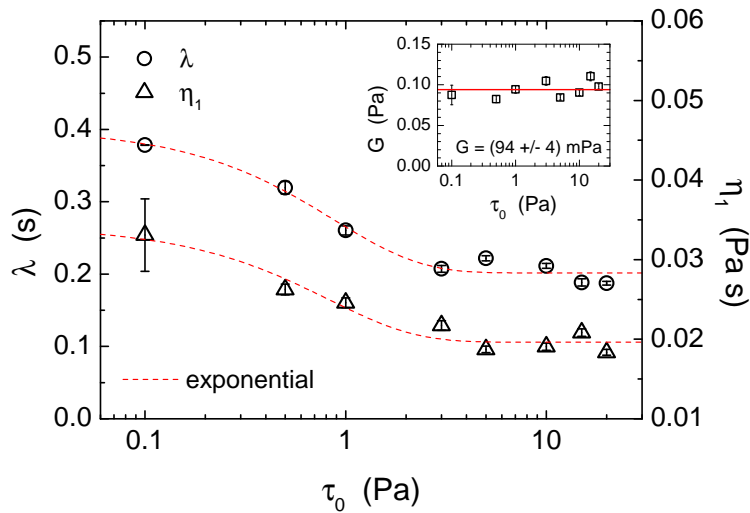


**Figure 3.6:** Characteristic relaxation time  $\lambda$  and viscosity  $\eta_1$  of the P600<sub>G80</sub> polymer solution, extracted from the shear rate relaxation experiment as a function of the initially applied shear stress according to equation 3.13. Both the data can be fitted by an exponential:  $y(\tau_0) = y_\infty + (y_0 - y_\infty)e^{-C\tau_0}$ . The shear modulus is rather constant  $G = \eta_1/\lambda \approx 94$  mPa (cf. inset).

to account for the reproducible kink which gives a little shift for the extrapolated instant of time  $t_0 > 0$  when the stress is shut off. Before the kink, the shear rate exponentially drops (cf. dashed line). We suppose some delay in the proper stress control or data acquisition of the rheometer that causes this systematic deviation from the expected curve. However, the further behavior beyond the kink is in good agreement with the theoretical model. Here, we allowed for some offset  $\lim_{t \rightarrow \infty} \dot{\gamma}(t) \neq 0$  which is likely to be due to a resolution problem at very low shear rates. The extracted values for the relaxation time  $\lambda$  and viscosity  $\eta_1$  are shown in figure 3.6. Both parameters exhibit some exponential converging behavior. The

extrapolated zero-shear values are

$$\eta_1 = (34 \pm 3) \text{ mPa s} , \quad (3.15)$$

$$\lambda = (401 \pm 24) \text{ ms} . \quad (3.16)$$

Consistent with our linear viscoelastic model which characterizes the elasticity by means of a Hookean spring with an elastic modulus  $G = \eta_1/\lambda$ , the ratio of our viscosity and relaxation time data appears to be constant independent of the initial shear stress  $\tau_0$ . Its value is given by

$$G = (94 \pm 4) \text{ mPa} . \quad (3.17)$$

Hence, for the presented polymer solution the linear Jeffreys model seems to provide a reasonable description of the viscoelastic behavior in our stress-controlled experiment. An evaluation of respective measurements of other polymer solutions is presented later.

### 3.3 Small amplitude oscillatory rheometry (SAOR)

#### 3.3.1 Methodology

In the previous relaxation experiment we analyzed the system's oscillatory response to a sudden change in the shear stress which has been applied by the sensor of a rheometer. With the stress being the control parameter, we refer to this method as a stress experiment. In contrast, in a strain experiment the system's stress response to a forced deformation is analyzed. In this context, a small-amplitude sinusoidal excitation is commonly used and the frequency-dependent response is investigated. Here, the amplitudes are explicitly limited in magnitude in order to guarantee for the validity of linear modeling.

For small deformation frequencies  $\omega$  and high viscosities, the instantaneous velocity profile produced by small amplitude oscillations is almost linear [Bir87], i.e. the accumulated shear strain  $\gamma$  can be calculated from the past shear rate  $\dot{\gamma}$  by simple integration over the respective time period, i.e.

$$\gamma(t) = \int_0^t \dot{\gamma}(t') dt' = \gamma_0 \sin(\omega t) , \quad (3.18)$$

$$\dot{\gamma}(t) = \gamma_0 \omega \cos(\omega t) . \quad (3.19)$$

While for Newtonian fluids, the shear stress response is in phase with the applied shear rate (giving the Newtonian shear viscosity), for non-Newtonian (viscoelastic) materials, the stress response is out of phase, i.e.

$$\tau(t) = \tau_0 \sin(\omega t + \varphi) = G'(\omega) \gamma^0 \sin(\omega t) + G''(\omega) \gamma^0 \cos(\omega t) . \quad (3.20)$$

This is equivalent with the complex formulation<sup>1</sup>

$$\tau^*(t) = G^*(\omega) \gamma^*(t) = [G'(\omega) + iG''(\omega)] \gamma^*(t) \quad (3.21)$$

From the storage modulus  $G'(\omega)$  (giving the stress contribution which is stored in terms of elastic energy) and the loss modulus  $G''(\omega)$  (which gives the stress contribution that is lost by viscous dissipation), one can derive the fluid properties by applying a respective linear viscoelastic model.

In this small strain experiment, we used again the cone-and-plate setup as presented in the previous sections. The cone is forced by the rheometer to oscillate at given frequencies  $\omega$ ;

<sup>1</sup>A star denotes a complex variable.

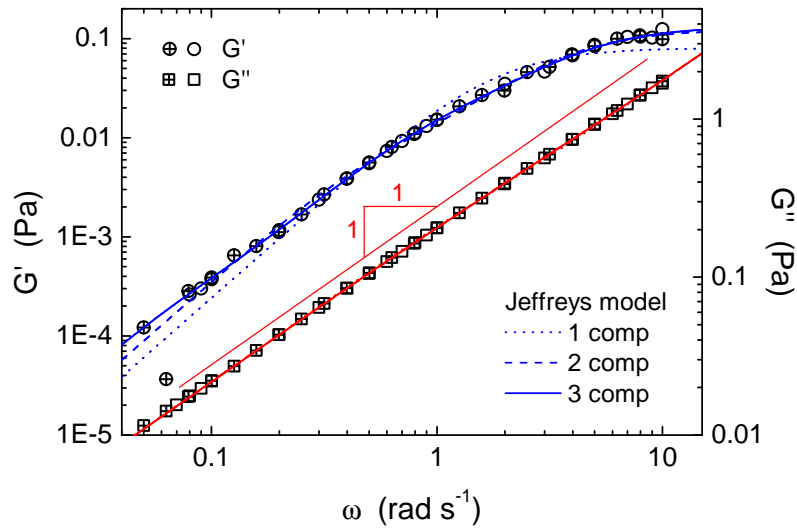


**Figure 3.7:** Results from small amplitude oscillatory rheometry of the P600<sub>G80</sub> solution. The storage modulus  $G'(\omega)$  (circles) and loss modulus  $G''(\omega)$  (squares) are shown for two independent measurements. Best fit approximations of a one- (dotted), two- (dashed) and three-component (solid) Jeffreys model are added. The corresponding model curves of  $G''(\omega)$  collapse as  $\eta_2$  is almost constant for all the fitted curves (cf. table 3.2).

and fixed amplitude  $\gamma_0$  and the in-phase and out-of-phase component of the stress response is recorded. This provides the material functions  $G'(\omega)$  and  $G''(\omega)$  which are characteristic of the given viscoelastic fluid. In order to guarantee for the applicability of the linear viscoelastic models, the deformation amplitude  $\gamma_0$  has to be appropriately chosen. To find its upper limit, the material functions are analyzed at a fixed frequency but increasing deformation amplitude. In this preliminary so-called strain-test, exceeding the linear regime is highlighted by a drop in the material functions.

### 3.3.2 Representative data

Figure 3.7 shows the result of oscillatory shear measurements of the P600<sub>G80</sub> polymer solution. The storage and loss modulus  $G'(\omega)$  and  $G''(\omega)$  are presented as functions of the oscillation frequency  $\omega$  ranging from 0.05 rad s<sup>-1</sup> to 10 rad s<sup>-1</sup>. The data is taken from two different independent measurements, using different incrementation in frequency. The deformation amplitude is set to  $\gamma_0 = 1$  which is at the upper limit of the linear response regime. While the storage modulus  $G'(\omega)$  ranges from 10<sup>-4</sup> Pa to 10<sup>-1</sup> Pa in the investigated frequency range, the loss modulus  $G''(\omega)$  is significantly higher between 10<sup>-2</sup> Pa and 2 Pa. Thus the stress response of the P600<sub>G80</sub> solution appears to be mostly Newtonian. Next, we want to quantify this finding.

### 3.3.3 Evaluation of rheometric data

When inserting the applied deformation (3.18) into the constitutive equation for the Jeffreys model (2.17), we find for the stress response

$$\tau(t) = \frac{\eta + \eta_2 \lambda^2 \omega^2}{1 + \lambda^2 \omega^2} \gamma_0 \omega \sin(\omega t) + \frac{\eta_1 \lambda \omega}{1 + \lambda^2 \omega^2} \gamma_0 \omega \cos(\omega t) \quad (3.22)$$

model	$\eta_2$ (mPa s)	$\eta_1$ (mPa s)	$\lambda_1$ (ms)	$\eta_3$ (mPa s)	$\lambda_3$ (s)	$\eta_4$ (mPa s)	$\lambda_4$ (s)
1 comp	174 ± 5	44 ± 1	550 ± 23	-	-	-	-
2 comp	172 ± 2	32 ± 1	274 ± 13	14 ± 1	1.9 ± 0.1	-	-
3 comp	172 ± 1	26 ± 1	223 ± 13	19 ± 1	1.1 ± 0.1	2.6 ± 0.3	12 ± 4
3 comp	<b>119</b>	56 ± 2	5 ± 2	31 ± 1	0.35 ± 0.03	11 ± 1	2.3 ± 0.2

**Table 3.2:** Parameters of the (generalized) Jeffreys model adapted to the oscillatory data  $G'(\omega)$  and  $G''(\omega)$  of the P600<sub>G80</sub> solution. The bold entry is fixed within the fit. The dashpot element is given by  $\eta_2$  ( $\lambda_2 = 0$ ). The corresponding fitting curves are shown in figure 3.7 and 3.8.

with  $\eta = \eta_1 + \eta_2$  and the components of the elastic modulus are respectively

$$G'(\omega) = \frac{\eta_1 \lambda \omega^2}{1 + \lambda^2 \omega^2}, \quad (3.23)$$

$$G''(\omega) = \eta_2 \omega + \frac{\eta_1 \omega}{1 + \lambda^2 \omega^2}. \quad (3.24)$$

The additivity of stresses according to (2.14) reflects the additive structure in (3.24) and it reveals how to account for more than one relaxation time. When different Maxwell elements ( $\lambda_k, \eta_k$ ) are arranged in parallel, the respective material functions  $G'_k(\omega)$  and  $G''_k(\omega)$  just sum up to the total storage and loss moduli

$$G'(\omega) = \sum_k G'_k(\omega) = \sum_k \frac{\eta_k \lambda_k \omega^2}{1 + \lambda_k^2 \omega^2}, \quad (3.25)$$

$$G''(\omega) = \sum_k G''_k(\omega) = \sum_k \frac{\eta_k \omega}{1 + \lambda_k^2 \omega^2}. \quad (3.26)$$

This gives the so-called Generalized Maxwell model [Bir87]. Keeping the notation in our (generalized) Jeffreys model, the relaxation time of the second (dashpot) element equals zero, i.e.  $\lambda_2 = 0$ . In figure 3.7, best model fits are presented for one, two and three (Maxwell) components in parallel with a single dashpot ( $\eta_2$ ). Again, a weighting method is used to find the optimal model parameters via the minimization of the sum of relative quadratic errors. The moduli are adapted simultaneously to the accumulated data set gathered from the different measurements. In table 3.2, the corresponding set of best fit parameters is listed. Clearly, the dominating stress response is Newtonian. The viscosity of the single dashpot element  $\eta_s \approx 172$  mPa s is significantly higher than the viscosities included in the Maxwell elements which add up to only about 20% of the total viscosity  $\eta = \sum_i \eta_i$ . This becomes obvious when we define a complex viscosity via

$$\tau^*(t) = \eta^*(\omega) \dot{\gamma}^*(t) \quad (3.27)$$

with

$$\eta^*(\omega) := \eta'(\omega) - i\eta''(\omega) = \frac{G^*(\omega)}{i\omega} \quad (3.28)$$

which gives the identities

$$\eta''(\omega) = \frac{G'(\omega)}{\omega} = \sum_k \frac{\eta_k \lambda_k \omega}{1 + \lambda_k^2 \omega^2}, \quad (3.29)$$

$$\eta'(\omega) = \frac{G''(\omega)}{\omega} = \sum_k \frac{\eta_k}{1 + \lambda_k^2 \omega^2}. \quad (3.30)$$

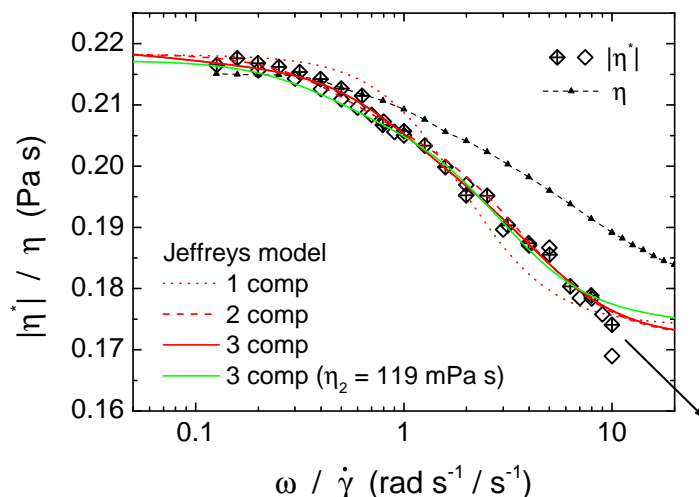


**Figure 3.8:** Absolute value of the complex viscosity  $|\eta^*|$  as a function of the oscillation frequency  $\omega$ . The best fit functions from figure 3.7 have been transferred. The flow curve from steady shear rheometry are added for comparison ( $\eta$ , triangles).

The so-called dynamic viscosity  $\eta'(\omega)$  can be interpreted as the equivalent to the apparent viscosity  $\eta(\dot{\gamma})$  in the steady shear experiment. However, it is well known, that  $\eta'$  decreases more rapidly with  $\omega$  than  $\eta$  does with  $\dot{\gamma}$  [Bir87]. Cox and Merz [Cox58] empirically found out, that for many viscoelastic fluids the values of the shear viscosity  $\eta(\dot{\gamma})$  equal the absolute values of the complex viscosity  $|\eta^*(\omega)|$ , evaluated at  $\omega = \dot{\gamma}$ , i.e.

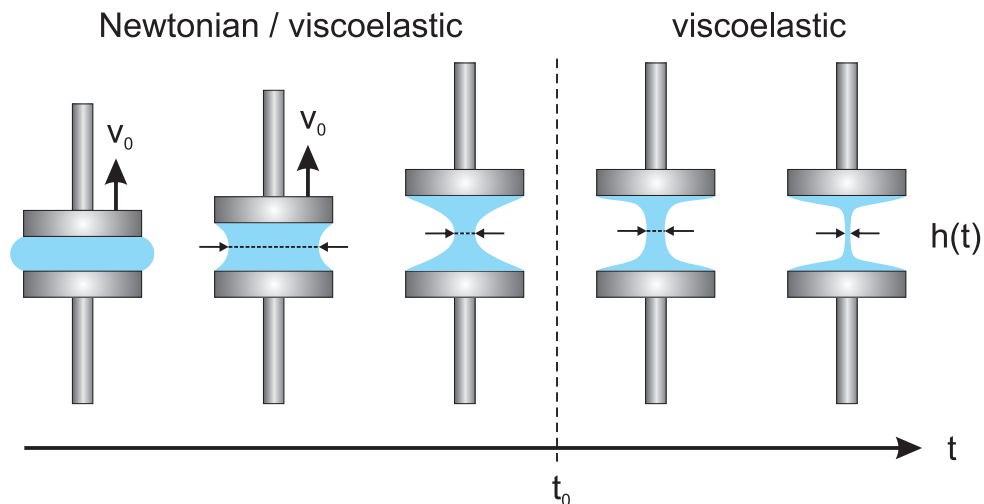
$$\eta(\dot{\gamma}) = |\eta^*(\omega)| \Big|_{\omega=\dot{\gamma}} = \sqrt{(\eta'(\omega))^2 + (\eta''(\omega))^2} \Big|_{\omega=\dot{\gamma}} = \frac{|G^*(\omega)|}{\omega} \Big|_{\omega=\dot{\gamma}} \quad (3.31)$$

Figure 3.8 provides a comparison of the viscosity data. In our case, the viscometric flow curve  $\eta(\dot{\gamma})$  is still above the oscillatory data. However, the values in the limit of zero shear and zero frequency, respectively, are identical within the variation of the data. The model-based expressions for the storage and loss moduli (3.29) and (3.30) can be combined to compare the model with the viscosity data. The respective curves according to the parameters extracted from fitting the experimental moduli are shown (red curves). Clearly, all the models overestimate the oscillatory data at high shear rates which is due to an overestimation of  $\eta_2$ . As there is a lack of reliable oscillatory data for higher frequencies  $\omega \gtrsim 10 \text{ rad s}^{-1}$ , the extrapolation to the high frequency regime fails. Even if one fixes  $\eta_2$  to the solvent viscosity as measured in steady shear rheometry and allows for three Maxwell elements in the linear model (cf. green curve), the model fails to reproduce the trend which emerges at high frequencies (as indicated by the arrow).

## 3.4 Capillary breakup extensional rheometry (CaBER)

### 3.4.1 Methodology & experimental setup

So far, we have presented different experimental methods aiming to extract characteristic properties of a polymeric fluid from its viscoelastic response to a steady or dynamic stimulus in simple shear flows in which the polymers are necessarily stretched. However, in terms of efficiency, the simple shear is not the most reasonable one to provide a pronounced conformational response of the polymers [Sch05]. This is due to the fact that any simple



**Figure 3.9:** Sketch of the CaBER setup at different steps during the constriction process of the capillary bridge.

shear flow can be decomposed into a pure rotational and a pure extensional contribution, where only the latter yields a stretching of the fluid elements. In contrast, the rotational part just re-orientates the fluid elements and does not contribute to the stretching and it may even weaken the average stretching when the stretched polymers are rotated while partially relaxing. This tumbling motion has been observed in experiments and it has been shown that polymers (in this case: DNA) in shear flow never reach a steady extension [Hur01].

Hence, in order to optimize the efficiency in stretching the polymers and in addressing the elastic properties of, in particular, very low concentrated polymer solutions which possibly do not show any significant elastic response in simple shear flow, it is reasonable to add a pure extensional experiment to our rheometric toolkit, namely the capillary break-up extensional rheometer (CaBER). Its setup is rather simple (cf. figure 3.9): a small amount of the sample fluid is placed between two small, coaxial plates which face each other in short distance, such that a capillary fluid thread is formed. Subsequently, the two plates are pulled apart from each other in a predefined way. In doing so, the fluid thread deforms due to the liquid/air surface tension which tends to minimize the surface area. Consequently, the minimal width of the fluid thread  $h$  decreases. At a critical separation length, the capillary bridge becomes unstable according to the linear Rayleigh-Plateau instability which is based on an interplay between surface and volume forces depending on the local curvature  $\propto h^{-1}$ . As a consequence, the liquid filament thins exponentially [Sat09]. Right before the virtual breakup at  $t = t_0$ , which is commonly observed for Newtonian fluids, the width of the fluid thread follows a characteristic power law [Bre97, Day98]

$$h(t) \propto \begin{cases} (t_0 - t)^{\frac{2}{3}} & : \text{inertio-capillary} \\ t_0 - t & : \text{viscous-capillary} \end{cases} \quad (3.32)$$

Depending on the importance of viscosity, one discriminates between inertio-capillary (negligible or low viscosity) or viscous-capillary (non-negligible viscosity) thinning [Gie10, Cla10]. Here, the capillary forces (Laplace pressure) balance with inertial or viscous forces in the filament. While this initial thinning process is basically the same for both a Newtonian and a non-Newtonian (polymer) fluid, in the latter case the final breakup of the fluid thread at  $t = t_0$  is postponed by the formation of a stable, straight filament. In this regime, the surface pressure is balanced by the elastic stresses of the polymer chains and the filament thins exponentially

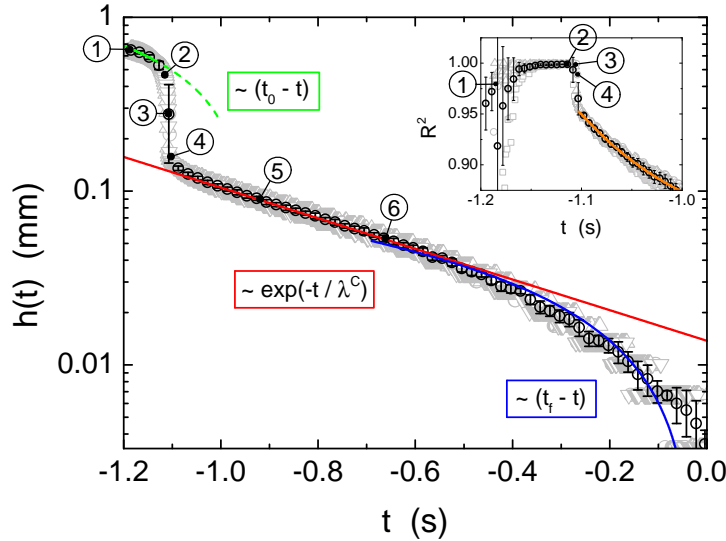


**Figure 3.10:** Minimal width  $h(t)$  of the capillary thread of the P600<sub>G80</sub> solution during the constriction process in the CaBER experiment. Three independent measurements are shown (gray) together with their average (black circles). Clearly, the curves can be divided into the three regions described in the text. The raw images from individual points, numbered from 1 to 6, are represented in figure 3.11. The inset shows how the contour of the filament develops in terms of its deviation from a perfect parabola ( $R^2 = 1$ ).

with time [Bou86, Rod05, Cla10, McK05],

$$h(t) \propto e^{-\frac{t}{\lambda^C}}, \quad (3.33)$$

associated with a specific CaBER relaxation time  $\lambda^C$ . According to an explicit theoretical analysis of the pure extensional flow of a multi-mode FENE (finitely extensible nonlinear elastic) fluid [Ent97], the characteristic time scale  $\lambda^C$  can be related to the spectrum of relaxation times of the nonlinear dumbbells. The result can be simplified to approximate the single-mode Oldroyd-B fluid (see section 2.3), and according to this model the CaBER relaxation time is three times the relaxation time of the Hookean dumbbell, i.e.  $\lambda^C = 3\lambda$ .

During the exponential thinning process, the polymers within the filament are increasingly stretched and oriented, and depending on the viscous timescale, they can take a stationary orientation. The surrounding liquid phase is drained into the remaining liquid caps at the withdrawing plates. In a later stage of the thinning process, the formation of small beads on a remaining string may be observed. This so-called “blistering” is triggered by a linear capillary instability at some critical filament width. With further draining into the end caps and/or the beads, the remaining filament increasingly behaves like a suspension of extended (rigid) rods with some effective viscosity [Ent97]. Thus, a final transition from the exponential to the linear viscous behavior  $h(t) \propto (t_f - t)$  can be observed which guides to the final rupture of the filament at  $t = t_f$ .

In our standard protocol, the upper plate raises from the lower one by a constant, low velocity  $V_0$  (cf. figure 3.9). This method is favorable when investigating low viscous, diluted polymer solutions since a rapid stretching of the fluid causes oscillations on the surface of the fluid which may hinder a proper examination of the filament. A projection of the silhouette of the fluid thread is recorded using a high-speed camera, equipped with a magnification lens (a more detailed description of the standard experimental setup can be found elsewhere [Zel10, Gie10]). The lateral profile is evaluated subsequently by means of a customized image analysis software.

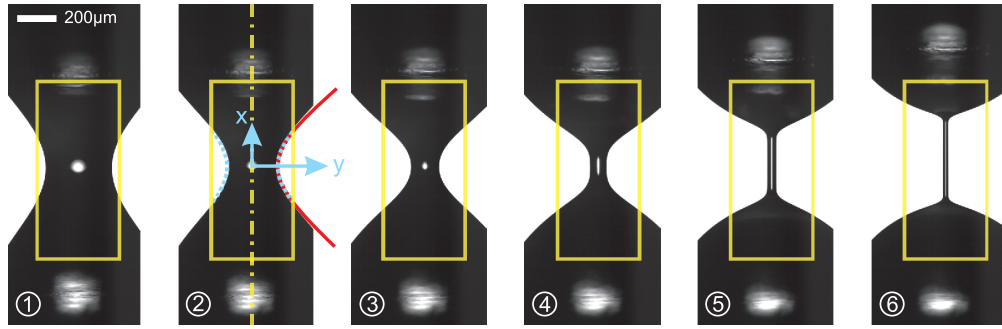


**Figure 3.11:** Images of the fluid thread of a P600<sub>G80</sub> solution at individual points during the CaBER experiment. The width of each image is 320 pixels which corresponds to 1.1 mm. The images can be related to the respective numbering in figure 3.10.

### 3.4.2 Representative data

Figure 3.10 shows experimental CaBER data of the P600<sub>G80</sub> solution in terms of the minimal filament width  $h(t)$  as a function of time. The data of three independent measurements (gray) are shown with the curves being horizontally shifted with respect to the resolution limit of one pixel or the final breakup. Additionally, the averaged data are shown (black circles). The constriction process has been recorded with a frame rate of 1 kHz using a 4-fold magnification which maps a physical length of 3.36  $\mu\text{m}$  to one pixel of the camera chip. Each image displays a region of  $w \times h = 320 \times 776$  pixels which gives physical dimensions of  $w \times h \approx 1.1 \text{ mm} \times 2.6 \text{ mm}$ . The upper plate was moved with  $V_0 = 0.44 \text{ mm/s}$ . In figure 3.11, six raw images of the filament are shown as acquired by the high-speed camera. They illustrate different steps during the constriction process (cf. the numbering in figure 3.10).

### 3.4.3 Evaluation of data

The evaluation of the raw images (as represented in figure 3.11) has been carried out by means of a Matlab (by MathWorks) script. For each image  $j$  of the whole sequence (e.g., image no. 2), the contours of the filament  $y_i(x_i)$  has been extracted on both sides (red-blue-dashed lines) within a predefined region of interest (ROI, 200 pixels in width, yellow frame) centered at its axial centerline (yellow chain line). A threshold method was used to generate binary images which easily allowed to find the boundary line of the filament. The minimum width  $h$  of the filament has been extracted subsequently (cf. figure 3.10). The data clearly reflects the three different regimes described above: the viscous-capillary (green line), the highly-viscous (blue line) and the viscoelastic regime (red line). The latter is clearly characterized by an exponential law  $h(t) \propto e^{-t/\lambda^C}$ , and the respective CaBER relaxation time  $\lambda^C$  can be extracted correspondingly. Here, it gives

$$\lambda^C = (492 \pm 1) \text{ ms} . \quad (3.34)$$

Additionally, the shape of the filament has been characterized. Within the region of interest, one contour line of the filament has been approximated by a parabola ( $p_2(x)$ , red line). The coefficient of determination

$$R^2 = 1 - \frac{\sum_{i=1}^N [y_i(x_i) - p_2^j(x_i)]^2}{\sum_{i=1}^N [y_i(x_i) - \bar{y}]^2} \quad (3.35)$$

with the mean  $\bar{y} = \sum_{i=1}^N y_i(x_i)$  of the  $N = N_j$  contour points  $y_i(x_i)$  of image no.  $j$  gives a statistic of the goodness of the fit. It is one for a perfectly parabolic contour and it decays

with increasing mismatch. The inset in figure 3.10 gives the progress of  $R^2$  during the breakup experiment. It is obvious, that the transition from the Newtonian, inertio-capillary to the viscoelastic thinning process is featured by a significant change in the shape of the capillary thread. While it is almost perfectly parabolic in the beginning<sup>2</sup> ( $R^2 \approx 1$ , cf. image no. 1, 2 and 3) the shape changes due to the formation of the straight filament (cf. images no. 4 and 5). In doing so,  $R^2(t)$  exponentially decays during the further thinning process (cf. orange line in the inset).

Obviously,  $R^2$  is appropriate to resolve even the smallest deviation from the Newtonian thinning process (image no. 4) which is highlighted by a deviation from a perfect parabolic filament shape by the formation of a straight filament which postpones the breakup of the capillary bridge. Furthermore it will turn out to be an adequate variable to quantify the different extensional rheology of similar viscoelastic fluids.

---

<sup>2</sup>The initial noise in  $R^2$  is due to a poor statistics as the number of contour points within the region of interest is initially very low.

## **Part II**

# **Study of viscoelastic Taylor-Couette flow [Sch13]**



---

## Introduction

The Taylor-Couette flow is the flow of a fluid confined in the annular gap between concentric cylinders which in general co- or counter-rotate with independent velocities. It has been extensively investigated in the past for simple (Newtonian) fluids and to some extent for viscoelastic polymer solutions, and for both it is known to be featured with a rich flow diagram when changing the control parameters of the flow. For the Newtonian Taylor-Couette problem, the control parameters are the Reynolds numbers  $Re_1$  and  $Re_2$  of the inner and outer cylinder, respectively, which depend on the angular velocities  $\Omega_1, \Omega_2$  and radii  $R_1, R_2$  of inner and outer cylinder as well as on the density  $\rho$  and viscosity  $\eta$  of the revolving fluid. As long as the Reynolds numbers are small, for any combination of them, the only stable base state is a purely azimuthal, laminar flow. However, when increasing the control parameters beyond some critical values, this laminar base flow becomes linearly unstable and a rich sequence of non-trivial flow patterns appears. The critical condition for the primary transition depends on the combination of Reynolds numbers in a non-trivial manner and thus on the explicit trajectory through the stability diagram. Remarkably, flow instability is absent when restricting to a system where only the outer beaker is rotating. This impressively reflects the fact that the fundamental mechanism for the instability is governed by inertia.

The Taylor-Couette flow of a viscoelastic fluid features a completely contrary scenario. Even at vanishing Reynolds numbers far below the critical condition for primary inertial instability, i.e. in the absence of inertia, the initially laminar flow of a viscoelastic fluid may become linearly unstable. This transition is non-inertial by nature and it originates from the elastic instability mechanisms described in section 2.4: elastic normal stresses are amplified in the presence of small perturbations of the radial velocity field and couple to the curvature of streamlines. They build up a so-called “hoop stress” which actuates a secondary flow in the radial direction towards the center of the Taylor-Couette cell when the elastic forces are big enough (Weissenberg effect). The critical condition is given by a critical Weissenberg number  $Wi_c = \lambda \dot{\gamma}_c$  which can be interpreted as the product of a characteristic polymer relaxation time  $\lambda$  and a critical shear rate  $\dot{\gamma}_c$ . As the latter is proportional to the difference of the rotation rates of inner and outer cylinder, the same scenario is observed at outer cylinder rotation with the inner cylinder being at rest. This clearly hints at the fundamental differences between Newtonian and viscoelastic Taylor-Couette flow.

Next, a short introductory abstract of the fundamental story line of elastic instability in the Taylor-Couette flow is given, including experimental as well as theoretical and numerical approaches from the last fifty years.

## 4.1 Basic literature and milestones

Ever since M. Couette's very first experimental investigations on the flow of a simple liquid between two concentric cylinders [Cou87] in the late 19th century and G. I. Taylor's first theoretical description of its linear stability [Tay23] in 1923, the accordingly called Taylor-Couette flow has been extensively investigated in experiments as well as in theory. Apart from its first transition from the azimuthal, laminar base flow (called circular Couette flow) to stationary Taylor Vortex Flow (TVF) which has been theoretically quantified [Gan64, Yu164, Ess96, Dut07] in agreement with numerous experiments (e.g., [And86]), many more flow patterns and structures appear in the rich stability diagram of Newtonian Taylor-Couette flow. An instructive overview of the various flow patterns can be found in [And86] and a comprehensive review on the Newtonian Taylor-Couette flow is given by Tagg [Tag94]. And even nowadays, after more than a century of vivid research on Taylor-Couette flow, there are still open questions and more profound aspects such as, e.g., the explicit transition mechanisms between neighboring flow regimes (cf., e.g., [Alt10, Hof09]). This is also owed to the fact that the Taylor-Couette flow occurs not only in the context of fundamental physics (here, also the spherical Taylor-Couette flow is of great interest in geo- and astrophysics) but also of manifold industrial applications such as mixing or phase separation devices.

With the extension to the physics of complex (non-Newtonian) materials such as ferro-[Alt11], bio-[Mus13], magnetic [Wil02] or viscoelastic (polymer) fluids, the Taylor-Couette problem exhibited even more fascinating features and the list of available relevant literature is presumably even larger than for the Newtonian problem. In the following, we focus here on some fundamental publications which embed our own study within the understanding of viscoelastic instability. Most of them are discussed in a recent review by Susan Muller [Mul08].

Based on a profound understanding of the Newtonian flow problem, early studies were focusing on the influence of elasticity on the onset of the inertial Taylor-Couette instability observed at high Reynolds numbers. Respective experimental studies were operated by Ginn *et al.* [Gin69], Denn *et al.* [Den69], and others. They found a stabilizing effect of elasticity on the laminar flow against Taylor vortices [Lar90]. However, other studies appeared to yield contradictory results, i.e. experiments on higher concentrated solutions showed a decrease in the critical numbers and oscillatory secondary flow was observed before stationary vortices were established. Theoretical studies on the effect of weak elasticity in small gap systems [Gin69, Sun72, Pet76] predicted stabilization or destabilization depending on two dimensionless groups,  $(\Psi_1/2\rho d^2)$  and  $(\Psi_2/2\rho d^2)(R_1/d)$  which are consequently governed by the first and second normal stress differences,  $N_1 = \Psi_1\dot{\gamma}^2$  and  $N_2 = \Psi_2\dot{\gamma}^2$ , respectively ( $\rho$  is the mass density). Thereby, positive values of both groups tend to destabilize the flow, whereas a negative value of  $\Psi_2$  stabilized the flow for small gaps  $d = R_2 - R_1$  where the second group becomes dominant.

After Giesekus [Gie66] first reported in 1966 the existence of a non-inertial Taylor-Couette instability, particular attention has been paid to this new kind of *purely elastic instability*, and during the last almost fifty years numerous studies have been contributing to a deeper understanding of the fundamentals of this phenomenon. Based on sophisticated constitutive viscoelastic models such as the Oldroyd-B model, linear stability analysis has been used to theoretically investigate the stability of viscoelastic Taylor-Couette flow and to predict the onset and characteristics of purely elastic instability, depending on the fluid's explicit rheology (shear-thinning, spectrum of relaxation times) and the system's geometrical parameters (small gap, finite gap, eccentricity). Here, one has to cite some of the fundamental investigations by Muller *et al.* [Mul89], Larson *et al.* [Lar90, Lar94], Shaqfeh *et al.* [Sha92], Avgousti *et al.* [Avg93a, Avg93b], Joo *et al.* [Joo94] and Dris *et al.* [Dri95]. With the ongoing improvement

of image acquisition and processing techniques, more and more experiments were conducted by means of flow visualization and with focusing on a quantitative examination of the diverse flow patterns which appear in the course of the elasticity-induced transition to non-trivial coherent flow states. Here, explicit pattern selection (Groisman *et al.* [Gro96, Gro97, Gro98a], Baumert *et al.* [Bau95]) and the analysis of the spatial and temporal characteristics of the flow (Muller *et al.* [Mul93], Baumert *et al.* [Bau99]) were addressed amongst other aspects.

In view of the proposition of a universal criterion for the onset of elastic instability of curvilinear viscoelastic flow by Pakdel and McKinley [Pak96, McK96] (cf. section 2.4), the viscoelastic Taylor-Couette flow problem appeared as a paradigm in the story of elastic instability since its circular base flow naturally provides a simple identification of a characteristic radius of curvature which is one of the main ingredients of the underlying instability mechanism. In total agreement with linear stability analysis, a formulation of the criterion for an upper convected Maxwell fluid (UCM) reproduces the instability criterion in terms of the geometrical scaling prediction, i.e.  $Wi \propto (R_1/d)^{0.5}$ . Whereas the authors showed consistency between the geometrical scaling prediction and experimental results for the lid-driven cavity flow as well as for the flow in the wake of a cylinder [McK96, Pak98], moderate discrepancies for the viscoelastic cone-and-plate flow appeared. For the Taylor-Couette flow, Groisman *et al.* [Gro96, Gro98b, Gro98a] experimentally validated the scaling prediction for the dependency on the rheology  $Wi_c \propto (\eta/\eta_p)^{0.5}$  based on the Oldroyd-B model and accounting for the explicit shear-thinning properties of the investigated fluids. Being a conceptual proof of the non-linear nature of the instability, the authors further showed that the transition of elastic instability is subcritical as it yields a hysteretic behavior. However, the authors did not address the geometrical scaling prediction.

Beside the consistencies which could be revealed between the theoretical considerations and experimental observations, there still existed a significant discrepancy: the onset of elastic instability in Taylor-Couette flow experiments showed up at critical Weissenberg numbers which were commonly about one magnitude smaller than the predictions given by linear stability analysis. However, by taking into account the energetics of the investigated system, i.e. temperature-depend viscosity as well as viscous heating and a temperature difference of the boundaries, Al-Mubaiyedh *et al.* [Al-99, Al-00] theoretically predicted a transition to instability at significantly lower critical Weissenberg number than in the isothermal case. It is associated with a new kind of stationary, axisymmetric instability mode which is driven by viscous heating as the latter leads to a stratification of the hoop stress which further drives a radial secondary flow. By accounting for the long time scale on which the temperature profile fully develops and accurate temperature control of the boundaries, White *et al.* [Whi00, Whi03] were able to experimentally validate the theoretical prediction.

## 4.2 Scientific relevance and perspective of the present study

On the first sight, the short overview from above about elastic instability in the Taylor-Couette flow may appear fully coherent when carefully accounting for all the relevant parameters such as viscous heating or shear-thinning. However, a closer look exhibits some open questions and inconsistencies which motivated to elaborate the following study. First, we have to point out that there exist to our knowledge no other experimental data about the onset of elastic instability in the Taylor-Couette flow with an explicit focus on the scaling on the geometrical parameters of the system than those by Muller *et al.* [Mul89] (dealing with a Boger fluid). However, their data show some clear inconsistency when comparing it with the geometrical scaling coming along with the linear stability analysis (accounting for axisymmetric disturbances) and the prediction of the instability criterion by Pakdel and McKinley, both based on the Oldroyd-B model (which is known to reproduce the rheological shear

properties of Boger fluids). The authors proposed to account for a spectrum of relaxation times to improve the agreement. Second, the data by Muller *et al.* give the onset of elastic instability based on different Taylor-Couette geometries that differ not only in the radius of curvature but also in the gap width. As it is the parameter which defines the length scale of the system and of the secondary flow in the gap, it should be kept constant in order to investigate the pure influence of the curvature on the onset of instability. Additionally, the numerical data by Joo *et al.* [Joo94] showed some lack of integrity, i.e. when extracting the data of critical Weissenberg number  $Wi$  and modified Weissenberg number  $(d/R_1)^{0.5}Wi$  for the non-axisymmetric ( $m = 1$ ) perturbation mode in the finite gap system, the data cannot be transformed to each other by rescaling with the root of the relative gap width  $(d/R_1)^{0.5}$ .

Facing these remaining discrepancies in the elaboration of viscoelastic Taylor-Couette flow, the objective of the present study is to supplement to the extensive understanding of viscoelastic Taylor-Couette flow instability gained over the last decades as presented above and to provide an even more consistent picture of the story. In doing so, we first have to introduce the Oldroyd-B model in more detail, featuring its linear stability analysis for small and finite gaps and its adaption to the Pakdel-McKinley criterion in the small gap formulation. This will be found in section 4.3 where the aforementioned discrepancies to the experimental data by Muller *et al.* are specified. In the main part of the study, we subsequently present the results of our extensive investigations on the viscoelastic Taylor-Couette flow, combining experimental data with theoretical and numerical considerations. Here, we start with an in-depth characterization of the set of various polymer solutions by means of steady rotational shear, small amplitude oscillatory, relaxation and capillary breakup measurements (section 5) and involving an interpretation by means of appropriate rheological models with the aim to extract the characteristic rheometric properties. Equipped with a thorough characterization of the working fluids, we continue in section 6 with a presentation of the experimental setup which involves a set of customized Taylor-Couette cells with a joint width of the annular gap ( $d = 1$  mm) as suggested above. The evaluation of the systematic Taylor-Couette measurements with regard to the Pakdel-McKinley criterion based on its formulation for finite gap widths is the subject of the sections 7 and 8. Here, we explicitly focus on its geometrical as well as its rheological scaling prediction. The results are contrasted with a comprehensive linear stability analysis (section 9) based on the standard Oldroyd-B model as well as on a customized hybrid model that describes fairly well the rheometry of our investigated polymer solutions. Here, we also address the observed discrepancy in the data by Joo *et al.* [Joo94] and we provide a widespread set of accurate critical Weissenberg numbers for the onset of purely elastic instability of various Oldroyd-B fluids. Facing the hybrid model, the effect of non-isothermal flow properties on the geometrical scaling of instability are additionally considered. Section 10 addresses the problem of polymer degradation which appears to be omnipresent in our experiments. Its impact is investigated within the scope of a supplementary experimental study in an individual Taylor-Couette cell. Finally, the overall findings are summarized and discussed in section 11.

### 4.3 The Taylor-Couette flow of an Oldroyd-B fluid... reloaded

#### 4.3.1 The base flow

The Oldroyd-B model (cf. section 2.3.2) is known to describe fairly well the rheology of dilute solutions of highly elastic polymers with constant shear viscosity (so-called Boger fluids). It is a paradigm for the investigation of viscoelastic Taylor-Couette flow instabilities, as the underlying constitutive equations can be easily solved for the base flow. Starting with the set of constitutive equations (2.47)–(2.50), the time-independent purely azimuthal, axisymmetric Taylor-Couette base flow of an Oldroyd-B fluid

$$\left(\mathbf{v}(\mathbf{r}), p(\mathbf{r}), \underline{\boldsymbol{\tau}}(\mathbf{r})\right)_{\text{Base}} = \left(V_\theta(r)\mathbf{e}_\theta(\mathbf{r}), P(r), \underline{\boldsymbol{T}}_s(r) + \underline{\boldsymbol{T}}_p(r)\right) \quad (4.1)$$

is governed by the equations

$$\frac{\partial P(r)}{\partial r} = -\frac{T_{p,\theta\theta}(r)}{r} + \frac{\rho V_\theta(r)^2}{r}, \quad (4.2)$$

$$0 = (\eta_s + \eta_p) \left( \frac{\partial^2}{\partial r^2} + \frac{1}{r} \frac{\partial}{\partial r} - \frac{1}{r^2} \right) V_\theta(r), \quad (4.3)$$

$$T_{s,r\theta}(r) = \eta_s \left( \frac{\partial}{\partial r} - \frac{1}{r} \right) V_\theta(r) = -\eta_s \dot{\gamma}(r), \quad (4.4)$$

$$T_{p,r\theta}(r) = \eta_p \left( \frac{\partial}{\partial r} - \frac{1}{r} \right) V_\theta(r) = -\eta_p \dot{\gamma}(r), \quad (4.5)$$

$$T_{p,\theta\theta}(r) = 2\lambda T_{p,r\theta}(r) \left( \frac{\partial}{\partial r} - \frac{1}{r} \right) V_\theta(r) = 2\lambda \eta_p \dot{\gamma}(r)^2. \quad (4.6)$$

With the common ansatz  $V_\theta(r) = r^\alpha$  and by forcing the most general boundary conditions

$$V_\theta(r = R_1) = \Omega_1 R_1, \quad V_\theta(r = R_2) = \Omega_2 R_2, \quad (4.7)$$

equation (4.3) gives the radial velocity profile

$$V_\theta(r) = \frac{\Omega_2 R_2^2 - \Omega_1 R_1^2}{R_2^2 - R_1^2} r + \frac{(\Omega_1 - \Omega_2) R_1^2 R_2^2}{(R_2^2 - R_1^2) r}. \quad (4.8)$$

Obviously, in the Oldroyd-B model the base velocity profile is not influenced by the polymeric contribution in the stress tensor. Furthermore the only non-zero component of the rate-of-deformation tensor  $\dot{\underline{\boldsymbol{\gamma}}}$  is given by the shear component (shear rate)

$$\left| (\nabla \mathbf{v} + \nabla \mathbf{v}^\dagger)_{r\theta} \right| = \left| \left( \frac{\partial}{\partial r} - \frac{1}{r} \right) V_\theta(r) \right| = \frac{|\Omega_1 - \Omega_2|}{\varepsilon} \frac{2(\varepsilon + 1)^2}{\varepsilon + 2} \frac{R_1^2}{r^2} =: \dot{\gamma}(r) \quad (4.9)$$

with the relative gap width  $\varepsilon = d/R_1 = (R_2 - R_1)/R_1$ . Hence, the Taylor-Couette base flow is a pure shear flow and the total shear stress is proportional to the shear rate

$$T_{r\theta}(r) = (\eta_s + \eta_p) \dot{\gamma}(r) = \eta \dot{\gamma}(r) \quad (4.10)$$

with the total shear viscosity  $\eta = \eta_s + \eta_p$ . Thus, in terms of the velocity profile and the shear component of the stress tensor, the polymer contribution in the Oldroyd-B model does not give rise to any non-Newtonian flow property. However, in contrast to the pure Newtonian case, the first normal stress (difference) is no longer zero but scales quadratically with the shear rate and linearly with the polymer relaxation time  $\lambda$  as well as with the viscosity  $\eta_p$ , i.e.

$$N_1(r) = T_{p,\theta\theta}(r) = 2\lambda \eta_p \dot{\gamma}(r)^2 = \Psi_1 \dot{\gamma}(r)^2. \quad (4.11)$$

$\Psi_1$  is called the first normal stress coefficient. This additional normal stress component couples to the pressure field  $P(r)$  via (4.2) and counteracts the inertial forces  $\propto \rho V_\theta^2$ . This is the physical manifestation of the “hoop” stress which finally gives rise to the elastic instability mechanism presented in section 2.4.1. As expected and already emphasized in the introductory section of this chapter, this non-linear effect on the normal (hoop) stress depends only on the difference of the angular rotation rates  $\Omega_1 - \Omega_2$ , and it does not make a difference between inner or outer cylinder rotation which is contrary to the inertial instability mechanism.

Thus, without loss of generality, we can simplify to the case of a rotating inner cylinder ( $\Omega_1 = \Omega$ ) and an outer cylinder at rest ( $\Omega_2 = 0$ ), and in the following we will focus on this standard Taylor-Couette flow throughout the presented work.

### 4.3.2 The Pakdel-McKinley criterion for the Taylor-Couette flow in the small gap approximation

The viscoelastic Taylor-Couette flow of an Oldroyd-B fluid is a paradigm of a flow that provides the essential conditions needed to actuate the elasticity-induced instability mechanism proposed by Pakdel and McKinley (cf. section 2.4.2): one can easily identify a well-defined characteristic curvature of streamlines and the components of the polymer stress tensor take simple forms (cf. (4.10), (4.11)). In the common approximation of small gap

$$0 < d \ll R_1 < \infty \quad \Leftrightarrow \quad 0 < \varepsilon \ll 1 \quad (4.12)$$

the shear rate (4.9) is constant across the gap,

$$\dot{\gamma}_{\text{sg}} \doteq \frac{\Omega}{\varepsilon}, \quad (4.13)$$

and with the definitions of a characteristic velocity  $\mathcal{U} = \Omega R_1$ , radius of curvature  $\mathcal{R} = R_1$  and the stress components (4.10) and (4.11), the instability condition (2.74) is given by

$$\sqrt{DeWi} = \sqrt{\varepsilon}Wi \geq \frac{M}{\sqrt{2(1-\beta)}} \quad (4.14)$$

with the dimensionless Deborah number  $De = \lambda\Omega$  and the dimensionless Weissenberg number

$$Wi = \frac{\tau_{p,\theta\theta}(\dot{\gamma})}{2\tau_{p,r\theta}(\dot{\gamma})} = \lambda\dot{\gamma} = \lambda \frac{\mathcal{U}}{\mathcal{L}} \quad (4.15)$$

which are interrelated by (4.13). The definition of the Weissenberg number according to (2.51) corresponds to the formulation via the non-dimensionalization of the constitutive equations of the Oldroyd-B model (cf. equation (2.73)) with the definition of the characteristic length  $\mathcal{L} = d = \varepsilon R_1$ . Aside from  $\varepsilon$  and  $Wi$ , the relative viscosity  $\beta = \eta_s/\eta$  appears in the criterion (4.14).

The term  $\sqrt{\varepsilon}Wi$  is denoted as the *modified Weissenberg number* [Lar92]. For the most simple case of an upper convected Maxwell (UCM) fluid (i.e.  $\beta = 0$ ), equation (4.14) simplifies to  $2\varepsilon Wi^2 \geq M^2$  which gives a criterion analogous to the inertial Taylor-Couette instability [Tay23, Cha61, Lar92, Gan64]

$$Ta = 2\varepsilon Re^2 \gtrsim 3400 \quad (4.16)$$

by replacing the Reynolds number

$$Re = \frac{\rho \mathcal{U} \mathcal{L}}{\eta} = \frac{\rho \Omega R_1 d}{\eta} \quad (4.17)$$

with the Weissenberg number. Thus, in the elastic Taylor-Couette instability, the modified Weissenberg number plays an analogous role as the Taylor number  $Ta$  in the description of

the inertial instability. However, we have to keep in mind that the critical Taylor number (4.16) exclusively gives the onset of inertial instability for inner cylinder rotation at fixed outer cylinder. It takes a much more complicated form when outer cylinder rotation is accounted for (cf. [Ess96, Dut07]).

Equation (4.14) predicts the onset of elastic instability in terms of a critical modified Weissenberg number being a function of the relative viscosity  $\beta = \eta_s/\eta$  only and proportional to some constant  $M$ . In particular, in the small gap approximation of the Taylor-Couette flow of an Oldroyd-B fluid, the modified Weissenberg number is predicted to be independent of the explicit geometrical parameter  $\varepsilon$  at hand.

### 4.3.3 Review on Linear Stability Analysis

**Small gap (sg) approximation.** Apart from the explicit dependence on the relative viscosity  $\beta$ , the prediction given by the Pakdel-McKinley criterion is consistent with a linear stability analysis of the Taylor-Couette base flow of an Oldroyd-B model assuming small axisymmetric ( $m = 0$ ) perturbations. In the small gap approximation, the analysis predicts [Lar90] the criterion for instability to be

$$\text{small gap } (\varepsilon \ll 1) \quad \rightarrow \quad \sqrt{\varepsilon}Wi \geq \frac{5.92 \pm 0.02}{\sqrt{K(S)}} \quad (4.18)$$

with the definition of the Weissenberg number according to (4.15) and an analytic function<sup>1</sup>

$$K(S) = \frac{4\sqrt{\chi} [S^2\chi^2 + 4S^2(S+1)\chi + (4S^3 + 7S^2 + 4S + 1)]}{(1+\chi)^2 [(S+1)^2 + \chi S^2]^2}, \quad (4.19)$$

where  $\chi$  is the minimum positive solution of the cubic equation

$$S^3\chi^3 + S(7S^2 + S - 1)\chi^2 + (3S^2 + 2S^2 + 2S + 1)\chi - (3S^2 + 7S^2 + 5S + 1) = 0 \quad (4.20)$$

and  $S = \eta_s/\eta_p = \beta/(1 - \beta)$ .  $K$  is unity in the UCM limit ( $\beta = S = 0$ ), it raises to a maximum of  $K_{\max} \approx 1.73$  at  $S \approx 0.24$  ( $\beta \approx 0.19$ ) and monotonically decreases towards zero when further increasing  $S \rightarrow \infty$  (or  $\beta \rightarrow 1$ , respectively). Figure 4.1 represents this rheometric scaling in terms of the modified Weissenberg number, comparing the results of the linear stability analysis (small gap (sg), axisymmetric ( $m = 0$ ), black line) and the small gap prediction of the Pakdel-McKinley criterion (red line). Here, the parameter  $M$  is arbitrarily set to  $M = 8.37 \approx 5.92\sqrt{2}$  in order to meet the result of the linear stability analysis for  $\beta = 0$ . For both limits  $\beta \rightarrow 0$  and  $\beta \rightarrow 1$  (dashed and chain line, respectively), i.e. for Maxwell-like and Newtonian-like fluids, the asymptotical scalings are strikingly similar. Figure 4.2 shows the numerical data for  $\beta = 0.79$  ( $S \approx 3.8$ ) and different gap widths  $\varepsilon$  (open triangles). It predicts the critical modified Weissenberg number to be  $\sqrt{\varepsilon}Wi_c \approx 5.92/\sqrt{K(3.8)} \approx 7.58$ . The Pakdel-McKinley criterion reproduces this geometric scaling, but significantly overestimates the absolute value  $\sqrt{\varepsilon}Wi_c(\beta = 0.79) \approx 12.92$  when (arbitrarily) fixing  $M = 8.37$  to obtain the same value at  $\beta = 0$ .

<sup>1</sup>In the original formula for  $K(S)$  in the publication by Larson *et al.* [Lar90], a misprint is found in the first term of the bracket in the numerator: there, it reads  $S\chi^2$  which is incorrect. Furthermore, a discrepancy is found in the limit  $\chi_\infty := \lim_{S \rightarrow \infty} \chi(S) \approx 0.475$ . We calculate a value of  $\chi_\infty \approx 0.464$ . Consequently, as  $\lim_{S \rightarrow \infty} K(S) = 16\sqrt{\chi_\infty}/(1+\chi_\infty)^3/S$ , the asymptote is given by  $\lim_{S \rightarrow \infty} K(S) \approx 3.473/S$  (and not  $3.436/S$ ).

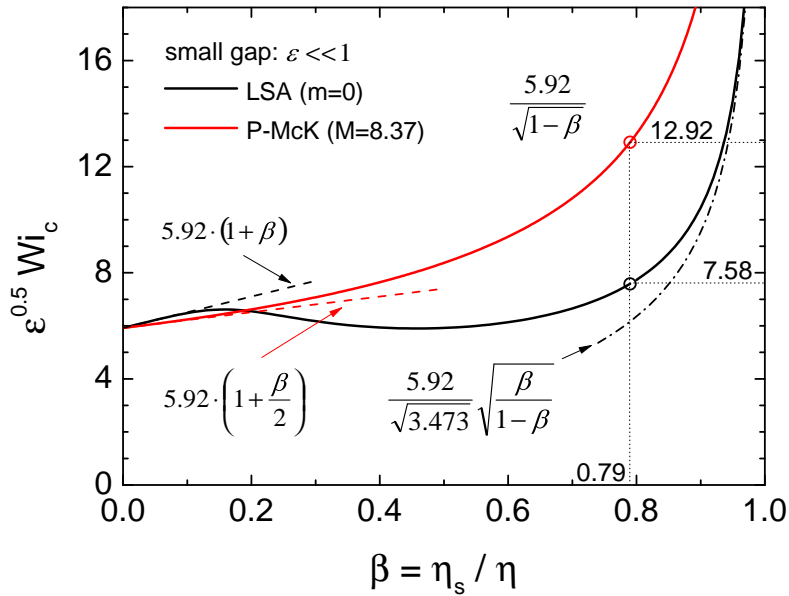


**Figure 4.1:** Pakdel-McKinley criterion (4.14) versus linear stability analysis (axisymmetric ( $m = 0$ ), Larson *et al.* [Lar90]) within the limits of small gap  $\varepsilon \ll 1$ .

**Finite gap (fg).** Both, equation (4.14) and (4.18) are based on the assumption of small gap  $\varepsilon \ll 1$  and the corresponding approximation (4.13), respectively. If this assumption does not hold, the equations (4.13)–(4.18) lose their validity. Joo and Shaqfeh [Joo94, Sha92] expanded the linear stability analysis by accounting for the exact value of the shear rate in the gap, given by equation (4.9). Figure 4.2 shows the respective numerical results<sup>2</sup> for an Oldroyd-B fluid ( $\beta = 0.79$ ,  $m = 0$ , open squares). Obviously, finite-gap effects are monotonically stabilizing and generally increasing the critical value of the modified Weissenberg number at which the flow becomes unstable. This finding is consistent with the inertial instability of Newtonian Taylor-Couette flow which is equally stabilized by finite gap effects [Ess96, Dut07]. While the previous results of linear stability analysis only consider the axisymmetric mode of perturbation, non-axisymmetric modes  $m \geq 1$  are well known to be more unstable [Joo94, Avg93a]. In figure 4.2 the analysis for the first non-axisymmetric mode ( $m = 1$ ) for  $\beta = 0.79$  and finite gap is shown (filled squares). Obviously, the  $m = 1$  neutral curve shows a different geometric scaling on  $\varepsilon$  compared to the axisymmetric ( $m = 0$ ) mode.

#### 4.3.4 Experimental data

To our knowledge, the only experimental study focusing on the explicit geometric scaling of elastic instability in the Taylor-Couette system can be found in the work of Muller *et al.* [Mul89, Lar90]. It refers to the investigation of a Boger fluid with  $\beta \approx 0.79$  and thus can be directly related to the above presented findings of the linear stability analysis (actually, the results of the experimental study and the already presented linear stability analysis were released in joint publications by Muller and Larson). The respective critical modified Weissenberg numbers are also presented in figure 4.2. They are calculated from the critical shear rates extracted from rheometric stress data by using the relaxation time provided by steady shear normal stress data and calculated according to equation (4.11). Both, the small gap (blue filled triangles) as well as the finite gap formulation (calculated at the inner cylinder

<sup>2</sup>Extracted from the original publication by Shaqfeh *et al.* [Sha92].

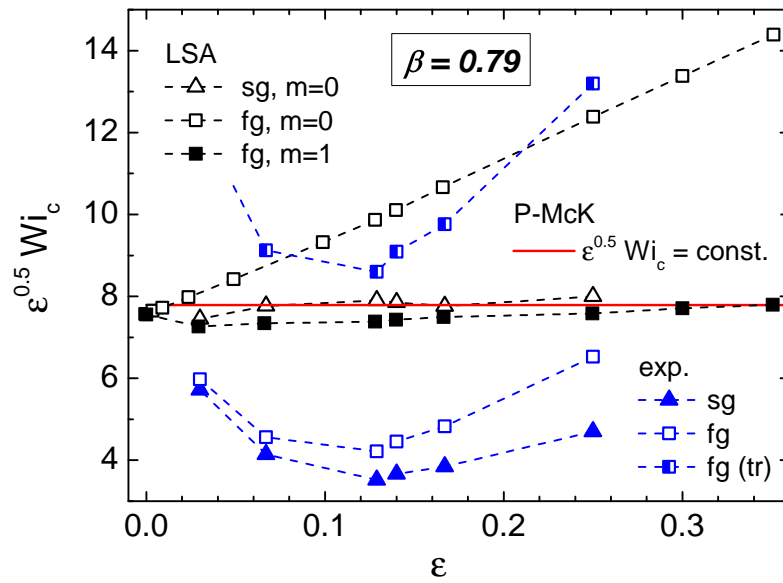


**Figure 4.2:** Results from various linear stability analyses (small gap (sg):  $m = 0$  [Lar90]; finite gap (fg):  $m = 0$  [Sha92],  $m = 1$  [Joo94]), theoretical considerations and experiments [Mul89] concerning the onset of purely elastic instability for an Oldroyd-B fluid with  $\beta = 0.79$ .

$\dot{\gamma}(R_1)$ , blue open squares) of the shear rate according to (4.13) and (4.9), respectively, give significant deviations from the results of the linear stability analysis, not only with respect to the absolute magnitude of the critical values but also with respect to their dependence on the geometrical parameter  $\varepsilon$ . Even when following the authors' proposition to use of an alternative relaxation time from transient normal stress relaxation (cf. blue half-filled squares), the mismatch could not satisfactorily be resolved.

Aiming to contribute to a more consistent picture of elastic instability by answering the still open question presented above, we present in the following sections the results of a vast Taylor-Couette study, in which we investigated various, initially thoroughly characterized viscoelastic polymer solution, with regard to their elastic flow behavior in different customized Taylor-Couette geometries. The experimental results are subsequently analyzed by means of both explicit linear stability analyses and based on the instability criterion by Pakdel and McKinley.



## Fluid samples

### 5.1 Preparation of polymer solutions

In our experimental study, we used commercial batches of highly elastic, long-chained polyacrylamide (PAAm,  $[C_3H_5NO]_n$ ) which was dissolved in different Newtonian solvents. Table 5.1 gives an overview of the investigated solutions. By varying the (weight-averaged) molecular weight  $M_w$  of the polymers ( $(5-6) \times 10^6$  Da or  $18 \times 10^6$  Da, in the following referred to as “lightweight” and “heavyweight”, respectively), their concentrations  $c_{\text{PAAm}}$  (ranging from 150 ppm to 1200 ppm) as well as the Newtonian solvents (aqueous glycerol or sucrose mixture), we get viscoelastic solutions with different rheological properties. Without proof, we assume the polymers to exhibit a Gaussian molar mass distribution centered at the nominal values mentioned above and characterized by a rather broad width for the “lightweight” compared to the “heavyweight” batch.

The glycerol-based solutions (P150<sub>G80</sub>, P600<sub>G80</sub> and P1200<sub>G80</sub>) were prepared in the following way: The polymer powder ( $M_w = (5-6) \times 10^6$  Da, polyacrylamide by Sigma-Aldrich No. 92560) was first dissolved in distilled water at moderate shaking and stirring for 24 hours at ambient temperature ( $\approx 23^\circ\text{C}$ ). Subsequently, the appropriate amount of glycerol was added and the whole solution was gently stirred for another period of 24 hours. The resulting solutions turned out to be very robust against chemical degradation and they could be used even months after the preparation without any change in their rheometric properties. The sucrose-based P500<sub>S58</sub> solution was prepared in the same way just by replacing the glycerol with sucrose. However, all the measurements with this solution had to be performed shortly after their preparation in order to avoid infestation of mold (the sucrose solution is a perfect culture medium for bacteria). The synthesis of the P80<sub>S64</sub> and P150<sub>S65.6</sub> solutions were performed according to a different procedure following the publications by Steinberg *et al.* [Gro00, Gro01, Bur07]. A polymer master solution contained 3000 ppm or 5000 ppm (for the 80 ppm and 150 ppm solution, respectively) of polyacrylamide ( $M_w = 18 \times 10^6$  Da, by Polysciences, no. 18522) which was dissolved in an aqueous solution of 1% sodium chloride under moderate stirring ( $\sim 250$  rpm) for 3 hours in order to put the solution under mechanical degradation and cut the upper tail of the molecular weight distribution. Subsequently, isopropanol and sodium azide were added to reach concentrations of 1% and 250 ppm, respectively, and after one hour of mixing, the solution was stored at  $4^\circ\text{C}$ . Appropriate amounts of the polymer master solution were mixed with respective amounts of a sugar master solution (an aqueous solution of 65.6% saccharose, 1% sodium chloride, 250 ppm sodium azide) and a buffer solution (an aqueous solution of 1% sodium chloride, 250 ppm sodium azide) to obtain the demanded concentrations of polymer and sugar. The use of small amounts of sodium azide which is a strong toxin for organic compounds, allowed to keep the solutions over a longer period

without chemical degradation.

No.	Name	Polymer conc. $c_{\text{PAAm}}$ (ppm)	Mol. weight $M_w$ ( $10^6$ Da)	Solvent (X+H <sub>2</sub> O)		Temp. $\vartheta$ (°C)
				X	%	
1	P150 <sub>G80</sub>	150	5–6*	glycerol	80	10
2	P600 <sub>G80</sub>	600		glycerol	80	10
3	P1200 <sub>G80</sub>	1200		glycerol	80	10
4	P500 <sub>S58</sub>	500	18**	sucrose	58	10
5	P80 <sub>S64</sub>	80		sucrose	64	22
6	P150 <sub>S65.6</sub>	150		sucrose	65.6	23

**Table 5.1:** Listing of the analyzed PAAm solutions (Sigma-Aldrich No. 92560 (\*), Polysciences No. 18522 (\*\*)). The high-molecular weight solutions (\*\*) additionally contain small amounts of sodium chloride and sodium azide.

## 5.2 Rheometric properties of polymer solutions

The polymer solutions were characterized by means of different rheometric experiments, namely steady shear, shear rate relaxation, small amplitude oscillatory and extensional rheometry. The respective methods are described in detail in section 3. For each solution, the particular operation temperature was fixed for all the measurements according to table 5.1 within the accuracy and precision of the respective setup. Multiple independent measurements of fresh samples were performed in order to quantify the quality of the data. A summary of the averaged rheometric parameters with respective standard deviations is given in table 5.3 and the corresponding raw data can be found in the appendix A.

### 5.2.1 Steady shear rheometry

Based on a two-component hybrid model according to the relations (3.7) and (3.8), both the apparent shear viscosity as well as the normal stress data of each polymer solution can be reasonably reproduced by means of a combination of an Oldroyd-B and an sPTT component with associated parameters ( $\eta_s, \eta^U, \lambda^U$ ) and ( $\alpha, \eta^P, \lambda^P$ ), respectively. While the first primarily reproduces the quadratic scaling of the normal stress data, the latter accounts for the shear thinning of the apparent viscosity as well as the slight non-quadratic corrections to the normal stress. The extracted parameters are reliable, i.e. independent measurements give best fit parameters within a rather small range and the associated standard deviations are rather small, accordingly. This is true for the Oldroyd-B parameters and also for the viscosity  $\eta^P$ . However, the relaxation time  $\lambda^P$  and the parameter  $\alpha$  cannot be reliably determined, as the standard errors of the parameters from a single fit are large and in the order of the fitted value itself. Thus, we cannot rely on this fitting parameter. However, when evaluating the product  $\alpha(\lambda^P)^2$  for each fit, one obtains reasonable results. We already discussed this problem above (cf. section 3.1).

An evaluation of the UCM relaxation times of the glycerol-based solutions exhibits a power law dependency on the polymer number density  $n \propto c_{\text{PAAm}}$ , i.e.  $\lambda^U \propto n^{0.46 \pm 0.01}$  with  $n = c_{\text{PAAm}} \rho N_A / M_w$  (cf. figure 5.1).  $c_{\text{PAAm}}$ ,  $\rho$ ,  $N_A$  and  $M_w$  are the polymer concentration, mass density, Avogadro constant and molecular weight, respectively. Furthermore, the corresponding viscosity component also scales via a power law with  $\eta^U \propto n^{1.12 \pm 0.01}$ . This

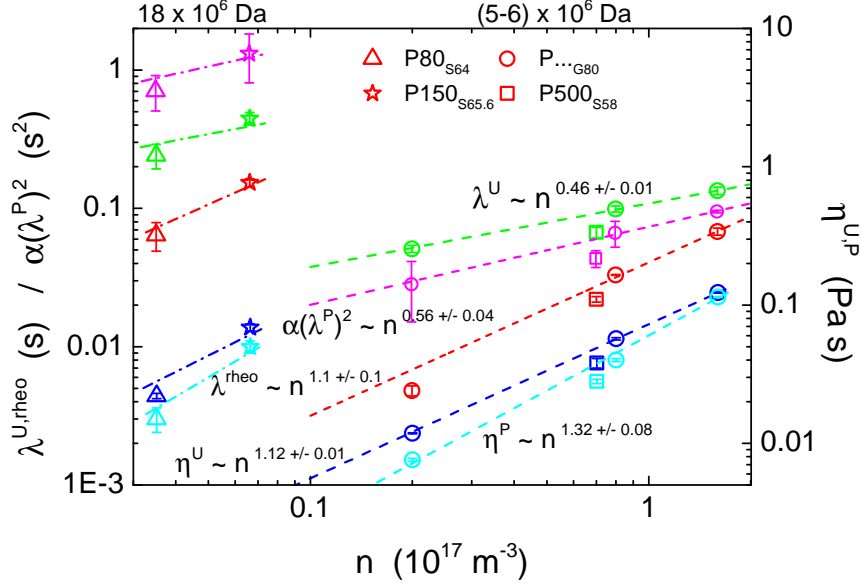


**Figure 5.1:** Relaxation times  $\lambda^{rheo}$  (red),  $\lambda^U$  (green), viscosities  $\eta^U$  (blue),  $\eta^P$  (pale blue) and product  $\alpha(\lambda^P)^2$  (magenta) from the steady shear rheometry in dependence of the polymer number density  $n = c_{PAAm} \rho N_A / M_w$ . The data of the glycerol-based solution (circles) obey power laws in dependence of  $n$  (dashed lines). The same scaling laws (dash-dotted lines) are adapted to the high-molecular weight solutions (triangles, stars).

gives a first normal stress coefficient  $\Psi_1 \propto \eta^U \lambda^U \propto n^{1.58 \pm 0.02}$  which is in notable agreement with the findings of Zell *et al.* [Zel10], who measured an exponent of 1.5 by evaluating a series of normal stress data according to the Oldroyd-B model (4.11). It is worth mentioning that the data by Zell *et al.* were acquired at room temperature and not at 10°C as in the present case. Obviously, a change in temperature only affects the polymer number density via changing the mass density and not the scaling itself. However, by using  $\eta \propto \lambda n$  (cf. (2.45)) the authors concluded a relaxation time  $\lambda \propto \sqrt{\Psi_1 / n} \approx n^{0.25}$ . Obviously, the discrepancy in the scaling for the relaxation time  $\lambda^U$  is due to the different scalings for the viscosity  $\eta^U$ . Here, one has to recall that we cannot explicitly separate between the different number densities  $n^U$  and  $n^P$  associated with the UCM and the sPTT component, which does not allow for a consistent evaluation based on  $n^U$ . Thus, it is not surprising, that in our case the ratio  $\eta^U / \lambda^U$  is not proportional to  $n$  but gives  $\eta^U \lambda^U \propto n^{0.66}$ . The sPTT component of the glycerol-based solutions obeys power laws for the viscosity and the parameter  $\alpha(\lambda^P)^2$  according to  $\eta^P \propto n^{1.32 \pm 0.08}$  and  $\alpha(\lambda^P)^2 \propto n^{0.56 \pm 0.04}$ , respectively.

The sucrose-based P500<sub>S58</sub> solution which involves the same polymer ( $M_w = (5-6) \times 10^6$  Da) as the glycerol-based solutions exhibits a systematic difference when comparing the respective model parameters from the steady shear experiment. All the values are lower than the interpolation from the glycerol-based solution suggests. This hints to the different quality of the sucrose solvent compared to the glycerol solvent, which affects the rheometric quantities. The scaling of the high-molecular weight solutions ( $M_w = 18 \times 10^6$  Da) cannot be quantitatively evaluated as the sucrose concentrations differ in the P80<sub>S64</sub> and P150<sub>S65.6</sub> solution. Furthermore, the respective measurements were conducted at slightly different temperatures. However, when neglecting these error sources (at least for the viscosity one can suggest a partially compensating effect of a slightly increased concentration and temperature) the data suggest a more pronounced dependency on the number density. This indicates a bigger size of the polymer chains, which affect the hydrodynamic interaction with the surrounding solvent.

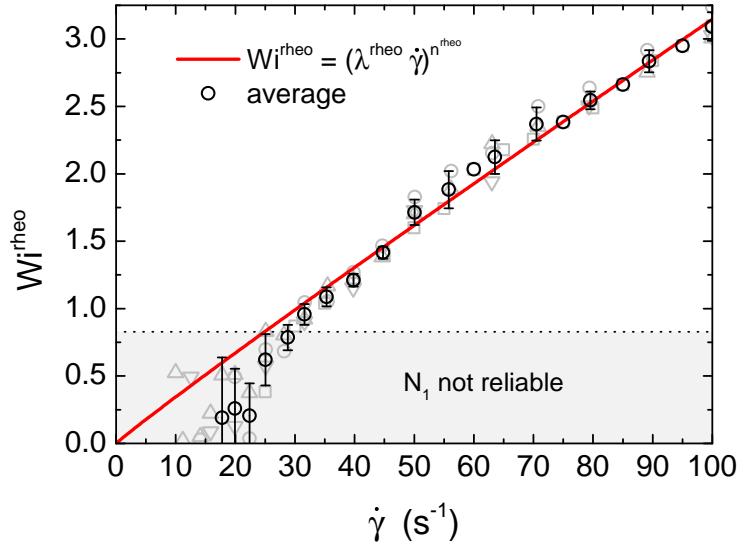


**Figure 5.2:** Rheological Weissenberg number  $Wi^{\text{rheo}}(\dot{\gamma}) = (N_1/2\eta\dot{\gamma})(\dot{\gamma}) = (\lambda^{\text{rheo}}\dot{\gamma})^{n^{\text{rheo}}}$  as the ratio of total first normal stress and twice the total shear stress. The data are extracted from several independent steady shear measurements in the cone-and-plate setup.

The definition of the Weissenberg number  $Wi$  as a function of the shear rate  $\dot{\gamma}$  according to (2.51) is straightforward for the Oldroyd-B model, as the model only provides a single relaxation time  $\lambda$  which scales the normal stress according to  $N_1 = 2\lambda\eta_p\dot{\gamma}^2$ . With the knowledge of  $\eta_p$ , it can be simply extracted by fitting the normal stress data. This is consistent with the more natural definition of  $Wi$  via equation (2.73), i.e. the first normal stress difference to the (polymeric) shear stress. In our hybrid model, the situation is more complex as it incorporates two relaxation times  $\lambda^U, \lambda^P$  of the two polymer components of viscosity  $\eta^U, \eta^P$ . Consequently, there is no a priori definition of  $Wi$  according to (2.51) and we have to modify it. Instead, we will make use of the definition via the stress components and, as we don't need to care about consistency to (2.51), we additionally include the Newtonian stress component in the formulation. Thus, the most intuitive definition of the Weissenberg number for our hybrid model is

$$Wi^{\text{rheo}}(\dot{\gamma}) = \frac{\Sigma\tau_{11}(\dot{\gamma})}{2\Sigma\tau_{12}(\dot{\gamma})} = \frac{\Sigma N_1(\dot{\gamma})}{2\Sigma\tau_{12}(\dot{\gamma})} = \frac{2\eta^U\lambda^U\dot{\gamma}^2 + \tau_{11}^P(\dot{\gamma})}{2(\eta_s + \eta^U)\dot{\gamma} + 2\tau_{12}^P(\dot{\gamma})}. \quad (5.1)$$

Here, the first normal stress data  $N_1$  equals the normal stress  $\tau_{11}$  as  $\tau_{22}$  equals zero for both Oldroyd-B and sPTT fluids (cf. chapter 9). We call (5.1) the *rheological Weissenberg number*, as it allows us to directly translate the shear rheology, i.e. the steady shear and normal stress data as a function of the shear rate, to the dimensionless parameter. Figure 5.2 represents the rheological Weissenberg number for the P600<sub>G80</sub> solution as calculated from the rheometry data (cf. figure 3.2). Within the range of reliable normal stress data  $\dot{\gamma} \gtrsim 25\text{ s}^{-1}$ , the data follow a power law, i.e.

$$Wi^{\text{rheo}}(\dot{\gamma}) = (\lambda^{\text{rheo}}\dot{\gamma})^{n^{\text{rheo}}}. \quad (5.2)$$

with parameters

$$\lambda^{\text{rheo}} = (33 \pm 2) \text{ ms}, \quad (5.3)$$

$$n^{\text{rheo}} = 0.96 \pm 0.03. \quad (5.4)$$

The deviation from the linear dependence on the shear rate as given by the Oldroyd-B model is rather weak for this solution since the shear thinning of the viscosity as well as the deviations of the normal stress from the quadratic scaling with the shear rate are minor, i.e. the power law exponent  $n^{\text{rheo}}$  approximately equals unity for most of the investigated polymer solutions (cf. the appendix for the other corresponding data plots). Furthermore, we can define a rheometric Weissenberg number  $\lambda^{\text{rheo}}$  which is characteristic for the solutions. Table 5.3 summarizes the best fit parameters. Again, for the glycerol-based solutions one can extract a power law dependence on the number density  $n$  according to  $\lambda^{\text{rheo}} \propto n^{1.1 \pm 0.1}$  (cf. figure 5.2).

The derivation of the Oldroyd-B model is based on the assumption of non-interacting Hookean dumbbells and thus it is in fact only valid for dilute polymer solutions and small elongations (i.e. low shear rates), where the molecules have minimal overlap [Lar92]. Even if it is reported in literature (e.g., [Ann01]) that semidilute solution may show in viscometric experiments a behavior consistent with that of a dilute solution, an estimate of the so-called overlap concentration  $c^*$  is important to interpret our rheometry. For this purpose, we further evaluate our viscosity data.

As a rule of thumb, for polymer solutions of high molecular weight, the concentrations must not be higher than a few tens of a weight percent. Otherwise, above some overlap concentration  $c^*$ , the polymer molecule begin to “touch” each other and interactions cannot be neglected any longer. A reasonable estimate of the overlap concentration has to account for all properties of the molecules (molecular weight, chemical composition) as well as the quality of the solvent (poor or good solvent, cf. section 10.1) which further depends on the temperature. All these intrinsic properties influence the initial conformation of a single polymer chain (i.e. an infinite dilute solution) and thus its size, but their explicit effect and interplay is hard to quantify. However, it can be motivated, that the dimension of an isolated polymer chain in solution, i.e. the occupied volume  $\propto \langle R^2 \rangle^{3/2}$  of a single polymer molecule, depending on some estimate of the mean-square end-to-end length  $\langle R^2 \rangle$ , is related to the so-called intrinsic viscosity  $[\eta]$  which is defined as the ratio of the increase in the specific viscosity  $\eta_{\text{sp}}$  to the concentration  $c$  of the solute (polymer) in the limit of zero concentration [Flo74], i.e.

$$[\eta] = \lim_{c \rightarrow 0} \frac{\eta_{\text{sp}}(c)}{c} = \lim_{c \rightarrow 0} \frac{\eta_{\text{rel}}(c) - 1}{c}, \quad (5.5)$$

with the relative viscosity  $\eta_{\text{rel}} = 1 + \eta_{\text{sp}} = \eta/\eta_s$ . Graessley [Gra74] suggested the range  $1 < c[\eta] < 10$  to separate the regimes of low and high concentration for random (unloaded) coils in a good solvent [Yin87] which makes the critical concentration for the transition from the dilute to the semi-dilute regime to be  $c^* = 1/[\eta]$ . Later on [Gra80], the authors suggested a concentration of  $c^{**} \approx 0.77c^*$  to give a more rigorous overlap condition. There are many suggested methods to extract the intrinsic viscosity from the viscosity data  $\eta_{\text{rel}}(c)$  [Koz96] which typically involve the extrapolation of the rescaled viscosities to zero concentration according to 5.5, and they are associated with different formulations of the relative/specific viscosity in the concentration. One possible established formulation is the Huggins equation

$$\eta_{\text{rel}}(c) = 1 + [\eta]c + k_H[\eta]^2c^2 \quad (5.6)$$

which satisfies equation (5.5). The Huggins coefficient  $k_H$  measures the inter-particle interaction of the solute (polymers) at appreciably concentrations. In the accordingly called Huggins plots, the rescaled viscosity  $\eta_{\text{sp}}(c)/c$  is plotted versus the concentration, and the intrinsic viscosity is the extrapolated intercept at  $c = 0$ . However, this method requires highly accurate viscosity data for the small concentrations as errors in the measurements of the viscosities magnify the error in  $\eta_{\text{rel}/\text{sp}}(c)/c$  when  $c$  is small. Furthermore, by means of this evaluation method, the data at  $c = 0$  (which is the solvent viscosity  $\eta_s$ ) cannot be

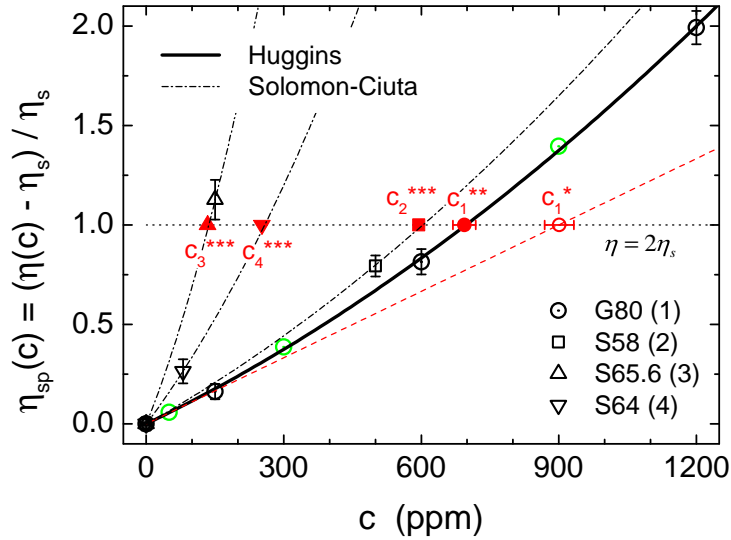


**Figure 5.3:** Specific viscosities of the investigated polymer solutions. The overlap concentrations are estimated based on different approaches (cf. the text).

accounted for. Alternatively [Koz96], it is more reasonable to fit the specific viscosity data to a function that satisfies  $\eta_{sp}(0) = 0$  and to extract the slope  $[\eta] = d\eta_{sp}/dc|_{c=0}$ . In doing so, the data at zero concentration is added to the set of evaluable data. Figure 5.3 presents the specific zero-shear viscosities according to the steady shear rheometry. For the glycerol-based solutions, further data points were added for concentrations  $c = 50$  ppm, 300 ppm and 900 ppm (green circles). A quadratic fit according to equation (5.6) estimates the intrinsic viscosity  $[\eta] = (1.11 \pm 0.05) \cdot 10^{-3} \text{ ppm}^{-1}$  and the Huggins coefficient  $k_H = 0.37 \pm 0.07$ . Accordingly, the overlap concentration for polyacrylamide ( $M_w = (5-6) \times 10^6$  Da) dissolved in an aqueous 80% glycerol solvent at  $\vartheta = 10^\circ\text{C}$  is  $c^* = 1/[\eta] = (901 \pm 37)$  ppm or  $c^{**} = (694 \pm 28)$  ppm.  $c^*$  is the concentration where the linear approximation of the specific viscosity is unity. Interestingly, the more rigorous estimate  $c^{**} \approx 0.77c^*$  gives the point where the Huggins interpolation of the specific viscosity equals unity, i.e. the additional contribution of the polymer of concentration  $c^*$  to the viscosity approximates the solvent viscosity  $\eta_p(c^*) = \eta(c^*) - \eta_s \approx \eta_s$ . This finding corroborates the choice of  $c^{**}$  as a reasonable estimate for the overlap concentration and it agrees with the approach by Larson *et al.*, who evaluated the relation  $0 < \eta_{sp}(c) \lesssim 1$  for a dilute polymer solution [Lar92]. According to this criterion, we have to consider our P1200<sub>G80</sub> solution as a semi-dilute polymer solution.

For each of the sucrose-based solutions, only one concentration data point is available and an evaluation based on a dilution series is not possible. However, as the concentration  $c^{**}$  appears to be a coherent estimate of the overlap concentration in terms of the virtual intersection of the  $\eta_{sp}(c)$ -curve and the horizontal ( $\eta_p(c) = \eta_s$ )-line, i.e.  $\eta_{sp}(c^{**})$ , we can give a qualitative answer to the question, whether the solution is to be considered as dilute or semi-dilute. As the data of the P500<sub>S58</sub> and the P80<sub>S64</sub> solution are definitely smaller than 1 ( $\eta_p(c) < \eta_s$ ), they can be considered as dilute whereas the P150<sub>S65.6</sub> appears to be already in the semi-dilute regime. Nonetheless, for the sake of a complete quantitative determination of the overlap concentration, we emphasize the use of the so-called Solomon-Ciuta equation [Pam08]

$$[\eta]^{SC} = \frac{\sqrt{2}}{c} \sqrt{\eta_{sp}(c) - \ln \eta_{rel}(c)} = \frac{\sqrt{2}}{c} \sqrt{\eta_{sp}(c) - \ln[\eta_{sp}(c) + 1]} \quad (5.7)$$

which allows for a quantitative approximation of the intrinsic viscosity from just a single concentration measurement. It is based on the combination of the Huggins equation and the so-called Kraemer equation which gives an alternative second order expansion of the

Method	Parameter	G80	S58	S64	S65.6
Dilution series	$[\eta]$ ( $10^{-3}\text{ppm}^{-1}$ )	$1.11 \pm 0.05$	–	–	–
	$c^{**}$ (ppm)	$694 \pm 28$	–	–	–
	$k_H$ (–)	$0.37 \pm 0.07$	–	–	–
Solomon-Ciuta	$[\eta]^{\text{SC}}$ ( $10^{-3}\text{ppm}^{-1}$ )	$1.12 \pm 0.05^\dagger$	$1.3 \pm 0.3$	$3.1 \pm 5.6$	$5.8 \pm 1.1$
	$c^{***}$ (ppm)	$691 \pm 29^\dagger$	$595 \pm 117$	$252 \pm 462$	$134 \pm 26$
	$k_H$ (–)	$0.36 \pm 0.40^\dagger$	$0.35 \pm 0.57$	$0.34 \pm 9.8$	$0.35 \pm 0.50$

**Table 5.2:** Intrinsic viscosities and overlap concentrations at zero shear rate, estimated by different approaches. Values denoted with a dagger (†) correspond to the statistics of the single-point evaluations for the various concentrations of the glycerol solutions.

logarithm of the relative viscosity in the concentration  $c$  according to

$$\ln \eta_{\text{rel}}(c) = [\eta]c + \frac{2k_H - 1}{2}[\eta]^2 c^2 \quad (5.8)$$

which is also compatible with the required condition (5.5).

Table 5.2 summarizes the estimates of the intrinsic viscosities, overlap concentrations and Huggins coefficients, evaluated according to the Huggins equation (5.6) for the dilution series of the glycerol solutions and calculated via the Solomon-Ciuta equation (5.7). Even if the single-point evaluation gives large errors based on a worst-case error propagation according to the errors in the specific viscosities, the accuracy of the mean values is remarkable. The calculated overlap concentrations  $c^{***} = 0.77/[\eta]^{\text{SC}}$  give excellent estimates for the inter- or extrapolated intersection points  $\eta_{\text{sc}}(c^{***}) = 1$  (cf. red points in figure 5.3). One has to emphasize that these points are calculated by the specific viscosity of just a single concentration which may be far below the overlap concentration. This finding is corroborated by the evaluation of the dilution series according to Solomon-Ciuta: when calculating  $[\eta]^{\text{SC}}$  according to (5.7) for the various concentrations of the glycerol solutions, the associated mean value perfectly agrees with the Huggins estimate. And so does the derived values of  $c^{***}$  and  $k_H$ , even if the standard error in  $k_H$  is large.

Pamies *et al.* [Pam08] showed that if the viscosity data is adequately represented in quadratic form due to the Huggins equation, the evaluation of the intrinsic viscosity according to the single point Solomon-Ciuta formalism is exact (i.e. independent of the chosen concentration  $c$ ), when  $k_H = 1/3$ . This is very close to the (mean) values of  $k_H$  extracted for the different solutions and it explains why the data turns out to be robust when evaluating the glycerol data of different concentrations. Vice versa, we can trust the overlap concentrations for the sucrose solutions regardless of the concentration used in the calculus. As mentioned above, the Huggins coefficient  $k_H$  characterizes the direct interaction between the polymers and it is strongly correlated to the shape of the polymers in the solution. In [Pam08], a comprehensive list of  $k_H$ -values is given for several systems. For flexible polymer chains, it ranges between 0.2 to 0.8 and it takes most frequently a value of about 0.3 in good solvents. Recently [Hua10], the Huggins coefficient has been estimated by mesoscale simulations to be 0.35 for a flexible polymer in a good solvent. This finding is highly convenient for the applicability of the Solomon-Ciuta method which is corroborated by our rheometric results.

In the above discussion, the intrinsic viscosity and the Huggins coefficient correspond to the

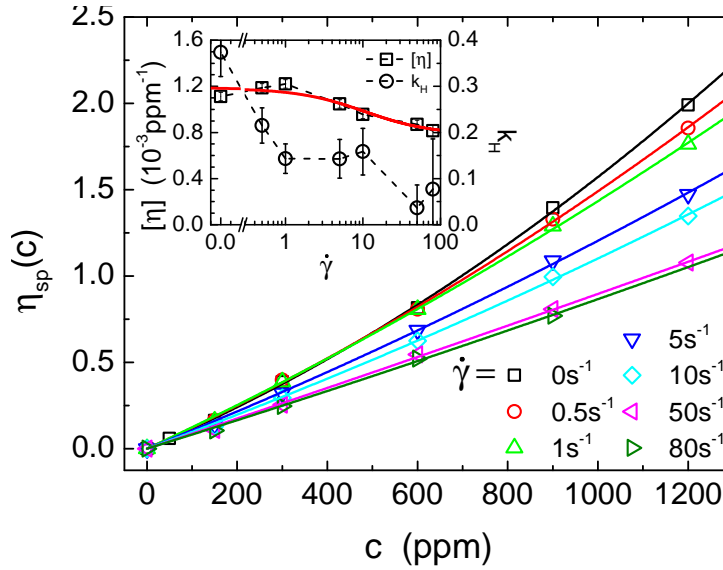


**Figure 5.4:** Specific viscosity of the  $P_{G80}$  solutions. The data were extracted from the viscometric flow curves of the steady shear rheometry at different shear rates. The curves correspond to fits of the Huggins formula (5.6) to the data, and the respective values of  $[\eta]$  and  $k_H$  are plotted versus the shear rate in the inset. The red curve is according to (5.9).

zero-shear limit, i.e. in the situation where the polymers are not affected by external shear stresses. In the following we refer to these values as  $[\eta]_0$  and  $k_{H0}$ , respectively. When exposed to an external shear flow, the polymer chains change their conformation, they are stretched and align within the flow. This is reflected in a shear thinning flow curve, i.e. the apparent shear viscosity  $\eta(\dot{\gamma})$  decreases with increasing shear rate. In analogy to the above evaluation of the zero-shear viscosity, one can map the effect of shear thinning to  $[\eta]$  and  $k_H$ . For any given shear rate  $\dot{\gamma} \geq 0$ , one can calculate the specific viscosity as a function of polymer concentration and one finds that the expansion coefficients  $[\eta](\dot{\gamma})$  and  $k_H(\dot{\gamma})$  according to (5.6) change with  $\dot{\gamma}$ . This is illustrated in figure 5.4 for the  $P_{G80}$  solutions. It is obvious that the influence of the polymer concentration  $c$  on the specific viscosity weakens with increasing shear rate and both, the intrinsic viscosity and the Huggins coefficient decrease in this case (cf. inset graph).

These results are consistently found in literature as presented by Moore [Moo67] in a recent review on the influence of the various factors on the values of  $[\eta]$  and  $k_H$ . Accordingly, it is experimentally found that the intrinsic viscosity  $[\eta]$  may be well approximated by a function

$$[\eta](\dot{\gamma}) = [\eta]_{\infty} + \left([\eta]_0 - [\eta]_{\infty}\right) \frac{b}{b + \dot{\gamma}} \quad (5.9)$$

with the values of the intrinsic viscosities  $[\eta]_0 > [\eta]_{\infty}$  at zero and infinite shear rate, respectively, and a positive parameter  $b$ . The inset in figure 5.4 shows an adaption of this relation (red line) to the data. It can be attributed to the deformation and orientation of the (initially coiled) polymer chains in parallel to the flow. This shear effect is commonly observed for flexible chain polymers with a molecular weight higher than  $M_w = 1 \times 10^6$  Da. Similarly, a dependence of the Huggins-coefficient on the shear rate is observed only for high molecular weight polymer solutions. Here, a decrease of  $k_H$  with increasing shear rate is attributed to the disentanglement of long, entangled polymer chains and the value is commonly observed to decrease to zero at sufficiently high shear rates which is in agreement with our results.

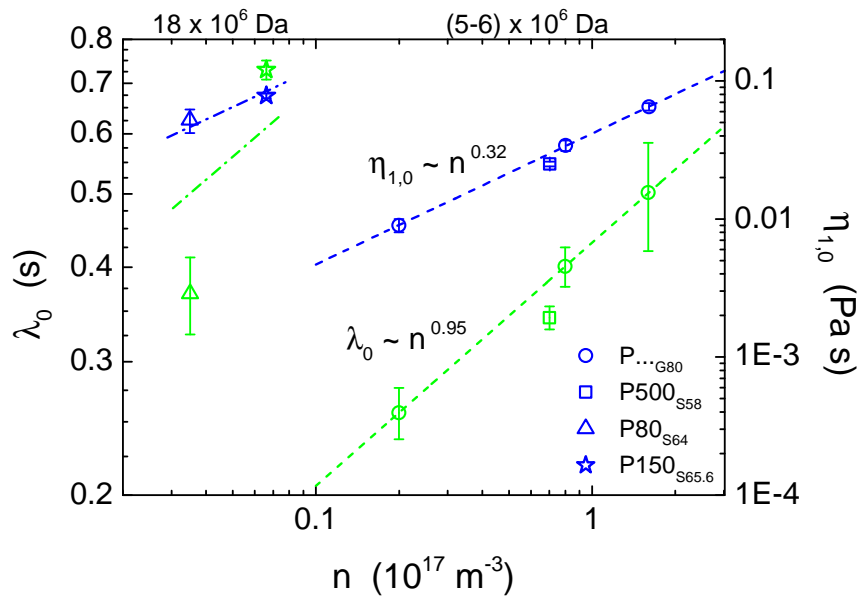


**Figure 5.5:** Relaxation time  $\lambda_0$  (green) and viscosity  $\eta_{1,0}$  (blue) from the shear rate relaxation measurements. For the glycerol-based solutions, both quantities scale according to power laws with the number density  $n$ . The same scaling laws (dash-dotted lines) are adapted to the high-molecular weight solutions (triangles, stars)

### 5.2.2 Oscillatory rheometry

The linear viscoelastic Jeffreys model is able to reproduce the results from the small amplitude oscillatory experiment in terms of the complex modulus  $G(\omega)$  within the reliable frequency range. A two-mode formulation of the Jeffreys model is sufficient to provide reasonable fits. The two-mode Jeffreys model gives a significant higher solvent contribution to the viscosity compared with the hybrid model. This is due to the limitation of our data to high frequencies which does not allow to extrapolate the polymer contributions to the viscosity for large frequencies. This becomes obvious when comparing the dynamic viscosity  $|\eta^*(\omega)|$  with the steady shear viscosity  $\eta(\dot{\gamma})$  according to the Cox-Merz rule: the Jeffrey model strongly overestimates the shear viscosity at high shear rates, even though  $|\eta^*(\omega)|$  is above  $\eta(\dot{\gamma})$  in most of the cases (this is consistently observed in literature [Bir87]). However, the Jeffreys parameters qualitatively reflect the different magnitudes of the parameters extracted from the steady shear rheometry. Remarkably, the oscillatory data perfectly match the steady shear data for the high-molecular weight P80<sub>S64</sub> solution.

### 5.2.3 Shear rate relaxation

All the shear rate relaxation measurements show a common recoil behavior: When the applied steady shear stress is stopped instantly, the sensor of the rheometer decelerates from its initial angular velocity and switches to counter-rotation which reaches a maximum velocity before relaxing to halt. The amplitude of the respective recoil as well as the time scale of its proceeding strongly depends on the properties of the polymer solution. The linear single-mode Jeffreys model is able to qualitatively reproduce the recoil by involving simple Newtonian mechanics for the inertial movement of the sensor. The model leads to the differential equation of a driven harmonic, damped oscillator with the common different cases of movement, depending on the system's parameters.

In [Bar98], the authors used the existence of a series of complete oscillations to extract

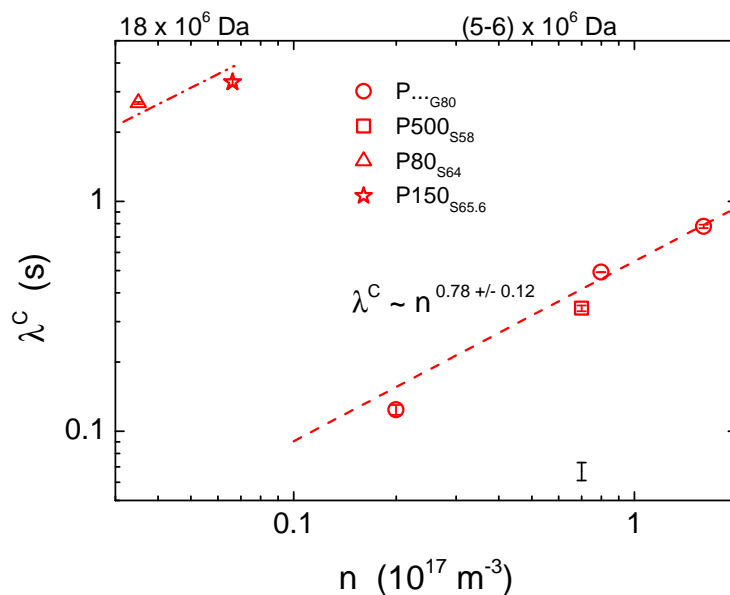


**Figure 5.6:** CaBER relaxation time  $\lambda^C$  in dependence of the polymer number density  $n$ . The glycerol-based solutions exhibit a power law  $\lambda^C \propto n^{0.78 \pm 0.12}$  which is in good agreement with data by Zell *et al.* [Zel10]. The same scaling law (dash-dotted line) is adapted to the high-molecular weight solutions (triangles, stars)

the viscoelastic properties of a yield stress fluid. Thereby, they benefited from a huge shear modulus of their solution. In our case, full oscillations are absent which is in agreement with the rather small values of  $G$  extracted from the model fits. These turn out to be worse for the  $M_w = 18 \times 10^6$  Da solutions, i.e. the experimental relaxation to halt is definitely longer than the model estimate and the global recoil is superposed by slight oscillations. Obviously, the process is governed by more than one characteristic time constant, and our simple model fails at a reasonable description. Furthermore, the values of the (zero-shear) Maxwellian viscosity  $\eta_{1,0}$  (i.e. the viscosity component within the Maxwell element of the Jeffrey model) are too low for all solutions by at least a factor of about two. Here, we allowed for it to be freely fitted although the constitutive model fixes its value according to the values of the initial shear stress  $\tau_0$  and the viscosity  $\eta_1$  according to  $\tau_0 = (\eta_1 + \eta_2)\dot{\gamma}$ . Assuming the proper value for  $\eta_1$  makes the fits even worse. In the end, we cannot rely on the predictions of the applied model. However, both the relaxation time  $\lambda_0$  and the viscosity  $\eta_{1,0}$  (zero-stress limits  $\tau_0 \rightarrow 0$ ) of the glycerol-based solutions obey power laws, i.e.  $\lambda_0 \propto n^{0.95}$  and  $\eta_{1,0} \propto n^{0.32}$ .

#### 5.2.4 Extensional rheometry

The results of the CaBER measurements turn out to be described fairly well by the Oldroyd-B model, i.e. the filament thins exponentially associated with a single relaxation time  $\lambda^C$  which is characteristic for the respective solution. Zell *et al.* found the universal relationship  $\lambda^C \propto n^{ac} \eta_s^{bc} \approx n^{0.8} \eta_s^1$  [Zel10] for the  $M_w = (5-6) \times 10^6$  Da polyacrylamide solutions and for dilute solutions of polyethylenoxide (PEO, Aldrich) with  $M_w = 4 \times 10^6$  Da at constant temperature (RT). For our glycerol-based solutions (which were all measured at  $10^\circ\text{C}$ ), we find  $\lambda^C \propto n^{0.78 \pm 0.12}$  (cf. figure 5.6) in notable agreement with Zell *et al.*. When rescaling the time axis with the relaxation time  $\lambda^C$  associated with the respective measurement, all curves  $h(t/\lambda^C)/h(t_0)$  for the low molecular weight solutions with the inflection point  $t_0$  of  $h(t)$  collapse to a single exponential master curve, i.e.  $h'(t') \propto e^{-t'}$  with  $t' = t/\lambda^C$ ,  $h'(t') = h(t)/h_0$  (cf. figure 5.8). Thus, on the dimensionless time scale  $t/\lambda^C$ ,

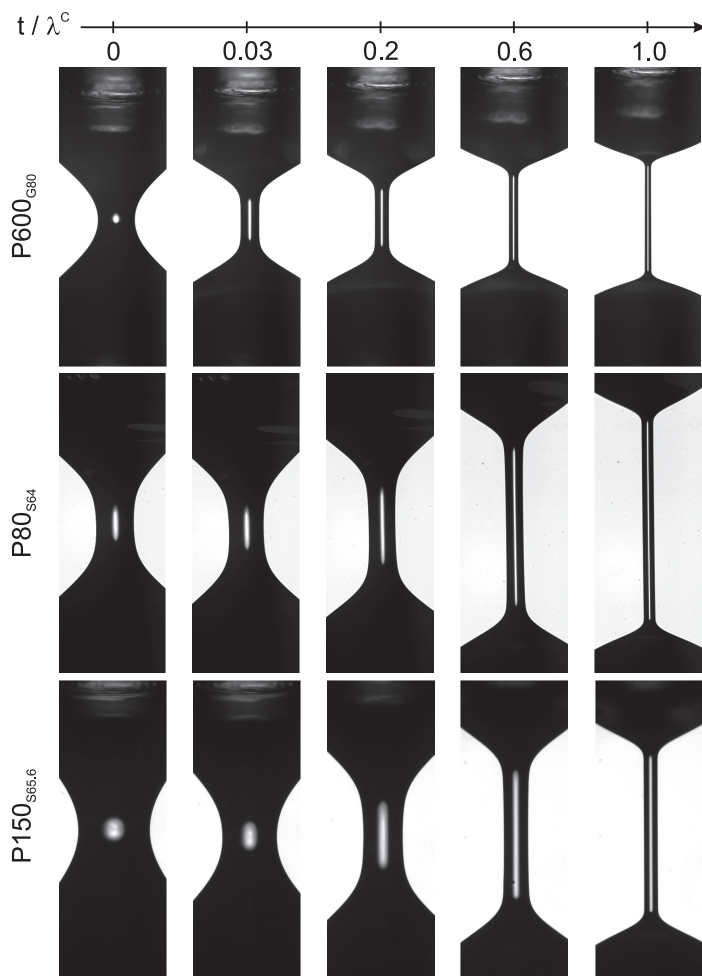


**Figure 5.7:** Sequence of contour images during the capillary thinning at specific rescaled time stamps for the different solutions presented in figure 5.9.

the dynamics of the thinning process appears to be universal and the relaxation time  $\lambda^C$  fully determines the dynamics of the thinning process. Furthermore,  $\lambda^C$  affects not only the width  $h(t)$  of the filament but also its shape. The inset in figure 5.8 represents the coefficient of determination  $R^2$  provided by the parabolic fit of the filament contour. Even after rescaling the time by  $\lambda^C$ ,  $R^2$  is still dependent on  $\lambda^C$ : the higher  $\lambda^C$ , the longer the filament can be described by a parabola-like shape, i.e. the slower decreases  $R^2(t)$ .

The capillary thinning of the solutions with high molecular weight ( $M_w = 18 \times 10^6$  Da) differs from the behavior of the “lightweights”. Figure 5.9 shows both the rescaled filament width and the coefficient of determination  $R^2$  from the parabola fit (cf. inset) plotted versus the rescaled time. Data are shown for the low molecular weight P600<sub>G80</sub> solution and the “heavyweights”. Clearly, the curves do not collapse to a master curve as observed for the “lightweights”. The heavyweight solutions lack in the characteristic sharp decline of  $R^2$  at the transition point and in contrast, the drop is smoothed out which becomes increasingly pronounced with increasing polymer concentration. Figure 5.7 presents contour images of the different solutions at specific rescaled instants of time associated with the highlighted points in figure 5.9. Obviously, due to the higher relaxation time, the dynamics of the thinning process is significantly slower and the associated higher elasticity of the heavyweight solution leads to a smoother contour of the filament which lets the filament appear more parabola-like.

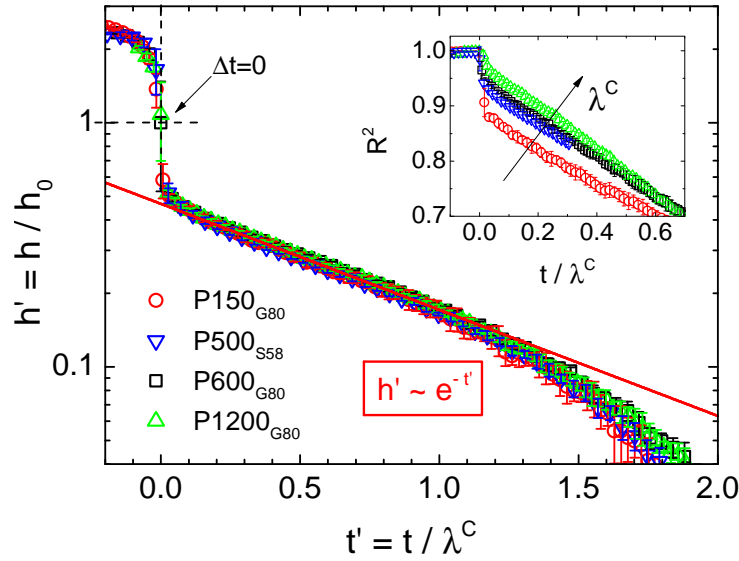


**Figure 5.8:** CaBER data for the  $M_w = (5-6) \times 10^6$  Da solutions. The curves  $h(t)$  collapse to a single master curve when rescaling the time by the respective relaxation time  $\lambda^C$  and additionally normalizing the width  $h$  by its value at the inflection point  $t_0$ . The inset shows the coefficient of determination  $R^2$  for the parabola fit to the filament contour.

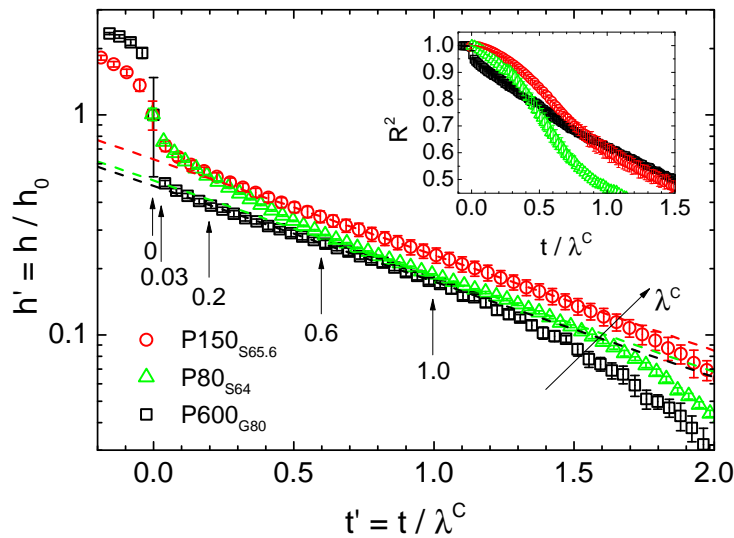


**Figure 5.9:** CaBER data of the P600<sub>G80</sub> solution and of the  $M_w = 18 \times 10^6$  Da solutions. The curves do not collapse to a single master curve after the rescaling. The inset shows the coefficient of determination  $R^2$  for the parabola fit to the filament contour.

### 5.3 Summing up the rheometry

Let's condense the results of our comprehensive rheometry. In view of the hereafter presented steady shear measurements in the Taylor-Couette setup which deserve an interpretation based on reliable information about the explicit rheology of the respective fluid, we consider the steady shear rheometry to provide the most reasonable assessment of the rheology in the Taylor-Couette flow. It is remarkable that all our polymer solutions which evidently differ from each other with respect to the type of solvent, molecular weight and/or concentration

of the added polymer can be described by a constitutive hybrid model, involving an Oldroyd-B and an sPTT component. Based on this model, both the shear-thinning viscosity and the normal stress data can be fitted fairly well with sets of appropriate model parameters  $\eta_s, \eta^U, \eta^P, \lambda^U, \lambda^P$  and  $\alpha$ . It turns out that the shear-thinning viscosity data are basically governed by the sPTT component whereas the normal stress data basically obey a quadratic dependency with the shear rate as given by the Oldroyd-B model.

Our model involves two relaxation times which may differ in magnitude. In the common definition of a Weissenberg number we would have to decide for a single relaxation time at the expense of a loss of rheological information. To avoid this, we prefer an alternative definition of a rheological Weissenberg number  $Wi^{\text{rheo}}$ . It involves full information about the shear and normal stress rheometry. Based on this combined data, every polymer solution can be characterized by a rheological relaxation time according to  $Wi^{\text{rheo}} = (\lambda^{\text{rheo}}\dot{\gamma})^{n^{\text{rheo}}}$  with characteristic exponents  $n^{\text{rheo}}$ . As expected, this characteristic rheological Weissenberg number takes different values for the various polymer solutions. Remarkably, it systematically depends on the polymer number density  $n \propto c_{\text{PAAm}}$ . Based on the data given by the low-molecular weight solutions, one can suggest a power law dependency according to  $\lambda^{\text{rheo}} \propto n^{1.1 \pm 0.1}$ . This also applies to the individual viscosities and relaxation times but with different exponents whereas agreement with the viscosity data by Zell *et al.* [Zel10] is revealed. This gives us a proof of concept for the evaluation of our steady shear rheometry. The data further show that the high-molecular weight solutions exhibit not only higher absolute values of the parameters (even at lower polymer number densities) but also higher power law exponents compared to those of low molecular weight can be suggested.

Power law scalings also show up in literally all of the parameters associated with the evaluation of the CaBER and shear rate relaxation data according to the respective models. Even if the exponents are different with no systematic relationship, this is remarkable. The data of the CaBER relaxation time of the glycerol-based solutions reveal again consistency with data by Zell *et al.* [Zel10] and the respective scaling is reproduced. Of course, it is not surprising at all that the absolute values of the parameters from CaBER and shear relaxation do not agree with the steady shear data. Their evaluation is based on different models with a different number of parameters. Moreover, the various viscometric experiments operate on the polymers in a totally different manner and the individual relaxation modes have to be considered as the result of a weighted superposition of many modes owing to the distribution of polymer chain-lengths.

Regardless of the molecular weight, all polymer solutions with the exception of P150<sub>S65.6</sub> which is slightly above the limit can reliably be considered to be dilute in terms of an estimation of their respective overlap concentration.

		$M_w = (5-6) \times 10^6$ Da				$M_w = 18 \times 10^6$ Da	
Parameter		P150 <sub>G80</sub>	P600 <sub>G80</sub>	P1200 <sub>G80</sub>	P500 <sub>S58</sub>	P80 <sub>S64</sub>	P150 <sub>S65.6</sub>
↓ Reference →		app. A.1	chap. 3	app. A.2	app. A.3.1	app. A.4	app. A.5
steady shear rheometry	$\eta_s$ (mPa s)	119 ± 2	119 ± 2	119 ± 2	83.1 ± 0.2	140 ± 2	105.6 ± 0.5
	$\eta^U$ (mPa s)	11.8 ± 0.1	57 ± 1	123 ± 1	38 ± 3	15 ± 3	50 ± 5
	$\eta^P$ (mPa s)	7.6 ± 0.2	40 ± 1	114 ± 1	28 ± 1	22 ± 1	69 ± 4
	$\lambda^U$ (ms)	51 ± 3	99 ± 5	134 ± 8	67 ± 6	242 ± 49	447 ± 46
	$\lambda^P$ (ms)	$(0.9 \pm 1.5) \cdot 10^3$	23 ± 39	229 ± 323	126 ± 204	$(3.1 \pm 4.8) \cdot 10^3$	$(4.2 \pm 7.4) \cdot 10^3$
	$\alpha(\lambda^P)^2$ ( $10^{-3}s^2$ )	28 ± 13	66 ± 14	94 ± 2	43 ± 6	$(0.7 \pm 0.2) \cdot 10^3$	$(1.3 \pm 0.5) \cdot 10^3$
	$\beta$ (-)	0.86 ± 0.03	0.55 ± 0.02	0.33 ± 0.01	0.56 ± 0.02	0.79 ± 0.04	0.47 ± 0.02
	$n^{\text{rheo}}$ (-)	0.91 ± 0.06	0.96 ± 0.03	0.97 ± 0.03	0.91 ± 0.02	0.56 ± 0.06	0.94 ± 0.06
	$\lambda^{\text{rheo}}$ (ms)	4.8 ± 0.4	33 ± 2	68 ± 4	22 ± 1	64 ± 15	153 ± 11
oscillatory	$\eta_2$ (mPa s)	137 ± 2	172 ± 2	218 ± 3	<b>83*</b>	153 ± 2	-
	$\eta_1$ (mPa s)	3.2 ± 0.1	32 ± 1	87 ± 3	54 ± 4	12 ± 1	-
	$\eta_3$ (mPa s)	4 ± 1	14 ± 1	47 ± 3	16 ± 2	21 ± 1	-
	$\lambda_1$ (ms)	698 ± 45	274 ± 13	269 ± 14	28 ± 8	243 ± 21	-
	$\lambda_3$ (s)	31 ± 8	1.9 ± 0.1	1.8 ± 0.1	0.8 ± 0.1	2.4 ± 0.1	-
relaxation	$\eta_{1,0}$ (mPa s)	9 ± 1	34 ± 3	65 ± 4	25 ± 1	52 ± 10	78 ± 3
	$\lambda_0$ (ms)	257 ± 20	401 ± 24	502 ± 82	343 ± 12	369 ± 43	729 ± 21
	$\bar{G}$ (Pa)	40 ± 3	94 ± 4	99 ± 6	121 ± 8	98 ± 7	87 ± 5
CaBER	$\lambda^C$ (ms)	124 ± 6	492 ± 1	779 ± 14	343 ± 10	$(2.68 \pm 0.03) \cdot 10^3$	$(3.3 \pm 0.1) \cdot 10^3$

**Table 5.3:** Rheometric properties of the different polymer solutions. \*The value had to be fixed in order to force convergence of the fit.

## The Taylor-Couette setup

Figure 6.1 (top) shows a photography of our experimental realization of nine different Taylor-Couette cells. Each cell consists of an inner cylinder with radius  $R_1$  ranging from 2.5 mm to 22 mm and a hollow cylinder with appropriate (inner) radius  $R_2 = R_1 + d$ . For all setups, the gap is kept constant at  $d = 1$  mm. Consequently, the relative gap width  $\varepsilon = d/R_1$  ranges from 0.045 to 0.4. In the operation mode, the inner (rotating) cylinder immerses into the fluid down to a distance of  $L' = 10$  mm to the bottom end of the outer beaker (cf. figure 6.1, bottom). The effective contact height of the fluid is adjusted to  $L = 73$  mm, giving a constant aspect ratio of  $\Gamma = L/d = 73$  for all the setups. The Taylor-Couette cells are

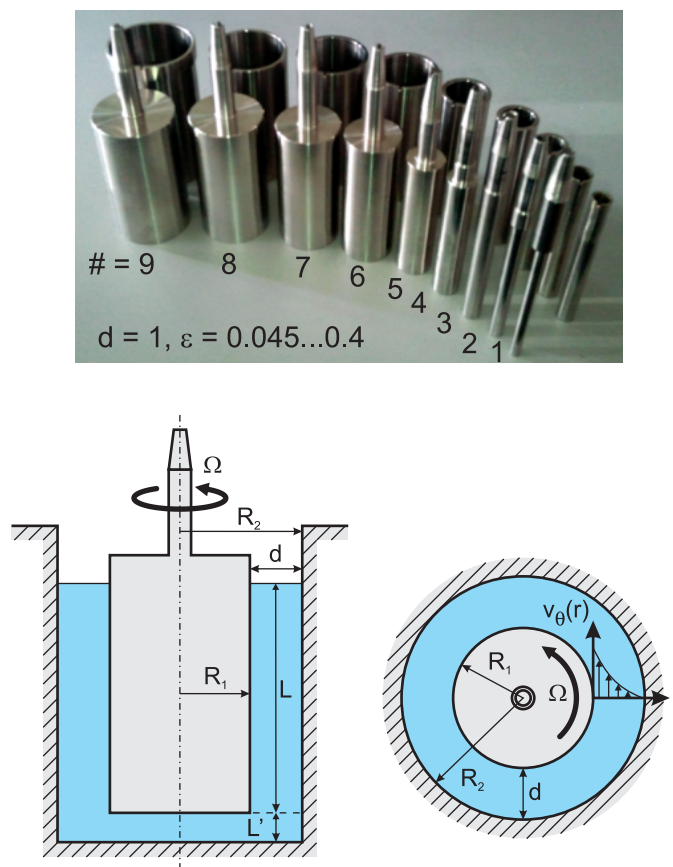


**Figure 6.1:** *Top:* Photography of the different Taylor-Couette geometries used in the experiments. *Bottom:* Sketch of the setup in side and top view.

No.	TC-...	$R_1$ (mm)	$R_2$ (mm)	$\kappa = \frac{R_1}{R_2}$	$\kappa^2$	$\varepsilon = \frac{d}{R_1}$
1	5-7	2.5	3.5	0.714	0.51	0.400
2	7.5-9.5	3.75	4.75	0.789	0.62	0.267
3	10-12	5	6	0.833	0.69	0.200
4	15-17	7.5	8.5	0.882	0.78	0.133
5	20-22	10	11	0.909	0.83	0.100
6	30-32	15	16	0.938	0.88	0.067
7	35-37	17.5	18.5	0.946	0.89	0.057
8	40-42	20	21	0.952	0.91	0.050
9	44-46	22	23	0.956	0.91	0.045

**Table 6.1:** Parameters of the used Taylor-Couette cells. The gap width  $d = R_2 - R_1 = 1$  mm is the same for the different setups.

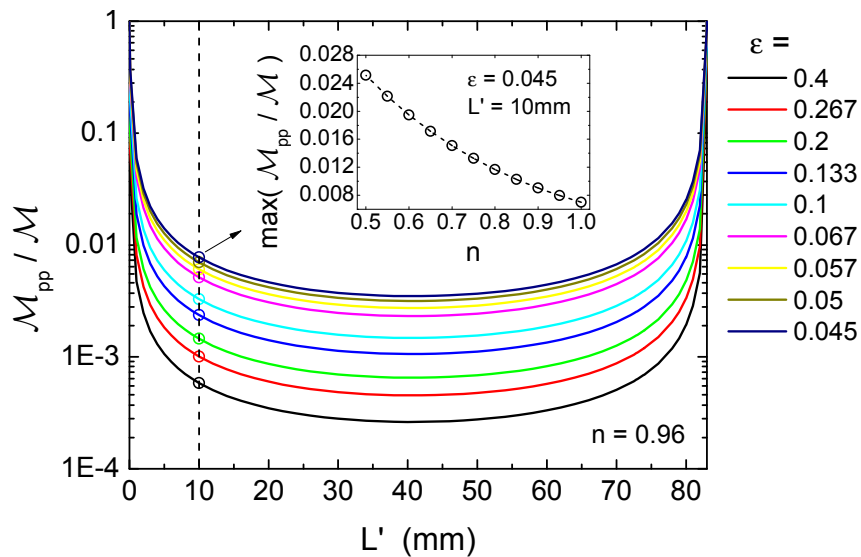


**Figure 6.2:** Relative torque contribution (6.3) of the fluid layer on the bottom of the beaker to the total torque exerted on the rotating inner cylinder as a function of height  $h$ . The curves represent different geometries ( $\varepsilon, d = 1$  mm,  $L = 73$  mm) for a power law fluid  $\tau \propto \dot{\gamma}^{0.96}$ . The inset depicts the relative torque contribution on the power law exponent  $n$  for the largest inner cylinder  $\varepsilon = 0.045$  for  $L' = 10$  mm which is the working distance in our experiments.

attached to our rotational shear rheometer presented in section 3.1. The inner cylinders can be mounted to the motor shaft and the outer beakers are embedded into the temperature bath of the refrigerator. Thus, the experiments can be carried out at well-defined stable thermal conditions.

Great care has been taken of a highly precise fabrication of the cylinders to minimize the errors by a misalignment or eccentricity. The run of the inner cylinders is precise in terms of a maximum precession amplitude (of the free end of the mounted rods) of about  $20 \mu\text{m}$  which is 5% of the gap width. We estimate the deviation from a perfect coaxial alignment to be in the same order. Thus, the effective precision in the measured torque during a rotation cycle turns out to be below 5% of the averaged signal.

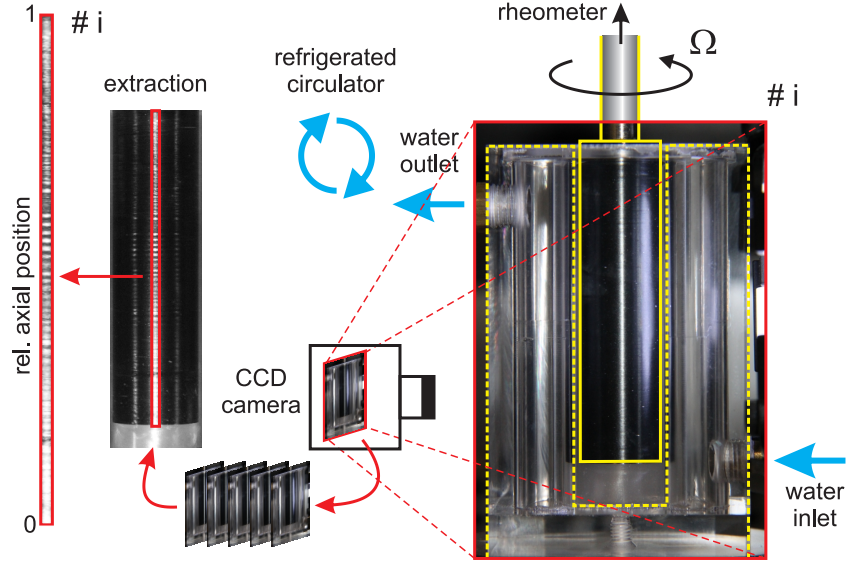


**Figure 6.3:** Sketch of the visualization setup. The front view of the transparent Taylor-Couette cell is captured by a commercial CCD camera and the relevant pixel column is extracted for further evaluation.

The rotation of the inner cylinder is controlled in CR mode, i.e. the instrument forces the desired angular velocity of the inner cylinder  $\Omega$  by adjusting the applied torque  $\mathcal{M}(\Omega)$ . In the case of a simple drag flow, the shear rate  $\dot{\gamma}$  and total shear stress  $\tau_{r\theta}$  at the inner cylinder can be calculated via

$$\dot{\gamma} = \dot{\gamma}(r = R_1) = \frac{\Omega}{\varepsilon} \frac{2(\varepsilon + 1)^2}{\varepsilon + 2}, \quad (6.1)$$

$$\tau_{r\theta} = \tau_{r\theta}(r = R_1) = \frac{\mathcal{M}(\Omega)}{2\pi R_1^2 L}. \quad (6.2)$$

The total torque  $\mathcal{M}$  is made up of two contributions: the torque  $\mathcal{M}_{TC}$ , that is exerted by the fluid in the annular gap between the cylinder walls, and  $\mathcal{M}_{pp}$  by the fluid layer of width  $h$  between the bottom face of the inner cylinder and the bottom of the beaker. Only the first one is related to the proper Taylor-Couette flow. The latter can be estimated for a power law fluid  $\tau_{r\theta} \propto \dot{\gamma}^n$  [Mac94] by

$$\mathcal{M}_{pp}(\Omega) = \mathcal{M}(\Omega) \left[ 1 + (3 + n) \frac{L}{R_1} \left( \frac{2}{n(1 - \kappa^{2/n})} \frac{L'}{R_1} \right)^n \right]^{-1} \quad (6.3)$$

with  $\kappa = R_1/R_2 = (1 + \varepsilon)^{-1}$ . In figure 6.2, the ratio  $\mathcal{M}_{pp}/\mathcal{M}$  is plotted as a function of the height  $L'$  for our different geometries ( $0.045 \leq \varepsilon_i \leq 0.04$ ,  $d = 1$  mm,  $L = 73$  mm) and fixed exponent  $n = 0.96$  (as representatively determined for the P600<sub>G80</sub> solution, cf. table 5.1). The relative torque is the highest for the smallest relative gap width  $\varepsilon = 0.045$ , i.e. the largest cylinders, and for our working distance  $L' = 10$  mm it does not exceed 1%. The inset shows the maximum value  $\mathcal{M}_{pp}/\mathcal{M}(\varepsilon = 0.045, L' = 10$  mm) as a function of the power law exponent  $n$ . Even down to  $n = 0.5$  it does not exceed 2.5%. In view of the minor shear thinning properties of our polymer solutions, the extra torque contribution can be ignored within the limits of the precision of the torque measurement. Alike, by the choice of the large distance  $L'$  of the inner cylinders to the bottom of the cup, the onset of plate-and-plate instabilities (inertial as well as elastic) can be expected to be much higher [Lar92] than those associated with the Taylor-Couette flow. Consequently, any effects originating from the flow

between the end face of the inner cylinder and the bottom of the cup are likely to be negligible in the present case.

For the purpose of a simultaneous flow visualization, the standard setup could be modified by replacing the outer steel beaker of the TC-20-22 setup by a freestanding, equally-sized cup fabricated out of transparent acrylic glass (cf. figure 6.3). Water-bearing cavities within the acrylic block which were connected to the temperature bath of the refrigerated circulator, sustained the temperature control of the system. A tiny amount of kalliroscope, an aqueous emulsion of micron-sized anisotropic, reflective metal flakes, were seeded to the fluid sample without significantly changing the rheology of the fluid. These metal flakes align within the flow due to their anisotropy and reflect the light of a light source according to their orientation. Thus, different flow patterns are represented by discriminable zones of light and dark. By blackening the surface of the inner cylinder, the contrast of the light/dark imaging could be enhanced. The resulting intensity images of the rotating fluid along the whole cylinder axis were captured by a commercial CCD camera and further post-processed for appropriate presentation and evaluation.

## Taylor-Couette measurements

### 7.1 Integral stress measurements

The polymer solutions which had been characterized prior to this, were investigated with respect to their transition to elastic instability in the customized Taylor-Couette cells of different relative gap widths  $\varepsilon$ . For every single polymer solution (cf. table 5.1), we performed transient scanning measurements in the various Taylor-Couette cells (cf. table 6.1) at predefined temperatures identical to the thermal conditions in the rheometric experiments. The standard scanning protocol is defined as follows: The given Taylor-Couette cell is filled with a predefined amount of a fresh fluid sample and we wait about 10 min to let the system reach thermal equilibrium with the thermal bath of a preset temperature. The rheometer automatically increases the angular velocities  $\Omega_i$  of the inner cylinder according to a predefined set of shear rates  $\dot{\gamma}_i$ : starting with the lowest setpoint  $\dot{\gamma}_{\min} = 1 \text{ s}^{-1}$ , the shear rate is increased by steps of  $1 \text{ s}^{-1}$  until the maximum setpoint at  $\dot{\gamma}_{\max} = 200 \text{ s}^{-1}$  is reached. In doing so, each single

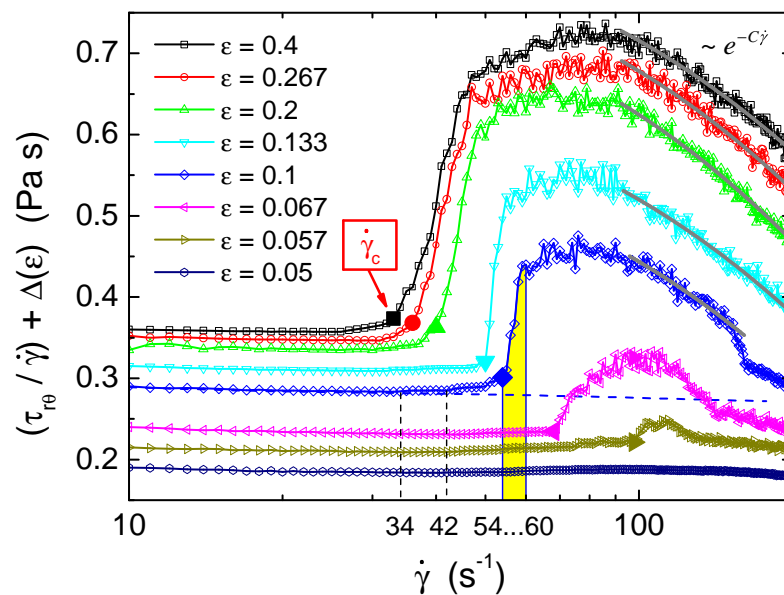


**Figure 7.1:** Taylor-Couette data of the P600<sub>G80</sub> solution. The curves, which are shifted vertically for the sake of a better illustration, correspond to the various geometries of different relative gap width  $\varepsilon$ . For  $\varepsilon = 0.1$ , the flow has been additionally visualized as presented in figure 7.3.

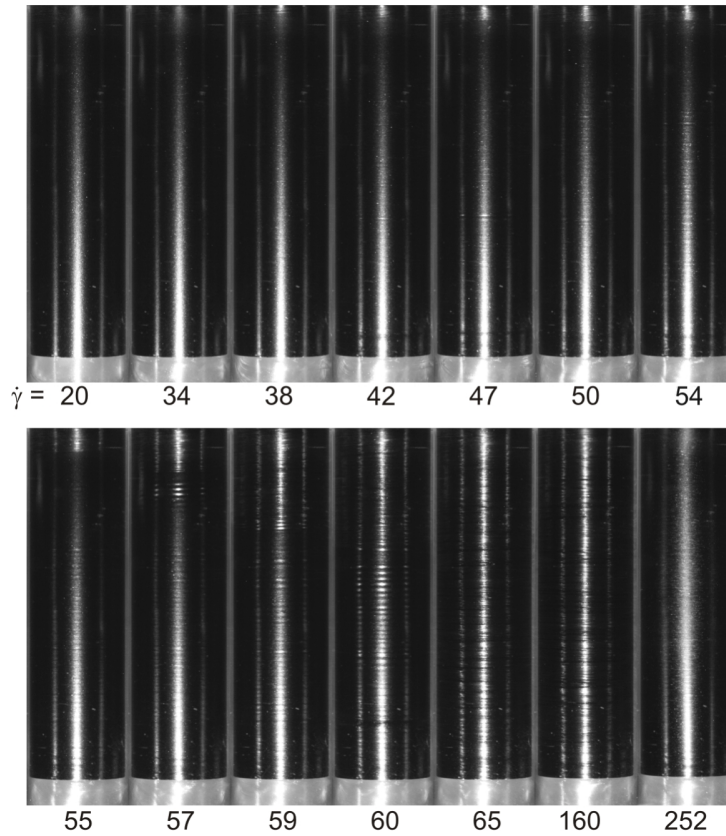


**Figure 7.2:** Representative visualization of the fluid flow (face view) during a standard shear rate sweep measurement of P600<sub>G80</sub> for  $\varepsilon = 0.1$ . Between  $\dot{\gamma}_c = 54 \text{ s}^{-1} \leq \dot{\gamma} \leq 60 \text{ s}^{-1}$ , non-trivial flow patterns spread across the whole cylinder axis.

shear rate is kept constant for  $\Delta t = 10 \text{ s}$  in total, whereas the data from the last  $\Delta t_{\text{meas}} = 5 \text{ s}$  are averaged to give an (integral) value of the applied shear stress  $\tau_{r\theta}(\dot{\gamma}_i)$  (calculated from the torque  $M(\Omega_i)$  according to equation (6.2)) at the corresponding shear rate  $\dot{\gamma}_i = \dot{\gamma}(\Omega_i)$ . The resulting data are presented in terms of the normalized shear stress  $\tau_{r\theta}(\dot{\gamma}_i)/\dot{\gamma}_i$ . Figure 7.1 shows representative data of the P600<sub>G80</sub> solution, measured at  $\vartheta = 10^\circ \text{C}$ . Every single flow curve corresponds to the measurement in a particular Taylor-Couette cell, characterized by the value of the relative gap width  $\varepsilon$ . Since the stress signal is proportional the effective filling height, possible errors in the proper filling level of the geometries which manifest in small mismatches of the curves proportional to the missing filling height, are corrected by appropriate rescaling. For the sake of a better illustration, the curves are vertically shifted upwards in proportion to the respective radius of the inner cylinder relative to the biggest one in use, here it is  $\Delta(\varepsilon) = 10 \text{ mPa s} \cdot (20 - \varepsilon^{-1})$ . The flow curves of the analogous measurements of the other solutions can be found in appendix A.

## 7.2 Flow visualization

In order to relate the observed characteristics of the integral stress measurements to potential changes in the flow field, we visualized the annular flow of the polymer fluid (P600<sub>G80</sub>) during the standard integral stress measurement described before. For every single shear rate initiated during the scanning measurement, one image of the Taylor-Couette cell in front view was captured at the end of the  $\Delta t = 10 \text{ s}$  time slot. Figure 7.2 shows a sequence of images, captured from a front view perspective as illustrated above at selected shear rates during

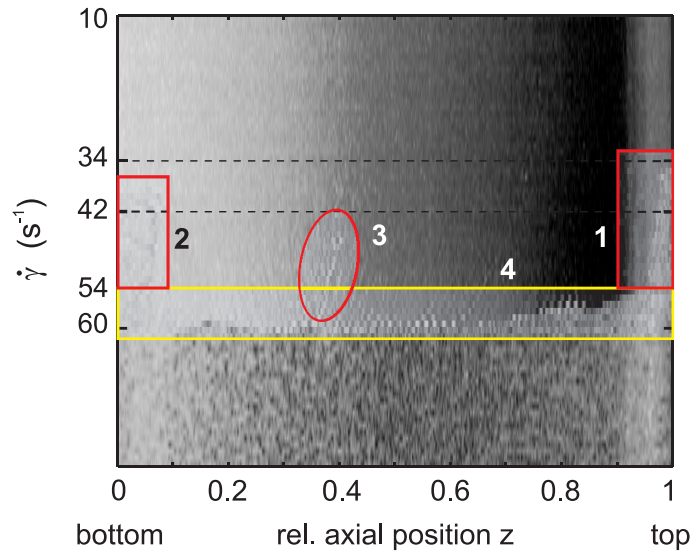


**Figure 7.3:** Space-time plot of the flow patterns during the standard shear rate sweep measurement of P600<sub>G80</sub> for  $\varepsilon = 0.1$  (cf. representative raw images in fig. 7.2. Transition points and characteristic patterns are highlighted.

the integral stress measurement of the P600<sub>G80</sub> solution. It relates to the ( $\varepsilon = 0.1$ )-curve presented in figure 7.1. The images were subsequently processed and the relevant pixel columns which yield the best information, were extracted and stacked in chronological order to finally provide a space-time representation (cf. figure 7.3) of the axially distributed flow patterns as a function of time (and shear rate, respectively).

### 7.3 Interpretation of Taylor-Couette data

The flow curves exhibit a uniform shape associated with characteristic features. At low shear rates, the data reflect the viscometric, purely azimuthal Couette flow and the rescaled shear stress  $\tau_{r\theta}/\dot{\gamma}$  gives the slightly shear thinning apparent viscosity  $\eta(\dot{\gamma})$  of the solution as measured in the steady shear cone-and-plate experiment (cf. for  $\varepsilon = 0.1$  the dashed blue line in figure 7.1). Occasionally, slight deviations appear at very low shear rates which are due to small errors in the coaxial alignment and rotation of the inner cylinder but which are not visible and do not manifest in any explicit pattern in the space-time plot of figure 7.3.

When increasing the shear rate above some value, the stress data start to lift above the viscometric flow curve. For the P600<sub>G80</sub> solution in the  $\varepsilon = 0.1$  cell, this happens at a shear rate of  $\dot{\gamma} \approx 34 \text{ s}^{-1}$ . In the space-time plot, this shear rate is highlighted by particular flow patterns localized at the top end of the inner cylinder (relative axial position  $z = 1$ ) and which slowly spread towards the center down to  $z \approx 0.9$  when further increasing the shear rate (cf. red frame “1”). We identify this event as the emergence of the so-called Ekman-vortices which are formed at the unsteady boundaries of the system and which are well known in Newtonian Taylor-Couette flow [And86], too. These Ekman-vortices exert an increasing additional torque to the inner cylinder on top of the viscometric value which has to be compensated by the rheometer in order to maintain the desired rotation speed and the stress signal from the integral measurement increases, consequently. Above  $\dot{\gamma} \approx 42 \text{ s}^{-1}$  one can observe further Ekman-vortices emerging at the bottom end of the cylinder ( $z \lesssim 0.1$ , cf. figure 7.3, red frame “2”) which is associated with a second, upward kink in the flow curve. In addition, faint transient patterns appear in the middle of the cylinder at position  $z \approx 0.4$  (red

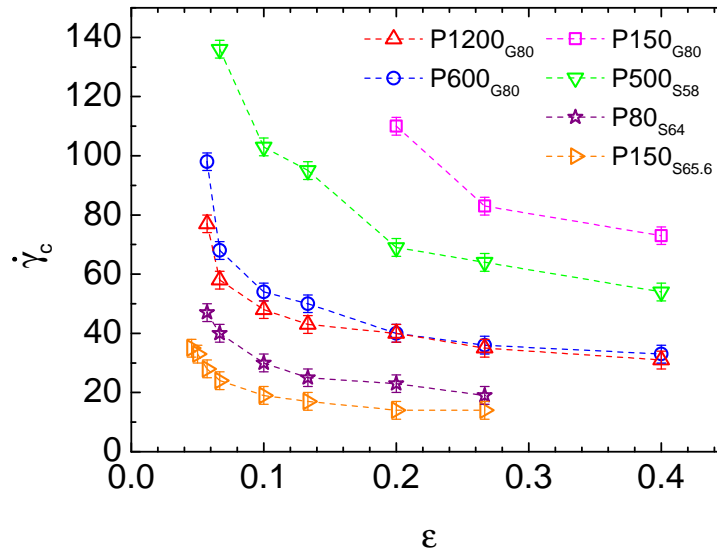


**Figure 7.4:** Critical shear rates  $\dot{\gamma}_c(\epsilon)$  mapping the onset of elastic instability in the Taylor-Couette setups of different gap widths  $\epsilon$ .

ring, “3”). We think of localized non-trivial solutions of the Taylor-Couette problem.

When exceeding a critical shear rate  $\dot{\gamma}_c \approx 54 \text{ s}^{-1}$  ( $Re = 0.31$ ), vortices which are initially located at the system’s boundaries quickly spread across the whole  $z$ -axis of the cylinder (cf. yellow frame) and at  $\dot{\gamma} \approx 60 \text{ s}^{-1}$ , they are located across the whole annular gap. This region corresponds to a sharp, pronounced increase in the flow curves. We refer to the highly characteristic point  $\dot{\gamma}_c$  as the onset of elastic Taylor-Couette instability, triggered by perturbations which drive the laminar base flow (which is now linearly unstable) to some non-trivial, more complex flow state. The associated flow patterns are not stationary but transient in space and time, as the time evolution of the space-time plot (cf. figure 7.3) shows, i.e. the flow patterns are not stable when further increasing the shear rate. Even at fixed shear rate (not shown), the patterns are not conserved. This is a matter of strong chaotic oscillatory vortex motion, called disordered oscillations (DO) which are reported by Groisman and Steinberg and which lead to suggest the development of elasticity-driven turbulence [Gro98a].

Figure 7.4 summarizes the transition points for all our polymer solutions and various geometries in terms of the critical shear rates  $\dot{\gamma}_c$  as listed in table 7.1. It systematically depends on the relative gap width  $\epsilon$  and the corresponding curves  $\dot{\gamma}_c(\epsilon)$  shift for the different polymer solutions. We will evaluate this findings in the following sections.

When the instability has spread across the whole gap, the sharp incline in the flow curves fades to a moderate rising up to some maximum before exponentially decaying (cf. solid gray lines in figure 7.1) down to a level close to the viscometric flow curves. Figure 7.6 depicts the situation at selected points  $A$ – $D$  during and after the decay. In  $A$ , the chaotic flow is fully developed and the secondary flows are strongest in terms of the additional torque exerted to the rotating cylinder. With increasing shear rate ( $B$ ), the flow curve significantly decays but the visualization of the flow does not show any obvious difference to  $A$ . However, at some point, the flow patterns start to vanish and in  $C$  they cover only a small fraction of the whole gap. Finally, no patterns can be observed ( $D$ ) when further increasing the shear rate associated to the values where the flow curves are totally flat again.

This scenario indicates a possible degradation of the polymer solutions which occurs under

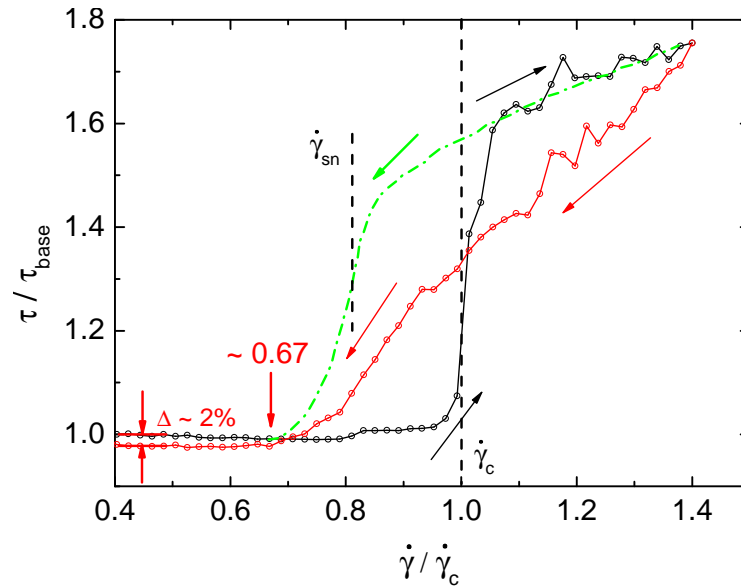


**Figure 7.5:** Hysteresis of the flow curves in the Taylor-Couette experiment. The experimental result (red) significantly differs from what is expected from a proper hysteresis loop (green).

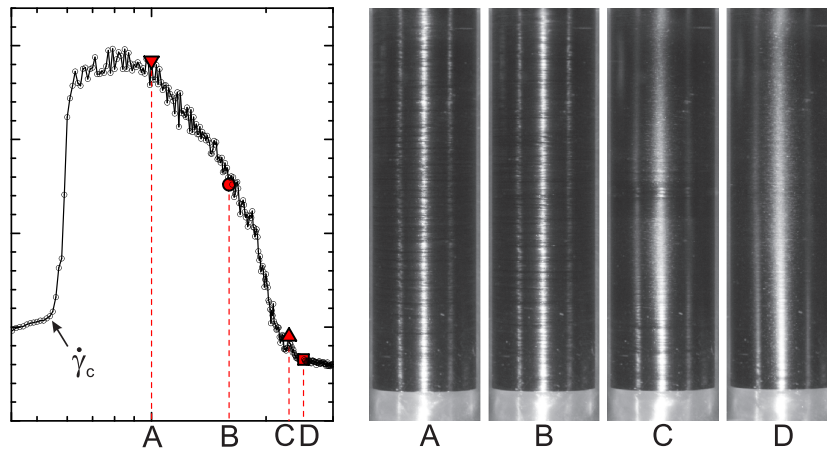


**Figure 7.6:** Representative images of the flow patterns at selected instants during the decaying part of the flow curve.

the influence of strong shearing (shear degradation). This notion is corroborated by the results of a shear rate loop measurement (cf. figure 7.5): It is well known, that the elastic Taylor-Couette instability is subcritical, i.e. there is an intermediate region  $\dot{\gamma}_{sn} < \dot{\gamma} < \dot{\gamma}_c$  where the laminar Couette base flow is unstable to finite perturbations which drive the flow to non-trivial flow states even before the onset of linear instability at  $\dot{\gamma}_c$  [Mor07]. Consequently, the transition to elastic instability is hysteretic, i.e. the flow curve associated with decreasing the shear rate is not on top of the increasing branch but it touches the stable, viscometric branch not until a critical shear rate  $\dot{\gamma}_{sn}$  is reached (here, it is about 67% of the critical onset  $\dot{\gamma}_c$ ) which corresponds to the so called saddle-node point. The green dash-dotted line in figure 7.5 sketches the expected form of the return path of the flow curve. However, the observed behavior deviates from this ideal picture: the flow curve immediately falls below the curve of the forward run and it even drops below the apparent viscosity given by the viscometric flow curve of the fresh sample at moderate shear rates  $\dot{\gamma} < 0.6\dot{\gamma}_c$  (the difference

$\epsilon$	Parameter	P150 <sub>G80</sub>	P600 <sub>G80</sub>	P1200 <sub>G80</sub>	P500 <sub>S58</sub>	P80 <sub>S64</sub>	P150 <sub>S65.6</sub>
0.4	$\dot{\gamma}_c$ (s <sup>-1</sup> )	73	33	31	54	–	–
	$Re$	0.45	0.13	0.09	0.34	–	–
	$Wi_c^{\text{theo}}$	0.39 ± 0.02	1.09 ± 0.16	2.06 ± 0.36	1.17 ± 0.11	–	–
	$\sqrt{\epsilon}Wi_c^{\text{theo}}$	0.24 ± 0.01	0.60 ± 0.10	1.30 ± 0.22	0.74 ± 0.07	–	–
0.267	$\dot{\gamma}_c$ (s <sup>-1</sup> )	83	36	35	64	19	14
	$Re$	0.59	0.17	0.12	0.47	0.11	0.08
	$Wi_c^{\text{theo}}$	0.43 ± 0.02	1.18 ± 0.17	2.32 ± 0.39	1.37 ± 0.12	1.12 ± 0.26	2.05 ± 0.64
	$\sqrt{\epsilon}Wi_c^{\text{theo}}$	0.22 ± 0.01	0.61 ± 0.09	1.20 ± 0.20	0.71 ± 0.06	0.58 ± 0.13	1.06 ± 0.33
0.2	$\dot{\gamma}_c$ (s <sup>-1</sup> )	110	40	40	69	23	14
	$Re$	0.84	0.20	0.15	0.55	0.15	0.09
	$Wi_c^{\text{theo}}$	0.56 ± 0.03	1.31 ± 0.18	2.64 ± 0.42	1.46 ± 0.13	1.24 ± 0.28	2.05 ± 0.64
	$\sqrt{\epsilon}Wi_c^{\text{theo}}$	0.25 ± 0.02	0.58 ± 0.08	1.18 ± 0.19	0.65 ± 0.06	0.56 ± 0.13	0.92 ± 0.29
0.133	$\dot{\gamma}_c$ (s <sup>-1</sup> )	–	50	43	95	25	17
	$Re$	–	0.27	0.17	0.83	0.17	0.12
	$Wi_c^{\text{theo}}$	–	1.62 ± 0.21	2.83 ± 0.44	1.96 ± 0.16	1.30 ± 0.29	2.46 ± 0.71
	$\sqrt{\epsilon}Wi_c^{\text{theo}}$	–	0.59 ± 0.08	1.03 ± 0.16	0.71 ± 0.06	0.48 ± 0.11	0.90 ± 0.26
0.1	$\dot{\gamma}_c$ (s <sup>-1</sup> )	–	54	48	103	30	19
	$Re$	–	0.31	0.20	0.94	0.22	0.14
	$Wi_c^{\text{theo}}$	–	1.74 ± 0.22	3.15 ± 0.48	2.11 ± 0.17	1.44 ± 0.33	2.73 ± 0.76
	$\sqrt{\epsilon}Wi_c^{\text{theo}}$	–	0.55 ± 0.07	1.00 ± 0.15	0.67 ± 0.05	0.46 ± 0.10	0.86 ± 0.24
0.067	$\dot{\gamma}_c$ (s <sup>-1</sup> )	–	68	58	136	40	24
	$Re$	–	0.40	0.26	1.31	0.31	0.18
	$Wi_c^{\text{theo}}$	–	2.17 ± 0.27	3.78 ± 0.56	2.71 ± 0.22	1.69 ± 0.39	3.40 ± 0.89
	$\sqrt{\epsilon}Wi_c^{\text{theo}}$	–	0.56 ± 0.07	0.98 ± 0.15	0.70 ± 0.06	0.44 ± 0.10	0.88 ± 0.23
0.057	$\dot{\gamma}_c$ (s <sup>-1</sup> )	–	98	77	–	47	28
	$Re$	–	0.59	0.36	–	0.37	0.22
	$Wi_c^{\text{theo}}$	–	3.09 ± 0.38	4.98 ± 0.72	–	1.85 ± 0.43	3.93 ± 1.00
	$\sqrt{\epsilon}Wi_c^{\text{theo}}$	–	0.74 ± 0.09	1.19 ± 0.17	–	0.44 ± 0.10	0.94 ± 0.24
0.05	$\dot{\gamma}_c$ (s <sup>-1</sup> )	–	–	–	–	–	33
	$Re$	–	–	–	–	–	0.26
	$Wi_c^{\text{theo}}$	–	–	–	–	–	4.58 ± 1.15
	$\sqrt{\epsilon}Wi_c^{\text{theo}}$	–	–	–	–	–	1.02 ± 0.26
0.045	$\dot{\gamma}_c$ (s <sup>-1</sup> )	–	–	–	–	–	35
	$Re$	–	–	–	–	–	0.28
	$Wi_c^{\text{theo}}$	–	–	–	–	–	4.84 ± 1.20
	$\sqrt{\epsilon}Wi_c^{\text{theo}}$	–	–	–	–	–	1.03 ± 0.26

**Table 7.1:** Summary of critical shear rates  $\dot{\gamma}_c$ , corresponding Reynolds numbers  $Re$  and rheological (modified) Weissenberg numbers  $(\sqrt{\epsilon})Wi_c^{\text{theo}}$  mapping the onset of elastic instability for the different polymer solutions in the various Taylor-Couette cells. In all the cases, the onset of elastic instability occurs at negligible Reynolds numbers  $Re \lesssim 1 \ll Re_c \sim \mathcal{O}(100)$  (cf. equation (4.16)).

is about 2%). Together with the finding that a subsequent run of the same (pre-sheared) sample exhibits a less pronounced instability emerging at an increased critical shear rate (not shown here), this strongly hints to some degradation that happens during the shear process. We will focus on the problem of degradation in more detail by means of an extensive series of measurements which are presented in section 10.

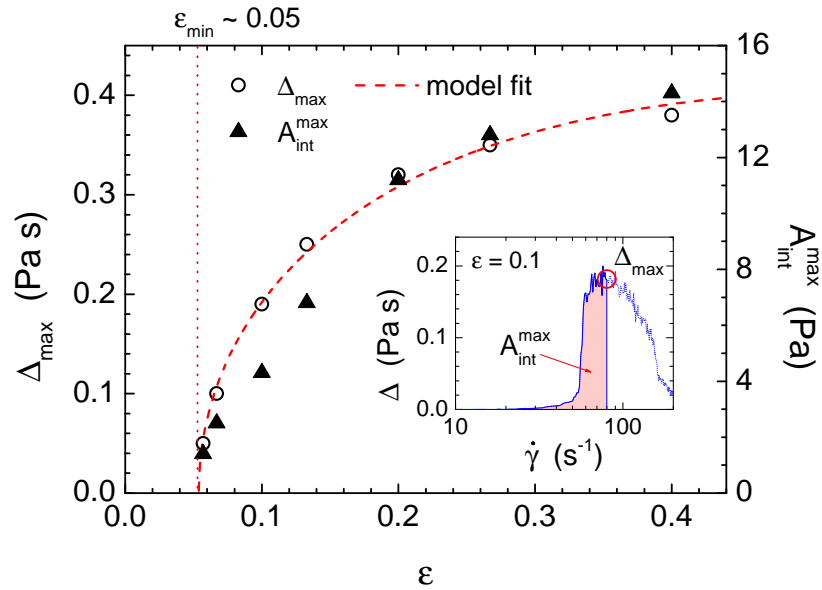


**Figure 7.7:** Evaluation of the flow curves of the P600<sub>G80</sub> sample (cf. figure 7.1). The stress signal in excess to the laminar flow  $\Delta = (\tau/\dot{\gamma}) - (\tau/\dot{\gamma})_{\text{lam}}$  reaches a maximum  $\Delta_{\text{max}}$  involving the integrated area  $A_{\text{int}}^{\text{max}}$  (cf. inset) and both,  $\Delta_{\text{max}}$  and  $A_{\text{int}}^{\text{max}}$  depend on the relative gap width  $\varepsilon$ .

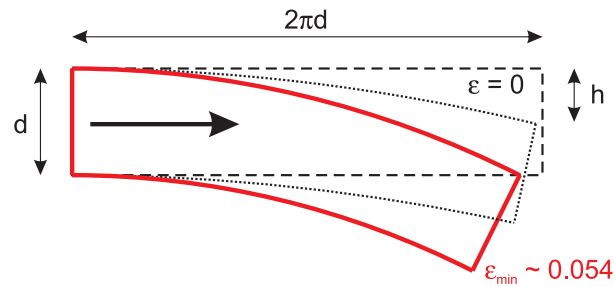


**Figure 7.8:** Geometrical interpretation of the minimum gap width  $\varepsilon_{\text{min}}$  which limits the occurrence of linear elastic Taylor-Couette instability. Adapted from Faisst *et al.* [Fai00].

Comparing the flow curves of the different polymer solutions for the various relative gap widths  $\varepsilon$  reveals another interesting, systematic finding: the smaller  $\varepsilon$  is chosen, the weaker the instability impacts in the stress measurements until it completely disappears (at least to the extent that we cannot reliably evaluate the excess stress signal anymore). This qualitative finding can be quantified by means of an analysis of the measured stress signal in excess to the viscometric flow curve, i.e.  $\Delta = (\tau/\dot{\gamma}) - (\tau/\dot{\gamma})_{\text{lam}}$ , as shown in figure 7.7 for the P600<sub>G80</sub> solution (cf. the inset). Each curve  $\Delta(\dot{\gamma}; \varepsilon)$  can be characterized by a respective maximum  $\Delta_{\text{max}}(\varepsilon)$  and corresponding integrated excess area  $A_{\text{int}}^{\text{max}}(\varepsilon) = \int \Delta(\dot{\gamma}; \varepsilon) d\dot{\gamma}$ . Both quantities represent equivalent measures of the occurrence of instability and they decrease in a similar manner when lowering  $\varepsilon$ . Remarkably, at a minimum value  $\varepsilon_{\text{min}} \approx 0.05$ , the instability completely disappears, i.e. no signal in excess to the viscometric flow curve can be measured for  $\varepsilon < \varepsilon_{\text{min}}$ . Thus, the linear elastic Taylor-Couette instability is suppressed for large radii  $R > R_{\text{max}} = d/\varepsilon_{\text{min}}$ .

This observation can be related to a simple geometrical consideration following the approach by Faisst *et al.* [Fai99, Fai00], who investigated the geometrical transition from the Taylor-Couette to the (linearly stable) plane Couette system (finite gap  $d$ ,  $R \rightarrow \infty$ ). Imagine a unity

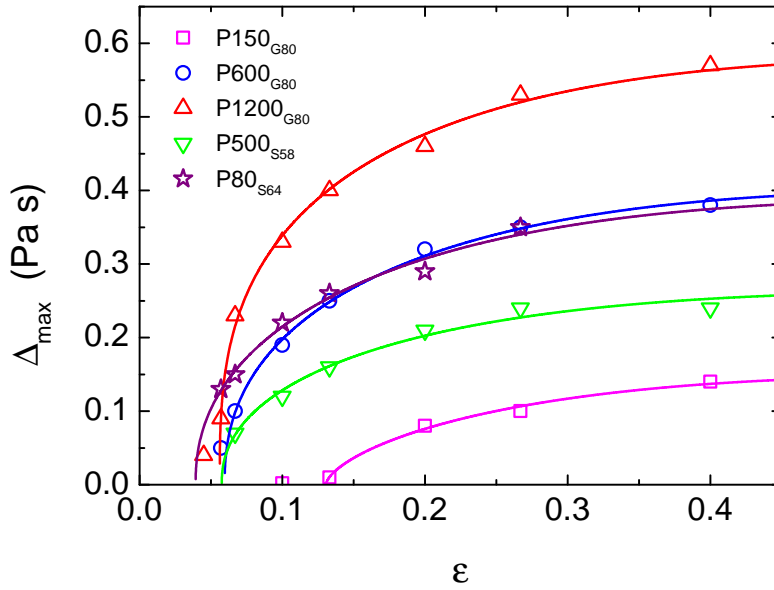


**Figure 7.9:** Maximum amplitude  $\Delta_{\max}(\varepsilon)$  of the instability signal for the different polymer solutions. The model (7.3) is fitted to the data points with a joint parameter  $B = 0.45 \pm 0.11$ .

cell of width  $d$  and (arc) length<sup>1</sup>  $2\pi d$  which represents a section of the (annular) gap of the plane (Taylor-) Couette system (cf. figure 7.8). Starting with the plane Couette system (no curvature,  $\varepsilon = 0$ ), increasing  $\varepsilon$  leads to a bending of the cell with an associated deflection length  $h$ . At a value  $\varepsilon_{\min}$ , the deflection equals the width  $d$  of the cell and from this point, further increasing  $\varepsilon$  results in a cell which is curved so much that one “cannot look” in a straight line (following the direction of the arrow in figure 7.8) through the cell anymore. This gives a very simple, qualitative criterion for the annular flow to “feel” the curvature of the cell. Vice versa, a Taylor-Couette “loses” its curvature (needed for the elastic instability) at this minimal relative gap width  $\varepsilon_{\min}$ . A simple geometrical calculus gives the equation

$$\frac{h(\varepsilon) - d}{d} = (1 + \varepsilon^{-1}) \left[ 1 - \cos\left(\frac{2\pi\varepsilon}{1 + \varepsilon}\right) \right] - 1 \doteq 2\pi^2 \frac{\varepsilon}{1 + \varepsilon} - 1 \stackrel{!}{=} 0 \quad (7.1)$$

with the solution

$$\varepsilon_{\min} \approx \frac{1}{2\pi^2 - 1} = 0.053. \quad (7.2)$$

Strikingly, this simple qualitative estimate  $\varepsilon_{\min} \approx 0.053$  agrees well with the experimental finding as seen above (with the exception of the P150<sub>G80</sub> solution). Let’s now assume that the impact of the elastic instability scales with the geometrical deflection of the unit cell according to

$$EI \propto \left( \frac{h(\varepsilon) - Cd}{d} \right)^B, \quad 0 < B < 1, \quad C > 0, \quad (7.3)$$

where we additionally allow for the critical deflection to vary according to  $h_{\min} = Cd$  (accounting for the qualitative nature of the criterion). This heuristic model can be reasonably fitted to the experimental data  $\Delta_{\max}(\varepsilon)$  as illustrated in figure 7.7 (dashed red curve). Figure 7.9 presents the respective evaluation for the different polymer solutions. The results exhibit a scaling given by

$$\Delta_{\max}(\varepsilon) \propto \left( \frac{h(\varepsilon) - Cd}{d} \right)^{0.45 \pm 0.11}. \quad (7.4)$$

<sup>1</sup>This is the characteristic length of coherent structures in the plane Couette flow [Fai99, Fai00].

---

In section [9.7](#), we will compare this finding with a thorough linear stability analysis of the Taylor-Couette base flow.



## Pakdel-McKinley criterion for finite gap

As seen above, the critical onset of the elastic Taylor-Couette instability systematically depends on the gap width  $\varepsilon$  and the corresponding curves shift with changing the polymer solution, i.e. changing the rheometry. In the investigated cases, the elastic instability occurs at Reynolds numbers  $Re \lesssim 1$  (cf. table 7.1) far below the onset of inertial instability  $Re_c = \sqrt{1700/\varepsilon} \sim \mathcal{O}(100)$ . Even though, strictly spoken, the Reynolds number is not zero, we will allude to *purely* elastic instability. This will be legitimated in section 9 by the results of our linear stability analysis which accounts for non-zero Reynolds numbers (whose effect will turn out to be negligible within the relevant range of  $Re$ ). First, we want to evaluate the experimental data with regard to the (purely elastic) instability criterion by Pakdel and McKinley focusing on both, the geometric as well as the rheometric scaling.

In view of the explicit dimensions of our Taylor-Couette cells listed in table 8.1, the approximation of small gap as demonstrated in section 4.3.2 is not reasonable. This shortcoming is represented in figure 8.1 in terms of the shear rate relative to the maximum one at the inner cylinder as a function of the relative distance from the latter  $r' = (r - R_1)/d \in [0, 1]$  in the case of laminar (Couette) flow. According to (4.9) it is given by

$$\frac{\dot{\gamma}(r; \varepsilon)}{\dot{\gamma}(r = R_1; \varepsilon)} = \frac{1}{(1 + r'\varepsilon)^2} . \quad (8.1)$$

The curves converge rather slowly to the small gap limit  $\varepsilon \rightarrow 0$  represented by a horizontal line, and even at the smallest gap  $\varepsilon = 0.045$ , the shear rate at the outer boundary is only about 90% of the maximum value at the inner cylinder. The relative accuracy of the small gap approximation given by

$$\frac{\dot{\gamma}_{\text{sg}}(\varepsilon)}{\dot{\gamma}(r, \varepsilon)} = \frac{(\varepsilon + 2)(r'\varepsilon + 1)^2}{2(\varepsilon + 1)^2} =: \text{rel}(\varepsilon; r') \quad (8.2)$$

is represented in figure 8.2 for different positions  $r'$ . The mismatch of the approximation is most pronounced for the shear rates at the inner cylinder ( $r' = 0$ ) and it only estimates about 61% of the exact value for  $\varepsilon = 0.4$ . Increasing  $r'$  improves the quality of the approximation and at  $r' \approx 0.63$  it turns to an overestimation of the local shear rates. For  $r' \gtrsim 0.75$  the shear rate is overestimated for any gap width  $\varepsilon$ . This clearly shows, that for the Taylor-Couette geometries used in our experiments (cf. red circles in figure 8.2) and also for those used by Muller *et al.* [Mul89, Lar90] (blue squares) deviations from the actual situation in the gap are significant and not only the absolute values of the shear rates but also the global dependence on the given geometry are falsified. Thus, one cannot expect to find consistency within the small gap approximation between experimental results, linear stability analysis and

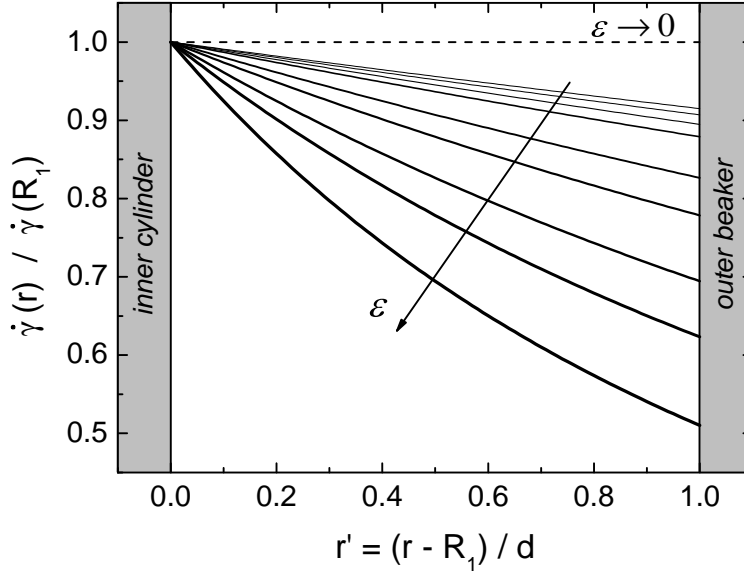


**Figure 8.1:** Relative drop of the local shear rate  $\dot{\gamma}(r)$  compared to the maximum shear rate at the inner cylinder  $\dot{\gamma}(R_1)$  as a function of the relative position  $r' = (r - R_1)/d$  in the gap for the different values of  $\epsilon$  as realized in the experiments (see table 6.1).

the Pakdel-McKinley criterion, neither in terms of absolute values nor in terms of scaling.

The adaption of the Pakdel-McKinley criterion to the general case of finite gap width is straightforward. The only question to answer is where to locate the onset of elastic instability. Taking the criterion seriously, one has to find the point within the gap where the criterion is met first, giving the locus where perturbations superposed to the base flow are amplified and convected to other spots in the gap where the criterion is not initially met [Pak96]. The most intuitive choice is the fluid layer at the inner cylinder  $r = R_1$  ( $r' = 0$ ), as at this location, the shear rate is maximum

$$\dot{\gamma}_{\max} := |\dot{\gamma}(R_1)| = \frac{\Omega}{\epsilon} \frac{2(\epsilon + 1)^2}{\epsilon + 2}. \quad (8.3)$$

Esser and Grossman [Ess96] argued that this is not the proper choice for the inertial Taylor-Couette instability but they found best agreement with the results of linear stability analyses for  $r' \approx 0.5$ . However, for a first estimate, we keep the choice  $r = R_1$  and we keep in mind that the dependence of the correction  $rel(r'; \epsilon)$  on  $\epsilon$  vanishes with increasing  $r'$ .

Equation (8.3) interrelates the Deborah number  $\lambda\Omega$  and the Weissenberg number  $\lambda\dot{\gamma}$  and according to (4.14), the instability criterion for the finite gap Taylor-Couette flow of an Oldroyd-B fluid yields

$$\sqrt{\epsilon}Wi \geq \frac{M}{\sqrt{2(1-\beta)}} \sqrt{\frac{2(\epsilon + 1)^2}{\epsilon + 2}} = \frac{M}{\sqrt{2(1-\beta)}} \sqrt{1 + \frac{3}{2}\epsilon + \frac{\epsilon^2}{2(\epsilon + 2)}}. \quad (8.4)$$

Here, the discriminant of the square root has been transformed via partial fraction decomposition to relate it directly to the case of small gap (given as the zero order  $\mathcal{O}(\epsilon^0)$ ). It is worth mentioning that Esser and Grossman [Ess96] deduced a similar finite gap formulation for the primary inertial Taylor-Couette instability

$$\sqrt{\epsilon}Re_c^{\text{in}} \propto \frac{(\epsilon + 2)^2}{2\sqrt{3\epsilon + 4}} \propto \sqrt{1 + \frac{5}{4}\epsilon + \frac{\epsilon^4 + 8\epsilon^3 + 9\epsilon^2}{4(3\epsilon + 4)}} \quad (8.5)$$

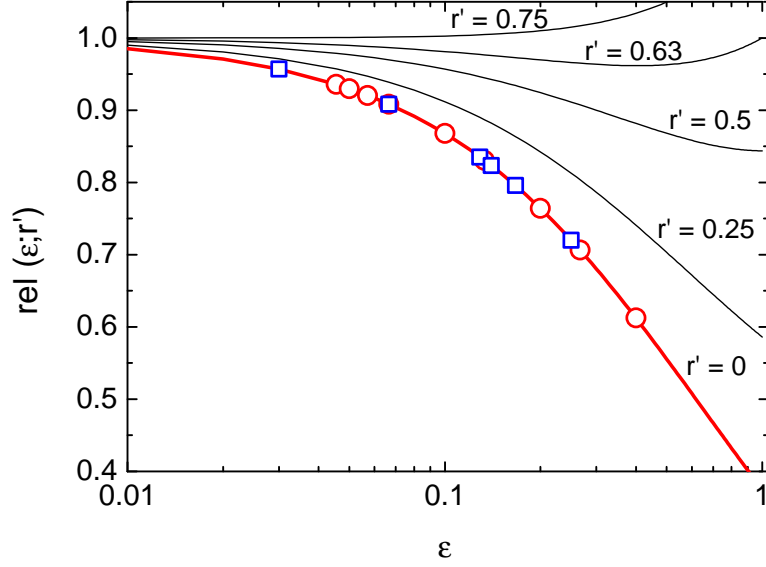


**Figure 8.2:** Ratio of the shear rate given by the small gap approximation compared to the exact value according to equation (8.2) at different positions in the gap. For the Taylor-Couette cells used in the experiments (red circles), at the inner cylinder ( $r' = 0$ , red curve) the ratio drops down to  $rel(0.4; 0) \approx 0.61$  for the biggest relative gap width  $\varepsilon = 0.4$ . Squares refer to the geometries used in the experiments by Muller *et al.* [Mul89, Lar90]

by expanding the fundamental Rayleigh criterion<sup>1</sup> by the energy loss due to viscosity and assuming  $r' = 0.5$ . It has been fine-tuned by Dutcher and Muller [Dut07] and excellent agreement with various experimental data could be achieved.

In order to compare the prediction of the finite gap Pakdel-McKinley criterion (8.4) with our experimental results, we convert the Weissenberg number (associated with the Oldroyd-B model) to the rheological (modified) Weissenberg number according to

$$Wi = \left| \frac{\tau_{11}}{2\tau_{12}} \right| = \left| \frac{\tau_{11}}{2\Sigma\tau_{12}} \frac{\Sigma\tau_{12}}{\tau_{12}} \right| = \frac{Wi^{\text{rheo}}}{1 - \beta} \quad (8.6)$$

which leads to

$$\sqrt{\varepsilon} Wi^{\text{rheo}} \geq \frac{M}{\sqrt{2}} \sqrt{1 - \beta} \sqrt{\frac{2(\varepsilon + 1)^2}{\varepsilon + 2}} \quad (8.7)$$

or

$$\sqrt{\varepsilon} Wi_c^{\text{rheo}}(\varepsilon; \beta) = f(\beta) \sqrt{1 + \frac{3}{2}\varepsilon + \frac{\varepsilon^2}{2(\varepsilon + 2)}} \quad (8.8)$$

with  $f(\beta) = M\sqrt{1 - \beta}/\sqrt{2}$ . In figure 8.3 an adaption of the criterion to the experimental data is shown (solid lines). Here, our experimental findings of the critical shear rates  $\dot{\gamma}_c$  (cf. table 7.1 and figure 7.4) are converted to the modified Weissenberg numbers  $\sqrt{\varepsilon} Wi^{\text{rheo}}$

<sup>1</sup>An early derivation of the critical condition for the inertial Taylor-Couette instability was performed by Lord Rayleigh [Ray17] for an inviscid fluid by balancing pressure and centrifugal forces. It leads to the simple instability criterion

$$\frac{d}{dr} [rv_\theta(r)]^2 < 0.$$

While the laminar Couette flow is unstable for all Reynolds numbers for an inviscid fluid, viscosity tends to delay the instability: Viscous drag reduces the effective centrifugal force on a fluid element and at the same time viscosity causes angular momentum to be exchanged with adjacent fluid elements so that the imbalance is diffused away [Tag94].

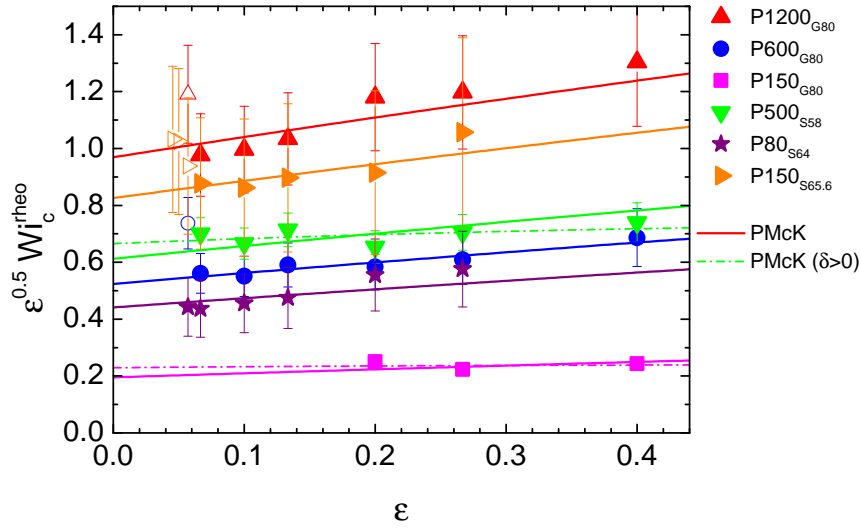


**Figure 8.3:** Experimental onsets of (purely) elastic instability in terms of the modified rheological Weissenberg number  $\sqrt{\epsilon} W_i^{rheo}(\epsilon)$ , calculated according to the respective rheometric results via (5.2). The solid lines reflect the prediction of the finite gap Pakdel-McKinley criterion (8.8). Here, the rheometric scaling function  $f(M, \beta)$  is fitted to the data. The dash-dotted lines are generated by additionally allowing for an “optimal” locus  $r'$ , where the criterion has to be fulfilled first.

according to equation (5.2). The error bars  $\delta\sqrt{\epsilon} W_i^{rheo} = \sqrt{\epsilon} \delta W_i^{rheo}$  give a worst-case error estimate based on simple error propagation, i.e.

$$\begin{aligned} \delta W_i^{rheo} &= \sum_i \left| \frac{\partial W_i^{rheo}}{\partial x_i} \right| \\ &= n^{rheo} (\lambda^{rheo} \dot{\gamma}_c)^{n^{rheo}-1} (\delta \lambda^{rheo} + \delta \dot{\gamma}_c) + \ln(\lambda^{rheo} \dot{\gamma}_c) (\lambda^{rheo} \dot{\gamma}_c)^{n^{rheo}} \delta n^{rheo}, \quad (8.9) \end{aligned}$$

accounting for the errors in the rheometric relaxation time  $\lambda^{rheo}$  as well as for the uncertainty in the localization of the critical shear rate  $\dot{\gamma}_c$  which is assumed to be  $\delta \dot{\gamma}_c = 3s^{-1}$ . When fitting the criterion to the data, the scaling factor  $f(\beta)$  is adapted for each solution by accounting for  $\sqrt{\epsilon} \delta W_i^{rheo}$  as an instrumental error.

With regard to the scaling on  $\epsilon$ , the Pakdel-McKinley criterion reproduces fairly well the experimental results for all polymer solutions in the range  $\epsilon \gtrsim 0.06$ . For  $\epsilon < 0.06$ , deviations from the prediction are found. By allowing for an arbitrary locus  $R_1 \leq r = R_1 + r'\epsilon \leq R_2$  for which the instability criterion is formulated, i.e. an arbitrary value  $0 \leq r' \leq 1$ , one can enhance the agreement with the experiments for two solutions (cf. dash-dotted lines,  $r' \approx 0.5$ ) showing a less important dependence on the gap width. However, as these corrected curves are within the error bars of the data points, we don't put a value on it.

Concerning the dependency on  $\beta$ , the experimental data are only roughly compatible with the prediction associated with the Pakdel-McKinley criterion. Figure 8.4 shows the fit parameter  $f(\beta)$  as a function of the zero-shear ratio  $\beta = \eta_s/\eta_0$  according to the parameters from the hybrid model ( $\Delta$ ). The data can be approximated by a function  $f(\beta) = A\sqrt{B-\beta}$  with parameters  $A = 1.2 \pm 0.1$  and  $B = 0.89 \pm 0.03$  which differs from the prediction  $f(\beta) \propto \sqrt{1-\beta}$ . A better agreement can be accomplished by accounting for the explicit rheology of the solutions by means of the shear thinning viscosity ratio  $\beta^+ = \eta_s/\eta^+ = \eta_s/\eta(\dot{\gamma})$ . For a given solution, it only slightly changes within the respective range of critical shear rates and it can be reasonably assumed to be a constant. Accordingly, applying the function  $f(\beta^+) = A^+ \sqrt{B^+ - \beta^+}$  to the

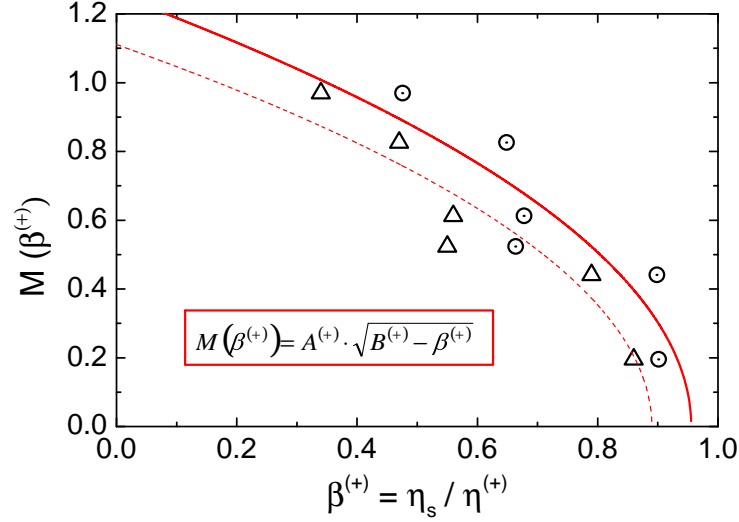


**Figure 8.4:** Experimental evaluation of the rheometric scaling of elastic instability. When accounting for the shear thinning properties of the solutions (respective quantities are denoted with a plus sign), the experimental data can reproduce the prediction according to the Pakdel-McKinley criterion from the Oldroyd-B model.

experimental data  $M(\beta^+)$  ( $\odot$ ) gives the parameters  $A^+ = 1.3 \pm 0.2$  and  $B^+ = 0.96 \pm 0.05$ . With that, in view of the Pakdel-McKinley criterion (8.4), the critical number  $M$  which characterizes the onset of elastic instability in the viscoelastic Taylor-Couette flow, takes the value

$$M = 1.8 \pm 0.3 . \quad (8.10)$$

In terms of the overall rheological scaling, this is in agreement with experiments of Groisman and Steinberg [Gro98b] who measured the onset of disordered oscillations (DO) at a fixed value of  $\varepsilon = 0.255$  for different polymer solution (and thus different values of  $\beta$ ) at different temperatures. However, they extracted a higher value of  $M = 3.58$ .

At this point, we have to recall that the criterion (8.4) is deduced based on the simple relations of the Oldroyd-B model, namely a first normal stress quadratically scaling with the shear rate and a constant shear viscosity which leads to the formulation of the Weissenberg number as the product of the (Oldroyd-B) relaxation time and shear rate. In view of this, it is not surprising that our criterion cannot fully reproduce the experimental rheometry, even though better agreement can be accomplished by accounting for the shear thinning viscosity ( $\beta \rightarrow \beta^+$ ) and global rheometric scaling is reproduced. The remaining discrepancies are contrasted by the striking agreement in terms of the geometric scaling which is provided by accounting for the proper value of the shear rate in a finite gap situation. Again, the respective formulation of the shear rate is based on the velocity profile of simple laminar Couette flow of an Oldroyd-B fluid, and this can only be an approximation to the real situation of a fluid described by the hybrid model.

Anyway, a more detailed analysis of our hybrid model seems to be reasonable, aiming to gain a deeper understanding of its features in comparison with the Oldroyd-B model. In the following, we will pursue this goal by means of a profound linear stability analysis of the Oldroyd-B and our hybrid model.



## Linear stability analysis

The stability criterion by Pakdel and McKinley (2.74) is motivated by considering the linearized disturbance equations [McK96] which govern the evolution of arbitrary infinitesimal disturbances imposed on the base flow of the investigated system at hand. Thus, it is reasonable to expect consistency between the predictions of the instability criterion and the results of a linear stability analysis.

In the following, we first present the mathematical toolkit for the analysis of linear stability in the Taylor-Couette geometry. This includes solving the Taylor-Couette base problem in three dimensions, the derivation of the (linearized) perturbation functions and solving the associated generalized eigenvalue problem. Here, we base our analysis on the most general viscoelastic, non-isothermal hybrid model which can be easily reduced to the isothermal case and, in particular, the isothermal Oldroyd-B fluid. The results of our stability analysis will be contrasted with approaches found in the literature and we will compare it to our experimental results as well as to the Pakdel-McKinley predictions.

### 9.1 Solving the Taylor-Couette base problem for the non-isothermal hybrid model

We recall the dimensionless constitutive equations (2.64)–(2.68) of the non-isothermal hybrid model. Analogous to the ansatz for the base flow of the isothermal circular Couette flow of an Oldroyd-B fluid (4.1), we ask for the steady state, time independent, purely azimuthal, axisymmetric solution

$$\left(\mathbf{v}(\mathbf{r}), p(\mathbf{r}), \underline{\boldsymbol{\tau}}(\mathbf{r})\right)_{\text{base}}^{\text{hybrid}} = \left(V_{\theta}(r)\mathbf{e}_{\theta}(\mathbf{r}), P(r), \Theta(r), \underline{T}^s(r), \underline{T}^U(r), \underline{T}^P(r)\right). \quad (9.1)$$

The constitutive equations translate to the following set of differential equations for the (non-zero) base functions:

$$\frac{\beta^P}{r} \left(T_{\theta\theta}^P(r) + T_{\theta\theta}^U(r)\right) = -\frac{\partial P(r)}{\partial r} + Re \frac{V_{\theta}(r)^2}{r}, \quad (9.2)$$

$$\begin{aligned} \beta^P \left(\frac{\partial}{\partial r} + \frac{2}{r}\right) \left(T_{r\theta}^P(r) + T_{r\theta}^U(r)\right) &= \beta e^{\nu\left(\frac{1}{\Theta(r)}-1\right)} \frac{\nu}{\Theta(r)^2} \frac{\partial \Theta(r)}{\partial r} \left(\frac{\partial}{\partial r} - \frac{1}{r}\right) V_{\theta}(r), \\ &- \beta e^{\nu\left(\frac{1}{\Theta(r)}-1\right)} \left(\frac{\partial^2}{\partial r^2} + \frac{1}{r} \frac{\partial}{\partial r} - \frac{1}{r^2}\right) V_{\theta}(r), \end{aligned} \quad (9.3)$$

$$T_{r\theta}^s(r) = \frac{\beta}{\beta^P} \left(\frac{\partial}{\partial r} - \frac{1}{r}\right) V_{\theta}(r) \quad (9.4)$$

$$T_{r\theta}^P(r) + 2\alpha \left( \frac{Wi}{\Theta(r)} \right)^2 T_{r\theta}^P(r)^3 = e^{\nu \left( \frac{1}{\Theta(r)} - 1 \right)} \left( \frac{\partial}{\partial r} - \frac{1}{r} \right) V_\theta(r), \quad (9.5)$$

$$T_{\theta\theta}^P(r) = 2 \frac{Wi}{\Theta(r)} T_{r\theta}^P(r)^2, \quad (9.6)$$

$$T_{r\theta}^U(r) = \beta_r e^{\nu \left( \frac{1}{\Theta(r)} - 1 \right)} \left( \frac{\partial}{\partial r} - \frac{1}{r} \right) V_\theta(r), \quad (9.7)$$

$$T_{\theta\theta}^U(r) = 2 \frac{\lambda_r Wi}{\beta_r \Theta(r)} T_{r\theta}^U(r)^2, \quad (9.8)$$

$$\begin{aligned} \frac{\partial^2 \Theta(r)}{\partial r^2} + \frac{1}{r} \frac{\partial \Theta(r)}{\partial r} + \beta^P Na \left( \frac{\partial}{\partial r} - \frac{1}{r} \right) V_\theta(r) \left( T_{r\theta}^P(r) + T_{r\theta}^U(r) \right) \\ = -\beta Na e^{\nu \left( \frac{1}{\Theta(r)} - 1 \right)} \left[ \left( \frac{\partial}{\partial r} - \frac{1}{r} \right) V_\theta(r) \right]^2. \end{aligned} \quad (9.9)$$

It is supplemented by the boundary conditions for the dimensionless velocity  $V_\theta(r)$  and temperature  $\Theta(r)$  via

$$\left( \frac{\partial V_\theta}{\partial r} - \frac{V_\theta}{r} \right) \Big|_{r=\frac{1}{\varepsilon}} = -1, \quad V_\theta \left( r = 1 + \frac{1}{\varepsilon} \right) = 0, \quad (9.10)$$

$$\Theta \left( r = \frac{1}{\varepsilon} \right) = Z, \quad \Theta \left( r = 1 + \frac{1}{\varepsilon} \right) = 1 \quad (9.11)$$

which fixes the temperature at the inner cylinder to  $\vartheta(r = R_2) \equiv Z\vartheta_0$  which may differ from the one at the outer beaker  $\vartheta(r = R_1) \equiv \vartheta_0$  given by the preset temperature of the outer thermal bath.

We already used the dimensional form of the stress equations (9.4)–(9.8) in the isothermal formulation to describe the steady shear rheometry of our polymer solutions. Here, we approximated the flow in the cone-and-plate geometry by the more simple plane Couette flow which naturally gives the base flow (in Cartesian coordinates) analogous to the Taylor-Couette flow. We further derived the explicit analytical expressions for the shear and the normal stress as a function of the shear rate  $\dot{\gamma} = \partial_r V_\theta(r) - V_\theta(r)/r$ . However, within the scope of the stability analysis, we require the explicit formulation of all the system's variables in dependence on the radial position  $r$  which are coupled according to the nonlinear differential equations of the base state (9.2)–(9.9). Therefore, there is no explicit analytic formulation of the base flow and we have to use a numerical method to approximate the base flow at a given set of discrete positions  $\{r_k\}$  in the gap which constitute the discrete working grid for the further analysis.

Based on a pseudospectral Chebyshev collocation method which is presented in detail in appendix B.1, the set of discrete Gauss-Lobatto points

$$x_k^{GL} = \cos \left( \frac{k\pi}{N} \right), \quad k = 0, 1, \dots, N \quad (9.12)$$

is an optimal grid to provide a fast converging approximation of the problem at hand. The points can be directly mapped to the dimensionless radial coordinate in the gap according to

$$r_k = \frac{1}{\varepsilon} + \frac{x_k^{GL} + 1}{2} \in \left[ \frac{1}{\varepsilon}; 1 + \frac{1}{\varepsilon} \right] \quad (9.13)$$

with the relative gap width  $\varepsilon = d/R_1$ . This method involves a discretization of the spacial derivate according to

$$\frac{\partial f(r)}{\partial r} \Big|_{r=r_k} \longrightarrow \sum_j D_{kj}^{(1)} f(x_j) \quad (9.14)$$

with the collocation derivative matrix  $D_{kj}^{(1)}$  and a function  $f$  representative for any variable of the system. Accordingly, the set of differential equations transforms to a set of algebraic equations for the base functions approximated at discrete collocation points which converge to the exact base solution with increasing number of collocation points  $N$ . Finally, the set of algebraic equations is solved by use of a well-established iterative Newton-Raphson method [Deu11].

## 9.2 Perturbation functions

In the special case of an idealized, infinitely long Taylor-Couette cell, any arbitrary perturbation superposed to the base flow can be represented in terms of a spectrum of Fourier modes involving an azimuthal and an axial wave number  $m$  and  $k_z$ , respectively. The circularity of the system imposes a periodic boundary condition to the flow and forces  $m$  to be an integer value, whereas  $k_z$  can be arbitrarily chosen. As motivated before, we address the question of exponential stability, i.e. we assume an exponential time evolution of the perturbation modes. All this leads to the formulation of the discrete perturbation modes in the form

$$\delta \mathbf{v}(t, r, \theta, z) = \mathbf{u}(r) e^{i(k_z z + m\theta) + \mu t}, \quad (9.15)$$

$$\delta \mathcal{T}(t, r, \theta, z) = \underline{\sigma}(r) e^{i(k_z z + m\theta) + \mu t}, \quad (9.16)$$

$$\delta p(t, r, \theta, z) = q(r) e^{i(k_z z + m\theta) + \mu t}, \quad (9.17)$$

$$\delta \Theta(t, r, \theta, z) = \Psi(r) e^{i(k_z z + m\theta) + \mu t} \quad (9.18)$$

which we impose to the respective components of the base flow. Addressing linear stability, we assume the perturbation functions  $\mathbf{u}(r)$ ,  $\underline{\sigma}(r)$ ,  $q(r)$  and  $\Psi(r)$  to be small in magnitude and when applying the perturbed base flow functions to the constitutive equations we only account for linear contributions of the perturbation functions and neglect terms of order greater than one. This gives the following linearized equations for the set of perturbation functions (the indication of their dependency on the radial coordinate  $r$  has been omitted):

1.  $r$ -component of the Navier-Stokes equation

$$\begin{aligned} & \left( \beta e^{\nu(\frac{1}{\Theta} - 1)} \left\{ \frac{\partial^2}{\partial r^2} + \frac{1}{r} \frac{\partial}{\partial r} - \frac{1 + m^2}{r^2} - k_z^2 - 2 \frac{\nu}{\Theta^2} \frac{\partial \Theta}{\partial r} \frac{\partial}{\partial r} \right\} - Re \frac{im}{r} V_\theta \right) u_r \\ & \quad + \left( 2 Re \frac{V_\theta}{r} - 2 \beta e^{\nu(\frac{1}{\Theta} - 1)} \frac{im}{r^2} \right) u_\theta - \frac{\partial q}{\partial r} \\ & \quad + \beta^P \left( \frac{1}{r} + \frac{\partial}{\partial r} \right) \sigma_{rr}^{P+U} + \beta^P \frac{im}{r} \sigma_{r\theta}^{P+U} + \beta^P i k_z \sigma_{rz}^{P+U} - \beta^P \frac{1}{r} \sigma_{\theta\theta}^{P+U} \\ & \quad - \beta e^{\nu(\frac{1}{\Theta} - 1)} \frac{\nu}{\Theta^2} \frac{im}{r} \left( \frac{\partial}{\partial r} - \frac{1}{r} \right) V_\theta \Psi \\ & \quad = \mu Re u_r \end{aligned} \quad (9.19)$$

2.  $\theta$ -component of the Navier-Stokes equation

$$\begin{aligned}
& \left( \beta e^{\nu(\frac{1}{\Theta}-1)} \left\{ \frac{\partial^2}{\partial r^2} + \frac{1}{r} \frac{\partial}{\partial r} - \frac{1+m^2}{r^2} - k_z^2 - \frac{\nu}{\Theta^2} \frac{\partial \Theta}{\partial r} \left[ \frac{\partial}{\partial r} - \frac{1}{r} \right] \right\} - Re \frac{im}{r} V_\theta \right) u_\theta \\
& + \left( 2\beta e^{\nu(\frac{1}{\Theta}-1)} \frac{im}{r^2} - Re \left\{ \frac{\partial V_\theta}{\partial r} + \frac{V_\theta}{r} \right\} - \beta e^{\nu(\frac{1}{\Theta}-1)} \frac{\nu}{\Theta^2} \frac{\partial \Theta}{\partial r} \frac{im}{r} \right) u_r - \frac{im}{r} q \\
& + \beta^P \left( \frac{2}{r} + \frac{\partial}{\partial r} \right) \sigma_{r\theta}^{P+U} + \beta^P \frac{im}{r} \sigma_{\theta\theta}^{P+U} + \beta^P ik_z \sigma_{\theta z}^{P+U} \\
& + \left( -\beta e^{\nu(\frac{1}{\Theta}-1)} \frac{\nu}{\Theta^2} \left\{ \frac{\partial^2 V_\theta}{\partial r^2} + \frac{1}{r} \frac{\partial V_\theta}{\partial r} - \frac{V_\theta}{r^2} \right\} \right. \\
& \left. + \beta e^{\nu(\frac{1}{\Theta}-1)} \frac{\nu}{\Theta^2} \left\{ \frac{\partial V_\theta}{\partial r} - \frac{V_\theta}{r} \right\} \left\{ \frac{\nu+2\Theta}{\Theta^2} \frac{\partial \Theta}{\partial r} - \frac{\partial}{\partial r} \right\} \right) \Psi \\
& = \mu Re u_\theta
\end{aligned} \tag{9.20}$$

3.  $z$ -component of the Navier-Stokes equation

$$\begin{aligned}
& \left( \beta e^{\nu(\frac{1}{\Theta}-1)} \left\{ \frac{\partial^2}{\partial r^2} + \frac{1}{r} \frac{\partial}{\partial r} - \frac{m^2}{r^2} - k_z^2 - \frac{\nu}{\Theta^2} \frac{\partial \Theta}{\partial r} \frac{\partial}{\partial r} \right\} - Re \frac{im}{r} V_\theta \right) u_z \\
& - \beta e^{\nu(\frac{1}{\Theta}-1)} \frac{\nu}{\Theta^2} \frac{\partial \Theta}{\partial r} ik_z u_r - ik_z q \\
& + \beta^P \left( \frac{1}{r} + \frac{\partial}{\partial r} \right) \sigma_{rz}^{P+U} + \beta^P \frac{im}{r} \sigma_{\theta z}^{P+U} + \beta^P ik_z \sigma_{zz}^{P+U} \\
& = \mu Re u_z
\end{aligned} \tag{9.21}$$

4. incompressibility condition

$$\left( \frac{\partial}{\partial r} + \frac{1}{r} \right) u_r + \frac{im}{r} u_\theta + ik_z u_z = 0 \tag{9.22}$$

5.  $(rr)$ -component of PTT equation

$$\begin{aligned}
& 2e^{\nu(\frac{1}{\Theta}-1)} \left( \frac{\partial}{\partial r} + \frac{Wi}{\Theta} \frac{im}{r} T_{r\theta}^P \right) u_r - \left( 1 + \frac{Wi}{\Theta} \left\{ e^{\nu(\frac{1}{\Theta}-1)} \frac{im}{r} V_\theta + \alpha T_{\theta\theta}^P \right\} \right) \sigma_{rr}^P \\
& = \mu e^{\nu(\frac{1}{\Theta}-1)} \frac{Wi}{\Theta} \sigma_{rr}^P
\end{aligned} \tag{9.23}$$

6.  $(r\theta)$ -component of PTT equation

$$\begin{aligned}
& e^{\nu(\frac{1}{\Theta}-1)} \left( \frac{im}{r} + \frac{Wi}{\Theta} \left\{ \frac{im}{r} T_{\theta\theta}^P - \frac{\partial T_{r\theta}^P}{\partial r} + \frac{1}{\Theta} \frac{\partial \Theta}{\partial r} T_{r\theta}^P \right\} \right) u_r + e^{\nu(\frac{1}{\Theta}-1)} \left( \frac{\partial}{\partial r} - \frac{1}{r} \right) u_\theta \\
& - ik_z e^{\nu(\frac{1}{\Theta}-1)} \frac{Wi}{\Theta} T_{r\theta}^P u_z + \frac{Wi}{\Theta} \left( e^{\nu(\frac{1}{\Theta}-1)} \left\{ \frac{\partial}{\partial r} - \frac{1}{r} \right\} V_\theta - \alpha T_{r\theta}^P \right) \sigma_{rr}^P \\
& - \left( 1 + \frac{Wi}{\Theta} \left\{ e^{\nu(\frac{1}{\Theta}-1)} \frac{im}{r} V_\theta + \alpha T_{\theta\theta}^P \right\} \right) \sigma_{r\theta}^P - \alpha \frac{Wi}{\Theta} T_{r\theta}^P \sigma_{\theta\theta}^P - \alpha \frac{Wi}{\Theta} T_{r\theta}^P \sigma_{zz}^P \\
& + \left( \alpha \frac{Wi}{\Theta^2} T_{r\theta}^P T_{\theta\theta}^P + e^{\nu(\frac{1}{\Theta}-1)} \frac{Wi}{\Theta^2} \frac{im}{r} V_\theta T_{r\theta}^P - e^{\nu(\frac{1}{\Theta}-1)} \frac{\nu}{\Theta^2} \left\{ \frac{\partial}{\partial r} - \frac{1}{r} \right\} V_\theta \right) \Psi \\
& = \mu \left( e^{\nu(\frac{1}{\Theta}-1)} \frac{Wi}{\Theta} \sigma_{r\theta}^P - e^{\nu(\frac{1}{\Theta}-1)} \frac{Wi}{\Theta^2} T_{r\theta}^P \Psi \right)
\end{aligned} \tag{9.24}$$

7. (rz)-component of PTT equation

$$\begin{aligned}
& e^{\nu(\frac{1}{\Theta}-1)} ik_z u_r + e^{\nu(\frac{1}{\Theta}-1)} \left( \frac{\partial}{\partial r} + \frac{Wi}{\Theta} \frac{im}{r} T_{r\theta}^P \right) u_z \\
& - \left( 1 + \frac{Wi}{\Theta} \left\{ e^{\nu(\frac{1}{\Theta}-1)} \frac{im}{r} V_\theta + \alpha T_{\theta\theta}^P \right\} \right) \sigma_{rz}^P \\
& = \mu e^{\nu(\frac{1}{\Theta}-1)} \frac{Wi}{\Theta} \sigma_{r\theta}^P
\end{aligned} \tag{9.25}$$

8. ( $\theta\theta$ )-component of PTT equation

$$\begin{aligned}
& e^{\nu(\frac{1}{\Theta}-1)} \left( \frac{2}{r} + \frac{Wi}{\Theta} \left\{ -\frac{\partial T_{\theta\theta}^P}{\partial r} + \frac{2T_{\theta\theta}^P}{r} + \frac{1}{\Theta} \frac{\partial \Theta}{\partial r} T_{\theta\theta}^P \right\} \right) u_r \\
& + 2e^{\nu(\frac{1}{\Theta}-1)} \left( \frac{im}{r} + \frac{Wi}{\Theta} \left\{ \frac{im}{r} T_{\theta\theta}^P - T_{r\theta}^P \left[ \frac{1}{r} - \frac{\partial}{\partial r} \right] \right\} \right) u_\theta \\
& - \alpha \frac{Wi}{\Theta} T_{\theta\theta}^P \sigma_{rr}^P + 2e^{\nu(\frac{1}{\Theta}-1)} \frac{Wi}{\Theta} \left( \frac{\partial V_\theta}{\partial r} - \frac{V_\theta}{r} \right) \sigma_{r\theta}^P \\
& - \left( 1 + \frac{Wi}{\Theta} \left\{ e^{\nu(\frac{1}{\Theta}-1)} \frac{im}{r} V_\theta + 2\alpha T_{\theta\theta}^P \right\} \right) \sigma_{\theta\theta}^P - \alpha \frac{Wi}{\Theta} T_{\theta\theta}^P \sigma_{zz}^P \\
& + \left( \alpha \frac{Wi}{\Theta^2} (T_{\theta\theta}^P)^2 - 2e^{\nu(\frac{1}{\Theta}-1)} T_{r\theta}^P \frac{Wi}{\Theta} \left\{ \frac{1}{\Theta} + \frac{\nu}{\Theta^2} \right\} \left\{ \frac{\partial}{\partial r} - \frac{1}{r} \right\} V_\theta \right. \\
& \quad \left. + e^{\nu(\frac{1}{\Theta}-1)} \frac{Wi}{\Theta^2} \frac{im}{r} V_\theta T_{\theta\theta}^P \right) \Psi \\
& = \mu \left( e^{\nu(\frac{1}{\Theta}-1)} \frac{Wi}{\Theta} \sigma_{\theta\theta}^P - e^{\nu(\frac{1}{\Theta}-1)} \frac{Wi}{\Theta^2} T_{\theta\theta}^P \Psi \right)
\end{aligned} \tag{9.26}$$

9. ( $\theta z$ )-component of PTT equation

$$\begin{aligned}
& e^{\nu(\frac{1}{\Theta}-1)} ik_z u_\theta + e^{\nu(\frac{1}{\Theta}-1)} \left( \frac{im}{r} + \frac{Wi}{\Theta} \left\{ \frac{im}{r} T_{\theta\theta}^P + T_{r\theta}^P \frac{\partial}{\partial r} \right\} \right) u_z \\
& + e^{\nu(\frac{1}{\Theta}-1)} \frac{Wi}{\Theta} \left( \frac{\partial}{\partial r} - \frac{1}{r} \right) V_\theta \sigma_{rz}^P - \left( 1 + \frac{Wi}{\Theta} \left\{ e^{\nu(\frac{1}{\Theta}-1)} \frac{im}{r} V_\theta + \alpha T_{\theta\theta}^P \right\} \right) \sigma_{\theta z}^P \\
& = \mu e^{\nu(\frac{1}{\Theta}-1)} \frac{Wi}{\Theta} \sigma_{\theta z}^P
\end{aligned} \tag{9.27}$$

10. (zz)-component of PTT equation

$$\begin{aligned}
& 2e^{\nu(\frac{1}{\Theta}-1)} ik_z u_z - \left( 1 + \frac{Wi}{\Theta} \left\{ e^{\nu(\frac{1}{\Theta}-1)} \frac{im}{r} V_\theta + \alpha T_{\theta\theta}^P \right\} \right) \sigma_{zz}^P \\
& = \mu e^{\nu(\frac{1}{\Theta}-1)} \frac{Wi}{\Theta} \sigma_{zz}^P
\end{aligned} \tag{9.28}$$

11. (rr)-component of UCM equation

$$\begin{aligned}
& 2e^{\nu(\frac{1}{\Theta}-1)} \left( \beta_r \frac{\partial}{\partial r} + \frac{\lambda_r Wi}{\Theta} \frac{im}{r} T_{r\theta}^U \right) u_r - \left( 1 + e^{\nu(\frac{1}{\Theta}-1)} \frac{\lambda_r Wi}{\Theta} \frac{im}{r} V_\theta \right) \sigma_{rr}^U \\
& = \mu e^{\nu(\frac{1}{\Theta}-1)} \frac{\lambda_r Wi}{\Theta} \sigma_{rr}^U
\end{aligned} \tag{9.29}$$

12.  $(r\theta)$ -component of UCM equation

$$\begin{aligned}
& e^{\nu(\frac{1}{\Theta}-1)} \left( \frac{im}{r} \left\{ \beta_r + \frac{\lambda_r Wi}{\Theta} T_{\theta\theta}^U \right\} + \frac{\lambda_r Wi}{\Theta} \left\{ -\frac{\partial T_{r\theta}^U}{\partial r} + \frac{1}{\Theta} \frac{\partial \Theta}{\partial r} T_{r\theta}^U \right\} \right) u_r \\
& \quad + e^{\nu(\frac{1}{\Theta}-1)} \beta_r \left( \frac{\partial}{\partial r} - \frac{1}{r} \right) u_\theta - ik_z e^{\nu(\frac{1}{\Theta}-1)} \frac{\lambda_r Wi}{\Theta} T_{r\theta}^U u_z \\
& + e^{\nu(\frac{1}{\Theta}-1)} \frac{\lambda_r Wi}{\Theta} \left( \frac{\partial}{\partial r} - \frac{1}{r} \right) V_\theta \sigma_{rr}^U - \left( 1 + e^{\nu(\frac{1}{\Theta}-1)} \frac{\lambda_r Wi}{\Theta} \frac{im V_\theta}{r} \right) \sigma_{r\theta}^U \quad (9.30) \\
& + \left( e^{\nu(\frac{1}{\Theta}-1)} \frac{\lambda_r Wi}{\Theta^2} \frac{im V_\theta}{r} T_{r\theta}^U - \beta_r e^{\nu(\frac{1}{\Theta}-1)} \frac{\nu}{\Theta^2} \left\{ \frac{\partial}{\partial r} - \frac{1}{r} \right\} V_\theta \right) \Psi \\
& = \mu \left( e^{\nu(\frac{1}{\Theta}-1)} \frac{\lambda_r Wi}{\Theta} \sigma_{r\theta}^U - e^{\nu(\frac{1}{\Theta}-1)} \frac{\lambda_r Wi}{\Theta^2} T_{r\theta}^U \Psi \right)
\end{aligned}$$

13.  $(rz)$ -component of UCM equation

$$\begin{aligned}
& e^{\nu(\frac{1}{\Theta}-1)} \beta_r ik_z u_r + e^{\nu(\frac{1}{\Theta}-1)} \left( \beta_r \frac{\partial}{\partial r} + \frac{\lambda_r Wi}{\Theta} \frac{im}{r} T_{r\theta}^U \right) u_z \\
& \quad - \left( 1 + e^{\nu(\frac{1}{\Theta}-1)} \frac{\lambda_r Wi}{\Theta} \frac{im}{r} V_\theta \right) \sigma_{rz}^U \quad (9.31) \\
& = \mu e^{\nu(\frac{1}{\Theta}-1)} \frac{\lambda_r Wi}{\Theta} \sigma_{r\theta}^U
\end{aligned}$$

14.  $(\theta\theta)$ -component of UCM equation

$$\begin{aligned}
& e^{\nu(\frac{1}{\Theta}-1)} \left( \beta_r \frac{2}{r} + \frac{\lambda_r Wi}{\Theta} \left\{ -\frac{\partial T_{\theta\theta}^U}{\partial r} + \frac{2T_{\theta\theta}^U}{r} + \frac{1}{\Theta} \frac{\partial \Theta}{\partial r} T_{\theta\theta}^U \right\} \right) u_r \\
& \quad + 2e^{\nu(\frac{1}{\Theta}-1)} \left( \beta_r \frac{im}{r} + \frac{\lambda_r Wi}{\Theta} \left\{ \frac{im}{r} T_{\theta\theta}^U - T_{r\theta}^U \left[ \frac{1}{r} - \frac{\partial}{\partial r} \right] \right\} \right) u_\theta \\
& + 2e^{\nu(\frac{1}{\Theta}-1)} \frac{\lambda_r Wi}{\Theta} \left( \frac{\partial}{\partial r} - \frac{1}{r} \right) V_\theta \sigma_{r\theta}^U - \left( 1 + e^{\nu(\frac{1}{\Theta}-1)} \frac{\lambda_r Wi}{\Theta} \frac{im}{r} V_\theta \right) \sigma_{\theta\theta}^U \\
& + \left( e^{\nu(\frac{1}{\Theta}-1)} \frac{\lambda_r Wi}{\Theta^2} \frac{im}{r} V_\theta T_{\theta\theta}^U - 2e^{\nu(\frac{1}{\Theta}-1)} \frac{\lambda_r Wi}{\Theta} \left\{ \frac{1}{\Theta} + \frac{\nu}{\Theta^2} \right\} \left\{ \frac{\partial}{\partial r} - \frac{1}{r} \right\} V_\theta T_{r\theta}^U \right) \Psi \\
& = \mu \left( e^{\nu(\frac{1}{\Theta}-1)} \frac{\lambda_r Wi}{\Theta} \sigma_{\theta\theta}^U - e^{\nu(\frac{1}{\Theta}-1)} \frac{\lambda_r Wi}{\Theta^2} T_{\theta\theta}^U \Psi \right) \quad (9.32)
\end{aligned}$$

15.  $(\theta z)$ -component of UCM equation

$$\begin{aligned}
& e^{\nu(\frac{1}{\Theta}-1)} ik_z \beta_r u_\theta + e^{\nu(\frac{1}{\Theta}-1)} \left( \beta_r \frac{im}{r} + \frac{\lambda_r Wi}{\Theta} \left\{ \frac{im}{r} T_{\theta\theta}^U + T_{r\theta}^U \frac{\partial}{\partial r} \right\} \right) u_z \\
& + e^{\nu(\frac{1}{\Theta}-1)} \frac{\lambda_r Wi}{\Theta} \left( \frac{\partial}{\partial r} - \frac{1}{r} \right) V_\theta \sigma_{rz}^U - \left( 1 + e^{\nu(\frac{1}{\Theta}-1)} \frac{\lambda_r Wi}{\Theta} \frac{im}{r} V_\theta \right) \sigma_{\theta z}^U \quad (9.33) \\
& = \mu e^{\nu(\frac{1}{\Theta}-1)} \frac{\lambda_r Wi}{\Theta} \sigma_{\theta z}^U
\end{aligned}$$

16.  $(zz)$ -component of UCM equation

$$2e^{\nu(\frac{1}{\Theta}-1)} ik_z \beta_r u_z - \left( 1 + e^{\nu(\frac{1}{\Theta}-1)} \frac{\lambda_r Wi}{\Theta} \frac{im}{r} V_\theta \right) \sigma_{zz}^U = \mu e^{\nu(\frac{1}{\Theta}-1)} \frac{\lambda_r Wi}{\Theta} \sigma_{zz}^U \quad (9.34)$$

17. energy equation

$$\begin{aligned}
& \left( -Pe \frac{\partial \Theta}{\partial r} + 2e^{\nu(\frac{1}{\Theta}-1)} \beta Na \frac{im}{r} \left\{ \frac{\partial}{\partial r} - \frac{1}{r} \right\} V_\theta \right. \\
& \quad \left. + \beta^P Na \left\{ \frac{im}{r} T_{r\theta}^{P+U} + \frac{1}{r} T_{\theta\theta}^{P+U} \right\} \right) u_r \\
& + \left[ 2e^{\nu(\frac{1}{\Theta}-1)} \beta Na \left( \frac{\partial}{\partial r} - \frac{1}{r} \right) V_\theta \left( \frac{\partial}{\partial r} - \frac{1}{r} \right) \right. \\
& \quad \left. + \beta^P Na \left( T_{r\theta}^{P+U} \left\{ \frac{\partial}{\partial r} - \frac{1}{r} \right\} + \frac{im}{r} T_{\theta\theta}^{P+U} \right) \right] u_\theta \quad (9.35) \\
& \quad + \beta^P Na \left( \frac{\partial}{\partial r} - \frac{1}{r} \right) V_\theta \sigma_{r\theta}^{P+U} \\
& + \left[ \frac{\partial^2}{\partial r^2} + \frac{1}{r} \frac{\partial}{\partial r} - \frac{1}{r^2} - Pe \frac{im}{r} V_\theta - \beta Na \frac{\nu}{\Theta^2} e^{\nu(\frac{1}{\Theta}-1)} \left( \left\{ \frac{\partial}{\partial r} - \frac{1}{r} \right\} V_\theta \right)^2 \right] \Psi \\
& \quad = \mu Pe \Psi
\end{aligned}$$

Here, we used the abbreviations  $\sigma_{ij}^{P+U} := \sigma_{ij}^P + \sigma_{ij}^U$ ,  $T_{ij}^{P+U} := T_{ij}^P + T_{ij}^U$  and  $\lambda_r = \lambda^U/\lambda^P$ ,  $\beta_r = \beta^U/\beta^P$ . We further assume that the perturbation functions are zero at the boundaries of the system, i.e.

$$\mathbf{w}(r) := \left( \mathbf{u}(r), q(r), \sigma_{ij}^{P,U}(r), \Psi(r) \right) = 0 \quad \text{at} \quad r = \frac{1}{\varepsilon}, 1 + \frac{1}{\varepsilon}. \quad (9.36)$$

Now, we have to ask for the solution of the boundary problem (9.19)–(9.36) which provides the desired information about the temporal development of a small perturbation superposed to the base flow.

### 9.3 Generalized eigenvalue problem & instability criterion

Analogous to the base flow, the set of perturbation equations (9.19)–(9.35) cannot be solved analytically and we have to numerically approximate the problem by means of the pseudospectral Chebyshev collocation method on the discrete grid of Gauss-Lobatto points. Consequently, we can write it in the form

$$\mathbf{A}\mathbf{w} = \mu \mathbf{B}\mathbf{w} \quad (9.37)$$

which constitutes an algebraic generalized eigenvalue problem of the matrices  $\mathbf{A}$ ,  $\mathbf{B}$  with associated eigenvalues  $\mu$  and eigenvectors  $\mathbf{w} = (\mathbf{u}(r_0), \mathbf{u}(r_1), \dots, \mathbf{u}(r_N), q(r_0), q(r_1), \dots, \Psi(r_N))$ . The matrices  $\mathbf{A}$  and  $\mathbf{B}$ , and hence also the eigenvectors  $\mathbf{w}_i$  and the eigenvalues  $\mu_i$ , depend on the global system parameters  $\{\varepsilon, \beta, \beta^P, Z\}$  which reflect a special choice of the Taylor-Couette geometry and viscoelastic fluid, the solution of the base problem at the collocation points  $\{V_\theta(r), P(r), \Theta(r), T_{ij}^{P,U}(r)\}_{r=r_k}$ , the parameters of the perturbation mode  $\{m, k_z\}$ , as well as the hydro- and thermodynamic control parameters  $Re, Wi$  and  $Pe, Na$ , respectively.

Addressing the question of stability of the base flow we have to focus on the eigenvalues  $\mu_i$  which are complex numbers in general (cf. figure 9.1 for an illustration of a representative spectrum of eigenvalues in the complex plane). The algebraic sign of the real part of an eigenvalue  $\mu_i$  governs the evolution of the associated vector of perturbation functions  $\mathbf{w}_i$ : for  $\Re(\mu_i) < 0$ , the perturbation exponentially decays with time and the base flow is linearly stable, whereas the perturbation exponentially grows for  $\Re(\mu_i) > 0$  which corresponds to a linearly unstable base flow. Neutral stability is given at  $\Re(\mu_i) = 0$ . The imaginary part of

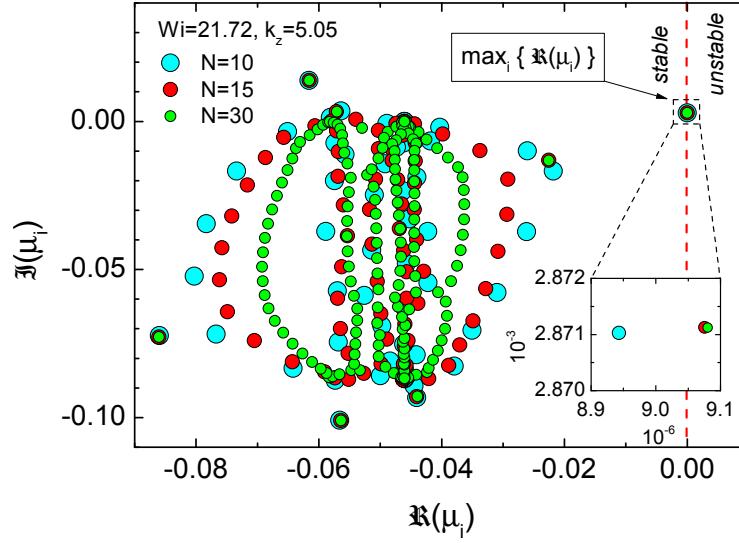


**Figure 9.1:** Convergence behavior of the spectrum of eigenvalues. The eigenvalue of the most unstable perturbation mode (i.e. the one with the biggest real part) quickly converges when increasing the number of collocation points  $N$  (see inset).

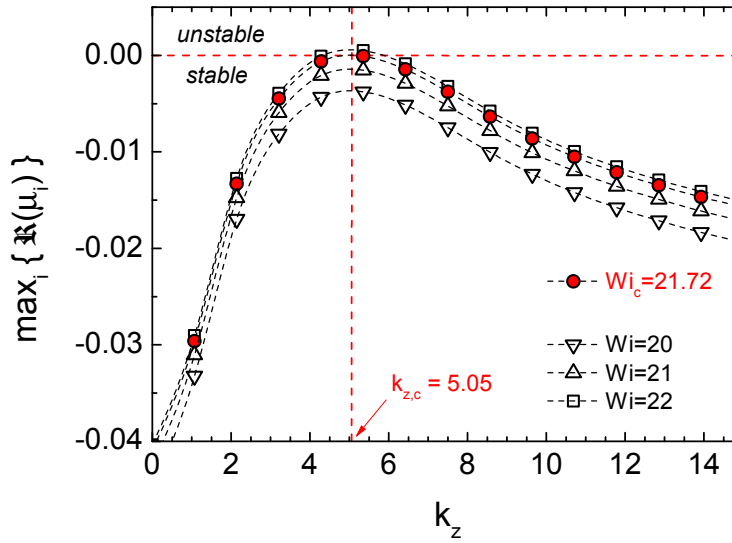


**Figure 9.2:** Representative spectrum of maximum eigenvalues  $\max_i\{\mu_i\}(k_z)$  for non-axisymmetric perturbations ( $m = 1$ ) of an Oldroyd-B fluid ( $\beta = 0.79, \beta^U = 0.21, \beta^P = 0, \alpha = 0$ ) in the isothermal, purely elastic case ( $Re = Pe = Na = 0, Z = 1$ ). It is the perturbation mode  $k_z = 5.05$ , that first becomes linearly unstable at a critical Weissenberg number  $Wi = Wi_c = 21.72$ . The number of collocation points is  $N = 30$ .

an eigenvalue addresses the question whether the respective perturbation mode is stationary ( $\Im(\mu_i) = 0$ ) or oscillatory ( $\Im(\mu_i) \neq 0$ ). In general, for a given set of parameters the real parts of the eigenvalues are not positive or negative altogether. Here we have to focus on the largest of them which gives the most unstable perturbation mode.

Accordingly, in order to find the onset of elastic instability in terms of the critical Weissenberg number  $Wi_c$ , we have to proceed according to the following protocol: for a given choice of system parameters  $\{\epsilon, \beta, \beta^P, Z\}$ , Reynolds number  $Re$ , Péclet number  $Pe$ , Nahme number

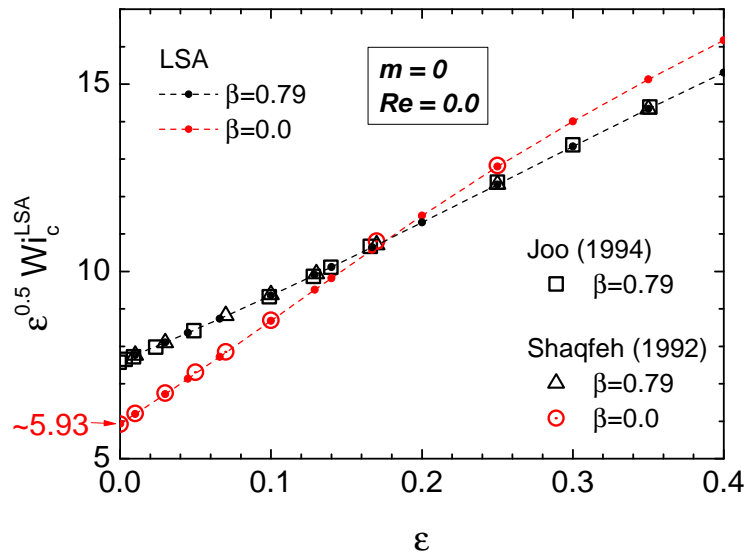


**Figure 9.3:** Results of the linear stability analysis of the isothermal ( $Pe = Na = 0, Z = 1$ ), purely elastic ( $Re = 0$ ) Taylor-Couette flow of a Maxwell ( $\beta = 0$ ) and Oldroyd-B fluid ( $\beta = 0.79$ ) with respect to small axisymmetric ( $m = 0$ ) perturbations.

$Na$  and perturbation mode  $m$ , we increase the Weissenberg number  $Wi$  starting with a value at which the base flow is linearly stable for all wave numbers  $k_z \geq 0$ , i.e.  $\mu_i(k_z) < 0 \forall \{i, k_z\}$ , until the largest eigenvalue (in terms of its real part)  $\mu^{\max}(k_z) := \max_{1 \leq i \leq n} \{\Re(\mu_i(k_z))\}$  changes to a positive value at a critical wave number  $k_{z,c}$  and Weissenberg number  $Wi_c$ . A representative spectrum  $\mu^{\max}(k_z)$  is shown in figure 9.2 for the first non-axisymmetric perturbation mode ( $m = 1$ ) of an Oldroyd-B fluid ( $\beta = 0.79, \beta^U = 0.21, \beta^P = 0, \alpha = 0$ ) in the purely elastic, isothermal case ( $Re = Pe = Na = 0, Z = 1$ ). In this case, it is the perturbation mode  $k_z = 5.05$  that first becomes linearly unstable at a critical Weissenberg number  $Wi_c = 21.72$ . The number of collocation points is preset to  $N = 30$  which is large enough to provide convergence of the maximum eigenvalue (cf. figure 9.1). The number of collocation points has to be adapted to the each explicit set of parameters, i.e.  $N$  has to be varied to check for numerical convergence of the largest eigenvalue.

The generalized eigenvalue problem was solved by use of standard numerical routines from an open source library (SciPy) for python™.

## 9.4 LSA of the Maxwell and Oldroyd-B fluid - Consistency check

In a first step, we check for errors of our code. Therefore, we recalculate the critical Weissenberg numbers  $Wi_c(\epsilon)$  for the isothermal, purely elastic ( $Re = Pe = Na = 0, Z = 1$ ) Taylor-Couette flow of a simple UCM fluid ( $\alpha = \beta = \beta^U = 0, \beta^P = 1$ )<sup>1</sup> and an Oldroyd-B fluid with  $\beta = 0.79$  ( $\beta^P = 0.21, \alpha = \lambda^U = 0$ ) by accounting for axisymmetric ( $m = 0$ ) as well as for the first non-axisymmetric ( $m = 1$ ) perturbation modes. For  $m = 0$ , our results are consistent with the data by Shaqfeh *et al.* [Sha92] ( $\odot$ ) and Joo *et al.* [Joo94] ( $\square$ ) (cf. figure 9.3). The result by Larson *et al.* [Lar90] in the small gap approximation (4.18) is reproduced

<sup>1</sup>Since we normalized the stresses with  $\eta^P \dot{\gamma}_{\max}$ , in order to obtain the UCM fluid we cannot set  $\beta^P = 0$  but we have to reduce the PTT-component by  $\alpha = 0$  and remove the virtual UCM component

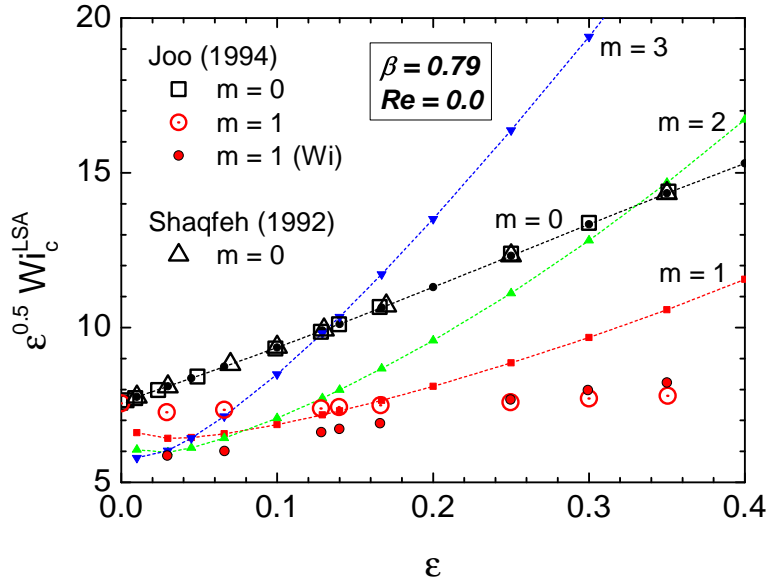


**Figure 9.4:** Critical modified Weissenberg number as a function of the relative gap width. The referenced data are extracted from the linear stability analysis (published in [Sha92, Joo94]) of an Oldroyd-B fluid ( $\beta = 0.79$ ) for both, axisymmetric ( $m = 0$ ) as well as first non-axisymmetric perturbation mode ( $m = 1$ ). The data are overlapped by the results of our analysis for  $m = 0, 1, 2, 3$  (dashed lines).

as well, i.e.  $\sqrt{\epsilon} Wi_c^{LSA} \xrightarrow{\epsilon \rightarrow 0} \sim 5.93$ . In contrast, our  $m = 1$  data significantly differ from the preliminary results (cf. figure 9.4). However, this is not due to an error in the code but we have to assume that the data by Joo *et al.* is incorrect as it is not possible to convert their data of the critical Weissenberg number ( $\bullet$ ) into their modified Weissenberg numbers ( $\odot$ ).

Figure 9.4 shows another result: the  $m = 1$  mode is the most unstable one only for a limited range of gap widths  $\epsilon \gtrsim 0.07$ . For  $\epsilon \lesssim 0.07$ , higher modes are more unstable and the value  $m$  of the first unstable mode steadily increases when decreasing  $\epsilon$  more and more. Table 9.1 summarizes all the critical Weissenberg numbers calculated for different values of  $\beta$ ,  $\epsilon$  and  $m$ . In the following, when talking about the critical onset of elastic instability, we will refer to the most unstable mode, i.e.  $Wi_c(\epsilon) = \min_{m \geq 0} \{Wi_c(\epsilon; m)\}$ . The respective values are highlighted in boldface in table 9.1 and presented in figure 9.5. Clearly, for all values of  $\beta$ , the critical modified Weissenberg numbers of the first unstable perturbation modes, rescaled by  $\sqrt{1 - \beta}$  as motivated by the Pakdel-McKinley criterion, obey a heuristic quadratic dependence on the gap widths within  $0 < \epsilon \lesssim 0.3$ , i.e.

$$\sqrt{1 - \beta} \sqrt{\epsilon} Wi_c^{LSA} = a(\beta) \left( 1 + b(\beta)\epsilon + c(\beta)\epsilon^2 \right) \quad (9.38)$$

with functions  $a(\beta), b(\beta), c(\beta) > 0$  presented alongside with figure 9.5. This is contrasted with a Fourier expansion of the modified Weissenberg number according to the Pakdel-McKinley criterion (8.4) which predicts in second order

$$\sqrt{1 - \beta} \sqrt{\epsilon} Wi_c = \frac{M}{\sqrt{2}} \left( 1 + \frac{3}{4}\epsilon - \frac{5}{32}\epsilon^2 \right) + \mathcal{O}(\epsilon^3). \quad (9.39)$$

It is obvious that the Pakdel-McKinley criterion (expanded in second order in  $\epsilon$ , cf. (9.39)) and the linear stability analysis (9.38) provide significantly different results. According to the former of the two, the rescaled, critical modified Weissenberg number  $\sqrt{1 - \beta} \sqrt{\epsilon} Wi_c^{LSA}$  is independent of  $\beta$  and in the limit of small gap it equals a constant  $M/\sqrt{2}$ . Our experiments

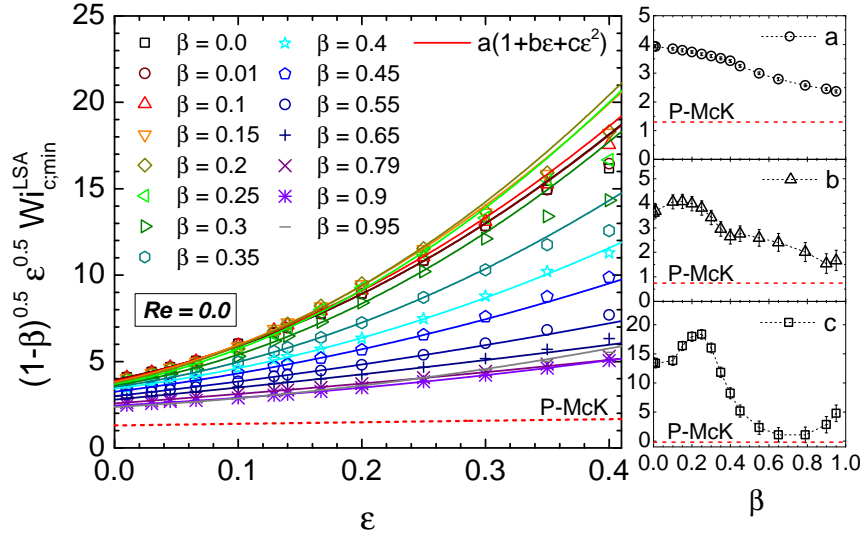


**Figure 9.5:** Minimal modified Weissenberg number based on the Oldroyd-B model as a function of the relative gap width for different values of relative viscosity  $\beta = \eta_s/\eta_0$ . The data are rescaled by a pre-factor  $\sqrt{1-\beta}$  according to the Pakdel-McKinley criterion. For values  $\epsilon \leq 0.35$ , the data can be fairly fit by heuristic quadratic functions (lines, cf. equation (9.38)). The right panel shows the respective fit parameters  $a$ ,  $b$  and  $c$ , each compared with the prediction of the Pakdel-McKinley criterion (9.39).

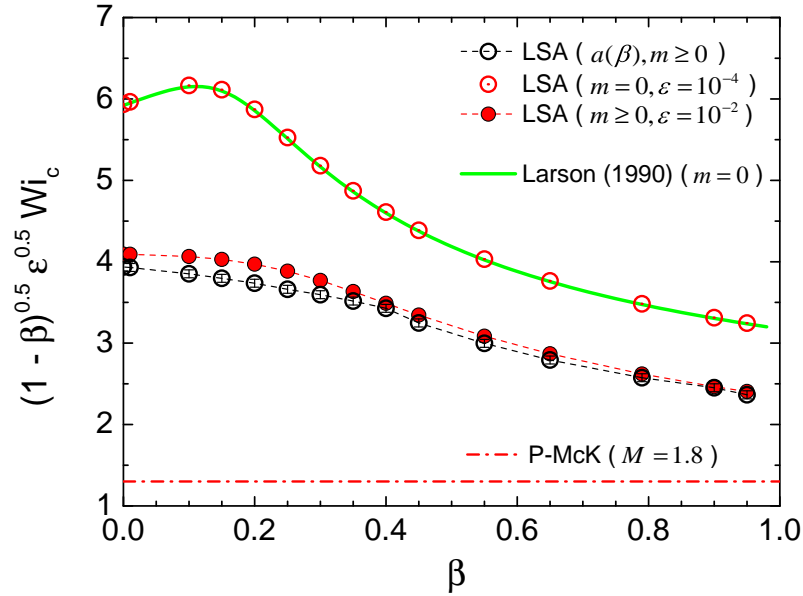


**Figure 9.6:** Comparison of the different approaches for the rheological scaling of the onset of elastic instability in the small gap limit.

provide a value of  $M = 1.8 \pm 0.3$ , cf. (8.10). In the linear stability analysis of the most unstable modes, this number is dependent on  $\beta$  and the associated function  $a(\beta)$  in (9.38) is monotonically decreasing (cf. the open black circles in the upper right panel in the figures 9.5 and 9.6). Consistently, as the analysis takes into account all perturbation modes  $m \geq 0$  including the most unstable one, the curve  $a(\beta)$  is below the curve associated with the axisymmetric mode  $m = 0$  according to equation (4.19). Our analysis for  $\epsilon = 10^{-4}$ , i.e. a

close approximation of  $\epsilon \rightarrow 0$ , can reproduce this function fairly well. In total, the Pakdel-McKinley criterion, in agreement with our experimental data, predicts a much less pronounced dependency on the gap width compared to the linear stability analysis. Accordingly, the coefficients of the correction terms  $\mathcal{O}(\epsilon)$  and  $\mathcal{O}(\epsilon^2)$  are much smaller than the stability analysis predicts for any  $\beta$ , cf. the panels in figure [9.6](#).

$\epsilon$	$m$	$\beta =$	0.00	0.01	0.10	0.15	0.20	0.25	0.30	0.35	0.40	0.45	0.55	0.65	0.79	0.90	0.95
0.4	0	$W_{i_c} =$	<b>25.57</b>	<b>26.15</b>	33.09	36.09	34.39	<b>30.44</b>	<b>27.07</b>	<b>24.67</b>	<b>23.02</b>	21.93	20.91	21.17	24.20	32.53	44.65
	1		27.17	27.30	<b>29.25</b>	<b>31.24</b>	33.80	33.59	30.64	27.08	23.92	<b>21.04</b>	<b>18.14</b>	<b>16.91</b>	<b>18.27</b>	<b>25.29</b>	<b>39.13</b>
	2		30.85	30.87	31.40	31.88	<b>32.37</b>	32.56	31.73	29.89	27.81	25.96	23.47	22.77	26.43	42.92	77.69
0.35	0	$W_{i_c} =$	25.57	26.15	33.09	36.09	34.39	30.44	<b>27.07</b>	<b>24.67</b>	23.02	21.93	20.91	21.18	24.23	32.60	44.78
	1		<b>25.26</b>	<b>25.39</b>	<b>27.20</b>	<b>29.05</b>	31.42	31.24	28.49	25.18	<b>22.26</b>	<b>19.96</b>	<b>17.19</b>	<b>16.32</b>	<b>17.88</b>	<b>24.71</b>	<b>37.87</b>
	2		28.67	28.70	29.19	29.64	<b>30.10</b>	<b>30.28</b>	29.50	27.79	25.86	24.14	21.83	21.24	24.81	40.18	72.35
0.3	0	$W_{i_c} =$	25.57	26.15	33.09	36.09	34.39	30.44	27.07	24.67	23.03	21.93	20.94	21.23	24.35	32.81	45.09
	1		<b>23.43</b>	<b>23.54</b>	<b>25.22</b>	<b>26.94</b>	29.14	28.96	<b>26.42</b>	<b>23.35</b>	<b>20.69</b>	<b>18.68</b>	<b>16.47</b>	<b>15.94</b>	<b>17.67</b>	<b>24.34</b>	<b>36.87</b>
	2		26.60	26.62	27.07	27.49	<b>27.91</b>	<b>28.08</b>	27.36	25.77	23.98	22.39	20.29	19.87	23.39	37.65	67.28
0.25	0	$W_{i_c} =$	25.59	26.16	33.09	36.09	34.39	30.44	27.07	24.68	23.05	21.98	21.04	21.41	24.64	33.28	45.78
	1		<b>21.66</b>	<b>21.77</b>	<b>23.32</b>	<b>24.91</b>	26.95	26.77	<b>24.41</b>	<b>21.61</b>	<b>19.30</b>	<b>17.67</b>	<b>16.04</b>	<b>15.80</b>	<b>17.71</b>	<b>24.27</b>	<b>36.23</b>
	2		24.60	24.61	25.03	25.41	<b>25.81</b>	<b>25.96</b>	25.29	23.83	22.17	20.72	18.90	18.73	22.22	35.42	62.53
0.2	0	$W_{i_c} =$	25.68	26.24	33.09	36.09	34.39	30.44	27.09	24.75	23.18	22.17	21.36	21.84	25.28	34.26	47.18
	1		<b>19.96</b>	<b>20.06</b>	<b>21.51</b>	<b>22.92</b>	24.79	24.63	<b>22.48</b>	<b>20.09</b>	<b>18.30</b>	<b>17.12</b>	<b>16.02</b>	<b>16.03</b>	<b>18.12</b>	<b>24.65</b>	<b>36.18</b>
	2		22.67	22.68	23.07	23.42	<b>23.78</b>	<b>23.92</b>	23.30	21.95	20.46	19.19	17.83	17.95	21.43	33.61	58.25
0.167	0	$W_{i_c} =$	25.88	26.42	33.10	36.09	34.39	30.46	27.18	24.92	23.44	22.51	21.82	22.41	26.05	35.39	48.78
	1		<b>18.97</b>	<b>19.09</b>	<b>20.50</b>	<b>21.68</b>	23.30	23.20	<b>21.33</b>	<b>19.41</b>	<b>18.03</b>	<b>16.32</b>	<b>16.49</b>	<b>18.72</b>	<b>25.33</b>	<b>36.67</b>	
	2		21.44	21.45	21.82	22.15	<b>22.48</b>	<b>22.60</b>	22.01	20.77	19.45	18.41	17.43	17.75	21.22	32.79	55.85
0.14	0	$W_{i_c} =$	26.24	26.76	33.16	36.10	34.41	30.55	27.40	25.27	23.88	23.03	22.46	23.17	27.04	36.81	50.78
	1		<b>18.54</b>	<b>18.67</b>	<b>20.04</b>	<b>20.99</b>	22.09	22.11	<b>20.68</b>	<b>19.23</b>	<b>18.17</b>	<b>17.47</b>	<b>16.86</b>	<b>17.16</b>	<b>19.54</b>	<b>26.28</b>	<b>37.58</b>
	2		20.45	20.47	20.83	21.14	<b>21.44</b>	<b>21.51</b>	20.98	19.91	18.85	18.06	17.40	17.87	21.34	32.46	54.28
0.129	0	$W_{i_c} =$	26.47	26.98	33.23	36.11	34.44	30.64	27.57	25.49	24.16	23.34	22.83	23.59	27.58	37.58	51.87
	1		<b>18.52</b>	<b>18.65</b>	<b>20.00</b>	<b>20.87</b>	21.77	21.78	<b>20.57</b>	<b>19.30</b>	<b>18.35</b>	<b>17.72</b>	<b>17.19</b>	<b>17.54</b>	<b>19.99</b>	<b>26.83</b>	<b>38.15</b>
	2		20.06	20.07	20.44	20.75	<b>21.03</b>	<b>21.08</b>	20.59	19.64	18.71	18.03	17.49	18.02	21.50	32.45	53.79
0.1	0	$W_{i_c} =$	27.45	27.94	33.66	36.29	34.69	31.18	28.39	26.52	25.32	24.60	24.25	25.19	29.59	40.42	55.83
	1		<b>19.04</b>	19.18	<b>20.48</b>	21.21	21.76	21.70	20.93	20.04	19.33	18.84	18.50	18.99	<b>21.71</b>	<b>28.93</b>	<b>40.49</b>
	2		19.11	19.17	<b>19.74</b>	<b>20.07</b>	<b>20.32</b>	<b>20.36</b>	<b>20.04</b>	<b>19.45</b>	<b>18.86</b>	<b>18.42</b>	<b>18.16</b>	<b>18.83</b>	22.38	33.01	53.18
0.066	0	$W_{i_c} =$	30.04	30.50	35.48	37.53	36.16	33.25	30.90	29.27	28.23	27.64	27.53	28.78	34.00	46.58	64.41
	1		21.32	21.47	22.82	23.49	23.90	23.81	23.27	22.62	22.08	21.71	21.57	22.29	25.55	<b>33.76</b>	<b>46.25</b>
	2		<b>19.63</b>	<b>19.72</b>	<b>20.56</b>	<b>20.97</b>	<b>21.28</b>	<b>21.39</b>	<b>21.25</b>	<b>20.94</b>	<b>20.61</b>	<b>20.37</b>	<b>20.38</b>	<b>21.23</b>	<b>25.03</b>	35.67	54.86
0.045	0	$W_{i_c} =$	33.61	34.07	38.68	40.30	39.14	36.68	34.58	33.08	32.12	31.60	31.68	33.25	39.42	54.11	74.87
	1		24.73	24.90	26.43	27.14	27.52	27.41	26.91	26.31	25.81	25.49	25.49	26.44	30.38	<b>39.93</b>	<b>53.92</b>
	2		<b>22.05</b>	<b>22.17</b>	<b>23.16</b>	<b>23.65</b>	<b>24.01</b>	<b>24.17</b>	<b>24.10</b>	<b>23.87</b>	<b>23.63</b>	<b>23.46</b>	<b>23.61</b>	<b>24.63</b>	<b>28.84</b>	40.03	59.23
0.03	0	$W_{i_c} =$	38.79	39.28	43.82	45.23	44.22	42.01	40.01	38.55	37.61	37.13	37.39	39.36	46.78	64.30	89.01
	1		29.72	29.93	31.75	32.56	32.96	32.80	32.25	31.61	31.11	30.80	30.92	32.17	37.07	48.58	<b>64.92</b>
	2		26.19	26.33	27.54	28.13	28.57	28.76	28.70	28.47	28.25	28.11	28.36	29.61	<b>34.46</b>	<b>46.82</b>	66.92
0.01	0	$W_{i_c} =$	61.89	62.55	68.39	69.97	69.00	66.60	64.25	62.45	61.32	60.81	61.62	65.11	77.64	106.92	148.10
	1		52.09	52.49	55.88	57.22	57.64	57.09	56.04	55.00	54.23	53.84	54.35	56.88	66.07	86.91	115.00
	2		46.40	46.68	49.11	50.20	50.89	51.02	50.70	50.19	49.75	49.53	50.07	52.31	60.52	79.75	<b>107.61</b>
0.01	3	$W_{i_c} =$	43.15	43.38	45.36	46.32	47.03	47.40	47.41	47.21	47.00	46.92	47.57	49.80	57.94	<b>77.95</b>	109.35
	4		41.46	41.66	43.44	44.33	45.03	45.48	45.64	45.60	45.51	45.53	46.31	48.64	<b>57.19</b>	79.22	
	5		<b>40.94</b>	<b>41.13</b>	<b>42.84</b>	<b>43.69</b>	<b>44.38</b>	<b>44.84</b>	<b>45.06</b>	<b>45.08</b>	<b>45.05</b>	<b>45.11</b>	<b>45.99</b>	<b>48.49</b>	57.78	82.75	
0.01	6	$W_{i_c} =$	41.52	41.71	43.40	44.22	44.88	45.32	45.51	45.51	45.47	45.53	46.12	49.19	59.45	88.29	

**Table 9.1:** Results of linear stability analysis of purely elastic ( $Re = 0$ ) Taylor-Couette base flow of an Oldroyd-B fluid. The table lists the critical Weissenberg numbers for the onset of elastic instability triggered by different perturbation modes  $m$  in dependence of different gap widths  $\epsilon$  and viscosity ratios  $\beta = \eta_s/\eta$ . In each case  $(\epsilon, \beta)$ , the smallest critical Weissenberg number (giving the most unstable perturbation mode) is highlighted in boldface.

## 9.5 LSA of the isothermal hybrid model

Since the rheology of our solutions is not consistently described by a simple Oldroyd-B model, a stability analysis based on the more appropriate hybrid model is compulsory in order to make it comparable with our experimental results. In doing so, we have to take care of a consistent calculation of the critical Weissenberg numbers. As already discussed in section 5.1, the rheological (modified) Weissenberg number is an appropriate choice. However, taking the hybrid model seriously, the experimental (critical) rheological Weissenberg numbers as calculated according to (5.2) from the shear rates given by the rheometer are inaccurate: The rheometer gives the shear rates based on equation (5.2), i.e. under the assumption of a Newtonian circular Couette velocity profile (4.8). While this is also correct for an Oldroyd-B fluid, it is incorrect for the hybrid model fluid: since the velocity profile differs from the Newtonian profile (this is not explicitly presented here, but it can be anticipated by the more complex structure of the differential equations constituting the base flow), the shear rate (at the inner cylinder) deviates from equation (5.2). For a given angular velocity  $\Omega$  of the inner cylinder, the respective dimensional azimuthal velocity (tildes denote dimensionless quantities and a “h” denotes a quantity based on the hybrid model) is given by

$$V_\theta(r = R_1) = \Omega R_1 = \tilde{V}_\theta^h \left( \tilde{r} = \frac{1}{\varepsilon} \right) \dot{\gamma}^h d \quad (9.40)$$

with the dimensionless velocity at the inner cylinder  $\tilde{V}_\theta^h(\varepsilon^{-1})$  which meets

$$\left. \frac{\partial \tilde{V}_\theta^h}{\partial \tilde{r}} - \frac{\tilde{V}_\theta^h}{\tilde{r}} \right|_{\tilde{r}=\frac{1}{\varepsilon}} = -1 \quad (9.41)$$

and the actual (maximum) shear rate at the inner cylinder

$$\dot{\gamma}^h = \left. \frac{\partial V_\theta}{\partial r} - \frac{V_\theta}{r} \right|_{r=R_1} \quad (9.42)$$

(the shear rate is still maximum at the inner cylinder). Thus, we can transform (9.40) to

$$\tilde{V}_\theta^h \left( \frac{1}{\varepsilon} \right) \dot{\gamma}^h = \frac{\Omega}{\varepsilon} = \frac{\varepsilon + 2}{2(\varepsilon + 1)^2} \dot{\gamma}^{\text{O-B}} \quad (9.43)$$

which gives a conversion of a shear rate  $\dot{\gamma}^h$  based on the hybrid model (at the corresponding rotation rate  $\Omega$ ) to the associated shear rate  $\dot{\gamma}^{\text{O-B}}$  in an Oldroyd-B fluid (at the same rotation rate, cf. (8.3)). Consequently, if we want to compare our experimental Oldroyd-B-like shear rates with the actual shear rates of a fluid described by the hybrid model, we have to correct the latter by

$$\dot{\gamma}^{\text{O-B}} = \frac{2(\varepsilon + 1)^2}{\varepsilon + 2} \tilde{V}_\theta^h \left( \frac{1}{\varepsilon} \right) \dot{\gamma}^h. \quad (9.44)$$

According to the power law relation (5.2) between the shear rate and the Weissenberg number, the correction for the Weissenberg number takes the form

$$Wi^{\text{O-B}} = \left[ \frac{2(\varepsilon + 1)^2}{\varepsilon + 2} \tilde{V}_\theta^h \left( \frac{1}{\varepsilon} \right) \right]^{n^{\text{rheo}}} Wi^h \quad (9.45)$$

with the exponents  $n^{\text{rheo}}$  according to table 5.3.

A comparison between the linear stability analysis of the Oldroyd-B and the hybrid model is presented in figure 9.7. The critical modified rheological Weissenberg numbers  $\sqrt{\varepsilon} Wi_c^{\text{rheo}}$

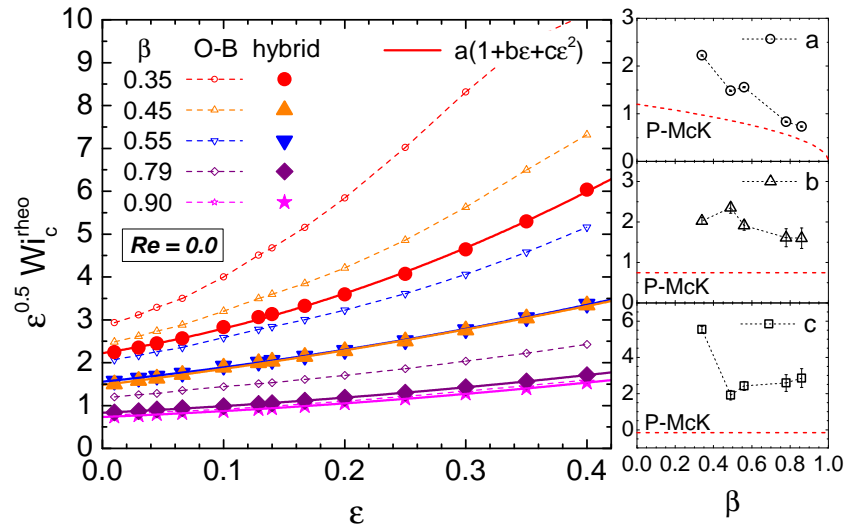


**Figure 9.7:** Linear stability analysis of the hybrid model as compared to the results from the analysis of the Oldroyd-B model with the same respective parameter  $\beta$ .

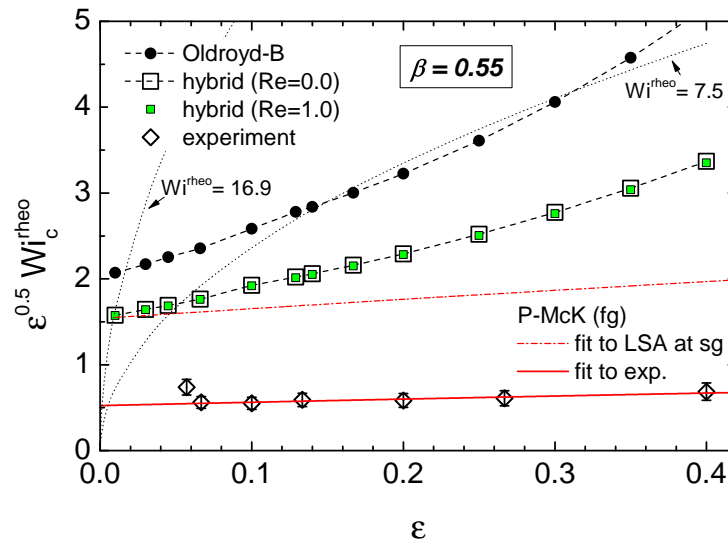


**Figure 9.8:** Comparison of the different models giving the onset of elastic instability for a polymer solution with  $\beta = 0.55$  which corresponds to the P600<sub>G80</sub> solution according to its rheology based on the hybrid model. A significant discrepancy is obvious between the linear stability analysis and the experimental data whose scaling is reproduced fairly well by the finite gap Pakdel-McKinley criterion. We refer to the dotted lines in section 9.7.

of the most unstable mode in dependence on the gap width  $\epsilon$  are shown for several values of  $\beta = \eta_s/\eta_0$  which are close to the estimates of the parameters from the steady shear rheometry of our polymer solutions according to the evaluation based on the hybrid model (see table 5.3).

Strikingly, the hybrid model predicts a notable lower onset as compared to the Oldroyd-B model. Again, the stability data of the hybrid model can be approximated by quadratic polynomials  $a(\beta)(1 + b(\beta)\epsilon + c(\beta)\epsilon^2)$  and the associated coefficients are shown in the panels in figure 9.7. Compared to figure 9.5, we can assess a better agreement with the coefficients associated with the Pakdel-McKinley criterion. Here, one has to pay attention to the fact

that we have evaluated the *rheological* modified Weissenberg number instead of the rescaled Weissenberg number from the Oldroyd-B model. For the latter, the rheological Weissenberg number takes the form

$$Wi^{\text{rheo, O-B}} = \frac{\Sigma\tau_{11}}{2\Sigma\tau_{12}} = \frac{2\eta^U\lambda^U\dot{\gamma}^2}{2(\eta_s + \eta^U)\dot{\gamma}} = \frac{\eta^U}{\eta_s + \eta^U}\lambda^U\dot{\gamma} = (1 - \beta)Wi^{\text{O-B}}. \quad (9.46)$$

However, a significant discrepancy to the experimental data is left as representatively illustrated in figure 9.8 for  $\beta = 0.55$  which we relate to the P600<sub>G80</sub> solution and the linear stability analysis of the hybrid model still overestimates the critical Weissenberg numbers. Even when accounting for inertia in terms of an upper estimate of the experimentally relevant Reynolds numbers  $Re = 1$  in the linear stability analysis of the hybrid model (green data points in figure 9.8), the base flow is only marginally destabilized. By far, this additional effect of inertia cannot reproduce the experimental findings, neither in the magnitude nor in the global scaling of the critical Weissenberg numbers as reflected by an adaption of the finite gap Pakdel-McKinley criterion to the experimental data, cf. solid red line. The dash-dotted line refers to the Pakdel-McKinley criterion with a forced matching to the data of the linear stability analysis for small gaps  $\varepsilon \rightarrow 0$ .

## 9.6 LSA of the non-isothermal hybrid model

With the intention to obtain a better agreement with our experimental data and hence with the prediction of the Pakdel-McKinley criterion, we additionally allowed for non-isothermal boundary conditions and the effect of viscous heating in the stability analysis. This involves values of the (normalized) temperature at the inner cylinder  $Z = \vartheta(R_1)/\vartheta_0$  different from unity and non-zero values of the Nahme and the Péclet number as well as of the activation energy  $\nu$ . As the inner cylinder of our Taylor-Couette setup is mounted to the driving motor which is at ambient temperature ( $\approx 23^\circ\text{C}$ ) and since the upper part of the cylinder is not immersed into the fluid (cf. figure 6.1), it is reasonable to assume that there is a temperature different to the one of the outer beaker (which is in contact with the surrounding thermal bath fixed at  $\vartheta = \vartheta_0$ ). Especially for the measurements at  $\vartheta_0 = 10^\circ\text{C}$ , we have to assume  $\vartheta(R_1) > \vartheta(R_2) = \vartheta_0$ . We verified this initial guess by measuring the steady state temperature difference between the thermal bath ( $\vartheta_0 = 10^\circ\text{C}$ ) and the temperature of the inner cylinder ( $\vartheta(R_1)$ , measured via a temperature sensor mounted in an bore hole close to the surface of the cylinder) which exhibited a difference (at thermal equilibrium) of approximately  $\Delta\vartheta = \vartheta(R_1) - \vartheta_0 \lesssim 0.2^\circ\text{C}$ .

According to the definitions of the Nahme and Péclet number (cf. the equations (2.72), (2.70)), we have to determine the thermal conductivity  $\kappa$  and the specific heat capacity  $c_p$  of our polymer solutions. Furthermore, an estimate of the activation energy  $\nu$  is required. Broniarz-Press and Pralat [Bro09] investigated the thermal conductivity of Newtonian and non-Newtonian liquids (amongst them they measured high molecular weight polyacrylamide solutions (Separan)) and found an empirical formula relating the apparent viscosity and the thermal conductivity according to

$$\frac{\eta}{\kappa} = 2.095 G^{0.95} \dot{\gamma}^{0.881n-1.021} \quad (9.47)$$

with the shear stress described by a power law  $\tau = \eta\dot{\gamma} = G\dot{\gamma}^n$ . Consequently, we can explicitly write

$$\kappa(\dot{\gamma}) = 0.477 \left( \frac{G}{\text{Pa s}^n} \right)^{0.05} \left( \frac{\dot{\gamma}}{\text{s}^{-1}} \right)^{0.119n+0.021} \frac{\text{W}}{\text{m K}}. \quad (9.48)$$

In the relevant range of critical shear rates  $\dot{\gamma} = \dot{\gamma}_c$ , the thermal conductivity does not change much for the polymer solutions and according to the different values of  $G$ ,  $\dot{\gamma}_c$  and

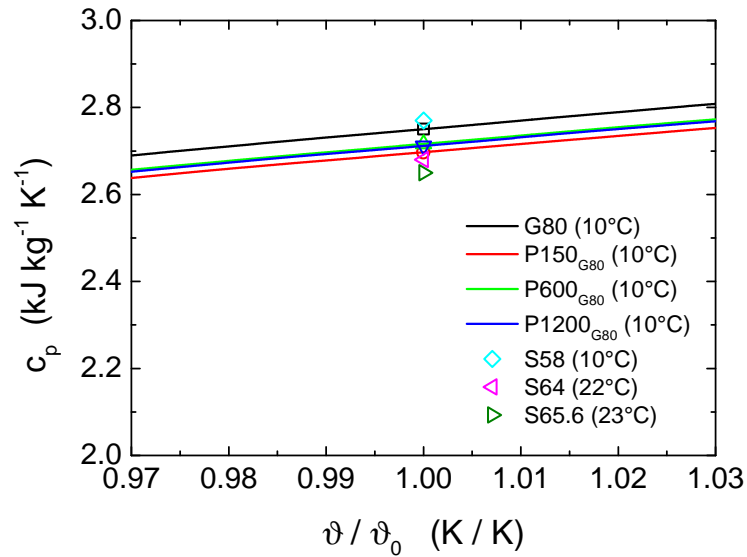


**Figure 9.9:** Specific heat capacities  $c_p$  of the polymer solutions. Whereas the glycerol-based solutions were measured in a differential scanning calorimeter (DSC Q2000, TA Instruments), the values for the sucrose solvents (sucrose concentration  $c_{\text{suc}}$ ) at the relevant temperatures  $\vartheta_0$  were calculated according to  $c_p = [1 - c_{\text{suc}}(0.6 - 0.0018\vartheta/^\circ\text{C})] \cdot 4.18 \text{ kJ kg}^{-1} \text{ K}^{-1}$  [Asa05].

$n$  for the various solutions, the thermal conductivity is in the range  $0.60 \text{ W m}^{-1} \text{ K}^{-1} \lesssim \kappa \lesssim 0.84 \text{ W m}^{-1} \text{ K}^{-1}$ . The specific heat capacity  $c_p$  also does not change much within a reasonable temperature range. It was measured for the glycerol-based solutions by means of a differential scanning calorimeter DSC Q2000 (TA Instruments) (cf. figure 9.9) and no systematic change in  $c_p$  could be observed upon variation of the polymer concentration. Additionally, it is reasonable to assume that there is no effect of the dissolved polymers in view of the particularly small concentrations. Besides, the heat capacities of the sucrose solvents were calculated following the approach by Asadi *et al.* [Asa05] via

$$c_p^{\text{sucrose}} = \left[ 1 - c_{\text{suc}} \left( 0.6 - 0.0018 \frac{\vartheta}{^\circ\text{C}} \right) \right] \cdot 4.18 \frac{\text{kJ}}{\text{kg K}} \quad (9.49)$$

$$\in (2.65, 2.77) \frac{\text{kJ}}{\text{kg K}} \quad (9.50)$$

and for the concentrations  $c_{\text{suc}}$  of our aqueous sucrose solutions the heat capacities are close to the ones of the glycerol solutions. The activation energies  $\nu$  of the polymer solutions were approximated by the temperature dependence of the viscosities of the respective solvents according to an Arrhenius law (2.63)

$$\frac{\eta(\vartheta)}{\eta(\vartheta_0)} \approx \frac{\eta_s(\vartheta)}{\eta_s(\vartheta_0)} = e^{\nu \left( \frac{\vartheta_0}{\vartheta} - 1 \right)}. \quad (9.51)$$

Here, we had to assume a negligible variation of the intrinsic viscosity and Huggins coefficient within the small temperature range. Figure 9.10 shows the viscosity functions  $\eta(\vartheta/\vartheta_0)$  of the aqueous glycerol and sucrose solvents. The sucrose data were taken from the literature [Asa05] and in the relevant temperature range, they can be interpolated satisfactorily by exponential functions (dashed lines). The viscosities of the glycerol solvents were calculated according to a pseudo-empirical formula by Cheng *et al.* [Che08]. By rescaling the data with the reference viscosity  $\eta(\vartheta_0)$  within the relevant range, the curves collapse fairly well to a master curve (cf. inset graph). This implies a small range of activation energies  $18.6 \lesssim \nu \lesssim 20.6$ .

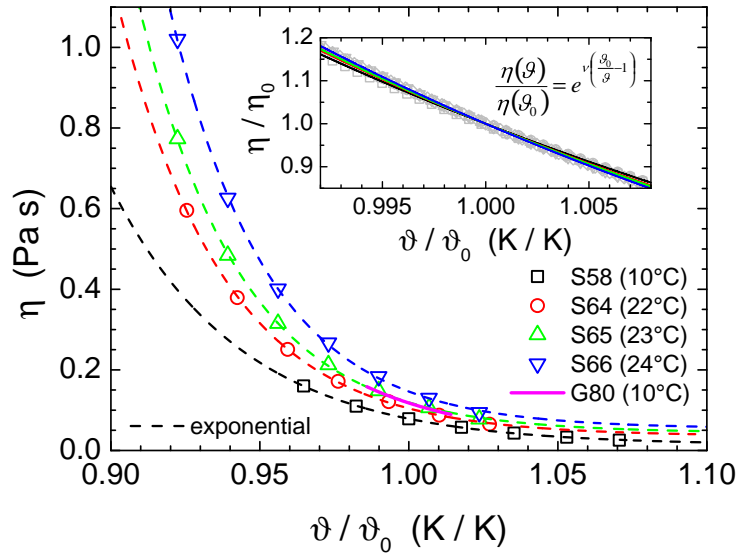


**Figure 9.10:** Estimation of the (rescaled) activation energies  $\nu = \Delta E/k_B\vartheta_0$  for the different polymer solutions based on an Arrhenius-type viscosity law. The viscosity data of aqueous sucrose solutions were taken from [Asa05] whereas the data of the 80% aqueous glycerol solution were calculated according to a pseudo-empirical formula by Cheng *et al.* [Che08].

Representatively, we analyzed the change in the critical (modified) Weissenberg number based on the hybrid model parameters of the P600<sub>G80</sub> solution. The thermal properties  $\nu \approx 20.27$ ,  $c_p \approx 2.7 \text{ kJ kg}^{-1} \text{ K}^{-1}$ ,  $\kappa_{\min} \approx 0.7 \text{ W m}^{-1} \text{ K}^{-1}$  and density  $\rho \approx 1214 \text{ kg m}^{-3}$  provide upper limit estimates of the Péclet and Nahme number,

$$Pe^{\max} \approx 400, \quad (9.52)$$

$$Na^{\max} \approx 1 \cdot 10^{-5}. \quad (9.53)$$

It turned out that with these values (due to a slightly different estimate, we have even chosen a slightly higher value of the activation energy  $\nu = 1.4 \cdot 10^{-5}$ ) in combination with a temperature difference of  $\Delta\vartheta = 2\text{K}$  (which is about ten times the experimental estimate), the critical onset of the linear elastic instability is only negligibly affected and the discrepancy to the experimental data remains significant. A more detailed analysis of the interplay between the thermodynamic parameters reveals a much stronger impact of the Péclet number compared to the Nahme number. When forcing the estimate of the critical modified (rheological) Weissenberg number from the linear stability analysis to agree with the experimental value at  $\varepsilon = 0.4$ , i.e.  $\sqrt{\varepsilon}Wi_c^{\text{theo}}(\varepsilon = 0.4, Pe, Na) = 0.65$ , the Péclet number has to be significantly increased above our estimate, depending on the choice of the Nahme number and the temperature difference  $\Delta\vartheta$ . This is illustrated in figure 9.11. Starting without a temperature difference, i.e.  $\Delta\vartheta = 0 \text{ K} (Z = 1)$ , the required Péclet number is in the order of  $10^5 \dots 10^{10}$ , depending on the Nahme number. At  $\Delta\vartheta = 2 \text{ K} (Z = 1.007)$ , the Péclet number has to be about  $Pe \approx 21550$  for values of  $Na$  in the range of  $10^{-6} \leq Na \leq 10^{-3}$ .  $Pe$  does not significantly change when increasing  $Na$  even further. Analogously, at  $\Delta\vartheta = 4 \text{ K} (Z = 1.014)$ , the Péclet number has to be  $Pe \approx 10150$  and does not change importantly over many orders of magnitude of  $Na$ . Even if the values of  $Pe = 10150$  and  $\Delta\vartheta = 4 \text{ K}$  are not reasonable assumptions for our experiments according to our estimates of the involved parameters, we investigated the corresponding non-isothermal effect on the geometric scaling of the elastic instability onset. Figure 9.12 illustrates the effect of the interplay between the temperature difference  $\Delta\vartheta$  and viscous heating associated with  $Na = 1.4 \cdot 10^{-5}$  and

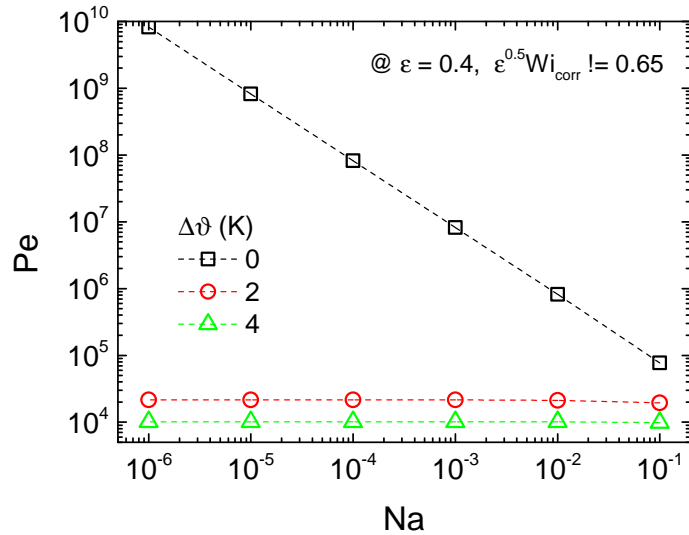


**Figure 9.11:** Interplay between the Nahme and Péclet number when forcing the critical modified Weissenberg number  $\sqrt{\varepsilon}Wi = 0.65$  for the P600<sub>G80</sub> solution at  $\varepsilon = 0.4$ ,  $\nu = 20.27$ .

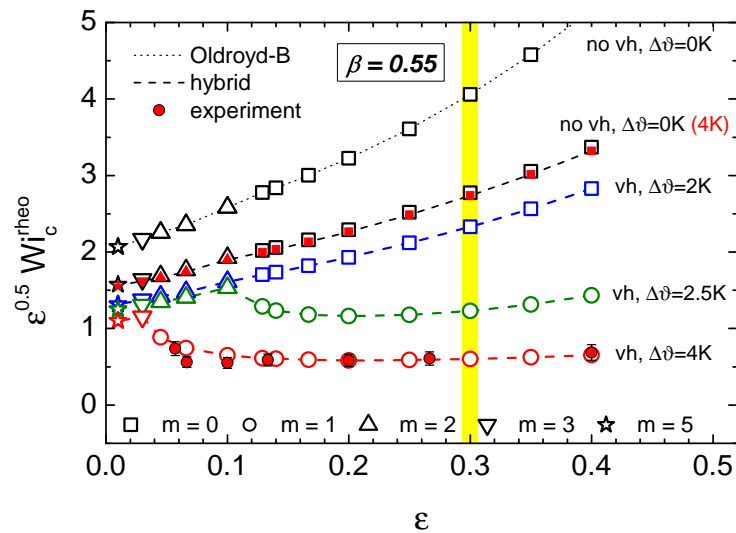


**Figure 9.12:** Effect of viscous heating in combination with a fixed temperature difference between the inner and outer wall  $\vartheta_1 - \vartheta_0 = \Delta\vartheta = (Z - 1)\vartheta_0$  based on the hybrid model. While the activation energy  $\nu$  as well as the Nahme number  $Na$  are assumed to be in reasonable agreement with the estimates, the Péclet number  $Pe$  is more than one magnitude higher than estimated. Representatively, the value  $\varepsilon = 0.3$  (yellow) is analyzed in more detail in figure 9.13.

$Pe = 10150$ . Remarkably, the geometric scaling dramatically changes and the experimental data, i.e. the scaling predicted by the Pakdel-McKinley criterion, can now be reproduced by the non-isothermal linear stability analysis for  $\varepsilon \gtrsim 0.05$ ! Obviously, as illustrated above for values  $\Delta\vartheta = 0\text{ K}, 2\text{ K}, 2.5\text{ K}$ , the scaling is very sensitive to the temperature difference. Furthermore, starting at large gap widths, the axisymmetric ( $m = 0$ ) perturbation mode becomes the first (most) unstable mode when increasing the temperature difference more and more.

This agrees well with the theoretical findings by Al-Mubaiyeh *et al.* [AI-99, AI-00] who investigated the effect of energetics on the linear stability of various constitutive models.

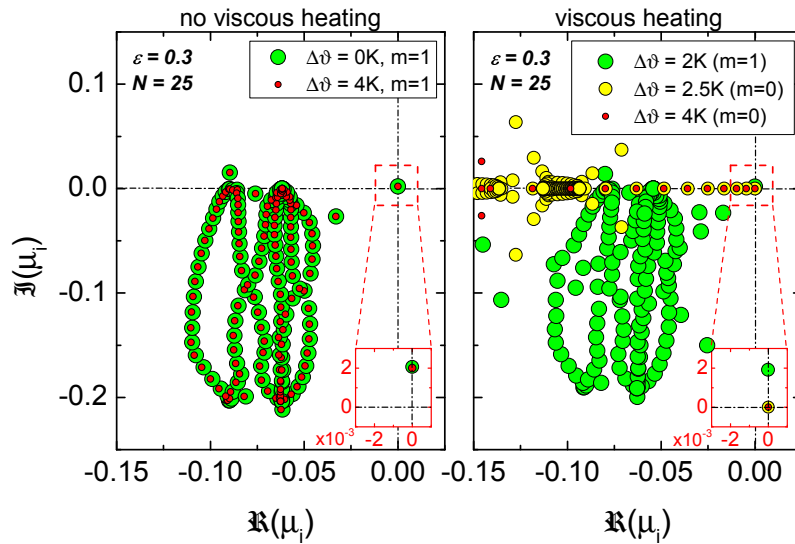


**Figure 9.13:** Eigenvalues of the most unstable perturbation mode for  $\varepsilon = 0.3$  in different situations with or without incorporating viscous heating and a fixed difference of temperature  $\Delta\vartheta = (Z - 1)\vartheta_0$  at the system's boundaries. Viscous heating is defined by the parameters  $\nu = 20.27$ ,  $Na = 1.4 \cdot 10^{-5}$ ,  $Pe = 10150$  and the model parameters correspond to the rheology of the P600<sub>G80</sub> solution ( $\beta = 0.55$ ,  $\beta_1 = 0.18$ ,  $\alpha = 17.7$ ,  $\lambda_r = 1.53$ , cf. figure 9.12).

They found a new axisymmetric instability mode which destabilized the base flow at critical Weissenberg numbers which are up to one magnitude lower relative to the isothermal case. The effect is induced by the convection of temperature gradients within the gap (caused by viscous heating) which leads to a stratification of hoop stress that may impose secondary flow. In particular, a significant amplification of the effect was observed when involving a temperature difference at the boundaries which is in agreement to our findings. Furthermore, the non-isothermal axisymmetric instability mode is stationary which contrasts the oscillatory, non-axisymmetric instability in the isothermal case. This is confirmed in our analysis of the hybrid model: Figure 9.13 presents the spectra of eigenvalues in the complex plane for a given geometry  $\varepsilon = 0.3$  based on the parameters of the P600<sub>G80</sub> solution for different thermal boundary conditions and perturbation modes as presented in figure 9.12. Without viscous heating (*left panel*), the most unstable mode is non-axisymmetric ( $m = 0$ ) for  $\Delta\vartheta = 0K$  (cf. figure 9.12) as well as for  $\Delta\vartheta = 4K$ . Here, the spectrum of eigenvalues is only marginally affected by the change in the temperature of the inner cylinder and, in particular, the imaginary part of the most unstable eigenvalue is still larger than zero, giving an oscillatory perturbation mode (see the magnified section). In contrast, when including viscous heating (*right panel*), the situation changes by increasing the temperature difference: at  $\Delta\vartheta = 2K$ , the most unstable mode is still non-axisymmetric and oscillatory (time-dependent) (green circles). However, when further increasing the temperature at the inner cylinder to the case  $\Delta\vartheta = 2.5K$  (yellow circles), the most unstable mode turns to be axisymmetric ( $m = 0$ ) and steady in time ( $\Im(\mu_{\max}) = 0$ ). At  $\Delta\vartheta = 4K$  (red circles), the spectrum is further changed but the most unstable mode is not affected.

## 9.7 LSA vs. geometrical transition

In a last step, we try to relate our experimental findings presented in figure 7.9, namely the decaying impact of the elastic instability in terms of  $\Delta_{\max}$  with decreasing  $\varepsilon$ , to the development of the perturbation modes. The latter is governed by the eigenvalues of the

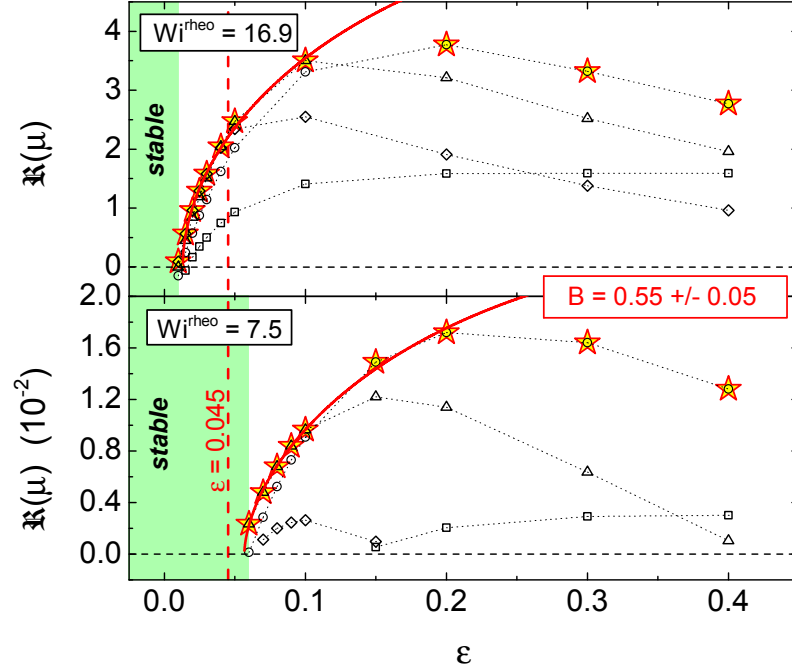


**Figure 9.14:** Eigenvalues  $\Re(\max_{k_z} \{\mu(k_z, m)\})$  of perturbation modes  $m = 0, 1, 2, 3$  (circles, squares, triangles, diamonds) of the hybrid model according to the parameters of the P600<sub>G80</sub> solution in dependence of the gap width  $\varepsilon$ . The behavior is shown for two different values of the rheological Weissenberg number  $Wi^{\text{rheo}}$ . The eigenvalues of the most unstable mode (given by the maximum of the eigenvalues of the various modes, red stars) can be approximates by a fit of the expression (7.3) with a scaling parameter  $B = 0.55 \pm 0.05$ .

respective perturbation modes, more precisely their real part. The higher the (positive) real part of an eigenvalue, the faster grows the associated mode, since the perturbation functions are proportional to  $e^{\mu t}$ , cf. (9.15)–(9.18). Representatively, we analyze the hybrid model based on the parameters of the P600<sub>G80</sub> solution in the isothermal, purely elastic case. We choose a fixed rheological Weissenberg number  $Wi^{\text{rheo}}$ , corresponding to a fixed shear rate  $\dot{\gamma}$ , and observe the development of the most unstable mode when changing the geometric parameter  $\varepsilon$ . The results are presented in figure 9.14 for two different values of  $Wi^{\text{rheo}}$  in terms of the real part of the eigenvalues  $\max_{k_z} \{\mu(k_z, m)\}$  for the perturbation modes  $m = 0, 1, 2, 3$  illustrated by circles, squares, triangles and diamonds, respectively. At  $Wi^{\text{rheo}} = 16.9$  (upper panel) the maximum eigenvalues are all positive in the range  $0.045 \leq \varepsilon \leq 0.4$  realized in our experiments and the base flow is unstable for all values of  $\varepsilon$ . Accordingly, the values of the modified rheological Weissenberg numbers  $16.9\sqrt{\varepsilon}$  are all above the critical numbers shown in figure 9.8 (squares) for  $\varepsilon \geq 0.045$ . In contrast, at a value  $Wi^{\text{rheo}} = 7.5$  (lower panel in figure 9.14), the base flow turns out to be linearly stable for values  $\varepsilon < \varepsilon_{\text{min}} \approx 0.06$ . Furthermore, the values of real parts of the eigenvalues are two orders of magnitude compared to the case  $Wi^{\text{rheo}}$ .

Now, we recall the scaling criterion (7.3) which fairly well reproduced our experimental findings. Assuming that the impact of elastic instability is governed by the growth of perturbation modes given by the real part of the respective eigenvalues, we adapt equation (7.3) to the data shown in figure 9.14 (cf. red curves): for both values of  $Wi^{\text{rheo}}$ , the real part of the most unstable perturbation mode  $\max_{k_z, m} \Re(\mu(k_z, m))$  scales with the gap width  $\varepsilon$  according to

$$\max_{k_z, m} \Re(\mu(k_z, m))(\varepsilon) \propto \left( \frac{h(\varepsilon) - Cd}{d} \right)^{B=0.55 \pm 0.05}. \quad (9.54)$$

The agreement with the experimental scaling law (7.4) which yields  $B = 0.45 \pm 0.11$  is remarkable and it evokes the square-root scaling of eigenvalues commonly observed in the context of bifurcation theory.

However, the agreement with the experimental data is not perfect as we cannot extend the adaption of the scaling law to the total data of eigenvalues. Consistency is observed only for small to intermediate values, giving the scaling of the main bifurcation. This may be attributed to the fixing of the (rheological) Weissenberg number to a single value which provides the limiting gap widths  $\varepsilon_{\min}$  below which the base flow is linearly stable independent of the choice of the perturbation mode. Even if this limitation to a single Weissenberg number (independent of  $\varepsilon$ ) may be too tight, there is strong evidence suggesting that the Weissenberg number cannot exceed an upper limit which maintains persistence of linear stability at low values of  $\varepsilon$ . This further strongly corroborates our initial guess of polymer degradation: the increasing loss of elasticity leads to a severe decay of polymer relaxation time which overcompensates the increase of the (rheological) Weissenberg number due to the increase in shear rate.

---

## Degradation of polymer solutions

Beside the characteristic onset of elastic instability at a critical shear rate  $\dot{\gamma}_c$ , comparing the Taylor-Couette measurements of the different polymer solutions reveals another clear similarity: the flow curves  $\tau/\dot{\gamma}$  show a severe loss in magnitude when shearing the samples at shear rates above the critical onset  $\dot{\gamma}_c$ , i.e. in the region of strong non-laminar (turbulent) flow. To be more precise, the stress signal which initially inclined due to the onset of elastic instability subsequently decays to a level close to the base viscometric curve as extrapolated from the region of low shear rates. This behavior is not expected for a “healthy” sample. Supported by the findings of our visualization measurements (cf. figure 7.6) and the outcome of the linear stability analysis assuming a limited Weissenberg number, there is evidence that the polymer solutions progressively *degrade* during our measurements. When we allude to *degradation*, one may think of a process of mechanically “chopping” the polymer chains in smaller and smaller pieces as a result of high shear forces which are strong enough to rupture the intra-molecular bonds between single carbon atoms in the polymer chains. Thereby, the solutions would increasingly lose their elastic properties.

In the following, we first give a synopsis of previous studies focusing on the degradation of polymer solutions in various flow situations. In view of this, we then further present the results of our own thorough experimental study based on the P600<sub>G80</sub> solution in a representative Taylor-Couette cell ( $\varepsilon = 0.267$ ) which allow a verification of the supposed polymer degradation during a standard scanning measurement.

### 10.1 Historical synopsis

Ever since the pioneer work of the later Nobel prize laureate Hermann Staudinger and his coworkers in the 1920–1930s about macromolecules (see, e.g., [Sta32]), the mechanical degradation of polymer solutions has been known and extensively studied. In [Bal81], an overview of relevant theoretical milestones with regard to the modeling of random scission of polymer chains is given. With the design of reliable methods to measure the molecular weight distribution which is an appropriate quantity to verify degradation, more insight in the fundamental mechanisms was achieved. Consequently, full kinetic information about the chain scission process was available in the context of proposed kinetic theory by applying it to the experimental weight distribution.

One of the earliest comprehensive degradation studies can be found in the publications by Bestul *et al.* [Bes54, Bes56, Bes57, Bes60] from the late 1950s. They focused on the degradation process of concentrated polymer solutions being subjected to the capillary flow at high shear stresses for different exposure times. Aside from experimental studies they aimed at developing a kinetic theory for the prediction of mechanical degradation in

terms of the rupture rate of inter- and intra-molecular aliphatic carbon-carbon bonds. Since then, numerous theoretical as well as experimental studies followed, aiming at a profound understanding of the fundamental mechanism that involves the observed dependencies on all of the different variables in the particular flow conditions. In the scope of these studies, molecular weight, polymer concentration, viscosity, solvent, as well as boundary conditions like temperature, rate and exposure time of shear and the respective stresses, etc. were addressed. For example, Ballauff *et al.* [Bal81, Bal84] investigated the degradation of semi-concentrated solutions of polystyrene in a  $\theta$ -solvent<sup>1</sup> exposed to laminar shear flow of shear rates  $5 \times 10^3 \text{ s}^{-1} \leq \dot{\gamma} \leq 10^4 \text{ s}^{-1}$  in a Couette-type apparatus. They found that the observed degradation is due to homolytic scission of the carbon-carbon bonds and thermodynamically determined by the solvent quality: in a poor solvent where contacts between polymer segments are energetically favored and hence the polymers coil up. In the external laminar shear field, the coils are rotated and have to disentangle from other coils. The associated frictional forces can be high enough for carbon-carbon bonds to split. In contrast, in a good solvent where interactions between polymer segments and solvent molecules are preferred, the shear rates needed to cause scission are significantly higher (cf. also [Har65]). Consistently, the experimental results by Ballauff *et al.* showed a strong dependence on the temperature which highly influences the quality of the solvent. Furthermore, the breakage probability showed a Gaussian distribution along the chain, i.e. the polymer chains favorably break in the middle, in particular when the shear rates are small. For highly concentrated polystyrene solutions, Breitenbach *et al.* [Bre73] observed degradation even at notably low shear rates ( $\dot{\gamma} = 600 \text{ s}^{-1}$ ) at  $\theta$ -condition.

While the aforementioned studies primarily focused on degradation in laminar shear flows, numerous later studies on polymer degradation (e.g., [Cha83, Too95, Sun04, Van05, Elb09, Per12]) addressed its effect on the drag reduction in turbulent flow which attracted great interest due to its importance in industrial applications such as the oil transport in pipelines as it strictly limits the applicability of long-chained drag reducing polymers. Remarkably, Vanapalli *et al.* [Van06] recently showed that polymer degradation by chain scission is primarily governed by turbulence. The authors showed that previous scission experiments which were analyzed according to accepted laminar flow scission theories, were in fact affected by turbulence. Based on the assumption that the drag force on an extended polymer chain is set by velocity fluctuations on the Kolmogorov length scale<sup>2</sup> of the turbulent flow, a universal scaling could be found which revealed consistency of the various experimental data. Groisman and Steinberg [Gro00, Gro01, Gro04] meanwhile experimentally showed that the non-inertial flow state of a viscoelastic fluid in a curvilinear flow beyond its onset of (purely) elastic instability (such as the viscoelastic Taylor-Couette flow) provide all the major features of developed turbulence, comparable to a state of turbulent flow for a Newtonian flow at very high Reynolds numbers. Such a state of so-called “elastic turbulence” particularly exhibit a power law spectrum of the velocity fluctuations and a pronounced increase in flow resistance. Remarkably, the authors also observed degradation of the investigated polymer solution (80 ppm PAAm  $M_w = 18 \times 10^6$  Da diluted in an aqueous 65% sugar solvent,  $\lambda = 3.4 \text{ s}$ ) in the Taylor-Couette flow ( $\varepsilon = 0.5$ ) already at shear rates of about  $3.5 \text{ s}^{-1}$  or  $5 \text{ s}^{-1}$  depending on the geometry and the associated onset of elastic instability at about  $0.6 \text{ s}^{-1}$  and  $1 \text{ s}^{-1}$ , respectively. However, the authors did not explicitly relate their observation to the state of turbulence, even if the particularly small shear rates give reason to it or even do not allow for another conclusion. The experiments by

<sup>1</sup>Since a polymer chain cannot adopt to a configuration where two of its parts occupy the same space, the configuration space of the polymer chain is reduced by a so-called excluded volume. It causes the end-to-end distance of a polymer to be bigger than in the case where no excluded volume exist. At the so-called  $\theta$ -point (associated with a  $\theta$ -temperature) the effects of excluded volume are suppressed, i.e. the polymer chain behaves like an ideal chain [Flo74].

<sup>2</sup>This is the length scale of smallest eddies present in turbulent flow, where energy is dissipated by viscosity.

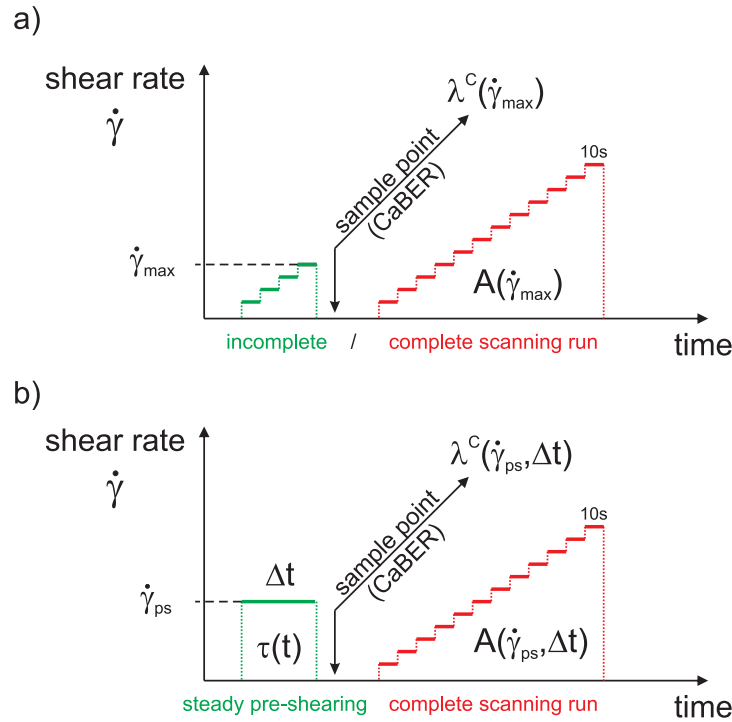


**Figure 10.1:** Sketch of the protocols used within the degradation study: a) incomplete scanning protocol b) steady pre-shearing protocol.

Groisman and Steinberg further revealed a significant difference between the energy spectra of inertial and elastic turbulence which could be confirmed by theoretical considerations by Fouxon and Lebedev [Fou03]. In particular, the authors found an additional length scale which affects the energy cascade of the turbulent state and on which energy is dissipated by the polymers and by internal friction in the polymer coils. This could be confirmed in experiments by Vonlanthen [Von10]. We interpret this as an indicator for the susceptibility to degradation due to enhanced energy dissipation in the elasticity-induced turbulent state at low Reynolds numbers.

## 10.2 Experimental degradation study

In the proposed picture of gradual polymer degradation due to the impact of elastic turbulence, it is reasonable to guess that the degree of degradation should depend on both the intensity and the duration of the associated non-laminar, turbulent flow acting on the polymer chains. Aiming at a separation of these two influencing factors and a quantification of the degradation in the course of our Taylor-Couette scanning measurements, we representatively analyzed the transient viscoelastic properties of the **P600<sub>G80</sub> polymer solution** according to two different protocols, namely a steady pre-shearing protocol and an incomplete scanning protocol. Thereby, we combined steady shear Taylor-Couette measurements in the  $\varepsilon = 0.267$  cell (at  $\vartheta = 10^\circ\text{C}$ ) and capillary breakup extensional rheometry (at ambient temperature,  $\vartheta \approx 23^\circ\text{C}$ ) which is highly sensitive to small changes in the elastic properties of a fluid.

Figure 10.1 sketches the two different protocols and they are presented in more detail in the following.

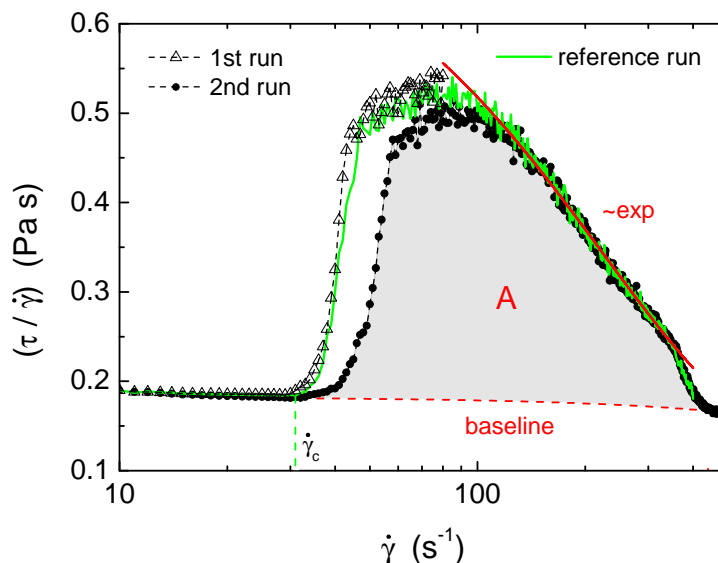


**Figure 10.2:** The green line shows a complete reference run of a fresh P600<sub>G80</sub> sample in the TC-7.5-9.5 Taylor-Couette cell, performed at  $\vartheta = 10^\circ\text{C}$  according to the standard protocol. When the run of a fresh sample is stopped at  $\dot{\gamma} = 80\text{ s}^{-1}$  (open triangles), a subsequent complete run of the same (pre-sheared) sample (full circles) significantly differs from the reference run.

### 10.2.1 Incomplete scanning protocol (cf. figure 10.1a)

In the standard Taylor-Couette scanning protocol presented in section 7.1, the shear rate is increased stepwise and every value of the shear rate is kept constant for 10 s. Consequently, when alluding to progressive degradation, the state of the sample is likely to change during a complete scan as the polymers gradually are subject to elastic instability and turbulent flow states.

In order to analyze the different stages during a standard scanning run, we stop the respective measurements at varying maximum shear rates  $\dot{\gamma}_{\text{max}}$ . Subsequently, a tiny amount of the processed sample ( $\lesssim 1\%$ ) is extracted and analyzed in the CaBER experiment. The rest of the (pre-sheared) sample is once again subject to a complete scanning protocol in the Taylor-Couette cell. Figure 10.2 and 10.3 show representative results of a sample that has been processed in the first Taylor-Couette run up to a maximum shear rate of  $\dot{\gamma}_{\text{max}} = 80\text{ s}^{-1}$ . The CaBER relaxation time of the pre-sheared sample  $\lambda^C(\dot{\gamma}_{\text{max}} = 80\text{ s}^{-1})$  is clearly below the relaxation time of the fresh sample  $\lambda_0^C$ . Here and in the following, the results of up to three independent CaBER measurements are averaged and the standard deviations give the respective error bars of the data points  $\bar{\lambda}^C \pm \delta\lambda^C$ . The flow curve of the pre-sheared sample (with reduced relaxation time) significantly differs from the reference run<sup>3</sup> of the fresh sample: the onset of instability is delayed and its magnitude is reduced. The latter is measured in terms of the area  $A = \int [\tau(\dot{\gamma})/\dot{\gamma} - \text{baseline}] d\dot{\gamma}$  in excess of the viscometric flow curve (which is extrapolated by the cone-and-plate steady shear measurements) and according to this, for the further evaluation we refer to the critical shear rate  $\dot{\gamma}_c$  not as the actual onset of elastic instability highlighted by the sharp incline in the flow curve but to the onset of Ekman vortices, which cause the initial lift of the flow curves. The involved error is minor and it simplifies the determination of the area  $A$  in excess of the viscometric baseline, which can be

<sup>3</sup>Small errors in the filling or misalignment, which manifest in a slight vertical mismatch in the flow curves, were compensated by rescaling the signal to provide congruence of the flow curves at the highest shear rates, where the different samples are assumed to be degenerated by maximum degradation

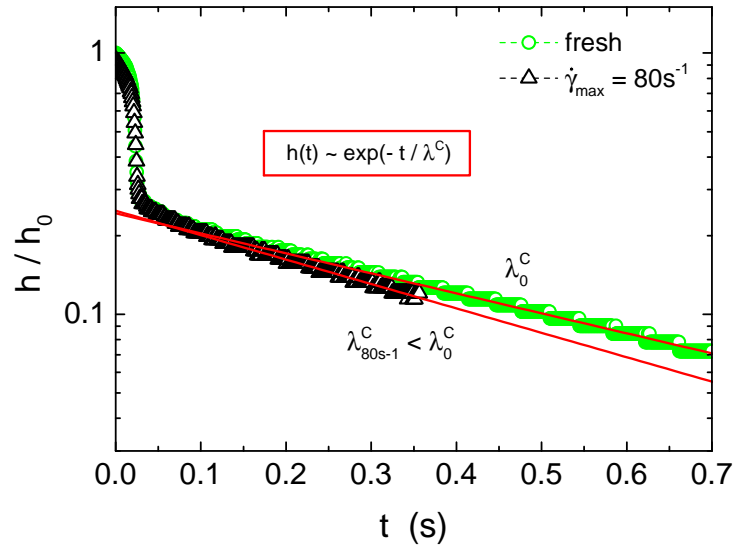


**Figure 10.3:** Representative CaBER measurements of a fresh (green circles) and a pre-sheared ( $\dot{\gamma}_{\max} = 80 \text{ s}^{-1}$ , black triangles) P600<sub>G80</sub> sample (cf. figure 10.2).

chosen to be a straight line in good approximation.

## Results

Figure 10.4 summarizes the results of the incomplete scanning protocol for various maximum shear rates  $\dot{\gamma}_{\max}$  of the initial scanning measurements: clearly, the higher  $\dot{\gamma}_{\max}$ , the more decrease both the CaBER relaxation time  $\lambda^C$  and the excess area  $A$  of the flow curves in the Taylor-Couette measurements. Whereas the decay of the relaxation time can be fairly described by an exponential-like function  $\lambda^C(\dot{\gamma}_{\max}) = C [1 - \exp(-\lambda_0^C \dot{\gamma}_{\max}/C)] / \dot{\gamma}_{\max}$  (the special form is motivated in the discussion part of this degradation study), the area  $A$  follows a Gaussian function  $A(\dot{\gamma}_{\max}) = A_0 \exp(-[\dot{\gamma}_{\max} - \dot{\gamma}_c]^2/2w^2)$ .

### 10.2.2 Steady pre-shearing protocol (cf. figure 10.1b)

The previous protocol combines variations of intensity and period of the initial pre-shearing: the higher the maximum shear rate is chosen in the initial Taylor-Couette scanning run, the longer the sample is subject to increasing shear rates. In order to decouple the two parameters, we apply a second protocol. In a first step we shear a fresh sample in the Taylor-Couette cell at a fixed shear rate  $\dot{\gamma}_{\text{ps}}$ . Analogous to the first protocol, a tiny amount of the sample is subsequently analyzed with the CaBER setup and the remaining fluid is subject to a standard scanning run. The steps were repeated for various time periods of the initial pre-shearing process over a wide range. Thereby, fresh P600<sub>G80</sub> samples are used in each run. Figure 10.5 represents the preprocessing at a representative constant shear rate  $\dot{\gamma}_{\text{ps}} = 80 \text{ s}^{-1}$  which is above the onset of elastic instability (cf. figure 10.2). When starting the steady shearing, the stress signal inclines virtually at once up to the maximum value reached in the reference run in the non-laminar flow regime. Subsequently, the signal exponentially decays and converges to some limiting value. Figure 10.6 shows the sequence of complete scanning Taylor-Couette measurements of the preprocessed samples, compared to the flow curve of the fresh sample. Each curve corresponds to a complete scanning run of a sample, that was initially sheared at  $\dot{\gamma}_{\text{ps}} = 80 \text{ s}^{-1}$  for different time periods  $\Delta t = 600 \text{ s}, 6000 \text{ s}$  and  $21600 \text{ s}$ . Obviously, the longer the period of the pre-shearing, the less pronounced develops the elastic instability in terms of

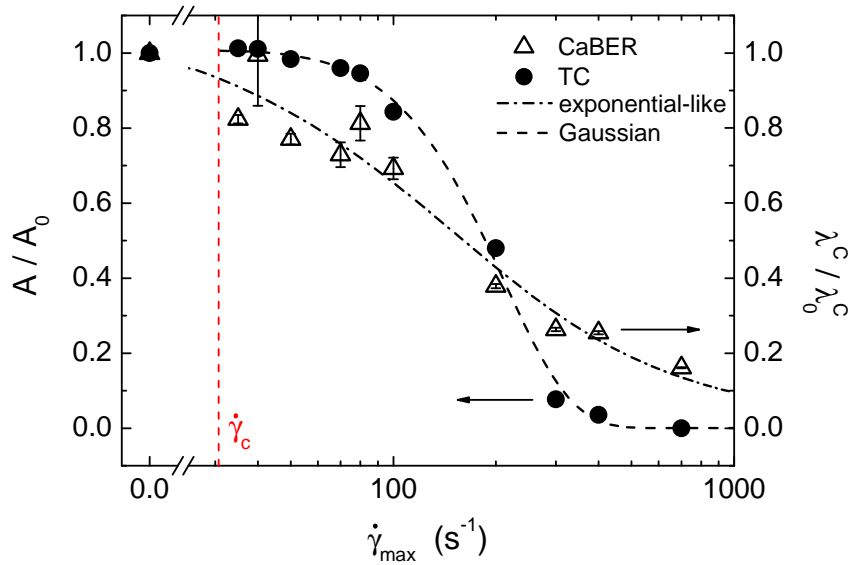


**Figure 10.4:** Excess areas of the flow curves from the Taylor-Couette measurements (filled circles) and corresponding CaBER relaxation times (open triangles) of differently pre-processed samples (P600<sub>G80</sub>), both normalized by the respective values of a fresh sample. The dashed line reflect a single-exponential function whereas the dash-dotted curve is a Gaussian function, centered at the critical shear rate  $\dot{\gamma}_c$ .

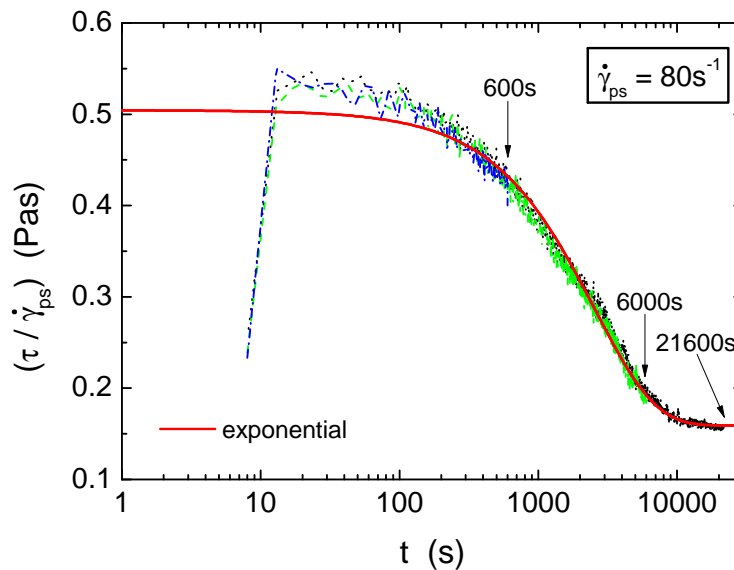


**Figure 10.5:** Stress signal  $\tau/\dot{\gamma}$  during the shearing at constant shear rate  $\dot{\gamma}_{ps} = 80 \text{ s}^{-1}$ . The signal exponentially decays with time and it converges to a minimum value  $\eta_{lim}$ .

the area  $A$  in excess of the viscometric flow curve during the subsequent run, and its onset is delayed to higher shear rates.

## Results

It is obvious that both the magnitude of the shear rate  $\dot{\gamma}_{ps}$  and its exposure time  $\Delta t$  strongly affect the degradation of the polymer solution. Figure 10.7 shows the temporal development of

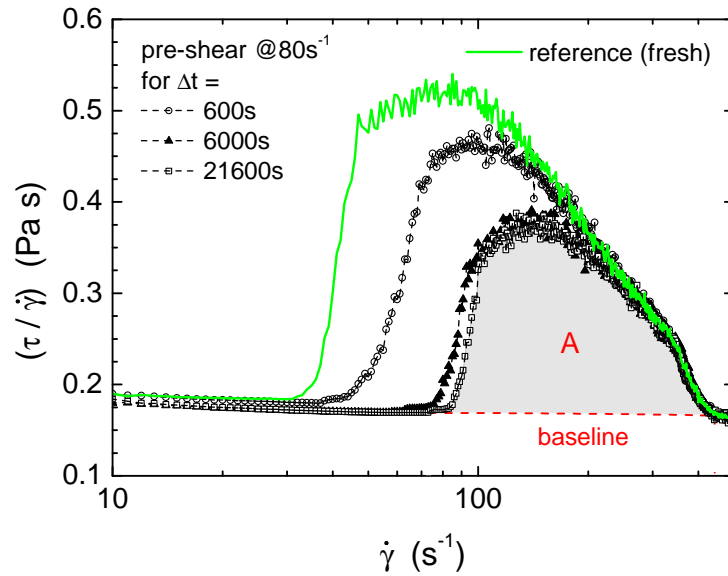


**Figure 10.6:** Sequence of complete scanning measurements, each performed after an initial pre-shearing at  $\dot{\gamma}_{ps} = 80 \text{ s}^{-1}$  for different periods  $\Delta t = 600 \text{ s}, 6000 \text{ s}, 21600 \text{ s}$ . All the curves are below the one of a fresh sample (green solid line).

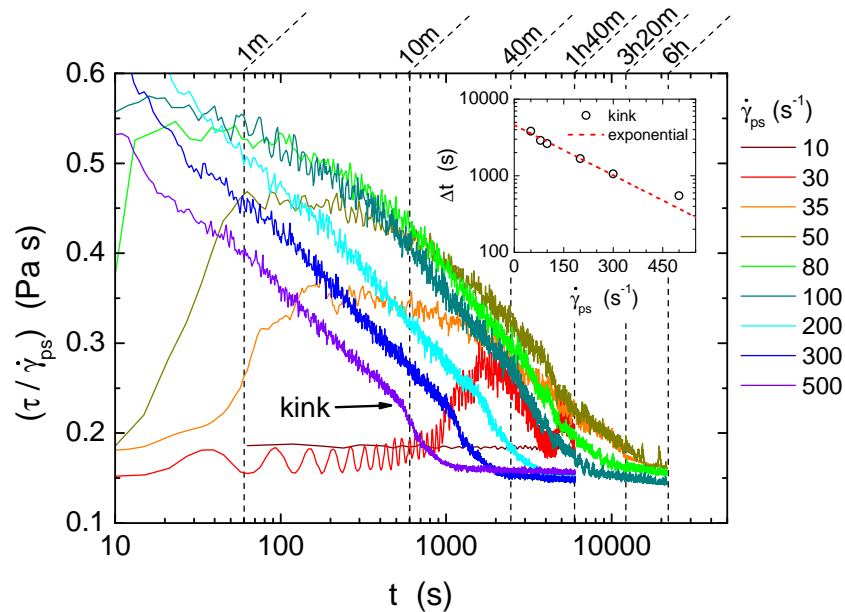


**Figure 10.7:** Temporal development of the stress signal  $(\tau/\dot{\gamma}_{ps})(t)$  during the preprocessing at different steady shear rates  $\dot{\gamma}_{ps}$  of P600<sub>G80</sub> in the TC-7.5-9.5 setup ( $\varepsilon = 0.267$ ) at  $\vartheta = 10^\circ \text{C}$ . The inset presents the appearance of the kink.

the stress signal  $\tau/\dot{\gamma}_{ps}$  at various constant shear rates  $\dot{\gamma}_{ps}$ . Whereas the signal is constant for  $\dot{\gamma}_{ps} = 10 \text{ s}^{-1}$  (over at least  $\Delta t = 6000 \text{ s}$ ) which is below the actual onset of elastic instability at  $\dot{\gamma}_c \approx 36 \text{ s}^{-1}$  (cf. table 7.1), exceeding  $\dot{\gamma}_{ps} = 30 \text{ s}^{-1}$  triggers non-laminar, unstable flow which emerges the sooner the higher the value of  $\dot{\gamma}_{ps}$ . After having reached their respective maxima, the curves decay in a similar manner. They show a characteristic kink (similar to the one observed in the scanning measurements according to the standard protocol) which is most pronounced for high shear rates. It appears the earlier, the higher the shear rate is chosen. The inset in figure 10.7 suggests an exponential dependence on the shear rate.

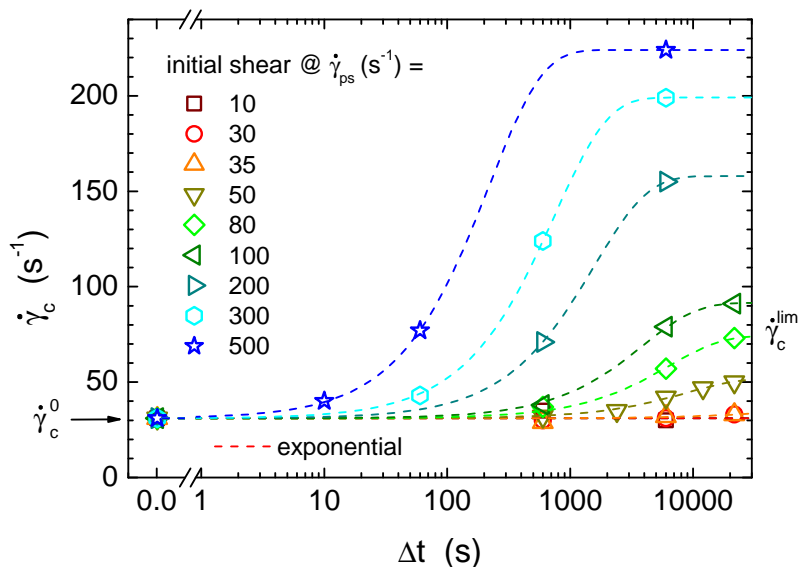


**Figure 10.8:** Onset of elastic instability in the TC-7.5-9.5 setup in dependence of the shear rate  $\dot{\gamma}_{ps}$  at which the sample was preprocessed for different periods  $\Delta t$ . The dashed lines refer to biased exponential fits.

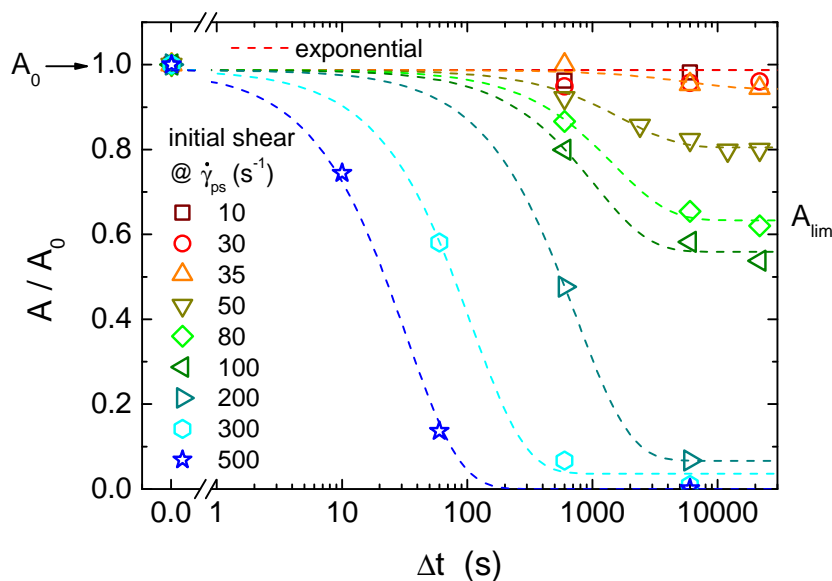


**Figure 10.9:** Area  $A(\Delta t)$  in excess of the viscometric flow curve as a function of the period  $\Delta t$  of initial pre-shearing for different values of corresponding shear rates  $\dot{\gamma}_{ps}$ .

Before and after the kink, the curves can be approximated by exponential laws which merge to a single one at moderate shear rates (cf. green curve ( $\dot{\gamma}_{ps} = 80 \text{ s}^{-1}$ ), also represented in figure 10.5).

When stopping the pre-shearing of the sample at selected times (cf. the dashed vertical lines), the solution is likely to be partially degraded. Subsequent standard Taylor-Couette scanning measurements differ from the one of the fresh sample: both, the upward shift in the onset of elastic instability as well as the excess area  $A$  on top of the viscometric flow curve exponentially scale with the exposure time  $\Delta t$  of the preceding shearing. The figures 10.8 and 10.9 represent this finding. However, it is to be noted in general, the instability does

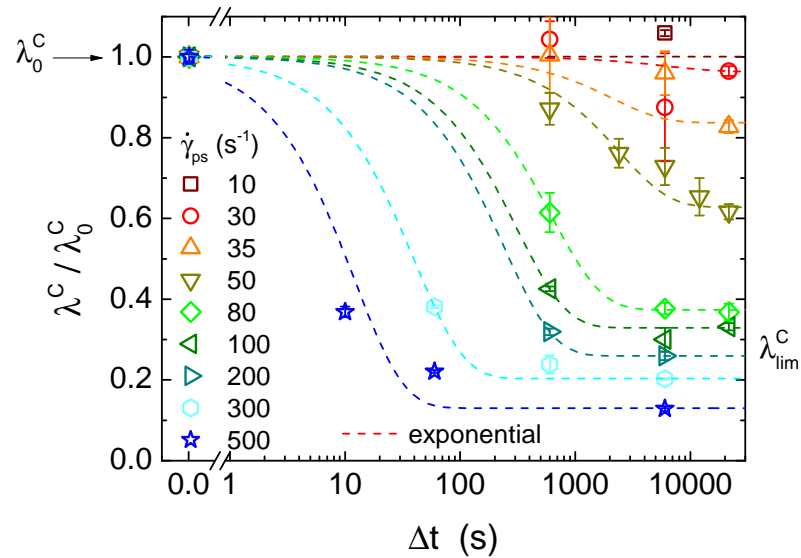


**Figure 10.10:** Relative CaBER relaxation time  $\lambda^C/\lambda_0^C$  of pre-sheared (at  $\dot{\gamma}_{ps}$ ) samples as a function of the respective pre-processing period  $\Delta t$ . The data are fitted by a function  $\lambda^C = \lambda_{lim}^C + (\lambda_0^C - \lambda_{lim}^C) \exp(-\Delta t/C)$ .

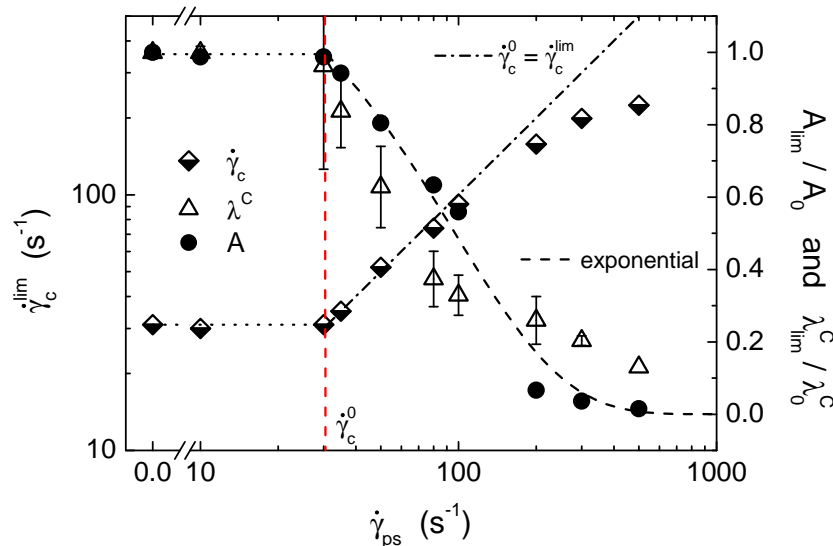


**Figure 10.11:** Limiting values  $\dot{\gamma}_c^{lim}$ ,  $A_{lim}$  and  $\lambda_{lim}^C$  of samples, that were (infinitely long) sheared at various shear rates  $\dot{\gamma}_{ps}$ .

not completely disappear when increasing the exposure time of the pre-shearing more and more. In fact, the flow curves seem to converge to limiting states as presented by figure 10.8 and 10.9: the data points suggest a limited exponential growth and decay of the critical shear rate  $\dot{\gamma}_c(\Delta t)$  and the associated excess area  $A(\Delta t)$ , respectively. The limiting values  $\dot{\gamma}_c^{lim}$  and  $A_{lim}$  systematically depend on the shear rate  $\dot{\gamma}_{ps}$  (cf. figure 10.11). Remarkably, the limiting threshold  $\dot{\gamma}_c^{lim}$  equals the initially applied pre-shear rate for moderate values. The deviation from this relation at higher pre-shear is likely due to the sparseness of data points which causes the fits to underestimate the limits. In contrast, the excess area exponentially decays to zero. However, both processes do not start until the pre-shear is above the critical onset  $\dot{\gamma}_c$  of the fresh sample.

The complementary data of the CaBER measurement support the results of the shear study.

Figure 10.10 presents the CaBER relaxation times of the pre-sheared samples. Each data point is an average of up to three independent measurements from the same batch. Analogous to the data of the excess area  $A$  in figure 10.9, the relaxation time  $\lambda^C(\Delta t)$  exponentially converges to limiting values  $\lambda_{\text{lim}}^C$  which gradually decreases with increasing  $\dot{\gamma}_{\text{ps}}$  (cf. figure 10.11).

### 10.3 Interpretation of degradation data

Facing the state of the art concerning polymer degradation as presented in the synopsis, the systematic findings of our thorough degradation study corroborate a scenario of polymer degradation caused by elasticity-induced turbulence.

Our experiments clearly reveal that degradation is associated with a severe, gradual decrease in the CaBER relaxation time as can be seen in the figures 10.4, 10.10 and 10.11. It already emerges at very low rotation rates which are definitely too low to force a breakage of polymer chains due to the related laminar shear forces. In fact, polymer degradation appears to be directly related to the onset of elastically driven secondary flow, associated with the emergence of elastic instability which establishes a turbulent flow state when exceeding a critical Weissenberg number. Obviously, already the formation of localized Ekman vortices (in the present case at  $\dot{\gamma}_c^0 \approx 30 \text{ s}^{-1}$ ) before the virtual onset of elastic instability at slightly higher shear rates ( $\dot{\gamma}_{EI} \approx 36 \text{ s}^{-1}$ ) provokes a first decrease of the CaBER relaxation time  $\lambda_{\text{lim}}^C$  (cf. figure 10.11). The longer the polymers are subject to the turbulent flow, the more decreases the relaxation time, cf. figure 10.10. However, in agreement with the hypothesis by Vanapalli [Van06], the extend to which the polymers are degraded is limited by the applied shear rate ( $\dot{\gamma}_{\text{ps}}$ ) which defines the maximum drag force applied to the polymer chains by the turbulent flow, i.e. the breakage of polymer chains is limited to a minimum length of chain fragments, associated with a respective minimum relaxation time  $\lambda_{\text{lim}}^C(\dot{\gamma}_{\text{ps}})$ .

The delay of the onset of elastic instability in a standard Taylor-Couette measurement of a pre-sheared sample in terms of an increase in the critical shear rate  $\dot{\gamma}_c$  (cf. figure 10.8 and 10.11) is directly related to the preceding degradation process and the associated drop in the relaxation time: regardless of the explicit rate of pre-shearing  $\dot{\gamma}$  or the respective period  $\Delta t$ , the product of  $\lambda^C(\dot{\gamma}_{\text{ps}}, \Delta t)$  and  $\dot{\gamma}_c(\dot{\gamma}_{\text{ps}}, \Delta t)$  turns out to be constant within the uncertainties of the individual quantities (see figure 10.12). Here, the relative errors in  $\dot{\gamma}_c$  are assumed to be 10% of the respective estimates and the CaBER relaxation times are rescaled to the values at  $\vartheta = 10^\circ \text{C}$  (according to the values of a fresh sample). The averaged data yield a constant critical Weissenberg number  $Wi_c^C = \lambda^C \dot{\gamma}_c \approx 14$ . Comparing the values of the CaBER relaxation time and the rheological relaxation time (i.e.  $\lambda^C \approx 492 \text{ ms}$  versus  $\lambda^{\text{rheo}} \approx 33 \text{ ms}$ , cf. table 5.3), this translates to a constant critical rheological Weissenberg number of about  $Wi_c^{\text{rheo}} \approx 0.9$  for the onset of elastic instability in the Taylor-Couette measurements (in an individual geometry  $\varepsilon = 0.267$ ) regardless of the explicit relaxation time which is consistent within our framework of elasticity-induced flow instability.

Since there is no more doubt that the CaBER relaxation time is gradually lowered by the impact of turbulent flow initiated at shear rates above the critical onset of elastic instability, we further have to address the pivotal question to which extend our Taylor-Couette standard scanning measurements are affected by this circumstance. Although the foregoing discussion suggests that the explicit onset of elastic instability of a fresh polymer sample is not affected by degradation (according to the principle of cause and effect, degradation cannot emerge before its causing instability), the latter will certainly alter the further progress. The degradation data extracted from the incomplete scanning measurements provide explicit information about the CaBER relaxation time during the different steps of a standard scanning measurement.

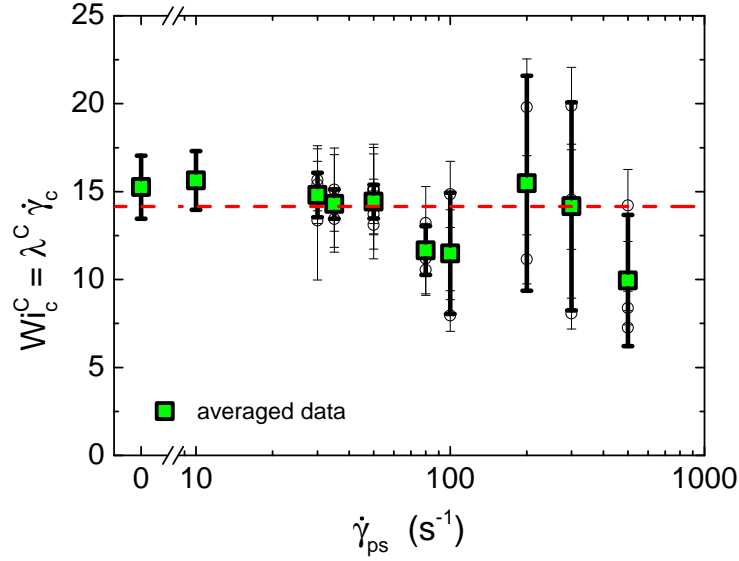


**Figure 10.12:** Critical Weissenberg number  $Wi_c^C = \lambda^C(\dot{\gamma}_{ps}, \Delta t)\dot{\gamma}_c(\dot{\gamma}_{ps}, \Delta t)$  calculated from the data of CaBER relaxation time (cf. figure 10.10) and the data of critical shear rate (cf. figure 10.8) which both depend on the rate of pre-shearing  $\dot{\gamma}_{ps}$  and corresponding pre-processing time  $\Delta t$ . The averaged data (green) can be approximated to be constant within the error bars.

By multiplying the CaBER data (cf. figure 10.4) with the respective shear rates  $\dot{\gamma}_{max}$ , we gain information of the typical (CaBER) Weissenberg number during the standard Taylor-Couette measurement. Figure 10.13 presents the product  $Wi^C = \lambda^C(\dot{\gamma}_{max})\dot{\gamma}_{max}$  in dependence on  $\dot{\gamma}_{max} \equiv \dot{\gamma}$ . Again, we rescaled the relaxation time to provide relaxation data at the temperature  $\vartheta = 10^\circ\text{C}$  at which the Taylor-Couette measurements were conducted. The presented data  $Wi^C(\dot{\gamma})$  suggest a convergence to some maximum level and it can be approximated by a function<sup>4</sup>  $Wi^C(\dot{\gamma}) = Wi_{max}^C [1 - \exp(-\dot{\gamma}/C)]$  with  $Wi_{max}^C \approx 49$ . This translates to an estimate of the maximum rheological Weissenberg number  $Wi_{max}^{rheo} \approx 3$  reached in the Taylor-Couette measurements.

This finding is remarkable in view of our previous experimental result presented in section 7.3, namely the decreasing impact of elastic instability with increasing gap width  $\varepsilon$  which could be consistently described based on a simple consideration of the geometrical transition from the plane to the Taylor-Couette system and an analysis of the eigenvalues of the perturbation modes in which we had to assume the (rheological) Weissenberg number to be limited to an upper value. This initial assumption is corroborated here by the result of our degradation study. Hence, facing figure 10.13, the complementary data associated with the incomplete scanning and steady pre-shear protocol can be interpreted with regard to a scenario of the transition to elastic instability consistent with our experimental findings: At values  $\dot{\gamma} < \dot{\gamma}_c^0 = 30 \text{ s}^{-1}$ , i.e. below the critical shear rate observed in the integral stress measurement (for  $\varepsilon = 0.267$ ), the associated Weissenberg number as calculated according to the CaBER data of the incomplete scanning measurements is below the critical value  $Wi_c^{rheo} \approx 0.9$  and no instability is observed. Above this critical shear rate, the associated Weissenberg number is bigger than  $Wi_c^{rheo}$  and elastic instability can be observed. When varying  $\varepsilon$ , it is reasonable to suppose that the dependence of the Weissenberg number on the shear rate is only marginally modified (due to the unchanged interplay between the degrading polymer relaxation time and the shear rate). However, the critical Weissenberg number increases with decreasing  $\varepsilon$  according to

<sup>4</sup>Accordingly, the CaBER relaxation time can be described by a function  $\lambda^C(\dot{\gamma}) = Wi_{max}^C [1 - \exp(-\dot{\gamma}/C)] / \dot{\gamma}_{max}$  with  $C = Wi_{max}^C / \lambda_0^C$ , cf. figure 10.4.

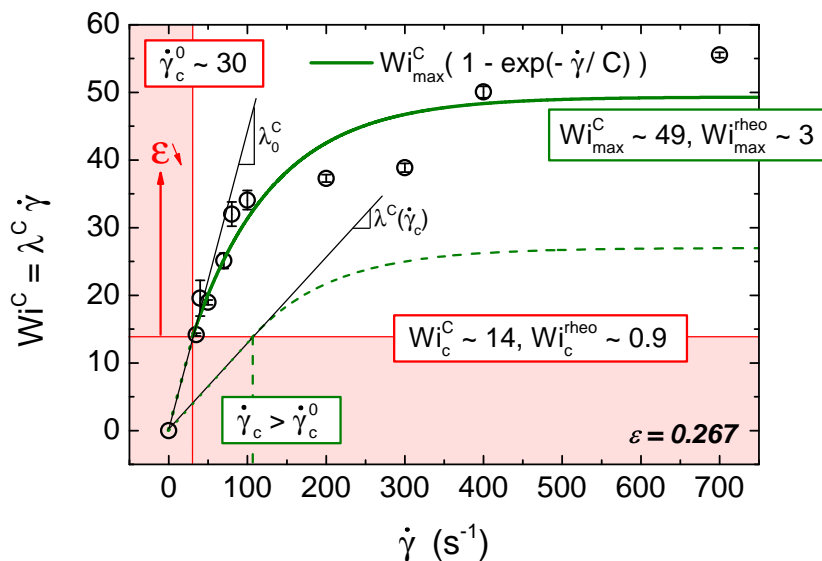


**Figure 10.13:** Weissenberg number  $Wi^C = \lambda^C(\dot{\gamma}_{\max})\dot{\gamma}_{\max}$  during a Taylor-Couette standard scanning measurement. The data were extracted from the measurements following to the incomplete scanning protocol.

the Pakdel-McKinley criterion (8.8) (highlighted by the red arrow) and thus there will be the situation in which the critical Weissenberg number exceeds the maximum Weissenberg number reached in the experiment. This consequently gives a minimum gap width below that no instability can be observed anymore (cf. figures 7.9 and 9.14).

This scenario is further compatible with the decreasing impact of elastic instability of a pre-sheared, i.e. partially degraded sample, as shown in figure 10.4, 10.9 and 10.11 in terms of the excess area  $A$ . Compared to a fresh sample of relaxation time  $\lambda_0^C$  and critical Weissenberg number  $Wi_c^{\text{theo}} \approx 0.9$ , a partially degraded sample ( $\lambda^C < \lambda_0^C$ ) becomes unstable at the same Weissenberg number  $\lambda^C(\dot{\gamma}_c)\dot{\gamma}_c \approx 0.9$  which is, however, reached not until a higher critical shear rate  $\dot{\gamma}_c > \dot{\gamma}_c^0$ . Consequently, the maximum Weissenberg number during a scanning measurement will be lower than in the case of a initially fresh sample (cf. the green dashed line). This naturally weakens the impact of elastic instability as it is governed by the magnitude of the eigenvalues of the unstable perturbation modes which directly scales with the Weissenberg number (cf. figure 9.14).

However, when revising the recent findings, the scenario suffers from one shortcoming: it lacks a consistent explanation for the decay of the stress signal during an individual scanning measurement. Since the CaBER data suggest a monotonous growth up to a maximum Weissenberg number, there is no reason for a decay of the stress signal when increasing the shear rate further. This may be attributed to the fact that the CaBER relaxation time is not the proper time scale to calculate the relevant rheological Weissenberg number. The more relevant shear relaxation time (from steady shear rheometry) may be more amenable to degradation at high shear rates which would lead to a final decay of both the rheological Weissenberg number and the impact of elastic instability after having reached their respective maximums.

Nevertheless, we can state that based on the conception of a progressive, systematic degradation of the polymer solutions we can propose a consistent explanation for our experimental findings on elastic instability in the various Taylor-Couette cells. It particularly involves the gradually decreasing impact of elastic instability which finally completely diminishes for the smallest gap widths.

## Summary

The presented experimental studies were based on the thorough investigation of various viscoelastic polymer solutions (polyacrylamide (PAAm), cf. table 5.1). They differed from each other not only in the polymer concentration  $c_{\text{PAAm}}$  which varied from 80 ppm to 1200 ppm but also in the (weight-averaged) molecular weight of the polymer batch (low:  $M_w = (5-6) \times 10^6$  Da, or high:  $M_w = 18 \times 10^6$  Da) as well as in the type of the Newtonian solvent (aqueous glycerol or sucrose solutions of different concentrations). They were investigated at different temperatures  $\vartheta = 10^\circ\text{C}, 22^\circ\text{C}$  or  $23^\circ\text{C}$ . Accordingly, a full characterization of the various fluids by means of rotational steady shear, small amplitude oscillatory, shear rate relaxation and capillary breakup extensional rheometry (CaBER) revealed a map of diverse rheological parameters (cf. table 5.3) for which an understanding is based on different rheological models. Remarkably, the steady shear rheometry of all polymer solutions without exception could consistently be described by a constitutive 2-component Oldroyd-B/sPTT hybrid model providing specific sets of parameters ( $\eta_s, \eta^U, \eta^P, \lambda^U, \lambda^P, \alpha$ ) (see section 5.2). In contrast to the ordinary Oldroyd-B model, the additional contribution of the sPTT mode accounts for the shear-thinning of the apparent viscosity and at the same time, it allows for deviations from the quadratic scaling of the normal stress with the shear rate. These deviations turned out to be minor for the low-molecular weight solutions but considerably more relevant for high molecular weights. Differences between solutions of different molecular weight were more obvious in all other rheometric methods and no overall consistent characterization based on single-mode (Oldroyd-B or Jeffreys model) or multi-mode (generalized Jeffreys model) models could be obtained, even if the results were partially satisfactory and agreement with the literature could be observed. A deeper analysis of the steady shear viscosity data revealed further consistent information about the polymer solutions: it could be shown that the polymer solutions were dilute (with the exception of the P150<sub>S65.6</sub> solution) with respect to the common estimate of the overlap concentration  $c_{\text{PAAm}} \lesssim c^{**} = 0.77/[\eta]$  with the intrinsic viscosity  $[\eta]$  and that they behave highly flexible when exposed to moderate shear forces. This was indicated by the special behavior of the intrinsic viscosity  $[\eta]$  and the Huggins coefficient  $k_H$  in dependence of the applied shear rate in agreement with the literature.

With the knowledge of their rheology, the polymer solutions were investigated in a set of various Taylor-Couette cells (see section 6). Every cell was built up of an inner cylinder with a radius  $R_1$  and an outer cup with (inner) radius  $R_2 = R_1 + d$ . The gap width  $d = 1$  mm was kept constant for the different cells and the radius  $R_1$  ranged from 2.5 mm to 22 mm. By keeping  $d$  constant, only the curvature of the cells varied. All integral stress measurements were conducted at the predefined temperatures following a standard scanning protocol in which the shear rate was gradually increased (section 7.1). They all exhibited a more or less pronounced flow instability in terms of a sharp incline in the flow resistance. It emerged at characteristic shear rates and corresponding Reynolds numbers  $Re \lesssim 1$  far below the onset of

inertia-induced secondary flow and we referred to this phenomenon as the onset of (purely) elastic Taylor-Couette instability. The outcome of all measurements could be condensed to a universal criterion

$$\sqrt{\varepsilon}Wi_c^{\text{rheo}}(\varepsilon, \beta^+) = (1.8 \pm 0.3)\sqrt{(0.96 \pm 0.05) - \beta^+} \sqrt{\frac{(\varepsilon + 1)^2}{\varepsilon + 2}} \quad (11.1)$$

incorporating both low- and high-molecular weight solutions. The above relation gives the onset of elastic instability in terms of the critical rheological Weissenberg number  $Wi_c^{\text{rheo}} = (\lambda^{\text{rheo}}\dot{\gamma}_c)^{n^{\text{rheo}}}$  depending on the relative gap width  $\varepsilon$  and the relative viscosity  $\beta^+ = \eta_s/\eta^+$  in which the plus sign denotes the fact that the shear-thinning of the apparent viscosity was explicitly accounted for. The parameters  $\lambda^{\text{rheo}}$ ,  $n^{\text{rheo}}$ ,  $\eta_s$  and  $\eta^+$  were taken from the steady shear rheometry according to its evaluation based on the hybrid model. Deviations from this scaling criterion are restricted to the smallest gap widths and they are supposed to be due to the uncertainties in the localization of the critical onset which increase with decreasing  $\varepsilon$ .

This experimental finding is in remarkable agreement with the prediction of the dimensionless scaling criterion by Pakdel and McKinley [Pak96, McK96] based on the formulation with respect to an Oldroyd-B fluid and accounting for finite gap widths (section 8). It is given by

$$\sqrt{\varepsilon}Wi_c^{\text{rheo}}(\varepsilon, \beta) = M\sqrt{1 - \beta} \sqrt{\frac{(\varepsilon + 1)^2}{\varepsilon + 2}} \approx \frac{M}{\sqrt{2}}\sqrt{1 - \beta} \left(1 + \frac{3}{4}\varepsilon - \frac{5}{32}\varepsilon^2\right) \quad (11.2)$$

where the rheological Weissenberg number is related to the Oldroyd-B (UCM) relaxation time  $\lambda^U$  according to  $Wi^{\text{rheo}} = (1 - \beta)Wi^{\text{O-B}} = (1 - \beta)\lambda^U\dot{\gamma}$ . The agreement includes both the geometrical as well as the rheological scaling prediction in terms of the dependencies on  $\beta$  and  $\varepsilon$ , respectively. The coefficient  $M$  is a constant but undefined by the criterion and hence the absolute values of the critical Weissenberg number are not predicted by this theory.

With respect to geometrical scaling, our results clearly contrast the early findings by Muller *et al.* [Mul89] whose experimental data based on the investigation of a Boger fluid showed some inconsistency compared to the geometrical scaling coming along with the linear stability analysis of an Oldroyd-B fluid for axisymmetric disturbances (cf. section 4.3.4). This corresponds to the conclusion of the Pakdel-McKinley criterion formulated with respect to small gap widths. First, we have to state that their assumption of small gap widths did not reasonably apply to the geometries used in their experiments. However, a simple recalculation of their critical Weissenberg numbers accounting for the finite gap widths did not resolve the problem. The authors did not put forward the obvious discrepancies with respect to the geometrical scaling but, instead, they addressed the differences in the magnitude of the critical Weissenberg numbers. In order to improve the agreement, they proposed the use of an alternative relaxation time from transient stress relaxation measurements which turned out to be about twice the characteristic time from steady shear measurements. But this, quite obviously, did not influence the geometrical scaling as it only uniformly rescaled the absolute values regardless of the gap width. At this point, a final explanation for the differing scalings in the experiments by Muller *et al.* has to remain unsettled. In contrast, we are observing the striking agreement exhibited by our experiments which is reproducible for all investigated polymer solutions, suggesting the conclusion that the Pakdel-McKinley criterion definitely does apply to the viscoelastic Taylor-Couette flow in terms of its geometrical scaling prediction when accounting for finite gap widths.

Referring to the rheological scaling, our experiments are further consistent with the findings by Groisman *et al.* [Gro98b] who verified the predicted dependence of the critical onset on the explicit rheological properties of a fluid. What differs from our results is their value of  $M = 3.58$  which is based on the (longest) relaxation time extracted from oscillatory rheometry. This is about twice our estimate and it agrees with the proposition by Muller *et al.* .

In view of this remaining inconsistency with respect to the absolute values of the critical onset, a further evaluation of our experimental values of the (rheological) Weissenberg number was needed. Therefore and in order to further validate the geometrical and the rheological scaling law, we performed a linear stability analysis of the Taylor-Couette base flow based on the ordinary Oldroyd-B (section 9.4) as well as the more appropriate hybrid model (section 9.5) formulated for finite gap widths. We confirmed the correctness of our code by reproducing the critical Weissenberg numbers published by Shaqfeh *et al.* [Sha92] for a Maxwell ( $\beta = 0$ ) and an Oldroyd-B fluid ( $\beta = 0.79$ ) with respect to the axisymmetric perturbation mode ( $m = 0$ ). Furthermore, we were able to extrapolate our results to the small-gap limit and to reproduce the data by Larson *et al.* [Lar90]. Analyzing the first non-axisymmetric perturbation mode ( $m = 1$ ) we were not able to reproduce the neutral stability curve presented by Joo *et al.* [Joo94]. This corroborates the initial guess that their data which already appeared to be inherently inconsistent are flawed. Summarizing the results from our extensive linear stability analysis of various Oldroyd-B fluids, we could show that in agreement with the literature the most unstable perturbation mode is always non-axisymmetric ( $m > 0$ ). Furthermore, we could show that its azimuthal wave number increases when decreasing the relative gap width and that the overall scaling of the most unstable perturbation mode can be described by a quadratic function

$$\sqrt{\varepsilon} W_c^{\text{rheo}}(\varepsilon, \beta) \approx a(\beta) \sqrt{1 - \beta} \left( 1 + b(\beta)\varepsilon + c(\beta)\varepsilon^2 \right) \quad (11.3)$$

with positive coefficients  $a, b, c$  dependent on  $\beta$ . Remarkably, this significantly contrasts the Pakdel-McKinley criterion (11.2) which predicts no dependence of the respective coefficients on  $\beta$ . Even when accounting only for the axisymmetric perturbation mode, the mismatch in the scaling is almost unchanged. These significant discrepancies between the Pakdel-McKinley criterion and the linear stability analysis for the Oldroyd-B fluid based on the formulation of finite gap widths in terms of rheological and geometrical scaling has to be emphasized and it highly contrasts the agreement found in the small gap limit for axisymmetric perturbations. Furthermore, not only the scaling but also the absolute values of the critical Weissenberg numbers significantly deviate, i.e. the linear stability analysis predicts much higher critical numbers than experimentally observed. Again, this is in systematic agreement with the findings by Muller *et al.* [Mul89]. However, one has to keep in mind that the rheometry of our polymer solutions could not consistently be described by the Oldroyd-B model.

Nonetheless, the analysis based on the more reasonable hybrid model provided a similar picture (section 9.5). Even if the systematic agreement between the experimental data and the critical data of the linear stability analysis in terms of the geometrical and the rheological scaling could be improved, significant discrepancies remained. Even when accounting for inertial effects up to the value  $Re = 1$  which approximates the highest value reached in our experiments no improvement could be observed.

Whereas the analysis had been isothermal so far, in a last step we allowed for non-isothermal flow properties combined with viscous heating and supplemented by a steady temperature difference between the cylinder walls (section 9.6). For all polymer solutions, the relevant thermal properties, namely the heat capacity  $c_p$ , the thermal conductivity  $\kappa$  and the activation energy  $\nu$  were reasonably estimated or measured and further translated to the dimensionless Nahme and Péclet number  $Na$  and  $Pe$ . With it, the effect of energetics was analyzed based on the non-isothermal hybrid model. However, no significant effect could be observed and the effect of energetics on the flow stability turned out to be negligible. Nevertheless, when strongly increasing the Péclet number a clear destabilization of the Taylor-Couette base flow could be observed in agreement with the literature [AI-99, AI-00]. Remarkably, the scaling dramatically changed when increasing  $Pe$  and our experimental data could finally be reproduced fairly well. In further agreement with the literature, during this destabilization

process the instability changes from an overstable (oscillatory) to a steady mode. Here, the system is most prone to this new kind of instability for large gap widths. Accordingly, for the smallest gap widths the Péclet number has to be even higher.

Hence, apart from the reasonable agreement between our experimental data and the theoretical prediction by the Pakdel-McKinley criterion in terms of geometrical and rheological scaling, a significant discrepancy to the data of the linear stability analysis remains even when accounting for inertia or energetics. This is surprising as the underlying constitutive model reasonably accounts for the explicit steady shear rheometry of our polymer solutions. However, as it is based on the viscometric flow in the cone-and-plate geometry we cannot guarantee that it really captures the rheometry that is relevant in the Taylor-Couette flow which definitely differs from the former one. In this respect, the proposals by Muller *et al.* and Groisman *et al.* to account for a relaxation time based on a different (transient or oscillatory) rheometric method may be justified. In view of this, the significantly higher relaxation times from our (transient) shear rate relaxation rheometry appear more reasonable but as our method lacks a fully consistent evaluation of the data we cannot really rely on it. However, the difference in the geometrical scaling remains untouched when referring to a different relaxation time (or a spectrum of relaxation times).

Within the framework of a supplementary experimental study (section 10), we could corroborate the assumption of polymer degradation leading to a reduced impact of elastic instability when decreasing the gap widths which was observed throughout the Taylor-Couette measurements for all polymer solutions. The associated gradual extenuation of the elastic properties of a polymer solution in the course of a Taylor-Couette measurement could be quantified by means of CaBER measurements of the pre-sheared samples, i.e. the associated CaBER relaxation time progressively decayed depending on the treatment of the polymer solutions. Following the approaches of relevant literature, we could interpret our experimental observations according to the conception of mechanical degradation induced by elastic turbulence which gradually emerges subsequent to the onset of elastic flow instability. According to this, in the course of a standard Taylor-Couette scanning run, gradual degradation led to a fast saturation of the Weissenberg number converging to a maximum value. This value turned out to be significantly lower than the monotonically increasing Weissenberg numbers reached during the ideal measurement of a robust polymer solution. Based on the linear stability analysis of the isothermal hybrid model and a quantitative evaluation of the eigenvalues of the perturbation modes, we could demonstrate that this limitation in the value of the Weissenberg number may lead to the observed extenuated impact of elastic instability for decreasing gap widths in combination with a complete vanishing of elastic instability for the smallest gap widths. In respect of this, the limitation in the Weissenberg number partially or fully stabilizes the base flow. Remarkably, a similar finding is provided by a simple consideration of a geometrical transition from the circular Couette system to the plane Couette system with increasing the radius of curvature and decreasing the relative gap width, respectively (cf. section 7.3).

---

## Conclusion

The objective of this study has been to contribute to a more profound understanding of the elastic flow instability of viscoelastic polymer solutions in the standard Taylor-Couette flow. By means of a comprehensive, comparative investigation including elaborate experiments as well as numerical and theoretical considerations, open questions and apparent inconsistencies within the existing literature were attempted to be clarified. The corresponding experiments were based on various dilute, thoroughly characterized viscoelastic polymer solutions whose steady shear rheometry could be consistently described by a two-component constitutive hybrid model. The integral stress measurements in various Taylor-Couette cells characterized by a joint gap width but variable radius of curvature were performed to investigate the onset of (purely) elastic flow instability and, in particular, on its scaling with the geometrical parameter of the Taylor-Couette setup, namely the relative gap width, and the rheological properties of the fluids in terms of the ratio of solvent to total viscosity. Both scalings turned out to be consistent with the theoretical predictions coming along with the Pakdel-McKinley criterion which gives the onset of elastic instability in curved flow geometries. Regarding the geometrical scaling, our findings could compensate the inconsistent picture provided by the existing literature. However, the onset occurred at significantly lower Weissenberg numbers as compared to previous results found in the literature. The linear stability analysis of both the Oldroyd-B and the hybrid model exhibited a similar picture, i.e. the critical onset of linear elastic instability was predicted to occur at significantly higher Weissenberg numbers for all values of the geometrical parameter. Even when accounting for reasonable non-isothermal flow properties and boundary conditions, the differences between the experimental data and the numerics remained significant. Even more remarkably, neither the geometrical nor the rheological scaling observed in our experiments could be satisfactorily reproduced by the linear stability analysis. Finally, gradual polymer degradation induced by elastic turbulence could be identified to affect the Taylor-Couette standard scanning measurements. The associated limitation in the maximum Weissenberg number could be consistently related to the varying impact of elastic instability in dependence of the geometrical parameter as experimentally observed.



**Part III**  
**Appendices**



---

## Rheometric data

Appendix [A](#) summarizes all measurements of the polymer solutions conducted within the scope of the experimental study of viscoelastic Taylor-Couette flow. It includes the rheological characterization by means of rotational steady shear, transient shear rate relaxation, oscillatory and capillary breakup extensional experiments as well as the Taylor-Couette data. The associated evaluation can be found in the chapters [5](#), [7](#) and [8](#).

## A.1 The P150<sub>G80</sub> polymer solution

### A.1.1 Steady shear rheometry

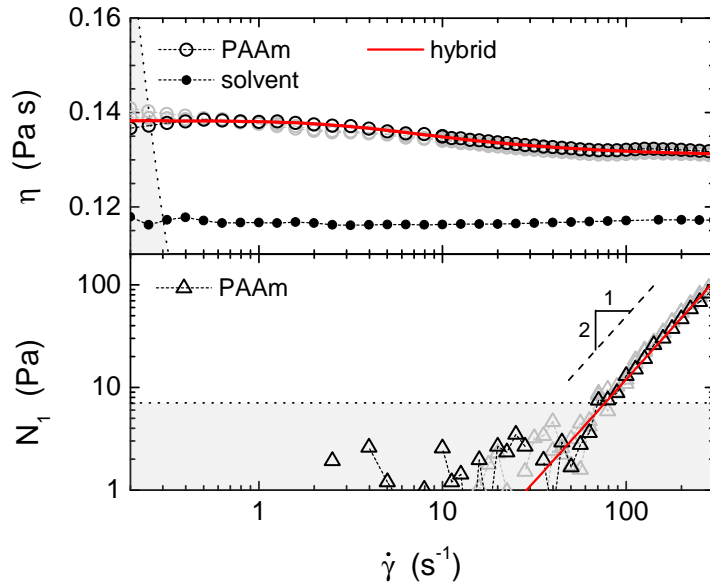


**Figure A.1:** *Top:* Representative (apparent) viscosity  $\eta(\dot{\gamma})$  of the P150<sub>G80</sub> solution (open circles) as well as of the corresponding solvent (filled dots), extracted from steady shear rotational rheometry in the cone-and-plate C60/2° setup at  $\vartheta = 10^\circ\text{C}$ . *Bottom:* Corresponding data of (first) normal stress difference  $N_1(\dot{\gamma})$  (triangles). The red curves refer to an adaption of the 2-component hybrid model according to (3.7) and (3.8).

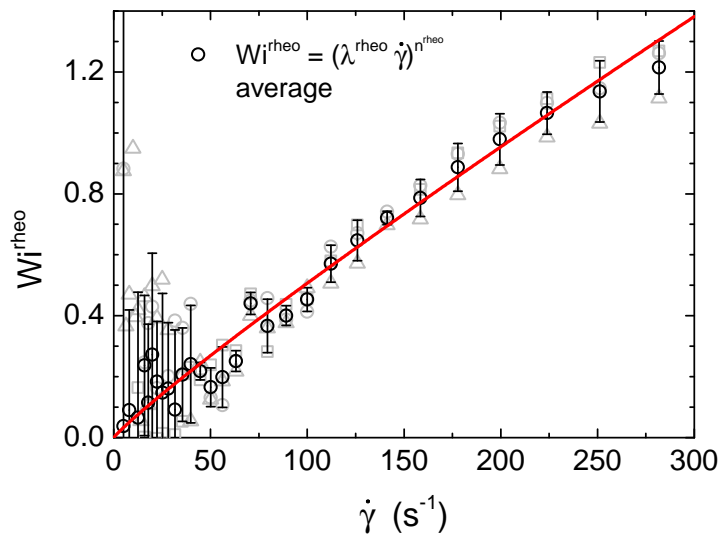


**Figure A.2:** Rheologic Weissenberg number  $Wi^{\text{rheo}}(\dot{\gamma}) = N_1(\dot{\gamma})/2\tau_{12}(\dot{\gamma})$  of the P150<sub>G80</sub> solution, calculated from the steady shear data (cf. figure A.1). The red curve corresponds to a power law fit according to (5.2).

## A.1.2 Shear rate relaxation rheometry

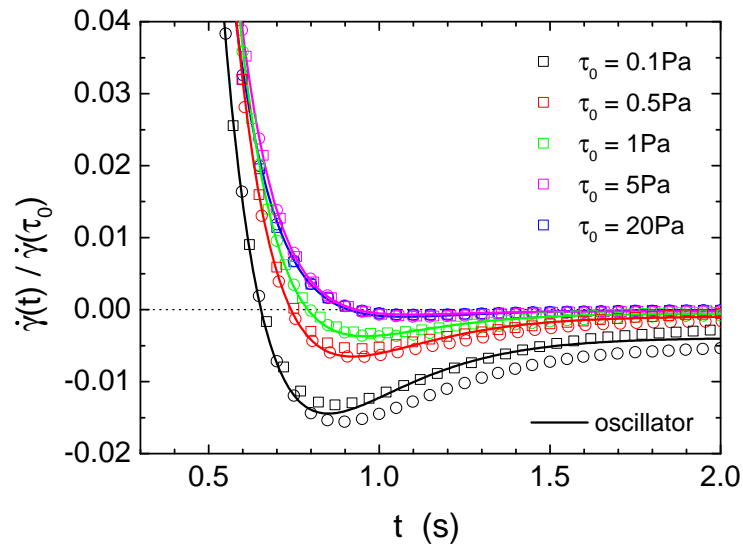


**Figure A.3:** Relaxation of shear rate after sudden cessation of constant shear stress  $\tau_0$  applied to the P150<sub>G80</sub> solution in the cone-and-plate C60/2° setup at  $\vartheta = 10^\circ\text{C}$ . Different curves correspond to different initial shear stresses  $\tau_0$ . The temporal behavior can be described by the viscoelastic, oscillatory recoil of a Jeffreys fluid according to (3.13).

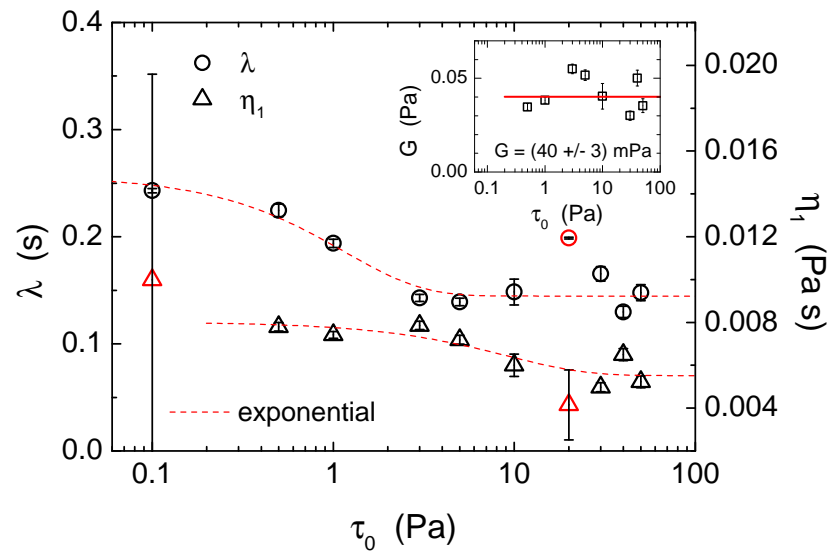


**Figure A.4:** Characteristic relaxation time  $\lambda$  and viscosity  $\eta_1$  of the P150<sub>G80</sub> solution, extracted from the shear rate relaxation data (cf. figure A.3) in dependence of the initially applied shear stress  $\tau_0$  according to (3.13). Red data points are omitted in the fits. The shear modulus  $G$  is shown in the inset.

### A.1.3 Small amplitude oscillatory rheometry

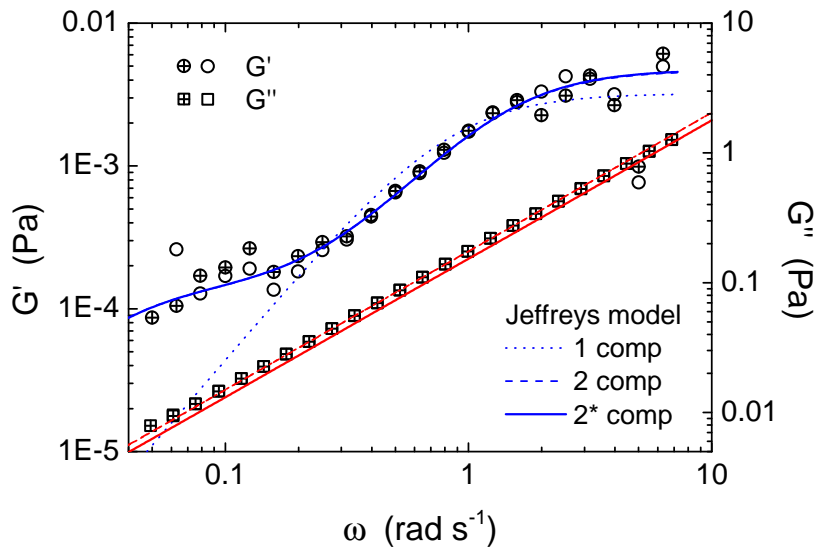


**Figure A.5:** Small amplitude oscillatory shear data of the P150<sub>G80</sub> solution at  $\vartheta = 10^\circ\text{C}$  in terms of the real (circles) and imaginary part (squares) of the complex modulus  $G(\omega) = G'(\omega) + iG''(\omega)$ . The curves correspond to different adaptations of the (generalized, multi-component) Jeffreys model (cf. (3.25),(3.26)): one-component (dotted), two-component (dashed), two-component with fixed solvent contribution  $\eta_2 = \eta_s = 119\text{ mPa s}$  (solid).

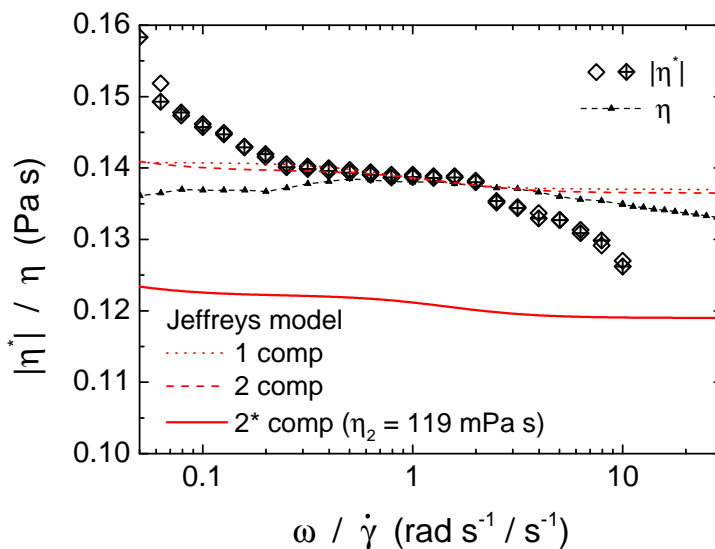


**Figure A.6:** Comparison of small amplitude oscillatory and steady shear data of the P150<sub>G80</sub> solution at  $\vartheta = 10^\circ\text{C}$  in terms of the complex viscosity  $|\eta^*(\omega)|$  and the apparent viscosity  $\eta(\dot{\gamma})$ . The red curves correspond to the (generalized, multi-component) Jeffreys model based on the parameters extracted from the adaption to the moduli  $G'$  and  $G''$  (cf. figure A.5).

## A.1.4 Capillary breakup extensional rheometry

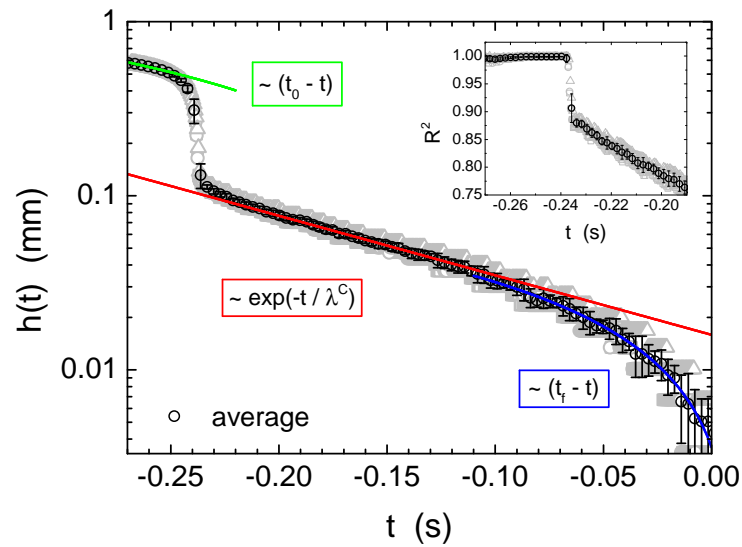


**Figure A.7:** Minimal width  $h(t)$  of the capillary bridge of various P150<sub>G80</sub> samples during the constriction process in the CaBER experiment, performed at  $\vartheta = 10^\circ\text{C}$ . The exponential section gives the characteristic CaBER relaxation time  $\lambda^C$  according to equation (3.33). The inset presents the coefficient of determination  $R^2$  of a quadratic fit to the filament contour, cf. equation (3.35).

## A.1.5 Taylor-Couette measurements

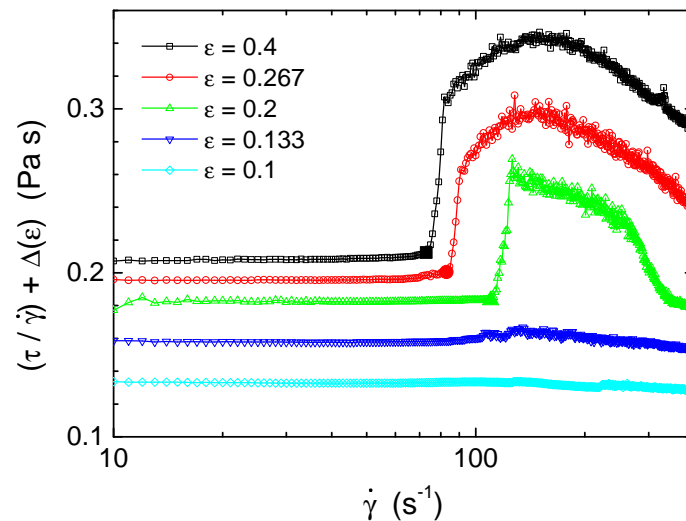


**Figure A.8:** Integral stress data from the Taylor-Couette measurements of the P150<sub>G80</sub> solution at  $\vartheta = 10^\circ\text{C}$  according to the standard scanning protocol. The different data sets correspond to different values of the relative gap widths  $\varepsilon$  ( $d = 1\text{ mm}$ ). For the sake of a better illustration, the curves are vertically shifted by  $\Delta(\varepsilon) = 10\text{ mPa s} \cdot (10 - \varepsilon^{-1})$ . The characteristic transition points are highlighted by filled markers.

## A.2 The P1200<sub>G80</sub> polymer solution

### A.2.1 Steady shear rheometry

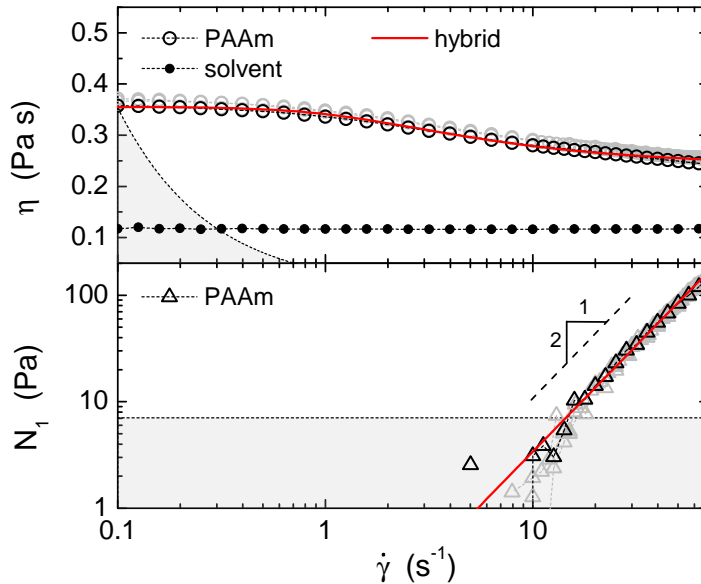


**Figure A.9:** *Top:* Representative (apparent) viscosity  $\eta(\dot{\gamma})$  of the P1200<sub>G80</sub> solution (open circles) as well as of the corresponding solvent (filled dots), extracted from steady shear rotational rheometry in the cone-and-plate C60/2° setup at  $\vartheta = 10^\circ\text{C}$ . *Bottom:* Corresponding data of (first) normal stress difference  $N_1(\dot{\gamma})$  (triangles). The red curves refer to an adaption of the 2-component hybrid model according to (3.7) and (3.8).

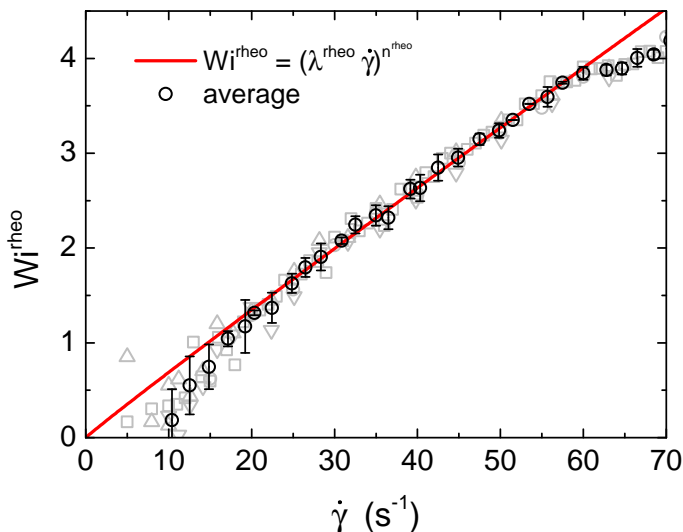


**Figure A.10:** Rheologic Weissenberg number  $Wi^{\text{rheo}}(\dot{\gamma}) = N_1(\dot{\gamma})/2\tau_{12}(\dot{\gamma})$  of the P1200<sub>G80</sub> solution, calculated from the steady shear data (cf. figure A.9). The red curve corresponds to a power law fit according to (5.2).

## A.2.2 Shear rate relaxation rheometry

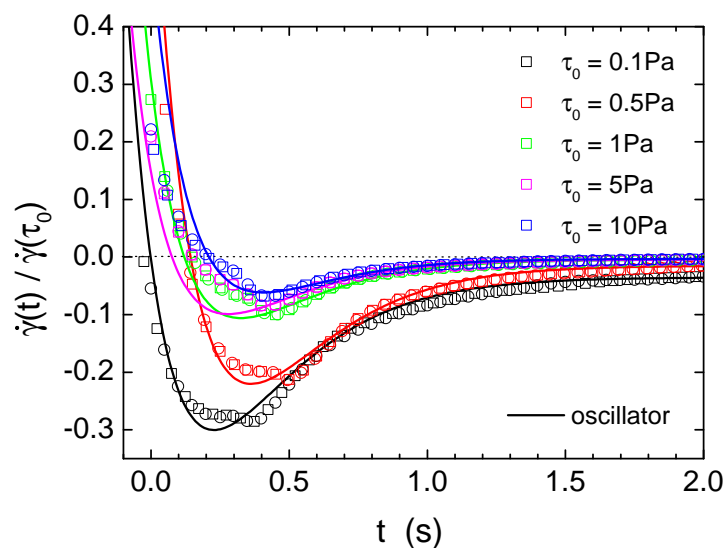


**Figure A.11:** Relaxation of shear rate after sudden cessation of constant shear stress  $\tau_0$  applied to the P1200<sub>G80</sub> solution in the cone-and-plate C60/2° setup at  $\vartheta = 10^\circ\text{C}$ . Different curves correspond to different initial shear stresses  $\tau_0$ . The temporal behavior can be described by the viscoelastic, oscillatory recoil of a Jeffreys fluid according to (3.13).

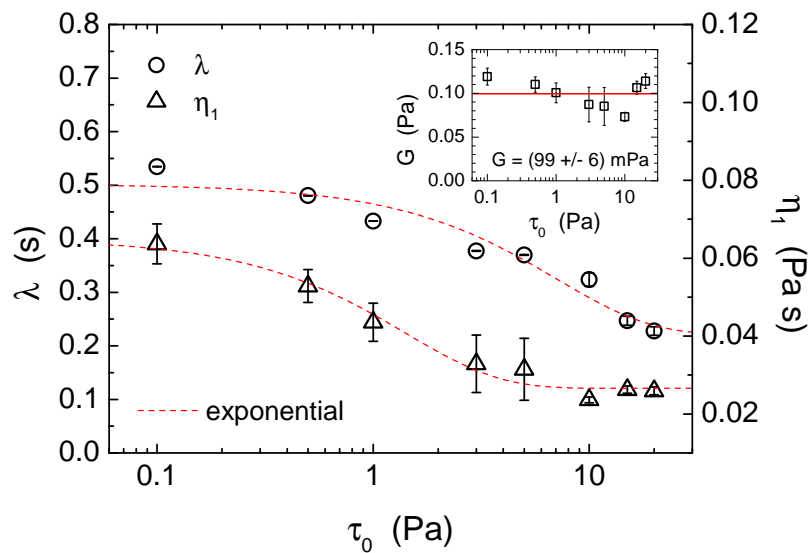


**Figure A.12:** Characteristic relaxation time  $\lambda$  and viscosity  $\eta_1$  of the P1200<sub>G80</sub> solution, extracted from the shear rate relaxation data (cf. figure A.11) in dependence of the initially applied shear stress  $\tau_0$  according to (3.13). The shear modulus  $G$  is shown in the inset.

### A.2.3 Small amplitude oscillatory rheometry

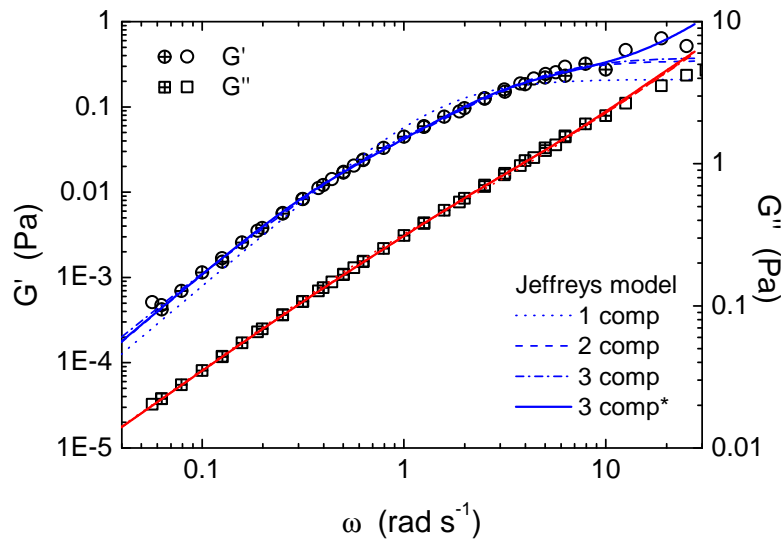


**Figure A.13:** Small amplitude oscillatory shear data of the P1200<sub>G80</sub> solution at  $\vartheta = 10^\circ\text{C}$  in terms of the real (circles) and imaginary part (squares) of the complex modulus  $G(\omega) = G'(\omega) + iG''(\omega)$ . The curves correspond to different adaptations of the (generalized, multi-component) Jeffreys model (cf. (3.25),(3.26)): one-component (dotted), two-component (dashed), three-component (dash-dotted), three-component with fixed solvent contribution  $\eta_2 = \eta_s = 119\text{ mPa s}$  (solid).

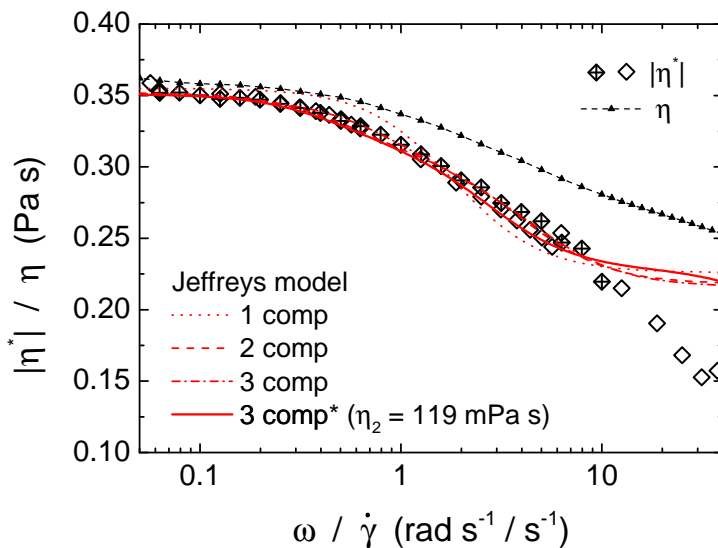


**Figure A.14:** Comparison of small amplitude oscillatory and steady shear data of the P1200<sub>G80</sub> solution at  $\vartheta = 10^\circ\text{C}$  in terms of the complex viscosity  $|\eta^*(\omega)|$  and the apparent viscosity  $\eta(\dot{\gamma})$ . The red curves correspond to the (generalized, multi-component) Jeffreys model based on the parameters extracted from the adaption to the moduli  $G'$  and  $G''$  (cf. figure A.13).

## A.2.4 Capillary breakup extensional rheometry

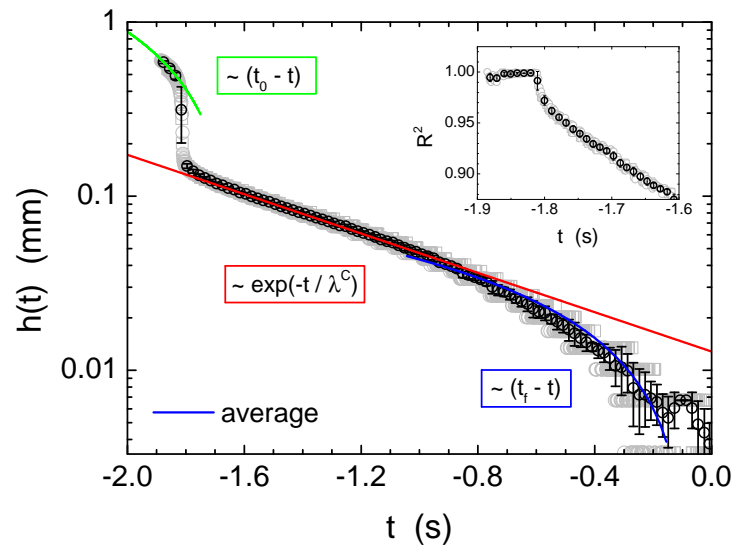


**Figure A.15:** Minimal width  $h(t)$  of the capillary bridge of various P1200<sub>G80</sub> samples during the constriction process in the CaBER experiment, performed at  $\vartheta = 10^\circ\text{C}$ . The exponential section gives the characteristic CaBER relaxation time  $\lambda^C$  according to equation (3.33). The inset presents the coefficient of determination  $R^2$  of a quadratic fit to the filament contour, cf. equation (3.35).

## A.2.5 Taylor-Couette measurements

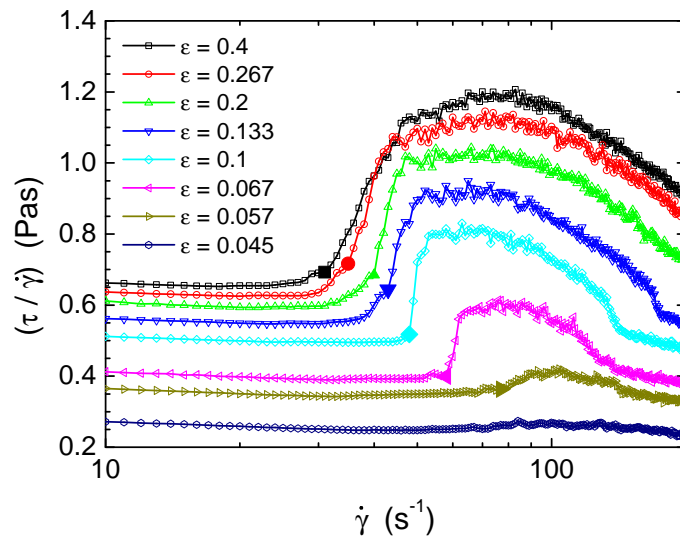


**Figure A.16:** Integral stress data from the Taylor-Couette measurements of the P1200<sub>G80</sub> solution at  $\vartheta = 10^\circ\text{C}$  according to the standard scanning protocol. The different data sets correspond to different values of the relative gap widths  $\varepsilon$  ( $d = 1\text{ mm}$ ). For the sake of a better illustration, the curves are vertically shifted by  $\Delta(\varepsilon) = 20\text{ mPas} \cdot (22 - \varepsilon^{-1})$ . The characteristic transition points are highlighted by filled markers.

## A.3 The P500<sub>S58</sub> polymer solution

### A.3.1 Steady shear rheometry

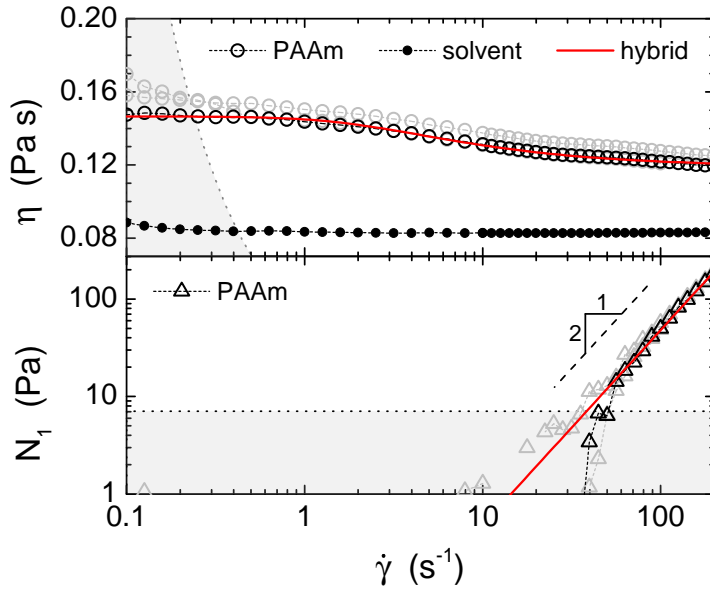


**Figure A.17:** *Top:* Representative (apparent) viscosity  $\eta(\dot{\gamma})$  of the P500<sub>S58</sub> solution (open circles) as well as of the corresponding solvent (filled dots), extracted from steady shear rotational rheometry in the cone-and-plate C60/2° setup at  $\vartheta = 10^\circ\text{C}$ . *Bottom:* Corresponding data of (first) normal stress difference  $N_1(\dot{\gamma})$  (triangles). The red curves refer to an adaption of the 2-component hybrid model according to (3.7) and (3.8).

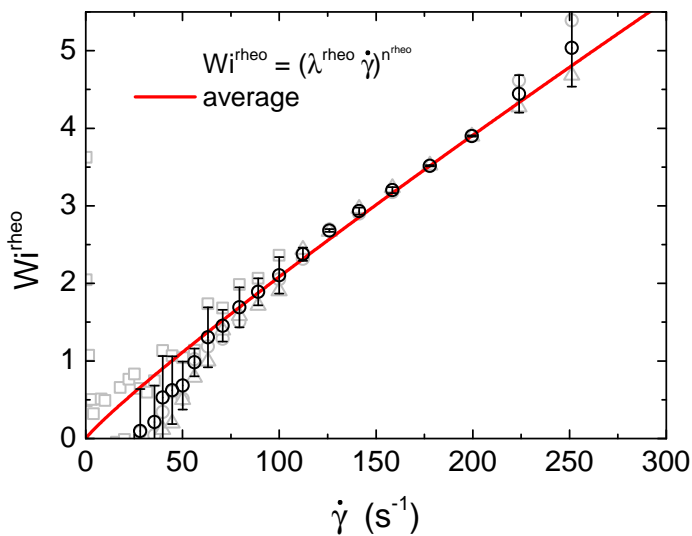


**Figure A.18:** Rheologic Weissenberg number  $Wi^{\text{rheo}}(\dot{\gamma}) = N_1(\dot{\gamma})/2\tau_{12}(\dot{\gamma})$  of the P500<sub>S58</sub> solution, calculated from the steady shear data (cf. figure A.17). The red curve corresponds to a power law fit according to (5.2).

## A.3.2 Shear rate relaxation rheometry

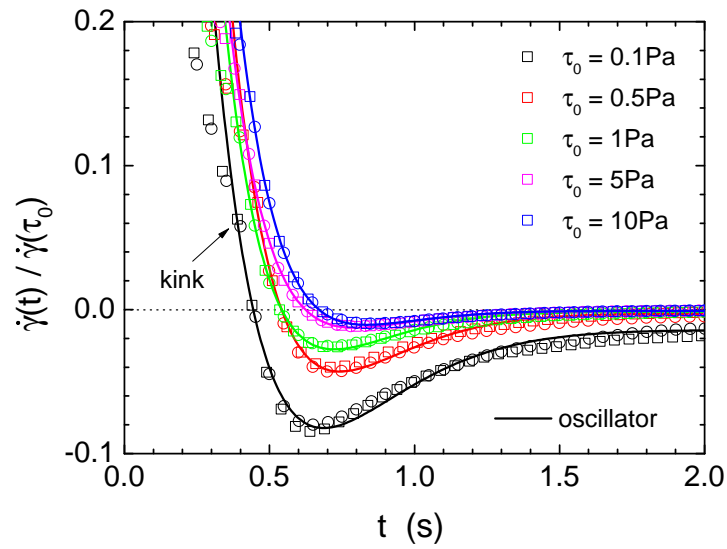


**Figure A.19:** Relaxation of shear rate after sudden cessation of constant shear stress  $\tau_0$  applied to the P500<sub>S58</sub> solution in the cone-and-plate C60/2° setup at  $\vartheta = 10^\circ\text{C}$ . Different curves correspond to different initial shear stresses  $\tau_0$ . The temporal behavior can be described by the viscoelastic, oscillatory recoil of a Jeffreys fluid according to (3.13).

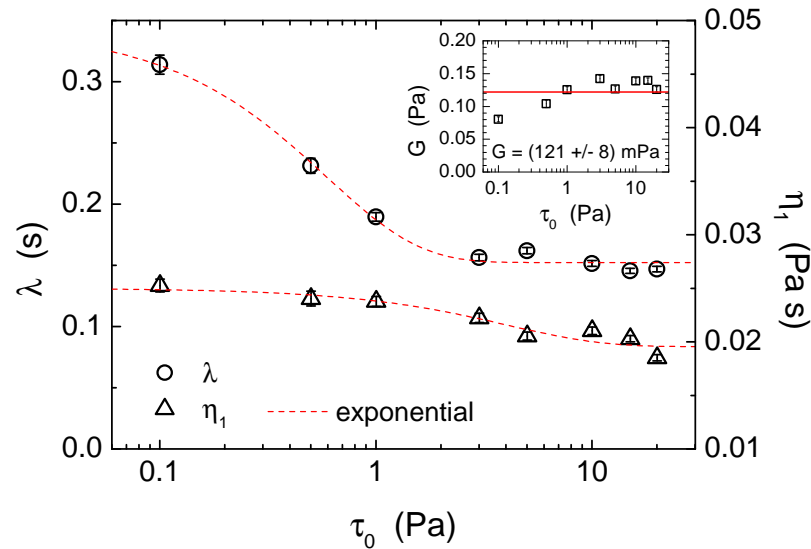


**Figure A.20:** Characteristic relaxation time  $\lambda$  and viscosity  $\eta_1$  of the P500<sub>S58</sub> solution, extracted from the shear rate relaxation data (cf. figure A.19) in dependence of the initially applied shear stress  $\tau_0$  according to (3.13). The shear modulus  $G$  is shown in the inset.

### A.3.3 Small amplitude oscillatory rheometry

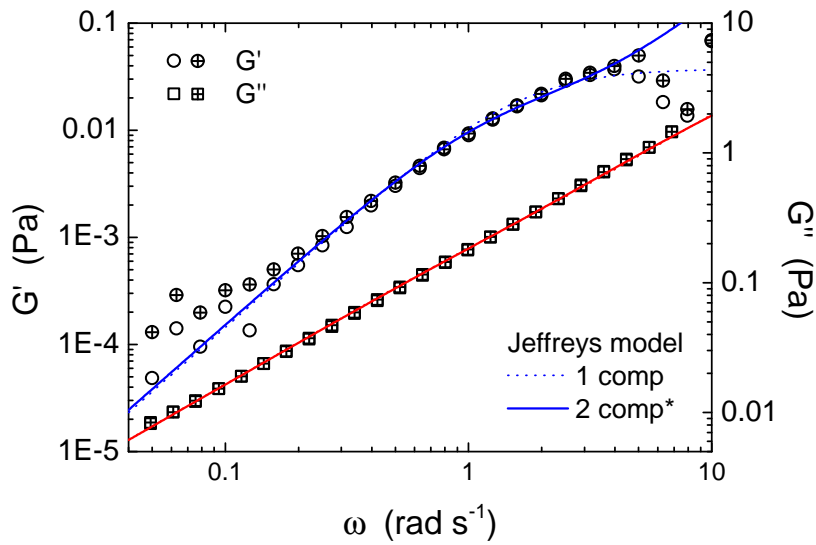


**Figure A.21:** Small amplitude oscillatory shear data of the P500<sub>558</sub> solution at  $\vartheta = 10^\circ\text{C}$  in terms of the real (circles) and imaginary part (squares) of the complex modulus  $G(\omega) = G'(\omega) + iG''(\omega)$ . The curves correspond to different adaptations of the (generalized, multi-component) Jeffreys model (cf. (3.25),(3.26)): one-component (dotted), two-component with fixed solvent contribution  $\eta_2 = \eta_s = 83\text{ mPa s}$  (solid).

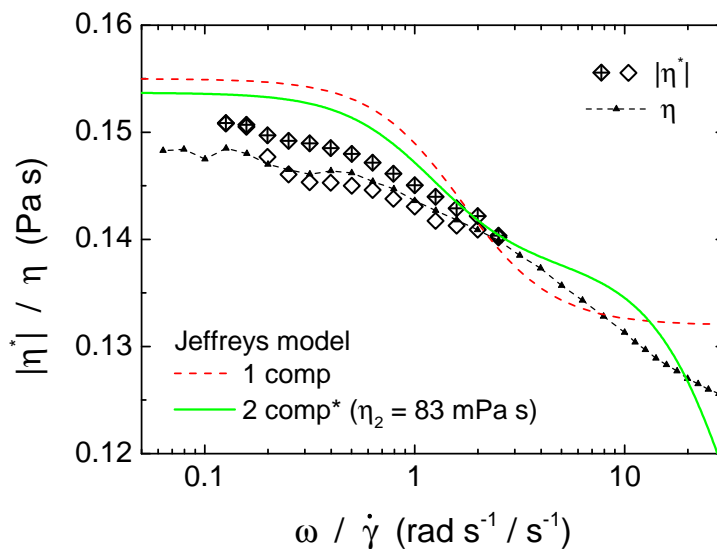


**Figure A.22:** Comparison of small amplitude oscillatory and steady shear data of the P500<sub>558</sub> solution at  $\vartheta = 10^\circ\text{C}$  in terms of the complex viscosity  $|\eta^*(\omega)|$  and the apparent viscosity  $\eta(\dot{\gamma})$ . The red and green curve correspond to the (generalized, multi-component) Jeffreys model based on the parameters extracted from the adaption to the moduli  $G'$  and  $G''$  (cf. figure A.21).

## A.3.4 Capillary breakup extensional rheometry

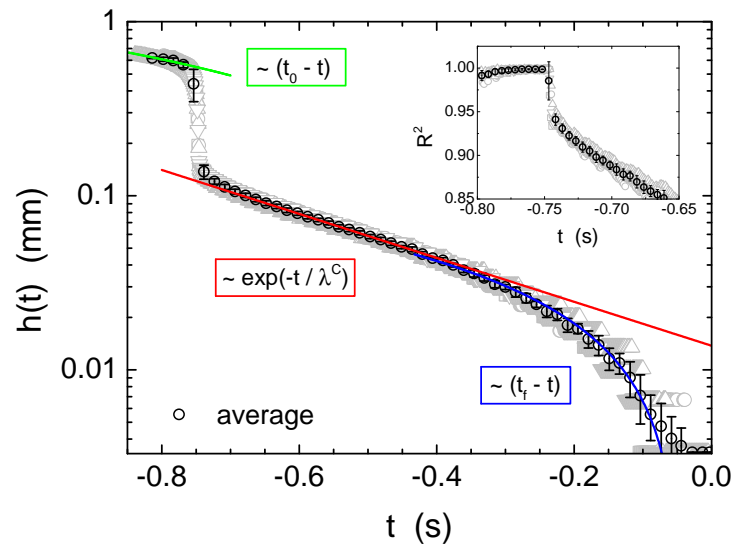


**Figure A.23:** Minimal width  $h(t)$  of the capillary bridge of various P500<sub>S58</sub> samples during the constriction process in the CaBER experiment, performed at  $\vartheta = 10^\circ\text{C}$ . The exponential section gives the characteristic CaBER relaxation time  $\lambda^C$  according to equation (3.33). The inset presents the coefficient of determination  $R^2$  of a quadratic fit to the filament contour, cf. equation (3.35).

## A.3.5 Taylor-Couette measurements

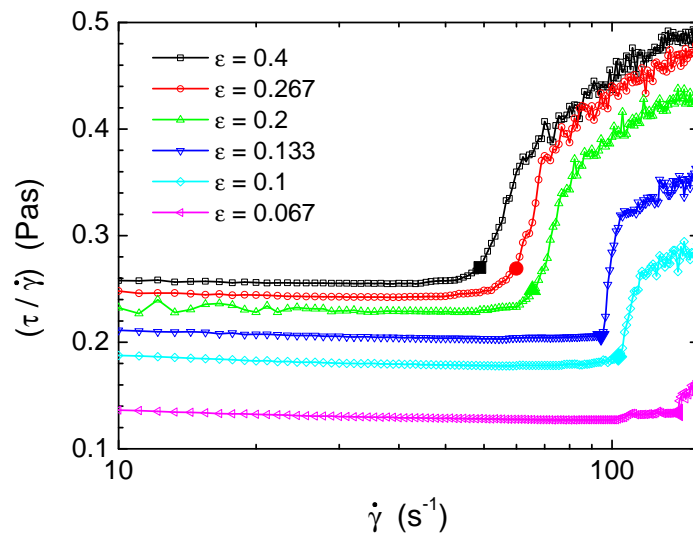


**Figure A.24:** Integral stress data from the Taylor-Couette measurements of the P500<sub>S58</sub> solution at  $\vartheta = 10^\circ\text{C}$  according to the standard scanning protocol. The different data sets correspond to different values of the relative gap widths  $\varepsilon$  ( $d = 1\text{ mm}$ ). For the sake of a better illustration, the curves are vertically shifted by  $\Delta(\varepsilon) = 10\text{ mPas} \cdot (15 - \varepsilon^{-1})$ . The characteristic transition points are highlighted by filled markers.

## A.4 The P80<sub>S64</sub> polymer solution

### A.4.1 Steady shear rheometry

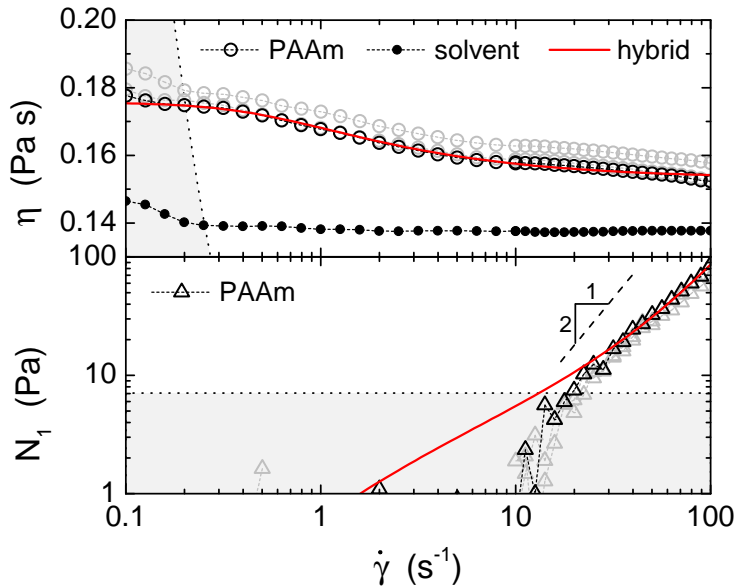


**Figure A.25:** *Top:* Representative (apparent) viscosity  $\eta(\dot{\gamma})$  of the P80<sub>S64</sub> solution (open circles) as well as of the corresponding solvent (filled dots), extracted from steady shear rotational rheometry in the cone-and-plate C60/2° setup at  $\vartheta = 22^\circ\text{C}$ . *Bottom:* Corresponding data of (first) normal stress difference  $N_1(\dot{\gamma})$  (triangles). The red curves refer to an adaption of the 2-component hybrid model according to (3.7) and (3.8).

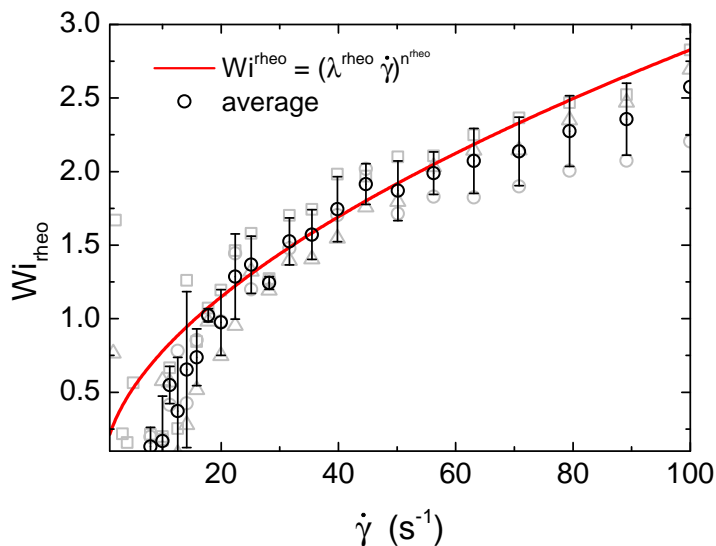


**Figure A.26:** Rheologic Weissenberg number  $Wi^{\text{rheo}}(\dot{\gamma}) = N_1(\dot{\gamma})/2\tau_{12}(\dot{\gamma})$  of the P80<sub>S64</sub> solution, calculated from the steady shear data (cf. figure A.25). The red curve corresponds to a power law fit according to (5.2).

## A.4.2 Shear rate relaxation rheometry

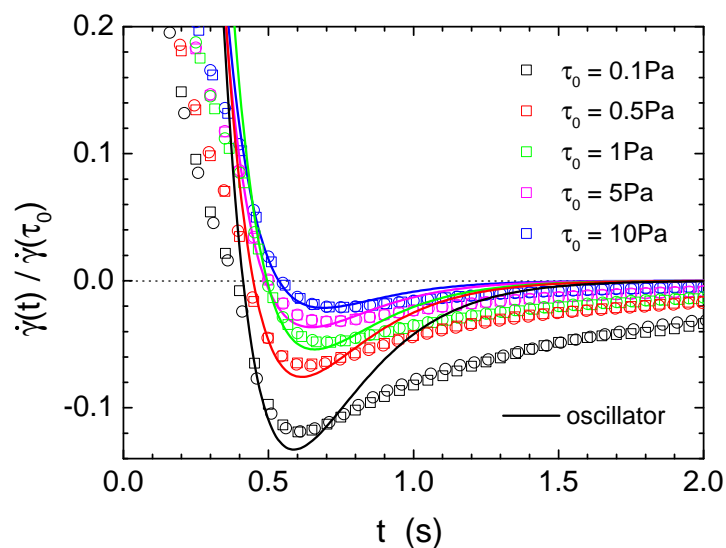


**Figure A.27:** Relaxation of shear rate after sudden cessation of constant shear stress  $\tau_0$  applied to the P80<sub>S64</sub> solution in the cone-and-plate C60/2° setup at  $\vartheta = 22^\circ\text{C}$ . Different curves correspond to different initial shear stresses  $\tau_0$ . The temporal behavior can be described by the viscoelastic, oscillatory recoil of a Jeffreys fluid according to (3.13).

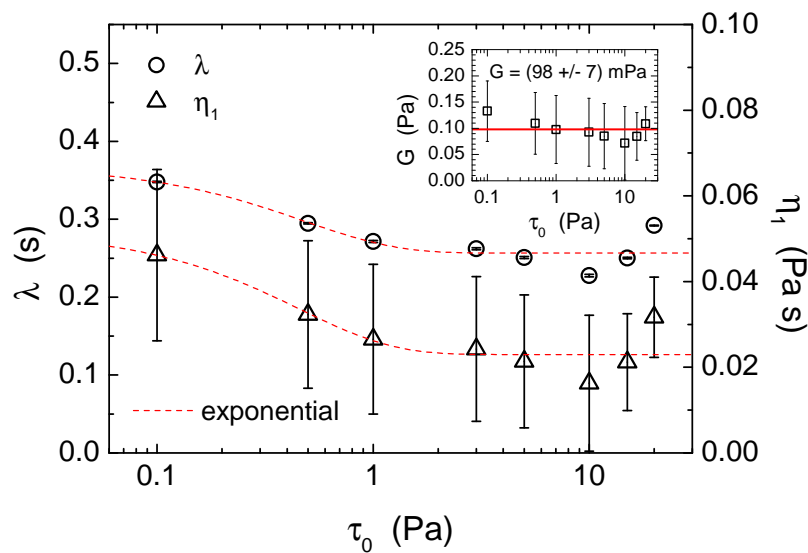


**Figure A.28:** Characteristic relaxation time  $\lambda$  and viscosity  $\eta_1$  of the P80<sub>S64</sub> solution, extracted from the shear rate relaxation data (cf. figure A.27) in dependence of the initially applied shear stress  $\tau_0$  according to (3.13). The shear modulus  $G$  is shown in the inset.

### A.4.3 Small amplitude oscillatory rheometry

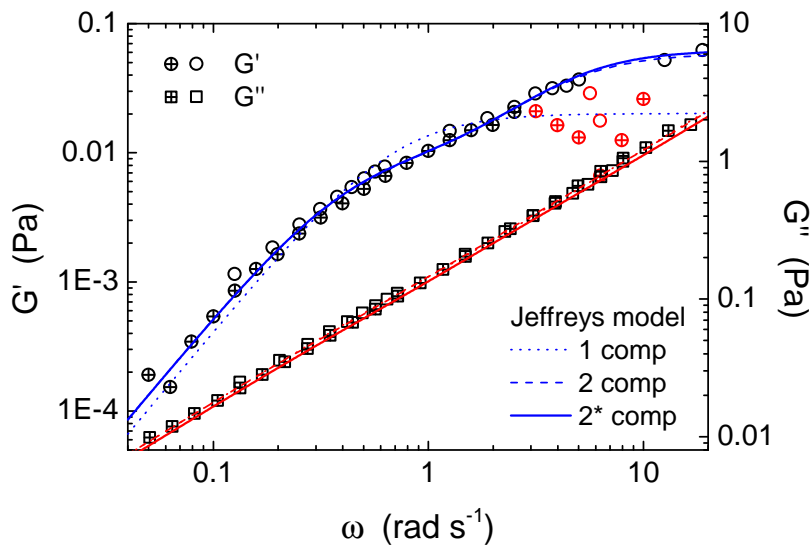


**Figure A.29:** Small amplitude oscillatory shear data of the P80<sub>S64</sub> solution at  $\vartheta = 22^\circ\text{C}$  in terms of the real (circles) and imaginary part (squares) of the complex modulus  $G(\omega) = G'(\omega) + iG''(\omega)$ . The curves correspond to different adaptations of the (generalized, multi-component) Jeffreys model (cf. (3.25),(3.26)): one-component (dotted), two-component (dashed), two-component with fixed solvent contribution  $\eta_2 = \eta_s = 140 \text{ mPa s}$  (solid).

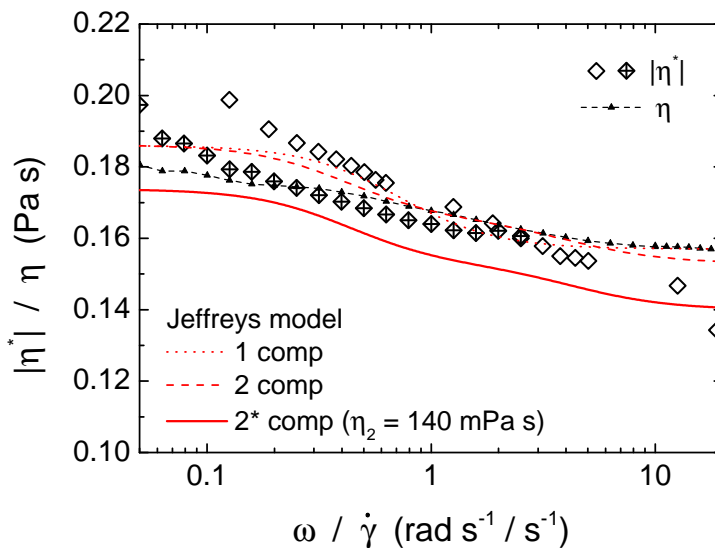


**Figure A.30:** Comparison of small amplitude oscillatory and steady shear data of the P80<sub>S64</sub> solution at  $\vartheta = 22^\circ\text{C}$  in terms of the complex viscosity  $|\eta^*(\omega)|$  and the apparent viscosity  $\eta(\dot{\gamma})$ . The red and green curve correspond to the (generalized, multi-component) Jeffreys model based on the parameters extracted from the adaption to the moduli  $G'$  and  $G''$  (cf. figure A.29).

## A.4.4 Capillary breakup extensional rheometry

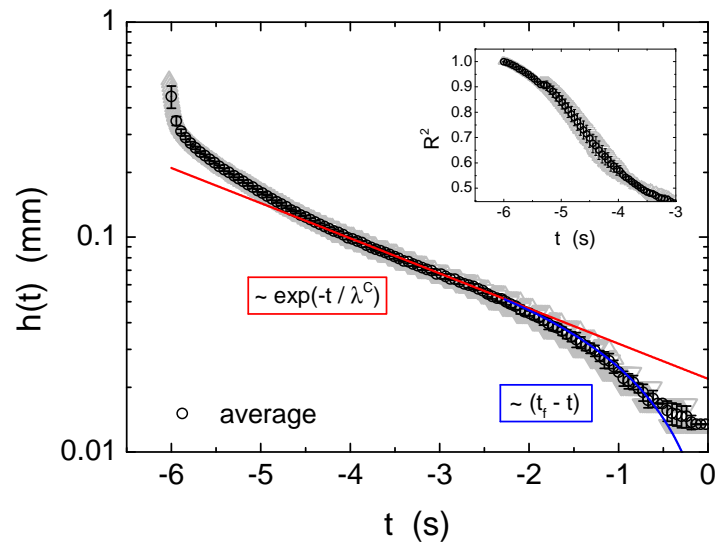


**Figure A.31:** Minimal width  $h(t)$  of the capillary bridge of various P80<sub>S64</sub> samples during the constriction process in the CaBER experiment, performed at  $\vartheta = 22^\circ\text{C}$ . The exponential section gives the characteristic CaBER relaxation time  $\lambda^C$  according to equation (3.33). The inset presents the coefficient of determination  $R^2$  of a quadratic fit to the filament contour, cf. equation (3.35).

## A.4.5 Taylor-Couette measurements

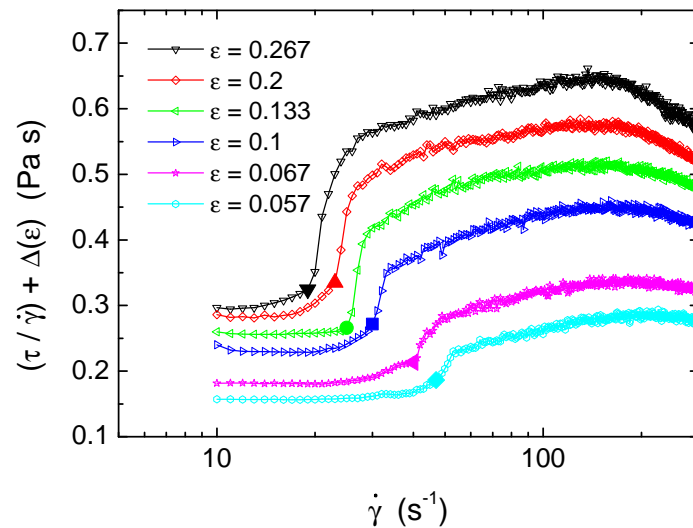


**Figure A.32:** Integral stress data from the Taylor-Couette measurements of the P80<sub>S64</sub> solution at  $\vartheta = 22^\circ\text{C}$  according to the standard scanning protocol. The different data sets correspond to different values of the relative gap widths  $\varepsilon$  ( $d = 1\text{ mm}$ ). For the sake of a better illustration, the curves are vertically shifted by  $\Delta(\varepsilon) = 10\text{ mPa}\cdot\text{s} \cdot (17.5 - \varepsilon^{-1})$ . The characteristic transition points are highlighted by filled markers.

## A.5 The P150<sub>S65.6</sub> polymer solution

### A.5.1 Steady shear rheometry

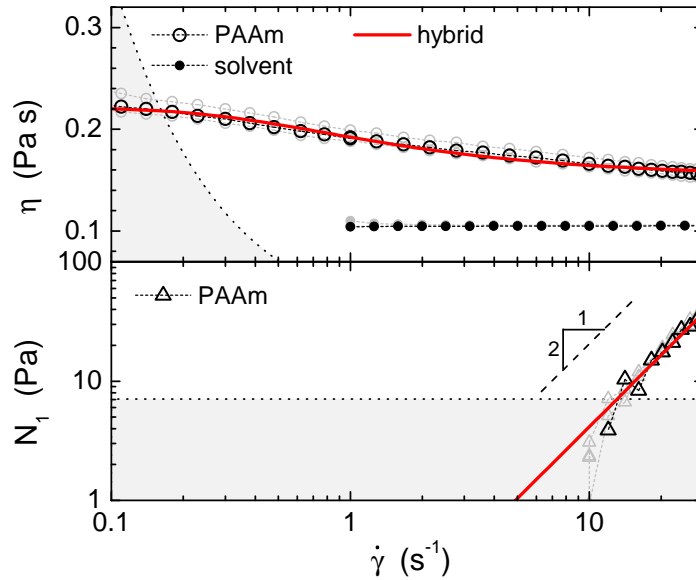


**Figure A.33:** *Top:* Representative (apparent) viscosity  $\eta(\dot{\gamma})$  of the P150<sub>S65.6</sub> solution (open circles) as well as of the corresponding solvent (filled dots), extracted from steady shear rotational rheometry in the cone-and-plate C60/2° setup at  $\vartheta = 23^\circ\text{C}$ . *Bottom:* Corresponding data of (first) normal stress difference  $N_1(\dot{\gamma})$  (triangles). The red curves refer to an adaption of the 2-component hybrid model according to (3.7) and (3.8).

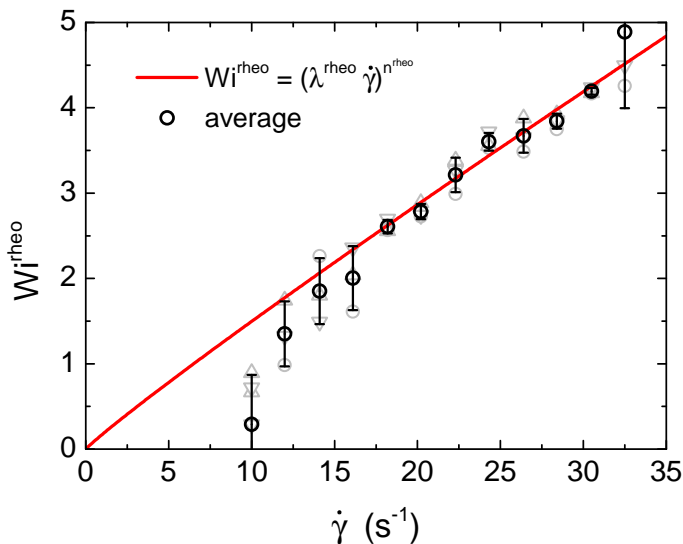


**Figure A.34:** Rheologic Weissenberg number  $Wi^{\text{rheo}}(\dot{\gamma}) = N_1(\dot{\gamma})/2\tau_{12}(\dot{\gamma})$  of the P150<sub>S65.6</sub> solution, calculated from the steady shear data (cf. figure A.33). The red curve corresponds to a power law fit according to (5.2).

## A.5.2 Shear rate relaxation rheometry

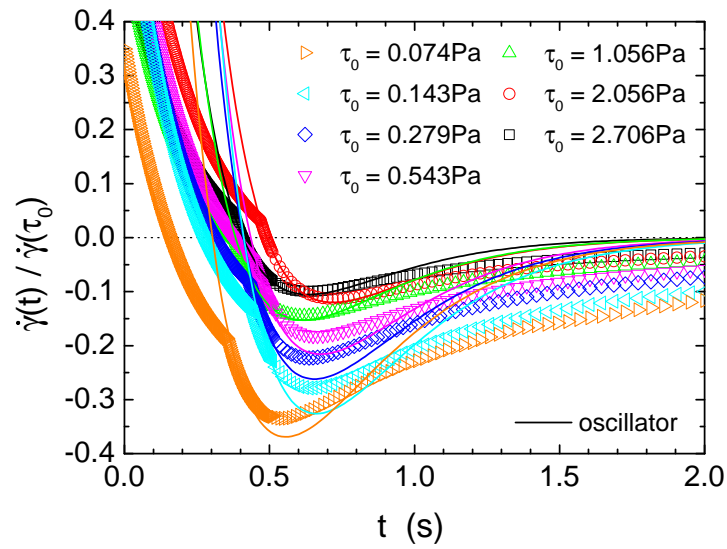


**Figure A.35:** Relaxation of shear rate after sudden cessation of constant shear stress  $\tau_0$  applied to the P150<sub>S65.6</sub> solution in the cone-and-plate C60/2° setup at  $\vartheta = 23^\circ\text{C}$ . Different curves correspond to different initial shear stresses  $\tau_0$ . The temporal behavior can be described by the viscoelastic, oscillatory recoil of a Jeffreys fluid according to (3.13).

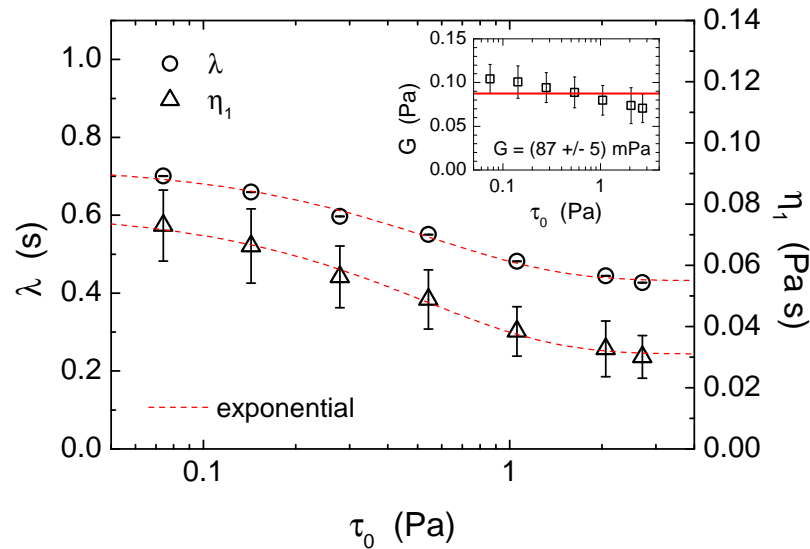


**Figure A.36:** Characteristic relaxation time  $\lambda$  and viscosity  $\eta_1$  of the P150<sub>S65.6</sub> solution, extracted from the shear rate relaxation data (cf. figure A.35) in dependence of the initially applied shear stress  $\tau_0$  according to (3.13). The shear modulus  $G$  is shown in the inset.

### A.5.3 Capillary breakup extensional rheometry

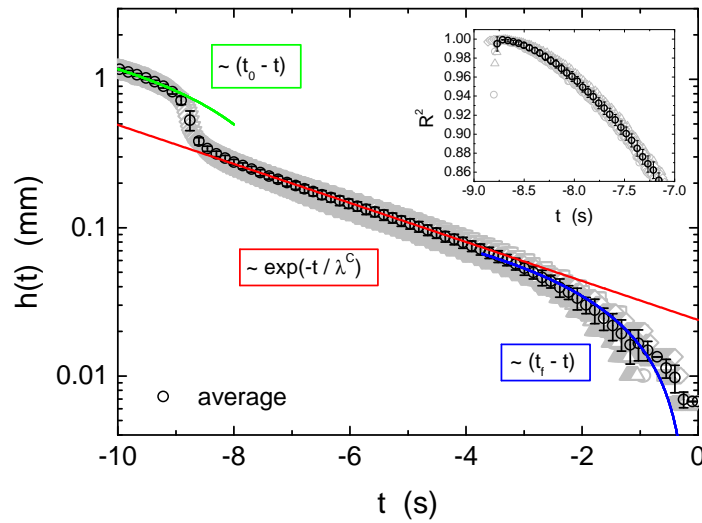


**Figure A.37:** Minimal width  $h(t)$  of the capillary bridge of various P150<sub>S65.6</sub> samples during the constriction process in the CaBER experiment, performed at  $\vartheta = 23^\circ\text{C}$ . The exponential section gives the characteristic CaBER relaxation time  $\lambda^C$  according to equation (3.33). The inset presents the coefficient of determination  $R^2$  of a quadratic fit to the filament contour, cf. equation (3.35).

### A.5.4 Taylor-Couette measurements

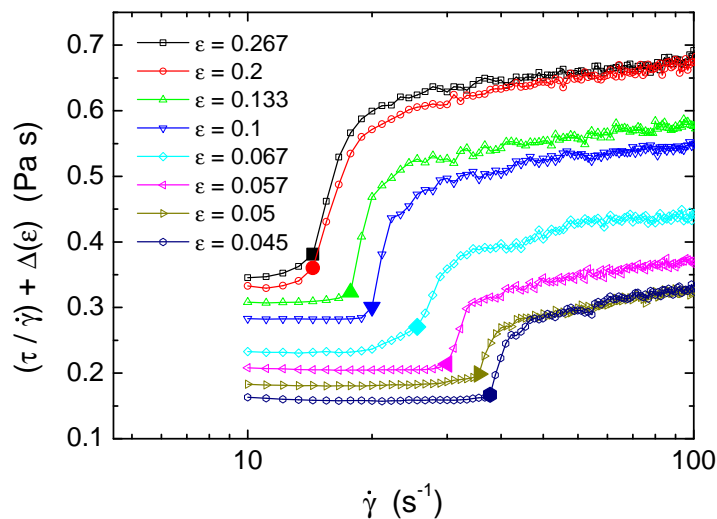


**Figure A.38:** Integral stress data from the Taylor-Couette measurements of the P150<sub>S65.6</sub> solution at  $\vartheta = 23^\circ\text{C}$  according to the standard scanning protocol. The different data sets correspond to different values of the relative gap widths  $\varepsilon$  ( $d = 1\text{ mm}$ ). For the sake of a better illustration, the curves are vertically shifted by  $\Delta(\varepsilon) = 10\text{ mPa s} \cdot (22 - \varepsilon^{-1})$ . The characteristic transition points are highlighted by filled markers.

## Mathematics

### B.1 Pseudospectral Chebyshev collocation method

To solve the generalized eigenvalue problem (9.37) numerically, we make use of the so-called pseudospectral Chebyshev collocation method. Spectral methods are based on the idea of approximating functions (e.g. the solutions of (partial) differential equations) by means of truncated series of orthogonal functions (e.g. polynomials in the present case) [Ghe07].

#### B.1.1 Chebyshev polynomials

One special choice of orthogonal functions are the Chebyshev polynomials  $\{T_n(x)\}_{n \in \mathbb{N}}$  of the first kind. They are defined by

$$T_n(x) := \cos(n \arccos(x)), \quad x \in I = [-1, 1] \quad (\text{B.1})$$

Using elementary relationships between algebraic and trigonometric polynomials, one can write

$$T_n(x) = \sum_{k=0}^{l(n)} (-1)^k \binom{n}{2k} x^{n-2k} (1-x^2)^k, \quad l(n) = \lfloor \frac{n}{2} \rfloor = \begin{cases} \frac{n}{2} & , \quad n \text{ even} \\ \frac{n-1}{2} & , \quad n \text{ uneven} \end{cases} \quad (\text{B.2})$$

Consequently, the Chebyshev polynomial  $T_n(x)$  is a polynomial of degree  $n$ . Table B.1 lists the Chebyshev polynomials for  $n = 0, 1, \dots, 7$  that are shown in figure B.1.

#### B.1.2 Chebyshev series

The set  $\{T_n(x)\}_{n \in \mathbb{N}}$  gives a complete orthogonal basis for the space  $L^2_w(I)$  with

$$L^2_w := \{f : I \rightarrow \mathbb{R} \mid f \text{ Lebesgue measurable and } \|f\|_w < \infty\} \quad (\text{B.3})$$

where the weighted inner product

$$(f, g)_w := \int_{-1}^1 f(x)g(x)w(x)dx \quad (\text{B.4})$$

induces the (weighted) norm

$$\|f\|_w = \sqrt{(f, f)_w} \quad (\text{B.5})$$

with respect to the weight function

$$w(x) = \frac{1}{\sqrt{1-x^2}}. \quad (\text{B.6})$$

$n$	$T_n(x)$
0	1
1	$x$
2	$2x^2 - 1$
3	$4x^3 - 3x$
4	$8x^4 - 8x^2 + 1$
5	$16x^5 - 20x^3 + 5x$
6	$32x^6 - 48x^4 + 18x^2 - 1$
7	$64x^7 - 112x^5 + 56x^3 - 7x$

**Table B.1:** Chebyshev polynomials  $T_n(x)$  of the first kind for  $n = 0, 1, \dots, 7$ .

Thus, each and every function  $f \in L_w^2(I)$  can be expanded in a Chebyshev series by

$$f(x) = \sum'_{k=0}^{\infty} a_k T_k(x) \quad (\text{B.7})$$

with coefficients

$$a_k = \frac{2}{\pi} (f, T_k)_w. \quad (\text{B.8})$$

Here,  $\sum'$  denotes that the first term is weighted by one half.

By applying the mapping  $x = \cos(\theta)$ , one can identify the Chebyshev series of the function  $f(x)$ ,  $x \in [-1; 1]$  as the Fourier series of the corresponding function  $h(\theta) := f(\cos(\theta)) = f(x)$ ; since  $h$  is periodic  $h(\theta) = h(\theta + 2\pi)$  and symmetric  $h(\theta) = h(-\theta)$  it takes the form

$$f(\cos(\theta)) = h(\theta) = \frac{a_0}{2} + \sum_{k=1}^{\infty} a_k \cos(k\theta), \quad (\text{B.9})$$

$$a_k = \frac{2}{\pi} \int_0^{\pi} h(\theta) \cos(k\theta) d\theta. \quad (\text{B.10})$$

With (B.1), this transforms to

$$h(\theta) = f(x) = \frac{a_0}{2} + \sum_{k=1}^{\infty} a_k \cos(k \arccos(x)) \quad (\text{B.11})$$

$$= \sum'_{k=0}^{\infty} a_k T_k(x), \quad (\text{B.12})$$

$$a_k = \frac{2}{\pi} \int_{-1}^{-1} f(x) T_k(x) \frac{-dx}{\sin(\arccos(x))} \quad (\text{B.13})$$

$$= \frac{2}{\pi} \int_{-1}^1 \frac{1}{\sqrt{1-x^2}} f(x) T_k(x) dx \quad (\text{B.14})$$

$$= \frac{2}{\pi} (f, T_k)_w. \quad (\text{B.15})$$

Thus, one can take the coefficients of  $f(x)$  of a Chebyshev series as the Fourier cosine coefficients of  $f(\cos(\theta))$ . Consequently, even if  $f$  is not a periodic function in  $x$ ,  $f(\cos(\theta))$  must be periodic in  $\theta$  and the exponential convergence of the Fourier series implies an equally

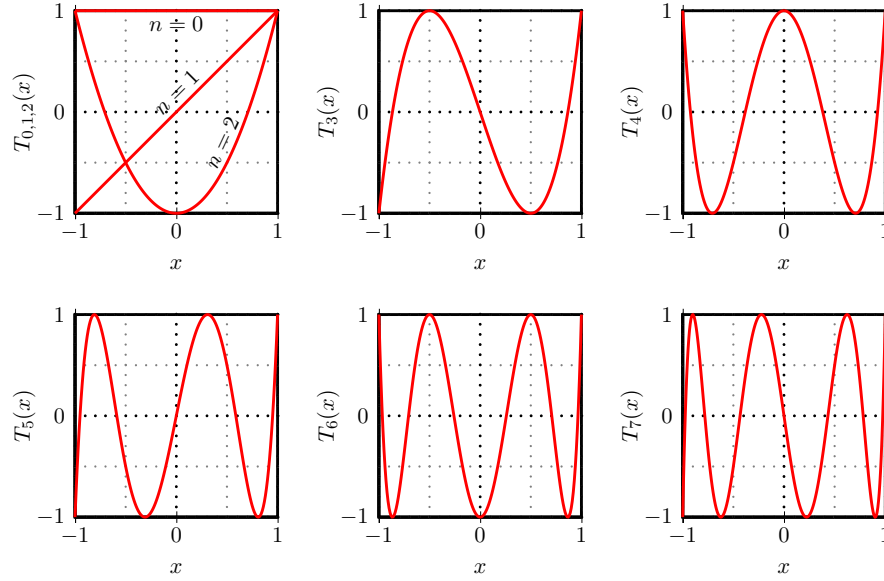


**Figure B.1:** Plots of the Chebyshev polynomials of the first kind for  $n = 0, 1, \dots, 7$ .

fast convergence of the Chebyshev series [Boy00]. Thus, the expansion to a Chebyshev series overcomes the problem of a “terminal discontinuity” in case of non-periodicity of  $f$ , which limits the convergence of the Fourier series in terms of remaining, non-zero mismatches even when  $N \rightarrow \infty$  (cf. to the Gibbs’ Phenomenon [Boy00, Ghe07]).

Adopting its properties from the Fourier series, the Chebyshev series (B.7)–(B.8) represents a least square approximation of the function  $f$  on the interval  $[-1, 1]$  with respect to the weight function (B.6), i.e.

$$\min \int_{-1}^1 w(x) \cdot \underbrace{[f(x) - f_N(x)]^2}_{R_N(x)} dx \quad (\text{B.16})$$

with

$$f_N(x) = \sum_{k=0}^N a_k T_k(x). \quad (\text{B.17})$$

Thus, in terms of a polynomial representation of  $f$  ( $f_N(x)$  is a polynomial of order  $N$ ), the (truncated) Chebyshev series (B.17) is the optimal representation of  $f$  with respect to the optimization (B.16).

### B.1.3 Gaussian quadrature rule and Gauss-Lobatto points

In general, it is not possible to calculate the expansion coefficients by analytical integration according to equation B.8. Thus, one has to find an approximation of the integral in form of a (weighted) sum, which leads to the well-known Gaussian quadrature rule. According to this, there is a suitable choice of quadrature points  $x_j$  and corresponding quadrature weights  $w_j$  for  $j = 0, 1, \dots, N$ , which give the exact relation

$$\int_{-1}^1 w(x) f(x) dx = \sum_{j=0}^N w_j f(x_j) \quad (\text{B.18})$$

for any arbitrary polynomial  $f(x) = q_{2N+1}(x)$  of order  $2N+1$ . Thereby, the quadrature points have to be chosen as the  $N+1$  roots of a polynomial  $p_{N+1}(x)$  of order  $N+1$  from a set of orthogonal polynomials which obeys

$$(p_n, p_m)_w = \delta_{n,m} \|p_n\|^2. \quad (\text{B.19})$$

Obviously, with the weight function  $w(x) = (1-x^2)^{-0.5}$  the Chebyshev polynomials are an appropriate choice and the roots

$$x_k = \cos\left(\frac{(2k+1)\pi}{2(N+1)}\right), \quad k = 0, \dots, N \quad (\text{B.20})$$

of  $p_{N+1}(x) = T_{N+1}(x)$  give the corresponding quadrature points. With the weights  $w_j = \pi/(N+1)$ , this is called the Chebyshev-Gauss quadrature and it is exact for polynomials of degree  $\leq 2N+1$ . However, this method does not include the boundaries  $x = \pm 1$  as quadrature points. To include these, which is favorable, inter alia in order to implement respective boundary conditions, one can alternatively use the roots of the function  $(1-x^2)p'_N(x)$ , which are given by

$$x_j^{GL} = \cos\left(\frac{j\pi}{N}\right), \quad j = 0, \dots, N. \quad (\text{B.21})$$

They are called the *Gauss-Lobatto points* and with the weights

$$w_j^{GL} = \begin{cases} \frac{\pi}{2N} & : \quad j = 0, N \\ \frac{\pi}{N} & : \quad 1 \leq j \leq N-1 \end{cases} \quad (\text{B.22})$$

we accordingly refer to the *Gauss-Lobatto quadrature* which is exact for polynomials up to order  $2N-1$ .

### B.1.4 Chebyshev collocation method

Collocation methods belong to the weighted residual methods for the determination of a function  $\tilde{u}_N$  which approximates the (in general unknown) exact solution  $u$  of a problem at hand [Fai99]. It demands a vanishing weighted residual

$$\int_I w_j(x) R_N(x) dx = \int_I w_j(x) [u(x) - \tilde{u}_N(x)] dx = 0, \quad j = 0, \dots, N \quad (\text{B.23})$$

with the computational domain  $I$  and weight functions  $w_j(x)$ . A collocation method is established by the special weight function  $w_j = \delta(x - x_j)$ , i.e. the approximate function  $\tilde{u}_N$  *interpolates* the exact solution at a discrete set of  $N+1$  collocation/interpolation points<sup>1</sup>  $\{x_j\}$ :  $\tilde{u}_N(x_j) = u(x_j)$ ,  $j = 0, 1, \dots, N$ . Recalling the expansion (B.17) and making use of the Gauss-Lobatto quadrature (B.18), (B.22), we can formulate an optimal interpolation polynomial

$$u_N(x) = \sum_{k=0}^N a_k T_k(x) \quad (\text{B.24})$$

with coefficients

$$a_k = \frac{2}{\pi} \int_{-1}^1 \frac{1}{\sqrt{1-x^2}} f(x) T_k(x) dx = \frac{2}{N} \sum_{l=0}^N u(x_l^{GL}) T_k(x_l^{GL}), \quad (\text{B.25})$$

<sup>1</sup>While the terminology “collocation points” is applied to interpolatory methods for solving differential equations for an unknown function  $u$ , “interpolation points” rather refers to the interpolation of an already known function [Boy00].

which interpolates the function  $u(x)$  at the Gauss-Lobatto points  $x_j^{GL}$ , i.e.

$$u(x_j^{GL}) = u_N(x_j^{GL}) = \sum_{k=0}^N a_k T_k(x_j^{GL}). \quad (\text{B.26})$$

Here, the notation  $\sum_{l=0}^N$  demands to take the half of the first ( $l = 0$ ) and last ( $l = N$ ) addend.

### B.1.5 Collocation derivative operator

The truncated Chebyshev series (B.26) constructs an interpolant polynomial in terms of the values of  $u(x)$  at the Gauss-Lobatto collocation points  $\{x_j^{GL}\}$ . Based on this polynomial, one can formulate an approximation of the local spacial derivatives at the collocation points by exact differentiation of the interpolate [Ghe07]. It can be written in the form of a matrix-vector multiplication

$$\left. \frac{du_N}{dx} \right|_{x=x_j^{GL}} = \sum_{k=0}^N D_{jk}^{(1)} u(x_k^{GL}) \quad (\text{B.27})$$

with the matrix (Chebyshev collocation derivative)

$$D_{jk}^{(1)} = \begin{cases} \frac{2N^2+1}{6}, & j = k = 0 \\ -\frac{2N^2+1}{6}, & j = k = N \\ \frac{c_j}{c_k} \frac{(-1)^{j+k}}{(x_j - x_k)}, & j \neq k \wedge j, k \notin \{0, N\} \\ -\frac{x_j}{2(1-x_j^2)}, & j = k \wedge j, k \notin \{0, N\} \end{cases} \quad (\text{B.28})$$

and

$$c_j = \begin{cases} 2 & : j \in \{0, N\} \\ 1 & : 1 \leq j \leq N-1 \end{cases}. \quad (\text{B.29})$$

Similarly, higher-order derivatives are calculated by

$$\left. \frac{d^n u_N}{dx^n} \right|_{x=x_j^{GL}} = \sum_{k=0}^N D_{jk}^{(n)} u(x_k^{GL}) \quad (\text{B.30})$$

with

$$D^{(n)} = \left( D^{(1)} \right)^n, \quad n = 1, 2, \dots \quad (\text{B.31})$$

Consequently, using the pseudospectral Chebyshev collocation method, a differential equation with solution  $u(x)$  can be translated to a set of algebraic equations for the discrete set of values  $u_k$  at the collocation points  $x_k$ , which can be solved by standard methods of linear algebra. Boundary conditions are implemented by simple manipulation of the algebraic equations.



---

## Publications

Appendix C comprises reprints of three selected publications to which the author significantly contributed. They deal with diverse non-Newtonian flow phenomena and associated flow instabilities.

### **C.1 Serpentine channels: micro-rheometers for fluid relaxation times [Zil14]**

As we could further confirm by our foregoing study on viscoelastic Taylor-Couette flow, the onset of (purely) elastic instability in viscoelastic curvilinear flow is predictable by means of the dimensionless criterion by Pakdel and McKinley.

Another system which adds to the collection of curved flow geometries which have proven to be described by the Pakdel-McKinley criterion in consistent agreement with numerical considerations is the curvilinear serpentine channel [Zil12]. In a supplementary study of which final results are presented in a recent publication [Zil14] (cf. the reprint on the following pages, reproduced by permission of The Royal Society of Chemistry), the authors propose the use of this curvilinear serpentine channel in a novel rheometric device with which it is possible to measure explicitly small relaxation times, thereby extending the range of classical rheometers. It is based on the detection of the onset of elastic instability which is finally mapped to the characteristic relaxation time of the investigated fluid.

The required thorough calibration of the device by means of reliable relaxation times obtained by steady shear normal stress data constitutes the author's contribution to this study.



# Lab on a Chip

## PAPER

View Article Online  
View Journal | View Issue

### Serpentine channels: micro-rheometers for fluid relaxation times

Cite this: *Lab Chip*, 2014, 14, 351

Josephine Zilz,<sup>a</sup> Christof Schäfer,<sup>b</sup> Christian Wagner,<sup>b</sup> Robert J. Poole,<sup>c</sup> Manuel A. Alves<sup>d</sup> and Anke Lindner<sup>\*a</sup>

We propose a novel device capable of measuring relaxation times of viscoelastic fluids as small as 1 ms. In contrast to most rheometers, which by their very nature are concerned with producing viscometric or nearly-viscometric flows, here we make use of an elastic instability that occurs in the flow of viscoelastic fluids with curved streamlines. To calibrate the rheometer we combine simple scaling arguments with relaxation times obtained from first normal-stress difference data measured in a classical shear rheometer. As an additional check we also compare these relaxation times to those obtained from Zimm theory and good agreement is observed. Once calibrated, we show how the serpentine rheometer can be used to access smaller polymer concentrations and lower solvent viscosities where classical measurements become difficult or impossible to use due to inertial and/or resolution limitations. In the absence of calibration, the serpentine channel can still be a very useful comparative or index device.

Received 8th July 2013,  
Accepted 30th September 2013

DOI: 10.1039/c3lc50809a

www.rsc.org/loc

## 1. Introduction

Polymer solutions of long and flexible polymers are known to exhibit striking non-Newtonian properties even at very small concentrations.<sup>1</sup> For example, in turbulent pipe or channel flow the friction factor (or drag) may be significantly reduced by adding a polymer at concentrations as low as a few ppm<sup>2</sup> (parts per million in weight). Such fluids are also used in enhanced oil recovery applications.<sup>3</sup> Measuring their rheological features is a challenging task and classical rheometry is often at its limits when determining for example the relaxation times of such dilute polymer solutions.<sup>4</sup>

Here we develop a microfluidic rheometer with a complex flow geometry to overcome these difficulties. Although a number of microfluidic rheometers have been proposed, most of these devices are restricted to measurements of shear viscosity,<sup>5–11</sup> although devices which attempt to estimate extensional viscosity<sup>12–16</sup> and dynamic properties<sup>17</sup> have also been proposed. In contrast to these previous microfluidic devices, in the current study we make use of an elastic instability,<sup>18–26</sup> which occurs in flows of viscoelastic fluids with curved streamlines even in the absence of inertia.<sup>20,21</sup> The

threshold of instability depends on the curvature of the flow and the fluid elasticity,<sup>27</sup> described by the Weissenberg number. Typically, viscoelastic effects will be observed when the product of a fluid relaxation time ( $\lambda$ ) and a characteristic shear rate reaches order one. Thus for fluids with  $\lambda$  on the order of milliseconds, shear rates on the order of  $10^3 \text{ s}^{-1}$  are required to access such viscoelastic effects. The use of a microfluidic device enables high shear rates to be obtained and thus strong viscoelastic effects (corresponding to large Weissenberg numbers) to be observed while keeping inertial effects, and hence the Reynolds number, small.

We have recently investigated the flow in a serpentine micro-channel to elucidate the scaling of the instability threshold with the flow curvature using a dilute polymer solution.<sup>28</sup> We have shown that the instability is very sensitive to even small normal-stress differences and can thus be used to detect their occurrence. We can now combine our precise knowledge regarding the dependence of the instability onset on the flow curvature with a precise knowledge of the rheological properties of a calibrating fluid to quantitatively measure relaxation times. To do so, we initially calibrate the serpentine rheometer using classical shear rheometry in the range of parameters accessible by this technology. The serpentine rheometer can then be used with fluids of smaller concentrations or lower solvent viscosities, where classical rheometry techniques become difficult either due to inertial instabilities or instrument resolution issues. Even when a precise calibration is not possible, the serpentine channel can be used as a comparative rheometer to compare the rheological

<sup>a</sup> PMMH, ESPCI, UPMC, Univ. Paris-Diderot, CNRS UMR 7636 10, rue Vauquelin, F-75231 Paris Cedex 05, France. E-mail: anke.lindner@espci.fr

<sup>b</sup> Experimentalphysik, Saarland University, D-66123, Saarbrücken, Germany

<sup>c</sup> School of Engineering, University of Liverpool, Brownlow Hill, Liverpool, L69 3GH, UK

<sup>d</sup> Departamento de Engenharia Química, Faculdade de Engenharia da Universidade do Porto, Rua Dr. Roberto Frias, 4200-465 Porto, Portugal



Paper

View Article Online

Lab on a Chip

properties of two given fluids. Finally we propose methods to fully integrate the serpentine channel into a microfluidic lab-on-a-chip device capable of measuring both shear viscosity and fluid relaxation time.

## 2. Scaling of the onset of elastic instability in a serpentine channel

Pakdel and McKinley<sup>21,27</sup> proposed a simple dimensionless criterion that must be exceeded for the onset of purely-elastic instability, combining the curvature of the flow and the tensile stress ( $\tau_{11}$ ) acting along the streamlines, in the following form:

$$\left[ \frac{\tau_{11}}{\eta \dot{\gamma}} \frac{\lambda u}{\mathcal{R}} \right] \geq M_{\text{crit}}^2 \quad (1)$$

with  $\mathcal{R}$ ,  $u$  and  $\dot{\gamma}$  representing the local streamline radius of curvature, velocity magnitude and shear rate, respectively.  $\tau_{11}$  represents the local streamwise normal-stress and  $\eta \dot{\gamma}$  the local shear stress, with  $\eta$  being the shear viscosity. The ratio  $\tau_{11}/\eta \dot{\gamma}$  thus represents a local Weissenberg number ( $Wi$ ), comparing normal stresses to shear stresses and  $\lambda u/\mathcal{R}$  compares a typical distance over which a polymer relaxes to the radius of curvature (or can be viewed as a local Deborah number).

We have recently elucidated the geometrical scaling for the onset of elastic-flow instability in a serpentine channel by adapting the Pakdel–McKinley criterion to the specific flow geometry.<sup>28</sup> The serpentine channel is composed of a series of circular half-loops of alternating curvature of constant width ( $W$ ), height ( $H$ ) and inner radius ( $R$ ), as shown schematically in Fig. 1a. For reasons of simplicity in our analysis, for the shear-dominated flow in the serpentine channel we used the upper-convected Maxwell (UCM) model, neglecting the solvent viscosity ( $\eta_s$ ) contribution. The total viscosity ( $\eta$ ) is thus simply equal to the polymer viscosity ( $\eta_p$ ) (i.e.  $\eta = \eta_p$ ) and the normal-stress is approximated as  $\tau_{11} = 2\eta_p \lambda \dot{\gamma}^2$ . In this case the ratio  $\tau_{11}/\eta \dot{\gamma}$  becomes equal to  $2\lambda \dot{\gamma}$ , corresponding to

twice the Weissenberg number. A simple analysis based on the Pakdel–McKinley criterion (eqn (1)) showed that the critical Weissenberg number at instability onset ( $Wi_c$ ) can be written as a square root dependence on the normalized radius ( $R/W$ ) with a small off-set at small radii. For a channel with square cross section, our numerical results<sup>28</sup> (see Fig. 2) are best described in the following form:

$$Wi_c = C \sqrt{1 + \frac{R}{W}}. \quad (2)$$

Note that the numerical value for the offset at small radii found from the numerical results differs slightly from the theoretical prediction given in ref. 28 as the flow asymmetry occurring at strong curvature is not captured by our theoretical model, as has already been pointed out in ref. 28. The predicted scaling is in excellent agreement with experimental observations, as shown in Fig. 2. Here we want to go further and not only obtain the scaling of the instability onset with the flow geometry, but reach a quantitative prediction of the instability threshold. To do so, one first has to take the solvent viscosity contribution into account, which cannot be neglected for the dilute polymer solutions we use. When using an appropriate model, for example the Oldroyd-B model,<sup>1</sup> to describe the polymer rheology so that the total viscosity ( $\eta$ ) is comprised of both a polymer contribution ( $\eta_p$ ) and a solvent contribution ( $\eta_s$ ), i.e.  $\eta = \eta_p + \eta_s$ , the scaling for the instability onset has to be corrected<sup>21,29</sup> using  $\tau_{11}/\eta \dot{\gamma} = 2(\eta_p/\eta)\lambda \dot{\gamma}$ . By doing so and then rewriting a modified form of eqn (2) to obtain the critical shear rate, one obtains:

$$\dot{\gamma}_c = \frac{C}{\lambda} \sqrt{\frac{\eta}{\eta_p}} \sqrt{1 + \frac{R}{W}} \quad (3)$$

where  $(C/\lambda)\sqrt{\eta/\eta_p}$  can be identified as the slope from a plot of the critical shear rate ( $\dot{\gamma}_c$ ) vs.  $\sqrt{1 + R/W}$ . At this juncture it

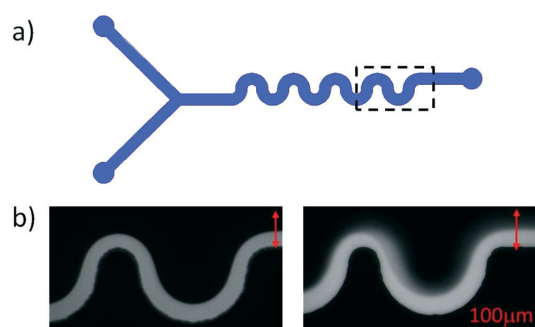


Fig. 1 a) Schematic of the microfluidic serpentine channel. b) Snapshots from the experiments showing the instability onset. Solutions of PEO are injected into a microchannel via two inlets; only one stream contains fluorescent dye and is visible on the snapshots. Left hand side: stable flow below instability onset, right hand side: unstable flow above instability onset.

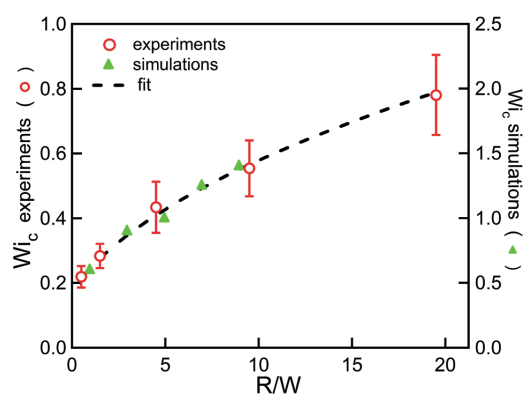


Fig. 2 Geometric scaling of the instability onset. The green triangles are numerical results and the red circles are results from experiments. The dotted line is a fit to eqn (2). Data from Zilz et al.<sup>28</sup> using a solution of 125 ppm of PEO 2Mio.



is also useful to define a parameter  $a = \lambda/C$ . To be able to make a quantitative prediction of the relaxation time ( $\lambda$ ) from measurements of the critical shear rate ( $\dot{\gamma}_c$ ) one thus needs a calibration experiment to determine  $C$  and the ratio of the polymer to the solvent viscosity. We note also that the serpentine rheometer strictly only allows for a quantitative measurement of the polymer relaxation time, as long as the rheology of the solution is such that the ratio between the normal stresses and the shear stresses is proportional to  $Wi$ .

### 3. Experimental

#### 3.1. The polymer solutions

A solution of the flexible polymer polyethylene oxide (PEO), supplied by Sigma Aldrich, with a nominal molecular weight ( $M_w$ ) of  $2 \times 10^6$  g mol<sup>-1</sup> and two different batches of PEO with nominal molecular weights of  $4 \times 10^6$  g mol<sup>-1</sup>, at concentrations ranging from 125 ppm to 500 ppm (w/w), were used in water–glycerol mixtures. In the following, the different polymers will be referred to as 2Mio, 4Mio-1 and 4Mio-2, respectively. The overlap concentration for 2Mio is  $c^* \approx 860$  ppm<sup>30</sup> and for the 4Mio solutions, estimated using the equations provided by Rodd *et al.*,<sup>30</sup> is  $c^* \approx 550$  ppm and therefore the solutions are dilute in all cases ( $c/c^* < 1$ ). The solvent viscosity ( $\eta_s$ ) varied from  $\eta_s = 1$  mPa s for pure water to 10.7 mPa s, at 20 °C, for varying concentrations of glycerol. All the polymer solutions and concentrations used are summarized in Table 1.

#### 3.2. The serpentine channel

The serpentine channels used in this work consist of a series of 8 half-loops of width ( $W$ ) = 100  $\mu$ m, height ( $H$ ) = 80  $\mu$ m and varying inner radius ( $R$ ). The number of loops and the geometry of the inlets of the serpentine channels used in this study are represented in Fig. 1a and have been described in detail in Zilz *et al.*<sup>28</sup> Experiments performed with varying numbers of loops ( $N$ ) confirmed that the results presented here are independent of the exact number of loops, provided that  $2 < N < 15$ . The channels are made from PDMS, but due to the small viscosity of the polymer solutions used, the applied pressure remained sufficiently small to avoid deformation of the channels. The solutions are supplied to the micro-channel *via* two inlets, one stream of which is

fluorescently dyed. The light grey area visible in the snapshots of Fig. 1b shows the location of the fluorescently labeled fluid. Its width variation along the streamwise direction shows the slight asymmetry of the flow field along the flow path due to local flow acceleration in the curved geometry. Note that the channel width is constant over the whole length of the channel. Fig. 1b shows a stable flow situation in the left panel and an unstable flow situation in the right panel. In this way the stability of the flow can easily be visually assessed and will always be monitored at the last loop. The time-dependent flow is easily identifiable in the real-time flow visualization. The flow rate ( $Q$ ) was varied from 1 to 50  $\mu$ l min<sup>-1</sup>, and was imposed *via* a syringe pump (PHD 2000, Harvard apparatus). The Reynolds number ( $Re$ ) is defined as  $Re = \rho UW/\eta$ , with  $\rho$  representing the density of the fluid and  $U = Q/WH$  representing the average velocity in the channel. The maximum  $Re$ , corresponding to the highest flow rate and lowest viscosity solution, never exceeded 5. The flow is visualized using an inverted microscope (Axio Observer, Zeiss) coupled to a CCD camera (PixeLink). Starting with the lowest flow rate,  $Q$  is then gradually increased. After each change in  $Q$  a sufficiently long time is allowed to achieve steady-state flow conditions (on the order of 10 minutes per step). The onset of fluctuations in the flow defines the onset of the time-dependent elastic instability, and the critical flow rate ( $Q_c$ ) is determined. From the critical flow rate, we obtain the critical average shear rate ( $\dot{\gamma}_c$ ), defined as  $\dot{\gamma}_c = Q_c/(W^2H)$ .

As an example, Fig. 3 illustrates the results obtained for PEO 2Mio at a concentration of 400 ppm. Similar experiments (not shown) have been performed at different concentrations and for different molecular weights, as given in Table 1. In parallel to each experiment, the solvent viscosity and the ratio between the polymer and solvent viscosity ( $\eta_p/\eta_s$ ) was determined using an Ubbelohde capillary viscometer. In

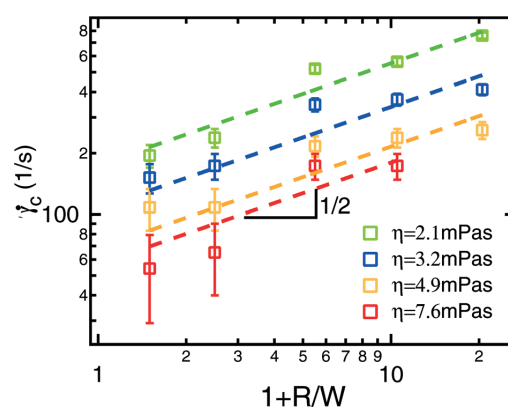


Fig. 3 Critical shear rate ( $\dot{\gamma}_c$ ) as a function of the normalized radius ( $1 + R/W$ ) for solutions of PEO 2Mio at a concentration of 400 ppm for different solvent viscosities ( $\eta_s$ ). The dotted lines represent fits to the data using eqn (3). Each experiment was repeated at least two times using fresh polymer solutions and the average value is shown together with the error bars.

Table 1 Polymer solutions used in the serpentine channel and fit parameters of  $\lambda = A\eta_s^{0.9}$

Polymer solutions used in the serpentine channel		
$M_w$	Concentration	$\eta_p/\eta_s$
2Mio	125–500 ppm	7%–39%
4Mio-1	400 ppm	34%
4Mio-2	400 ppm	34%
Fit parameters of $\lambda = A\eta_s^{0.9}$ from classical rheometry		
$M_w$	Concentration	$A$ ms/(mPa s) <sup>0.9</sup>
2Mio	400 ppm	$0.25 \pm 0.02$
4Mio-1	400 ppm	$0.59 \pm 0.02$
4Mio-2	400 ppm	$0.95 \pm 0.04$



Paper

View Article Online

Lab on a Chip

this way it was possible to correct for small changes in temperature that occurred in the laboratory (typically between 20 °C and 23 °C).

### 3.3. The classical rotational rheometer

A commercial rotational shear rheometer (MARS II, Thermo Scientific) in combination with a cone-and-plate geometry (diameter ( $D$ ) = 60 mm, cone angles ( $\alpha$ ) = 2° and 1°) in shear rate controlled mode was used to measure the viscosity ( $\eta$ ) and the first normal-stress difference ( $N_1 = \tau_{11} - \tau_{22}$ ) simultaneously, following the methodology laid out by Zell *et al.*<sup>31</sup> In models of dilute polymer solutions,  $\tau_{22}$  is negligible<sup>32</sup> in the steady simple shear flow experiments and thus  $N_1$  is identical to the streamwise normal-stress ( $\tau_{11}$ ). The shear rate was increased in a step-wise protocol from 1 s<sup>-1</sup> up to a maximum of 3000 s<sup>-1</sup>, with 15 s of equilibration time at each shear rate. The temperature was kept constant at  $T = 20 \pm 0.5$  °C by using a Haake Phoenix II refrigerated circulator. The normal-stress data of the polymer solutions were corrected by taking into account inertial contributions that can be easily obtained from  $N_1$  measurements of the Newtonian solvents. The constant solvent viscosities ( $\eta_s(\dot{\gamma}) \equiv \eta_s$ ) were also measured. The  $\Psi_1$  data of the polymer solutions were obtained from quadratic fits to the corrected data for  $N_1$  according to  $N_1(\dot{\gamma}) = \Psi_1 \dot{\gamma}^2$  within adequate ranges of shear rate. An example of the normal-stress data ( $N_1$ ) together with the results for the shear viscosity ( $\eta$ ) is shown in Fig. 4a for PEO 2Mio at a concentration of 400 ppm. A quadratic fit to the normal-stress data is also indicated. Note that for the representation of the data, an average over several runs (at least 3) has been plotted. The relaxation time ( $\lambda$ ) of the polymer was determined by taking

$$\lambda = \frac{\Psi_1}{2\eta_p(\dot{\gamma})} = \frac{\Psi_1}{2[\eta(\dot{\gamma}) - \eta_s(\dot{\gamma})]} \quad (4)$$

When calculating the relaxation time we refer to the polymer viscosity at a fixed shear rate of  $\dot{\gamma} = 100$  s<sup>-1</sup> and neglect the slight shear-thinning behavior of the polymer solutions. The associated uncertainties,  $\delta\eta$ ,  $\delta\eta_s$  and  $\delta\Psi_1$  (from the statistics of multiple independent measurements), can be interpreted in terms of an estimate of the uncertainty of  $\lambda$ , *i.e.*  $\delta\lambda^2 \lesssim (\delta\Psi_1 / 2\bar{\eta}_p)^2 + (\bar{\Psi}_1 / 2\bar{\eta}_p^2)^2 (\delta\eta^2 + \delta\eta_s^2)$  with mean values denoted by an overbar. The variations of  $\lambda = \bar{\lambda} \pm \delta\lambda$  with solvent viscosity are shown in Fig. 4b and can be described as  $\lambda = A\eta_s^{0.9}$ , which has been found as the best fit for all three curves presented in Fig. 4b. The fit parameters ( $A$ ) are shown in Table 1.

For a polymer chain in a good solvent, according to Zimm's theory,<sup>32</sup> the longest relaxation time of a dilute solution can be estimated using

$$\lambda_{\text{Zimm}} = \frac{F[\eta]M_w\eta_s}{N_A k_B T} \quad (5)$$

where  $N_A$  is the Avogadro constant,  $k_B$  is the Boltzmann constant (and the product  $N_A k_B$  is equal to the universal gas

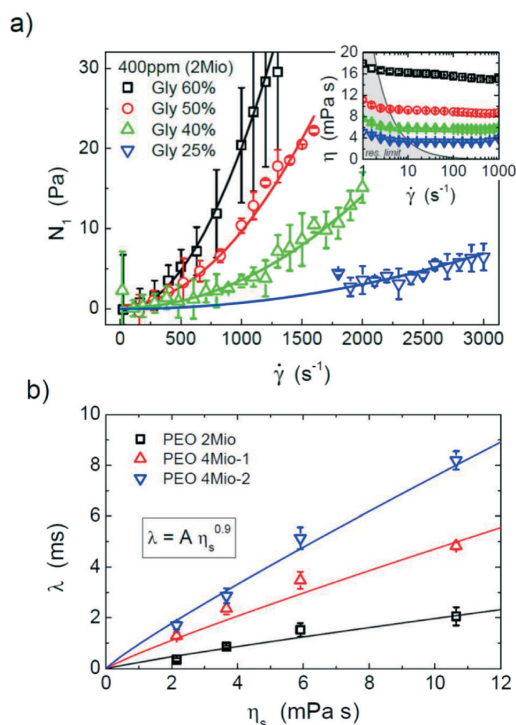


Fig. 4 a) First normal-stress difference ( $N_1$ ) as a function of the shear rate from classical rheometry for PEO 2Mio at 400 ppm. A quadratic fit to the normal-stress data is also indicated. Inset: shear viscosity ( $\eta$ ) as a function of shear rate. Note that for the representation of the data, an average over several runs (at least 3) has been plotted. b)  $\lambda$  vs.  $\eta_s$  from classical shear rheometry at a polymer concentration of 400 ppm. The fits correspond to  $\lambda = A\eta_s^{0.9}$ .

constant,  $R$ ),  $T$  is the absolute temperature and  $[\eta]$  is the intrinsic viscosity. Tirtaatmadja *et al.*<sup>33</sup> have shown experimentally that this can be expressed as  $[\eta] = 0.072M_w^{0.65}$  for the PEO solutions studied here (giving  $[\eta]$  in the usual units of ml g<sup>-1</sup>). The prefactor ( $F$ ) is given by Rodd *et al.*<sup>34</sup> to be 0.463. Rodd *et al.*<sup>30</sup> measured the intrinsic viscosity of different polymer-water-glycerol mixtures and have shown that it decreases due to a decrease in solvent quality. As a consequence, the dependence of  $\lambda$  on  $\eta_s$  becomes less than linear. In Fig. 5a we show how these estimates of the Zimm relaxation time compare to those determined from the first normal-stress difference measured in the cone-and-plate rotational rheometer, illustrating that the agreement is very good. Given the polydispersity inherent in such commercial polymers, and batch-to-batch variations which the data in Fig. 4b highlight, the almost quantitative agreement between the two estimates of  $\lambda$  is striking (especially given the various constants used in the determination of  $\lambda_{\text{Zimm}}$  from eqn (5)). Such agreement provides confidence in the robustness of our estimates of the relaxation time and hence in the calibration of the serpentine rheometer.



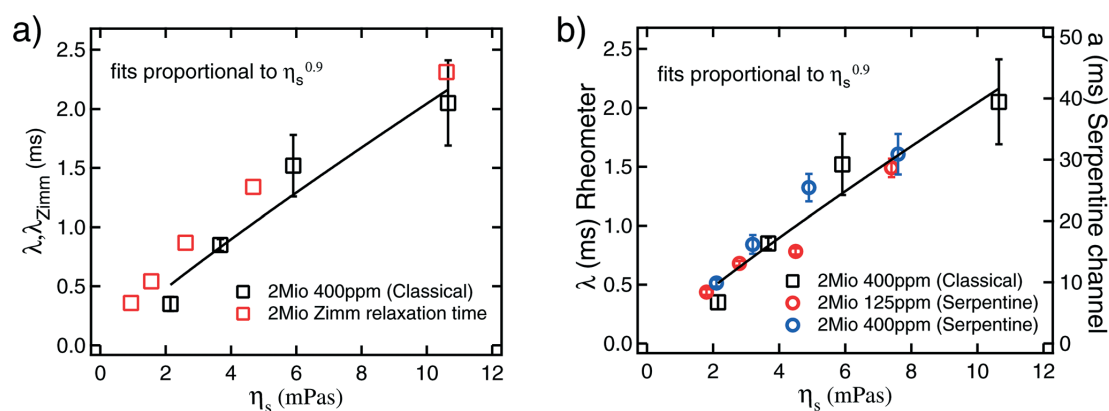


Fig. 5 a) Relaxation time from classical shear rheometry (eqn (4)) compared to the Zimm relaxation times<sup>30,34</sup> (eqn (5)). b) Relaxation time from classical shear rheometry (eqn (4)) versus solvent viscosity ( $\eta_s$ ) for PEO 2Mio at a concentration of 400 ppm (left axis).  $a = \lambda/C$  (eqn (3)) from the serpentine rheometer versus solvent viscosity ( $\eta_s$ ) for PEO 2Mio at concentrations of 125 ppm and 400 ppm (right axis). The error for the data from the serpentine rheometer corresponds to the error of the fit to  $\dot{\gamma}_c$  (eqn (3)), and for the data from the classical rheometer the errors are estimated by an error propagation according to the uncertainties of  $\Psi_1$  and  $\eta_p$ .

## 4. Calibration of the serpentine rheometer

To calibrate the serpentine rheometer the value of  $C$  (eqn (3)) has to be determined. To do so we compare results for  $a = \lambda/C$  from the serpentine channel to relaxation times from classical rheometry. To obtain better accuracy, we not only compare these values for a single polymer solution, but also use solutions of PEO 2Mio with different solvent viscosities and different concentrations.

Firstly we determine the values of  $a = \lambda/C$  from the slope obtained from the fits of the critical shear rate versus the radius of curvature (Fig. 3) and the ratio of the polymer to the solvent viscosity for PEO 2Mio for two different concentrations, 125 ppm and 400 ppm. These results are then compared to the results for  $\lambda$  from the classical shear rheometer (see Fig. 4b) for PEO 2Mio at a concentration of 400 ppm. Note that it was not possible to obtain reliable measurements for the smaller concentration of 125 ppm on the classical rheometer. Fig. 5b shows  $\lambda$  together with  $a$  as a function of the solvent viscosity ( $\eta_s$ ).

A number of things should be remarked from Fig. 5b. First, all three data sets show a comparable dependence of  $\lambda$  on the solvent viscosity, which we will continue to describe as  $\lambda \sim \eta_s^{0.9}$ . Second, the results obtained from the serpentine rheometer for the two different concentrations are in good agreement. This shows that our correction for the solvent viscosity is adequate and is a first validation that the proposed rheometer works very well. We adjusted  $a = \lambda/C = B\eta_s^{0.9}$  and obtained  $B = 4.99 \pm 0.23 \text{ ms}/(\text{mPa s})^{0.9}$  as the best fit for both curves together. Finally by comparing  $A = 0.25 \pm 0.02 \text{ ms}/(\text{mPa s})^{0.9}$  (see Table 1) from the classical rheometry to the value of  $B$  from the serpentine rheometer we obtain  $C = 0.05$ .

## 5. Using the serpentine channel

We now discuss possible applications of the serpentine rheometer.

### 5.1. A quantitative rheometer

**5.1.1. Extension to lower concentrations.** First we measure the relaxation times for different concentrations ( $c$ ) of a given polymer. As we are working in the dilute regime ( $c < c^*$ ), for a given molecular weight we expect to obtain identical relaxation times. The results for PEO 2Mio at concentrations of  $c = 125 \text{ ppm}$ ,  $250 \text{ ppm}$  and  $500 \text{ ppm}$  for a solvent viscosity of  $\eta_s = 4.9 \text{ mPa s}$  are presented in Fig. 6a. These results were obtained from an independent series of measurements and each experiment has been repeated three times using fresh polymer solutions. The results are compared to the value for the relaxation time at  $c = 400 \text{ ppm}$  from the calibration curve (highlighted by a circle in Fig. 6a). Note that we did not include the value for  $c = 125 \text{ ppm}$  from the calibration curve as we did not perform experiments with the corresponding solvent viscosity for this concentration.

Notwithstanding the rather large uncertainty for the smallest concentration, these results are very promising; a value of  $\lambda \approx 1.2 \text{ ms}$  is found independent of the polymer concentration. Note that it was not possible to measure the relaxation time of the low concentration,  $c = 125 \text{ ppm}$ , using the rotational rheometer, indicating the superior sensitivity of the serpentine channel, which is able to measure very small relaxation times down to very small concentrations. This is in agreement with the findings from the calibration curve that as long as the correction for the ratio between the solvent and the polymer viscosity is made correctly, identical results are obtained for different concentrations in the dilute regime. We remark that additional miniaturization of the



Paper

View Article Online

Lab on a Chip

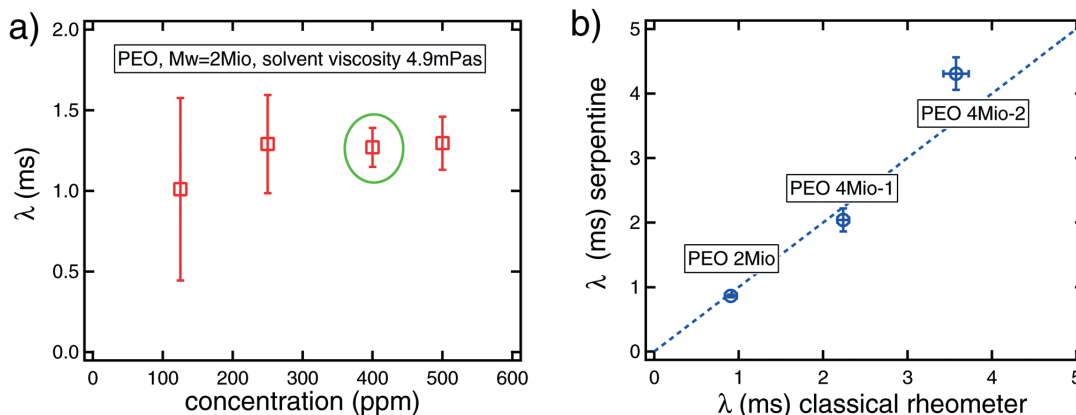


Fig. 6 a) Relaxation time ( $\lambda$ ) obtained from the serpentine rheometer for PEO 2Mio in a solvent with viscosity  $\eta_s = 4.9$  mPa s at varying concentrations, ranging from 125 ppm to 500 ppm. The data points represent the average over three sets of experiments and the corresponding error bars. The relaxation time at 400 ppm corresponds to the value from the calibration curve. b) Relaxation times from the serpentine rheometer versus relaxation times from classical shear rheometry. The results from the serpentine rheometer correspond to a concentration of 125 ppm for the three different polymers and a solvent viscosity of  $\eta_s = 5.2$  mPa s. The error bars are estimated from the error of the fit to  $\dot{\gamma}_c$ . The results from the classical rheometer for 400 ppm solutions are calculated from the fits of the relaxation time with the solvent viscosity, see Table 1. In this case, the error is estimated from the error of the fit on  $A$ .

serpentine channel enhances the elastic effects, thus increasing further the sensitivity of this rheometric device. A recent review<sup>16</sup> discusses the challenges of measuring viscoelastic properties of dilute polymer solutions, highlighting the relevance of using microfluidic devices, as in our work, to probe the elastic properties of such polymer solutions.

**5.1.2. Changing the molecular weight.** Secondly we measured the relaxation time for solutions of PEO of different molecular weight: 2Mio and two different batches of 4Mio, denoted 4Mio-1 and 4Mio-2. Fresh solutions for all three polymers were prepared at 125 ppm and a solvent viscosity of  $\eta_s = 5.2$  mPa s. The relaxation times obtained were compared to the relaxation times from classical shear rheometry measured at 400 ppm. As we are in the dilute regime, no dependence of  $\lambda$  with the polymer concentration is expected, and we have explicitly shown that this is true for the solution of PEO 2Mio in Fig. 6a. The values used from the classical rotational rheometry are calculated using the fit parameters from Table 1 to obtain the relaxation times at the solvent viscosity of  $\eta_s = 5.2$  mPa s.

The results from the serpentine channel are plotted in Fig. 6b against the results from the classical rheometry and satisfactory agreement between these two independent techniques is obtained. Note that the fact that the error bars are smaller than the differences between these two measurements in some cases is very likely due to the fact that independently prepared polymer solutions have been used in each measurement on the two different devices.

In addition, as was actually already apparent from the classical shear rheology data in Fig. 4b, we note that the data for the two batches of 4Mio PEO highlight large batch-to-batch variations that can occur between nominally-identical

samples. There is a factor of two difference in relaxation time between both samples. Such differences are likely a consequence of differing degrees of polydispersity in the two batches.

## 5.2. Integration into a microfluidic lab-on-a-chip device

As the foregoing makes clear, to determine a quantitative value of the relaxation time using the serpentine rheometer, an independent measurement of the polymer contribution to the total viscosity (and indeed a measurement of the solvent viscosity if it is unknown) is required such that the value of  $\sqrt{\eta/\eta_p}$  can be determined to use in eqn (3). In the current study, these values were obtained from separate measurements using an Ubbelohde capillary viscometer. Ideally one would like to be able to determine both the viscosity ratio and the critical shear rate from a single microfluidic lab-on-a-chip device. To do so one could either use pressure drop measurements in a straight section upstream of the serpentine channel, as in Pipe *et al.*<sup>12</sup> for example, or, alternatively, use the Y-junction approach of Guillot *et al.*<sup>6</sup> or Nghe *et al.*<sup>9</sup> As the easiest method to observe the purely-elastic instability in the serpentine channel is *via* an optical visualization technique, integration into a system based on the latter approach is probably to be preferred, thereby avoiding the requirement of incorporating pressure sensors into the device. To avoid issues of possible polymer degradation due to the instability, in the pressure-drop case the viscometer section of the device should be incorporated upstream of the serpentine channel and, in the Y-junction case, where a reference fluid is required, in a separate parallel micro-channel on the same chip.



### 5.3. Using the serpentine rheometer as a comparator or index device with an application to polymer degradation

If one is not concerned with the absolute value of a fluid's relaxation time *per se*, but rather with indexing different fluids according to their degree of elasticity, then the serpentine channel represents an extremely efficient device. In this scenario it is simply sufficient to test the different fluids in a single channel of known curvature and determine the critical shear rate in each case. Following eqn (3), this directly leads to  $\dot{\gamma}_{c,1}/\dot{\gamma}_{c,2} = \lambda_2/\lambda_1$ . Of course, strictly speaking, this equality only holds for fluids where the ratio  $\eta/\eta_p$  remains constant. In the absence of quantitative information regarding the contribution to polymer viscosity, a pragmatic approach, if the critical overlap concentration is known, is to use the scaling<sup>32</sup>  $c^*[\eta] \sim 1$ , which gives  $\eta_p \sim \eta_s c/c^*$ , or  $\eta/\eta_p = 1 + c^*/c$ .

Alternatively the critical shear rate can be used for multiple repeat experiments of the same fluid to test for degradation. Often one needs to check if polymer degradation has occurred due to either photo-induced, mechanical, thermal, chemical or biological causes.<sup>9,35,36</sup> Simple shear viscosity measurements are often fairly insensitive to such effects as degraded polymers often still contribute to the overall viscosity of the solution, which tends to be dominated by the solvent viscosity in any case for dilute polymer solutions (and is therefore a small effect). In contrast, the polymer relaxation time is a much more sensitive harbinger of degradation. In Fig. 7 we show the effect of photo-induced degradation on a virgin polymer solution, *i.e.* unsheread, stored at room temperature in a clear bottle exposed to sunlight over a period of several days. Each day a new measurement was made and, after seven days, a precursive slight increase in the critical shear rate was observed, which was followed by destruction of the sample *via* the formation of biofilms. Finally, our experience with the serpentine rheometer suggests its sensitivity makes it an ideal instrument for

monitoring possible degradation effects, regardless of the precise degrading mechanism.

## 6. Conclusions

By understanding the scaling behaviour of the onset of a purely-elastic flow instability in a microfluidic serpentine channel, we have proposed a microfluidic rheometric device that is capable of measuring fluid relaxation times down to 1 ms. In contrast to most other rheometers, which aim to produce viscometric flows to enable the extraction of rheological properties, the device makes use of an inherent instability within the flow to estimate the fluid relaxation time. Although using interfacial instabilities has previously been tentatively proposed<sup>22,26</sup> as a means of estimating material properties, as has the onset of viscoelastic vortices,<sup>37</sup> the current method, which only requires a single fluid, is the first to show that relaxation times can be successfully measured using such an approach. Also, very recently, Koser *et al.*<sup>38</sup> have proposed using creep-recovery tests in a microfluidic device to estimate polymer relaxation times. However, their device requires the use of a high-speed camera and is restricted to relaxation times at least an order of magnitude greater than those measured here. The serpentine rheometer can either (a) be used as a comparator or indexing device, in which case fluids can be ranked according to their elasticity, or changes can be monitored, such as those due to degradation or (b) be used as a true rheometer once calibration tests using classical cone-and-plate rheometry, for example, have been performed. In this latter case, the microfluidic serpentine device can access lower molecular weight materials, solvent viscosities or concentrations than is possible using state-of-the-art commercial rheometers.

## Acknowledgements

Some of this work was undertaken whilst R. J. P. was a visiting "Chaire Michelin" at the ESPCI Paris Tech in June 2013 and this support is hereby gratefully acknowledged. M. A. A. acknowledges funding from the European Research Council (ERC), under the European Commission "Ideas" Specific Programme of the Seventh Framework Programme (grant agreement no. 307499).

## References

- 1 R. Bird, R. Armstrong and O. Hassager, *Dynamics of Polymeric Liquids*, 1987.
- 2 P. S. Virk, *AIChE J.*, 1975, 21, 625–656.
- 3 D. Jones and K. Walters, *Rheol. Acta*, 1989, 28, 482–498.
- 4 A. Lindner, J. Vermant and D. Bonn, *Phys. A*, 2003, 319, 125–133.
- 5 P. Guillot, P. Panizza, J.-B. Salmon, M. Joanicot, A. Colin, C.-H. Bruneau and T. Colin, *Langmuir*, 2006, 22, 6438–6445.
- 6 P. Guillot, T. Moulin, R. Kötitz, M. Guirardel, A. Dodge, M. Joanicot, A. Colin, C.-H. Bruneau and T. Colin, *Microfluid. Nanofluid.*, 2008, 5, 619–630.

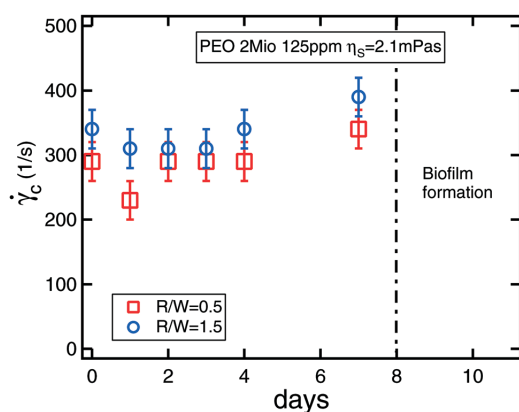


Fig. 7 Critical shear rate measured over time using the serpentine rheometer with two different radii for a PEO sample exposed to sunlight. The error bars correspond to the uncertainty in measuring the critical flow rate.



[View Article Online](#)

Paper

Lab on a Chip

- 7 C. J. Pipe, T. S. Majmudar and G. H. McKinley, *Rheol. Acta*, 2008, **47**, 621–642.
- 8 J. Chevalier and F. Ayela, *Rev. Sci. Instrum.*, 2008, 076102.
- 9 P. Nghe, P. Tabeling and A. Ajdari, *J. Non-Newtonian Fluid Mech.*, 2010, **165**, 313–322.
- 10 E. Livak-Dahl, J. Lee and M. A. Burns, *Lab Chip*, 2013, **13**, 297–301.
- 11 H. Berthet, J. Jundt, J. Durivault, B. Mercier and D. Angelescu, *Lab Chip*, 2011, **11**, 215–23.
- 12 C. J. Pipe and G. H. McKinley, *Mech. Res. Commun.*, 2009, **36**, 110–120.
- 13 M. S. N. Oliveira, L. E. Rodd, G. H. McKinley and M. A. Alves, *Microfluid. Nanofluid.*, 2008, **5**, 809–826.
- 14 W. C. Nelson, H. P. Kavehpour and C.-J. C. Kim, *Lab Chip*, 2011, **11**, 2424–2431.
- 15 S. J. Haward, M. S. N. Oliveira, M. A. Alves and G. H. McKinley, *Phys. Rev. Lett.*, 2012, **109**, 128301.
- 16 F. J. Galindo-Rosales, M. A. Alves and M. S. N. Oliveira, *Microfluid. Nanofluid.*, 2013, **14**, 1–19.
- 17 G. F. Christopher, J. M. Yoo, N. Dagalakis, S. D. Hudson and K. B. Migler, *Lab Chip*, 2010, **10**, 2749–2757.
- 18 R. G. Larson, E. S. G. Shaqfeh and S. J. Muller, *J. Fluid Mech.*, 1990, **218**, 573.
- 19 A. Groisman and V. Steinberg, *New J. Phys.*, 2004, **6**, 29–29.
- 20 E. S. G. Shaqfeh, *Annu. Rev. Fluid Mech.*, 1996, **28**, 129–85.
- 21 G. McKinley, P. Pakdel and A. Oztekin, *J. Non-Newtonian Fluid Mech.*, 1996, **67**, 19–47.
- 22 B. Khomami and K. Su, *J. Non-Newtonian Fluid Mech.*, 2000, **91**, 59–84.
- 23 A. Groisman and S. Quake, *Phys. Rev. Lett.*, 2004, **92**, 094501.
- 24 R. J. Poole, M. A. Alves and P. J. Oliveira, *Phys. Rev. Lett.*, 2007, **99**, 164503.
- 25 A. N. Morozov and W. van Saarloos, *Phys. Rep.*, 2007, **447**, 112–143.
- 26 O. Bonhomme, A. Morozov, J. Leng and A. Colin, *Phys. Rev. E: Stat., Nonlinear, Soft Matter Phys.*, 2011, **83**, 065301.
- 27 P. Pakdel and G. McKinley, *Phys. Rev. Lett.*, 1996, **77**, 2459–2462.
- 28 J. Zilz, R. J. Poole, M. A. Alves, D. Bartolo, B. Levaché and A. Lindner, *J. Fluid Mech.*, 2012, **712**, 203–218.
- 29 R. J. Poole, A. Lindner and M. A. Alves, *J. Non-Newtonian Fluid Mech.*, 2013, **201**, 10–16.
- 30 L. Rodd, J. Cooper-White, D. Boger and G. McKinley, *J. Non-Newtonian Fluid Mech.*, 2007, **143**, 170–191.
- 31 A. Zell, S. Gier, S. Rafa and C. Wagner, *J. Non-Newtonian Fluid Mech.*, 2010, **165**(19), 1–24.
- 32 R. G. Larson, *The Structure and Rheology of Complex Fluids*, 1999.
- 33 V. Tirtaatmadja, G. McKinley and J. Cooper-White, *Phys. Fluids*, 2006, **18**, 043101.
- 34 L. Rodd, T. Scott, D. Boger, J. Cooper-White and G. McKinley, *J. Non-Newtonian Fluid Mech.*, 2005, **129**, 1–22.
- 35 S. Vanapalli, M. Islam and M. Solomon, *Phys. Fluids*, 2005, **17**, 095108.
- 36 S. A. Vanapalli, S. L. Ceccio and M. J. Solomon, *Proc. Natl. Acad. Sci. U. S. A.*, 2006, **103**, 16660–16665.
- 37 L. Campo-Deano, F. J. Galindo-Rosales, F. T. Pinho, M. A. Alves and M. S. N. Oliveira, *J. Non-Newtonian Fluid Mech.*, 2011, **166**, 1286–1296.
- 38 A. E. Koser, L. Pan, N. C. Keim and P. E. Arratia, *Lab Chip*, 2013, **13**, 1850–1853.

Open Access Article. Published on 30 September 2013. Downloaded on 16/05/2014 13:32:26.  
This article is licensed under a Creative Commons Attribution-NonCommercial 3.0 Unported Licence.



## C.2 Elasto-inertial turbulence [Sam13]

One of the most extensively studied phenomena focusing on the effect of elasticity to Newtonian flow dynamics is the turbulent drag reduction [Vir75]. Here, the addition of small amounts of polymers (or surfactants) significantly reduces the frictional losses of turbulent flows depending on the concentration of the added compound but limited to an empirically found minimum drag reduction (MDR). Furthermore, the transition to turbulence has been commonly observed to be altered by the addition of polymers but the varying observations so far lacked a consistent interpretation of the transition scenario with regard to an early or delayed onset relative to the Newtonian case.

In a recently published experimental and numerical study [Sam13], Samanta *et al.* investigated the stability of pipe flow in more detail for different low concentrated polymer solutions in the high Reynolds number regime. Aside from a stabilizing effect of small amounts of polymers leading to a delay of Newtonian type turbulence shifted to higher Reynolds numbers, they found an elasto-inertial transition to turbulence which scales with the value of the shear rate and which occurs for higher polymer concentrations at Reynolds numbers significantly below the transition in Newtonian pipe flow.

The author contributed to this study by thoroughly characterizing the fluids under investigation by steady shear and extensional rheometry as presented in the supporting information which is appended to the following reprint of the published paper.

# Elasto-inertial turbulence

Devranjan Samanta<sup>a,b</sup>, Yves Dubief<sup>c</sup>, Markus Holzner<sup>a</sup>, Christof Schäfer<sup>b</sup>, Alexander N. Morozov<sup>d</sup>, Christian Wagner<sup>b</sup>, and Björn Hof<sup>a,e,1</sup>

<sup>a</sup>Max Planck Institute for Dynamics and Self-Organization, 37073 Göttingen, Germany; <sup>b</sup>Experimental Physics, Saarland University, 66041 Saarbrücken, Germany; <sup>c</sup>School of Engineering, University of Vermont, Burlington, VT 05405; <sup>d</sup>Scottish Universities Physics Alliance, School of Physics and Astronomy, University of Edinburgh, Edinburgh EH9 3JZ, United Kingdom; and <sup>e</sup>Institute of Science and Technology Austria, 3400 Klosterneuburg, Austria

Edited\* by Katepalli R. Sreenivasan, New York University, New York, NY, and approved May 3, 2013 (received for review November 11, 2012)

**Turbulence is ubiquitous in nature, yet even for the case of ordinary Newtonian fluids like water, our understanding of this phenomenon is limited. Many liquids of practical importance are more complicated (e.g., blood, polymer melts, paints), however; they exhibit elastic as well as viscous characteristics, and the relation between stress and strain is nonlinear. We demonstrate here for a model system of such complex fluids that at high shear rates, turbulence is not simply modified as previously believed but is suppressed and replaced by a different type of disordered motion, elasto-inertial turbulence. Elasto-inertial turbulence is found to occur at much lower Reynolds numbers than Newtonian turbulence, and the dynamical properties differ significantly. The friction scaling observed coincides with the so-called “maximum drag reduction” asymptote, which is exhibited by a wide range of viscoelastic fluids.**

elastic instabilities | polymer drag reduction | non-Newtonian fluids | transition to turbulence

The most efficient method with which to reduce the large drag of turbulent flows of liquids is through addition of small amounts of polymers or surfactants. As first observed in the 1940s (1), frictional losses can be reduced by more than 70% (2, 3), and this technique has found application in oil pipelines, sewage, heating, and irrigation networks (4, 5). For dilute solutions, the drag is found to reduce with polymer concentration and eventually approaches an empirically found limit, the maximum drag reduction (MDR) asymptote (6, 7). A number of theories have been put forward to explain the mechanism of drag reduction and the origin of the MDR asymptote (3). Most of them invoke the elasticity of long polymer molecules: They are stretched in strong shear and elongational flow, and they recoil in vortical regions. It has been shown that this process inhibits vortices, and hence suppresses the turbulence-sustaining mechanism (8–15). It has recently been proposed that such inhibition may bring dynamics of drag-reducing flows close to the low-dimensional structures that separate turbulent and laminar flows in Newtonian turbulence (16), and it has been argued that the MDR asymptote is a consequence of the marginal dynamics on this separating boundary. Regarding the effect of polymers on the onset of turbulence, seemingly conflicting observations have been reported. Many investigations reported transition delay (ref. 17 and references therein); that is, the onset was postponed to a higher Reynolds number ( $Re$ ; defined as a ratio of inertial to viscous forces). In other studies (18–20) (largely in pipes of small diameter), it has been observed that turbulence sets in at a  $Re$  smaller than in the Newtonian case, a phenomenon termed “early turbulence.” However, in other studies (17, 21), investigators found that the natural transition point of their pipe experiment (i.e., the point where the flow becomes turbulent without additional perturbations) moved to a lower  $Re$  compared with the Newtonian case.

Although the addition of small amounts of polymer reduces the drag at a large  $Re$ , its effect is dramatically different at a very small  $Re$ . In this regime, the flow is controlled by polymer stretching, orientation, and relaxation, which give rise to anisotropic elastic stresses in the fluid. The magnitude of these stresses,

and the degree of their anisotropy, is set by the product of the longest relaxation time of polymer molecules and a typical shear rate, the so-called Weissenberg number ( $Wi$ ). It has recently been demonstrated that at a large  $Wi$ , the anisotropic elastic stresses destabilize flows with curved streamlines even in the absence of inertia, resulting in so-called “purely elastic linear instabilities” (22, 23). At a yet higher  $Wi$ , these instabilities are followed by a unique type of disordered motion called elastic turbulence, which exhibits fluctuations at many spatial and temporal scales (24, 25). A direct transition from laminar to turbulent flows has also been observed for flows in curved channels (25). In parallel shear geometries, like flow in straight pipes, purely linear elastic instabilities are absent (26); however, in principle, there can be a subcritical transition to elastic turbulence and strong evidence for such a transition has been found (27–29).

Presently, very little is known about possible interaction between the two phenomena, Newtonian and elastic turbulence. The existing theories of drag reduction all share the same conceptual feature: They interpret the resulting flow as a modified form of ordinary Newtonian shear flow turbulence, with its properties being determined by the balance between elastic and viscous stresses (11, 15, 16, 30, 31). Theoretical studies of the influence of polymers on turbulence in unbounded (30–32) flows, however, showed some qualitative differences from Newtonian turbulence; in one case (32), the measured power spectra more closely resembled those found in elastic turbulence than those in Newtonian flows.

Here, we perform experiments on viscoelastic pipe flow and observe that addition of small amounts of polymer postpones the transition to Newtonian turbulence. However, we find that, additionally, there exists a different type of chaotic motion, controlled by the elastic stresses, that can set in at a lower  $Re$  than in the Newtonian case (in agreement with refs. 18–20), and we demonstrate that this state suppresses Newtonian turbulence. In particular, we find that after the latter instability sets in, the flow directly approaches (with increasing  $Re$ ) the MDR asymptote without any excursions to friction values indicative of Newtonian turbulence [note that a direct transition from laminar friction to MDR has also been seen in earlier studies (6), without relating it to an elastic instability, however]. Our observations imply that the MDR asymptote has its origin in the discovered instability and that it is dominated by elasticity. Although the instability mechanism is likely to be related to elastic turbulence, our studies are carried out in a different parameter regime where inertia cannot be neglected, and we therefore dub this state elasto-inertial turbulence (EIT). In addition, the existence of EIT and the direct approach to MDR are reproduced by direct numerical simulation

Author contributions: Y.D., C.W., and B.H. designed research; D.S., Y.D., M.H., C.S., and B.H. performed research; D.S., Y.D., M.H., C.S., and B.H. analyzed data; and Y.D., A.N.M., C.W., and B.H. wrote the paper.

The authors declare no conflict of interest.

\*This Direct Submission article had a prearranged editor.

<sup>1</sup>To whom correspondence should be addressed. E-mail: bhof@ist.ac.at.

This article contains supporting information online at [www.pnas.org/lookup/suppl/doi:10.1073/pnas.1219666110/-DCSupplemental](http://www.pnas.org/lookup/suppl/doi:10.1073/pnas.1219666110/-DCSupplemental).

(DNS) of model viscoelastic fluid flow in a straight channel in the same range of Reynolds numbers as in the experiment. This suggests that the observed instability and friction scaling is characteristic for viscoelastic fluids in wall-bounded flows.

## Results

At the lowest  $Re$  at which turbulence is sustainable in pipe flow, the turbulence appears (33) in the form of axially localized structures about  $20 D$  in length, so-called “turbulent puffs.” It has been shown that these structures decay back to laminar after sufficiently long times following a memoryless process (34, 35). Hence, for each  $Re$ , there is a distinct probability that a turbulent puff will survive beyond a certain time horizon. In the first set of measurements, this characteristic was used to quantify the influence of polymers on the transition to turbulence. Experiments were carried out in pipe flows for different polymer concentrations (50 ppm, 100 ppm, 125 ppm, 150 ppm, and 175 ppm). In all cases, the survival probability of puffs increases with the  $Re$  and, owing to the transient nature of the turbulent puffs, is only found to approach a probability of 1 asymptotically with the  $Re$  (Fig. 1A). Compared with pure water (Fig. 1A, blue curve), the curves are shifted to a larger  $Re$  as the concentration is increased, showing that the polymers delay transition and subdue turbulence. The  $Re$  required to reach a  $P=0.5$  survival probability is found to increase faster than linearly (Fig. 1B) with polymer concentration, providing a measure of the rate at which the turbulent state is postponed to a larger  $Re$  (i.e., transition delay).

Surprisingly, for polymer concentrations  $\geq 200$  ppm, turbulent puffs could not be detected; instead, a different type of disordered motion already sets in at a lower  $Re$ : Whereas in the Newtonian case, turbulent fluctuations can first be sustained for  $Re \sim 2,000$  (Fig. 2A, open squares), in a 500-ppm solution, disordered motion was observed for a  $Re$  as low as 800 (Fig. 2B). Also, in Newtonian fluids, flows just above onset are intermittent [i.e., turbulent regions are interspersed by laminar regions (33); *SI Text*], whereas in the polymer solutions, fluctuations set in globally throughout the pipe (*SI Text*). The instability observed in polymer solutions hence leads to a qualitatively different type of disordered motion, EIT. A further distinction between the two types of turbulence is that in the Newtonian case, the onset is strongly hysteretic: Unperturbed flows remain laminar up to a large  $Re$  (to  $Re = 6,500$  in our setup; black squares in Fig. 2A and C), whereas perturbed flows display turbulence from around  $Re = 2,000$ . In contrast, in a 500-ppm solution, perturbed and unperturbed flows become turbulent at the same  $Re$  (Fig. 2B). Equally, friction factors follow the same scaling and directly approach the MDR asymptote (Fig. 2D) without any excursions toward the Newtonian turbulence (so-called “Blasius”) friction scaling. This observation suggests that the MDR asymptote marks the characteristic drag of EIT rather than being the consequence of an asymptotic adjustment of ordinary turbulence.

Further inspection shows that the elasto-inertial instability also appears for lower polymer concentrations ( $< 200$  ppm). Here, the instability sets in at a larger  $Re$ , and hence in the regime where, in the presence of finite amplitude perturbations, flows already exhibit Newtonian-like (i.e., hysteretic, intermittent) turbulence. Starting from laminar flow without additional perturbations, we find that with an increasing  $Re$ , these more dilute solutions will unavoidably turn turbulent at a  $Re$  distinctly below the natural transition point ( $Re = 6,500$ ) of this pipe, as shown for a 100-ppm solution in Fig. 2A and C (solid triangles).

In contrast to the higher concentrations, the flow is intermittent here, consisting of localized turbulent regions (i.e., puffs) interspersed by nonlaminar, weakly fluctuating regions. As the  $Re$  is further increased, the spatial intermittency disappears and gives way to a uniformly fluctuating state and the friction values approach the MDR asymptote. The onset of instability is plotted in Fig. 3A as function of polymer concentration. Above the red curve in Fig. 3A,

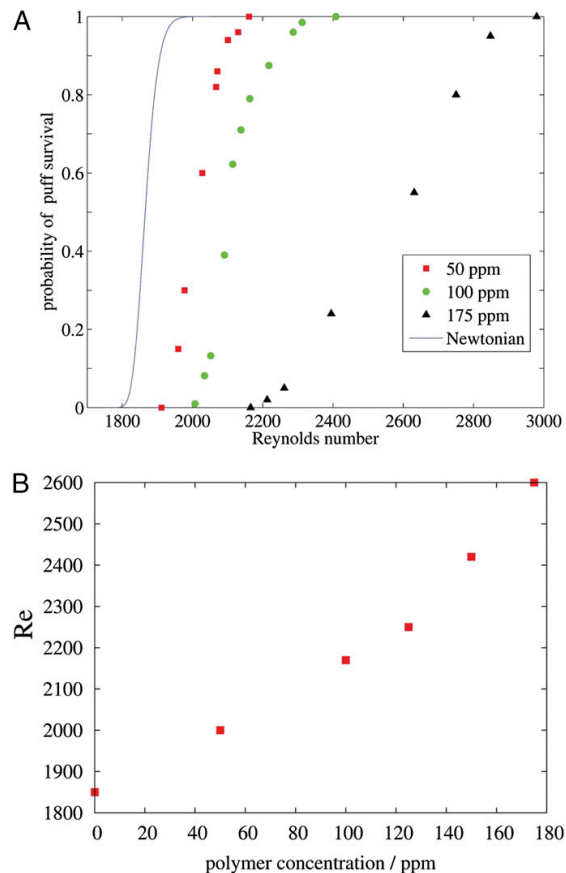


**Fig. 1.** Survival probability of turbulence. At the lowest  $Re$  at which turbulence can be observed in pipes, it has the form of localized structures that decay following a memoryless process (34, 35). The influence of polymers on this process is investigated for various concentrations. To create turbulence, the laminar flow was perturbed by an impulsive injection (of the same fluid) for 20 ms with sufficient amplitude to create a turbulent puff. The flow was then monitored at the exit of the pipe  $760 D$  downstream by means of visual inspection using the same method as described by Hof et al. (34). Although for laminar flow, the fluid exits the pipe smoothly and follows a parabolic path, turbulent fluid (resulting from the different velocity profile) will exit the pipe at a different angle, causing a downward deflection and temporary distortion of the outflowing jet. By continuously monitoring the outflow, the survival probability of turbulent puffs was determined as a function of the  $Re$ . (A) Survival probabilities decrease for increasing polymer concentrations, and the survival probability found in the Newtonian case is only recovered at a larger  $Re$ . With increasing polymer concentration, the typical S-shape of the probability distributions becomes more pronounced. (B)  $Re$  with a 50% survival probability at the  $760 D$  observation point as a function of polymer concentration.

the flow has become unstable and the friction factor begins to approach the MDR asymptote. The green data points in Fig. 3A mark the appearance of turbulent puffs shown in Fig. 1A (i.e., the threshold where the puff  $t_{1/2}$  exceeds  $t = 760$  advective time units, which corresponds to the time for puffs to travel from the injection point to the observation point). For parameter settings between the red and green datasets in Fig. 3A, ordinary turbulence can be triggered by finite-amplitude perturbations, and the flow is hence hysteretic. On further increase of the  $Re$ , once the red curve in Fig. 3A is crossed, the flow will become unstable regardless of initial conditions.

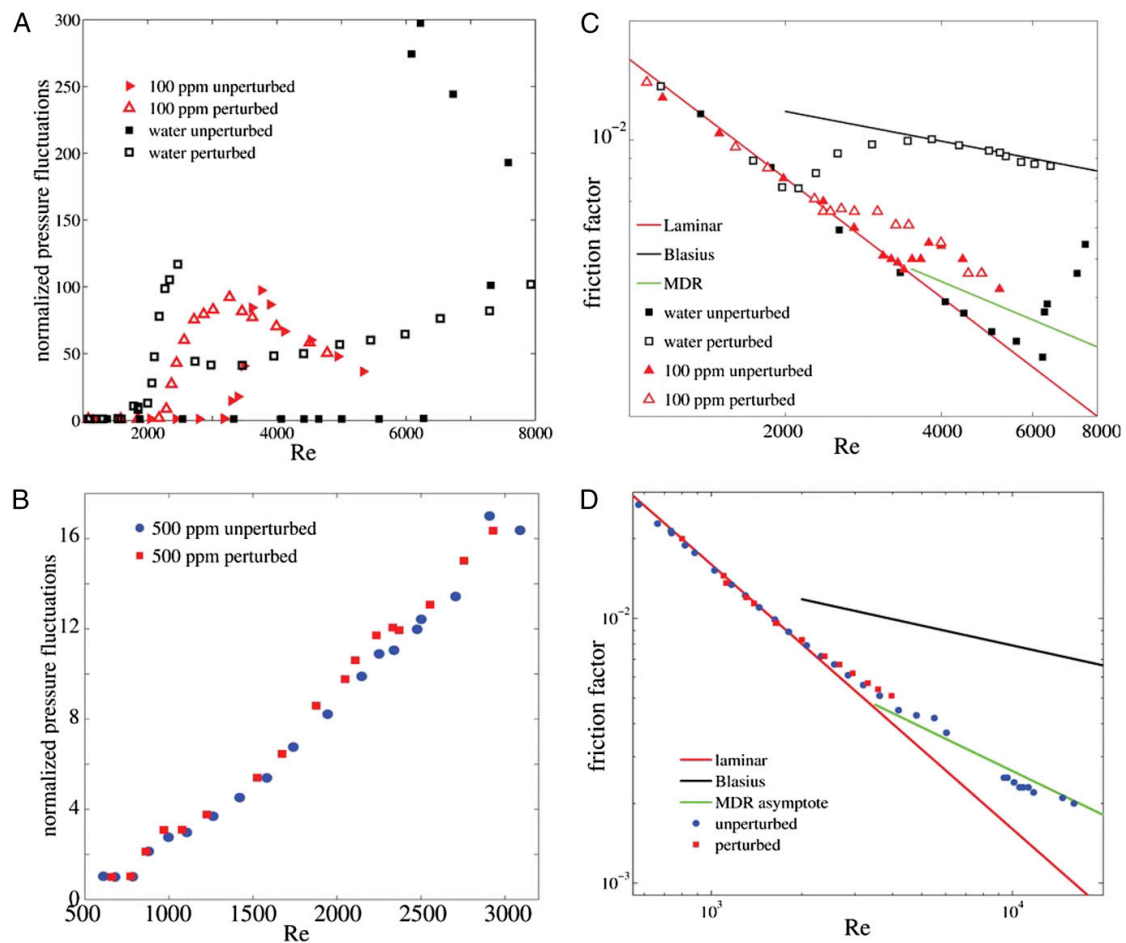


**Fig. 2.** Stability and friction scaling. (A) For the Newtonian case (black symbols), turbulence can first be triggered by perturbations for  $Re$  of about 2,000, where fluctuations increase rapidly. The quantity plotted is the fluctuation in pressure that was measured differentially between two pressure taps (1-mm holes in the pipe wall) separated by  $3D$  in the streamwise direction and located approximately  $250D$  from the pipe exit. (B) For a 100-ppm polymer solution (red data points), turbulence cannot be triggered below  $Re = 2,200$  (transition delay). At  $Re = 3,200$ , however, instability occurs (even in the absence of perturbations), and this instability is caused solely by the presence of the polymers. At higher polymer concentrations (B; 500 ppm here), this instability occurs at a much lower  $Re$  and the hysteresis typical for Newtonian turbulence has disappeared (A and C). The flow already becomes unstable at  $Re = 800$  (regardless of the presence of additional perturbations). From here (with an increasing  $Re$ ), the flow directly approaches the MDR friction scaling (D); also for a concentration of 500 ppm.

Finally, experiments were carried out in pipes with diameters of  $D = 2$  mm and  $D = 10$  mm (blue and red data points in Fig. 3B). When plotting the stability thresholds observed in the three pipes in terms of shear rate vs. polymer concentration, all datasets collapse. The latter observation shows that the elasto-inertial instability scales with the shear rate and not with the  $Re$  (18). Hence, in tubes with a larger diameter, the instability will occur at a large  $Re$  and typically will be obscured by Newtonian turbulence. Inversely, on microscales, this instability will occur at a very low  $Re$ , opening new avenues for mixing in microchannels. Until recently, elastic turbulence and strong mixing had only been reported in curved channels (25, 36, 37), which are linearly unstable.

To gain further insights into the nature of the EIT, we conducted DNS of channel flow for a non-Newtonian fluid using a constitutive model extensively utilized in the simulation of polymer drag reduction. The numerical methods and rheological

parameters are similar to those used in simulations of MDR (38, 39) (details are provided in *SI Text*). Great care was taken to resolve all flow scales relevant to the dynamics of such complex fluids requiring spatial and temporal resolutions significantly larger than for Newtonian turbulence. Each simulation is initially perturbed in such way that transition in Newtonian flow occurs at  $Re = 6,000$ , based on the bulk velocity  $U_b$  and channel height  $H$ .

In qualitative agreement with the experiments, we find that instability develops at a much lower  $Re$  in polymeric flows, which, again, directly leads to the MDR asymptote, as shown in Fig. 4A for  $Re = 1,000$ . Whereas the corresponding Newtonian flow is perfectly laminar, Fig. 4B shows pressure fluctuations on the lower wall of the channel, with a strong yet chaotic organization.

Closer inspection of the numerical data at the lowest simulated  $Re$ ,  $Re = 1,000$ , reveals (Fig. 4B) an interesting topological structure of EIT. Even though the flow is dominated by the mean

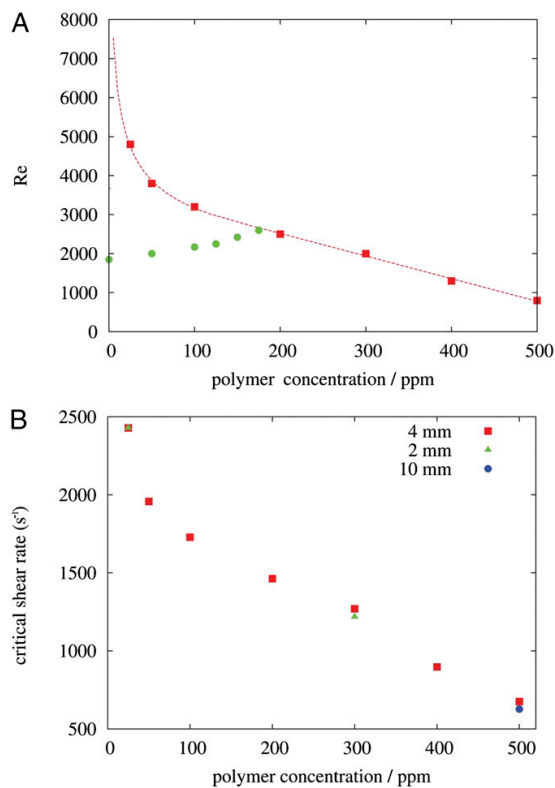


**Fig. 3.** Transition threshold to EIT is plotted for different concentrations (red squares). The red line is a guide for the eye. The green circles mark the transition delay to ordinary turbulence (Fig. 1B). Consequently, for concentrations below 200 ppm, the elasto-inertial instability sets in at a  $Re$  at which ordinary turbulence can already occur, whereas in the  $D=4$ -mm pipe, the elasto-inertial instability is found only above 200 ppm. (B) Red squares mark the critical shear rate for the onset of EIT in the 4-mm pipe (same as red squares in A). In addition, shear rates ( $\dot{\gamma}=8U/D$ ) were determined for the flow in a  $D=10$ -mm pipe and a  $D=2$ -mm pipe. In these cases, the transition occurs at the same critical shear rate. Hence, unlike ordinary turbulence, the onset of EIT is not governed by the  $Re$  but, instead, by the shear rate.

shear, polymers are extended (large values of  $\sqrt{\text{tr}(\mathbf{C})}/L$  see *Numerical Methods* and *SI Text*) in sheet-like regions of large streamwise ( $x$ ) and spanwise ( $z$ ) dimensions. The sheets are stretched at an upward angle from the streamwise direction, indicative of extensional flow topology. These sheets also produce larger polymer extension than the surrounding mean shear does; an increase of the effective flow viscosity, through extensional viscosity, is therefore confined to these very sheets. The response of the flow is observed in pressure fluctuations, shown in contours of wall pressure on the bottom wall of Fig. 4B. Fig. 4C shows isosurfaces of positive and negative  $Q$ , where  $Q = -(1/2) \nabla \cdot (\nabla \cdot (\mathbf{u} \otimes \mathbf{u}))$  is the second invariant of the velocity gradient tensor and also a measure of the local flow topology (40). As shown, the flow is structured in alternating regions of rotational flows ( $Q > 0$ ) and extensional/compressional flows ( $Q < 0$ ). These regions are aligned in the spanwise direction and appear to have a large spanwise coherence scale of about one-third to one-half of the domain span. Note that this spanwise orientation is markedly different from Newtonian turbulence, where the dynamics are dominated by vortices oriented in the

streamwise direction. At a larger  $Re$ , simulations show that after EIT sets in, flows contain streamwise-oriented as well as spanwise-oriented vortical structures. However, as the MDR asymptote is approached, with an increasing  $Wi$ , streamwise vortices are suppressed and the flow is dominated by spanwise structures, as in the case with a low  $Re$  shown in Fig. 4B.

Analogous to Newtonian turbulence also in the present simulations, perturbations of finite amplitude are required to trigger turbulence (albeit considerably smaller amplitude perturbations suffice). This suggests that as in Newtonian linearly stable shear flows (e.g., pipes), a self-sustaining mechanism is required to keep the turbulent motion alive. Whereas no hysteresis has been observed for the transition to EIT in the experiments (Fig. 2B and D), this does not necessarily rule out that the instability may still be subcritical. If, as simulations suggest, very small (compared with the Newtonian case) finite-amplitude perturbations do indeed trigger turbulence, it may prove to be very difficult to reduce disturbance levels in experiments sufficiently to observe hysteresis. We propose that the underlying EIT is hence a self-sustaining cycle, wherein small-velocity perturbations cause the formation of sheets of extended polymers through convective transport. The flow response, through pressure, sustains velocity fluctuations, thereby closing the cycle.

### Discussion and Conclusions

In summary, we have shown that small amounts of polymer added to a Newtonian solvent delay the transition point where Newtonian type turbulence can first be observed (i.e., resulting from a perturbation). At the same time, however, an elastic instability occurs at higher shear rates. At larger polymer concentrations, this elastic instability occurs at a  $Re$  sufficiently smaller than the transition in Newtonian pipe flow. In this regime of high elasticity, experimental measurements of friction factors for different polymer concentrations and different pipe diameters show that after this instability sets in, the friction factor follows the characteristic MDR friction law. This behavior is also confirmed by our numerical simulations, as can be seen from Figs. 2D and 4A. When we increase the  $Re$  further in our numerical simulations, we observe that the mean velocity profile approaches the Virk asymptote (Fig. 5A) and that the Reynolds stress becomes vanishingly small (Fig. 5B) at a large  $Wi$ . Both features are often quoted as the major characteristics of the MDR state (6, 16, 41). Our observation indicates that the MDR state is continuously linked to the EIT that we have discovered at relatively small  $Re$ .

It is noteworthy that the key elements of the mechanism of EIT (nonlinear advection of stress, stretching by flow and flow response via pressure) are common features to many viscoelastic fluids. Although EIT is possibly related to elastic turbulence, inertia cannot be neglected in our case, and there are no curved streamlines that would cause linear instability. Our observations infer that this type of fluid motion replaces ordinary turbulence and dominates the dynamics in elastic fluids at sufficiently large shear rates.

### Materials and Methods

**Experimental Methods.** Experiments were carried out in a pipe made of  $\sim 1.2$ -m-long precision bore segments with an inner diameter of  $D = (4 \pm 0.01)$  mm and a total length of about  $L/D = 900$ . The flow was gravity driven, and the fluid temperature was controlled so that the flow rate could be held constant, typically to within  $\pm 0.2\%$  [details of a similar setup can be found in a study by de Lozar and Hof (42)]. The sample solutions were either pure water or different amounts of polyacrylamide with a molecular weight of  $5 \times 10^6$  amu (PAAm; Sigma-Aldrich) in water. The shear viscosity increased with the polymer concentration, and almost no shear thinning was observed; however, a pronounced elastic behavior was found in the elongational flow of a capillary break-up elongational rheometer. The rheological characterization is given in *SI Text*. A carefully designed inlet of the pipe allowed us to keep flows of pure water laminar up to  $Re \sim 6,500$  (natural

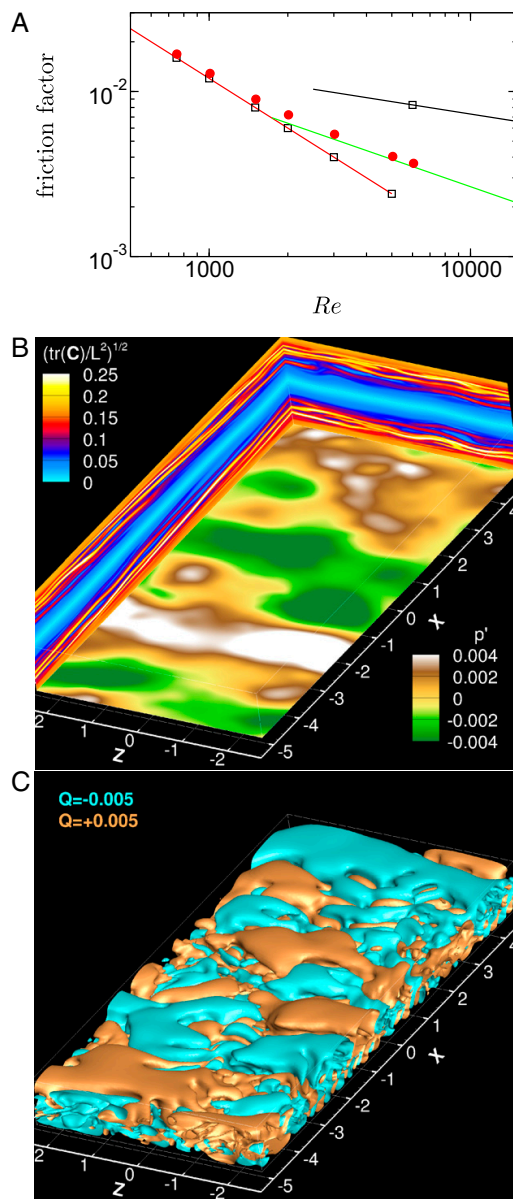


**Fig. 4.** Numerical simulation of EIT in a channel flow. (A) Red, green, and black lines highlight the laminar, turbulent, and MDR distributions of the friction factor, respectively, as a function of the  $Re$  based on the bulk velocity and the height of the channel. The simulations are performed in a channel flow of large transversal dimensions with periodic boundary conditions in horizontal dimensions. At time  $t = 0$ , a perturbation is introduced in the form of space and time oscillations of blowing and suction at the walls for a fixed, short duration. The intensity of the perturbations is tailored so that a transition is triggered at  $Re = 6,000$  for the simulated water flow. Using the same perturbation, the simulated polymeric channel flow already shows a departure from purely laminar flow at around  $Re = 750$  (red circles). (B) Contours of pressure fluctuations on the bottom wall and polymer stretch in vertical planes ( $Re = 750$ ). (C) Isosurfaces of regions of slightly rotational (orange) or extensional (cyan) nature ( $Re = 750$ ), as identified by the second invariant of the velocity tensor  $Q$  (details are provided in *SI Text*).

Samanta et al.

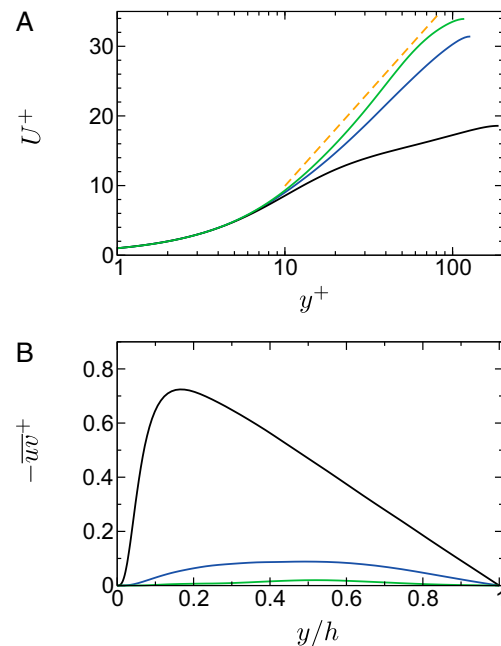


**Fig. 5.** Profiles of turbulence statistics at the highest simulated  $Re$  with the addition of a higher  $Wi$  simulation. For FENE-P fluids (see *SI Text*),  $Wi \gg 1$  leads to a universal form of the polymer tensor closely related to the MDR asymptotic state. Mean velocity profiles in the typical log-linear representation are shown, where the mean velocity  $U^+$  and the distance from the wall  $y^+$  are normalized by skin-friction velocity  $u_\tau$  and kinematic viscosity (A) vs. profiles of Reynolds shear stress,  $-\overline{u'v'} = -\overline{u'v'}/u_\tau^2$ , as a function of the distance from the wall normalized by the channel half-height  $h$  (B). Statistics are shown for  $Re = 6,000$ ; solid blue line,  $Wi = 100$ ; solid green line,  $Wi = 700$ ; solid black line, Newtonian turbulent flow. (A) Virk log-law (6) is denoted by the dashed orange line. The Virk mean velocity profile is a best fit of high  $Re$  data. The assumption of the existence log-law at a low  $Re$  was recently shown (39) to fail at a low to moderate  $Re$  (at least up to  $Re = 10,000$ ). The agreement of  $Wi = 700$  is consistent with previous MDR simulations and experiments. (B) Experiments of Warholic et al. (41) at MDR observe negligible Reynolds shear stress.

transition point for this pipe). Here, the  $Re$  is defined as  $Re = UD/\nu$ , where  $U$  is the mean flow speed and  $\nu$  is the kinematic viscosity. Although laminar (Newtonian) pipe flow is stable for all  $Re$ , turbulence of appreciable lifetime can be triggered by perturbations of finite amplitude once the  $Re$  approaches 2,000 (34, 43). In the present setup, turbulence was triggered by injecting fluid through a small hole in the pipe wall situated  $140 D$  from the inlet; alternatively, for continuous triggering of turbulence, an obstacle ( $\sim 2$ -cm-long  $\sim 1$ -mm-thick twisted wire) could be placed downstream of the inlet.

**Numerical Methods.** The flow is governed by the incompressible Navier–Stokes equations with the addition of a viscoelastic stress using the Finitely Extensible Nonlinear Elastic–Peterlin (FENE-P) model:

$$\partial_t \mathbf{u} + \mathbf{u} \cdot \nabla \mathbf{u} = -\nabla p + \frac{\beta}{Re} \nabla^2 \mathbf{u} + \frac{1-\beta}{Re} \nabla \cdot \mathbf{T}, \quad [1]$$

$$\nabla \cdot \mathbf{u} = 0, \quad [2]$$

in a rectangular domain with periodic boundary conditions in the streamwise and spanwise directions, and no slip at the walls, where  $\mathbf{u}$  is the velocity vector and  $p$  is the pressure. The flow is driven by a bulk force to maintain a constant mass flow rate. The velocity and length scales used to form the  $Re$  and to normalize the flow variables are the bulk velocity and the height of

the channel, respectively. The polymer stress tensor  $\mathbf{T}$  in Eq. 2 is derived from the following transport equation:

$$\partial_t \mathbf{C} + \mathbf{u} \cdot \nabla \mathbf{C} = \mathbf{C} \cdot \nabla \mathbf{u} + \nabla \mathbf{u}^T \cdot \mathbf{C} - \mathbf{T}, \quad [3]$$

with

$$\mathbf{T} = \frac{1}{Wi} (f(\mathbf{C})\mathbf{C} - \mathbf{I}), \quad [4]$$

$$f(\mathbf{C}) = \frac{1}{1 - \text{tr}(\mathbf{C})/L^2}, \quad [5]$$

where  $\mathbf{C}$  is the conformation tensor and  $f$  is the Peterlin function based on  $L$ , the upper limit of polymer extension. The polymer solution is characterized by the  $Wi$ , which is the ratio of polymer relaxation time to flow scale: here, it is the inverse of the wall shear. In Eq. 2, the coefficient  $\beta$  is the ratio of the solvent viscosity to the zero-shear viscosity of the polymer solution. The numerical method used to solve Eqs. 2 and 3 is described by Dubief et al. (38) and is briefly introduced here. The flow is discretized on a staggered grid. Velocity derivatives are computed with second-order, energy-conserving, finite-difference schemes. The divergence of the polymer stress tensor in Eq. 3 uses a fourth-order compact central scheme. To accommodate the sharp gradients arising from Eq. 3, the advection term is discretized with a third-order compact upwind scheme, supplemented by local artificial dissipation. The upper boundedness of the polymer conformation tensor is guaranteed

by an algorithm described by Dubief et al. (38). Time advancement uses the typical fractional step method utilized in most DNSs of turbulence.

The rheological parameters adopted here are consistent with those used in previous simulations of polymer drag reduction (11, 12, 44–46). We use a maximum polymer extension of  $L = 200$ ,  $\beta = 0.9$ , and  $Wi^* = 8$ . Here,  $Wi^*$  is the polymer relaxation time divided by the integral flow time scale (ratio of the channel half-height to bulk velocity). The increase in  $Re$  is achieved by decreasing the velocity, while keeping the channel height and bulk velocity constant. The  $Wi$  of interest is based on the wall shear of the corresponding Newtonian flow. Consequently, the  $Wi$  is equal to 24 in the laminar region and is 100 for  $Re = 6,000$ . The highest  $Wi$  discussed in Fig. 5 corresponds to  $Wi^* = 60$ .

The computational domain dimensions and resolution are  $10 H \times H \times H$  and  $256 \times 161 \times 256$ , respectively. For polymer flows, the streamwise  $\Delta x^+$  and spanwise  $\Delta z^+$  resolutions, normalized by their respective viscous scales, range from  $\Delta x^+ \in [1.5, 5]$  and  $\Delta z^+ \in [0.75, 2.5]$  across the range of  $Re \in [1,000, 6,000]$ . In the same range of  $Re$ , the minimum and maximum cell sizes in the wall normal direction are within  $[0.01, 0.05]$  and  $[1.5, 5]$ . Doubling the dimensions and resolution in transversal directions or increasing the resolution in the wall normal direction did not yield any appreciable change in statistics.

**ACKNOWLEDGMENTS.** D.S. and C.S. were partly funded by Deutsche Forschungsgemeinschaft Project WA1336-5-1. A.N.M. was funded by the Engineering and Physical Sciences Research Council (Grant EP/I004262/1).

- Toms BA (1948) Some observations on the flow of linear polymer solutions through straight tubes at large Reynolds numbers. *Proceedings of the First International Congress on Rheology* 2:135–141.
- Sreenivasan KR, White CM (2000) The onset of drag reduction by dilute polymer additives, and the maximum drag reduction asymptote. *J Fluid Mech* 409:149–164.
- White CM, Mungal MG (2008) Mechanics and prediction of turbulent drag reduction with polymer additives. *Annu Rev Fluid Mech* 40:235–256.
- Sellin RHJ, Ollis M (1980) Polymer drag reduction in large pipes and sewers: Results of recent field trials. *J Rheol (N Y N Y)* 24(5):667–684.
- Khalil MF, Kassab SZ, Elmiligui AA, Naoum FA (2002) Applications of drag-reducing polymers in sprinkler irrigation systems: Sprinkler head performance. *Journal of Irrigation and Drainage Engineering (ASCE)* 128(3):147–152.
- Virk PS, Mickley HS, Smith KA (1970) The ultimate asymptote and mean flow structure in Toms phenomenon. *Journal of Applied Mechanics - ASME* 37(2):488–493.
- Giles WB, Pettit WT (1967) Stability of dilute viscoelastic flows. *Nature* 216:470–472.
- Dimitropoulos CD, Sureshkumar R, Beris AN, Handler RA (2001) Budgets of Reynolds stress, kinetic energy and streamwise enstrophy in viscoelastic turbulent channel flow. *Phys Fluids* 13(4):1016–1027.
- Min T, Yoo JY, Choi H, Joseph DD (2003) Drag reduction by polymer additives in a turbulent channel flow. *J Fluid Mech* 486:213–238.
- Stone PA, Roy A, Larson RG, Waleffe F, Graham MD (2004) Polymer drag reduction in exact coherent structures of plane shear flow. *Phys Fluids* 16(10):3470–3482.
- Dubief Y, et al. (2004) On the coherent drag-reducing and turbulence-enhancing behaviour of polymers in wall flows. *J Fluid Mech* 514:271–280.
- Li CF, Sureshkumar R, Khomami B (2006) Influence of rheological parameters on polymer induced turbulent drag reduction. *J Nonnewton Fluid Mech* 140(1-3):23–40.
- Roy A, Morozov A, van Saarloos W, Larson RG (2006) Mechanism of polymer drag reduction using a low-dimensional model. *Phys Rev Lett* 97(23):234501.
- Kim K, Adrian RJ, Balachandar S, Sureshkumar R (2008) Dynamics of hairpin vortices and polymer-induced turbulent drag reduction. *Phys Rev Lett* 100(13):134504.
- Xi L, Graham MD (2010) Turbulent drag reduction and multistage transitions in viscoelastic minimal flow units. *J Fluid Mech* 647:421–452.
- Xi L, Graham MD (2012) Dynamics on the laminar-turbulent boundary and the origin of the maximum drag reduction asymptote. *Phys Rev Lett* 108(2):028301.
- Draad AA, Kuiken GDC, Nieuwstadt FTM (1998) Laminar-turbulent transition in pipe flow for Newtonian and non-Newtonian fluids. *J Fluid Mech* 377:267–312.
- Ram A, Tamir A (1964) Structural turbulence in polymer solutions. *J Appl Polym Sci* 8(6):2751–2762.
- Little RC, Wiegand M (1970) Drag reduction and structural turbulence in flowing polyox solutions. *J Appl Polym Sci* 14(2):409–419.
- Ostwald W, Auerbach P (1926) The viscosity of colloidal solutions in the area of structure, laminar and turbulence. *Kolloid Zeitschrift* 38:261.
- Paterson RW, Albernathy FH (1972) Transition to turbulence in pipe flow for water and dilute solution of polyethylene oxide. *J Fluid Mech* 51:177–185.
- Larson RG, Shaqfeh ESG, Muller SJ (1990) A purely elastic instability in Taylor Couette flow. *J Fluid Mech* 218:573–600.
- Shaqfeh ESG (1996) Purely elastic instabilities in viscometric flows. *Annu Rev Fluid Mech* 28:129–185.
- Groisman A, Steinberg V (2000) Elastic turbulence in a polymer solution flow. *Nature* 405(6782):53–55.
- Groisman A, Steinberg V (2001) Efficient mixing at low Reynolds numbers using polymer additives. *Nature* 410(6831):905–908.
- Ho TC, Denn MM (1977) Stability of plane Poiseuille flow of a highly elastic liquid. *J Nonnewton Fluid Mech* 3(2):179–195.
- Morozov AN, van Saarloos W (2007) An introductory essay on subcritical instabilities and the transition to turbulence in visco-elastic parallel shear flows. *Phys Rep* 447:112–143.
- Bonn D, Ingremeau F, Amarouchene Y, Kellay H (2011) Large velocity fluctuations in small-Reynolds-number pipe flow of polymer solutions. *Phys Rev E Stat Nonlin Soft Matter Phys* 84(4 Pt 2):045301.
- Pan L, Morozov A, Wagner C, Arratia PE (2013) Nonlinear elastic instability in channel flows at low Reynolds numbers. *Phys. Rev Lett* 110:174502.
- Fouxon A, Lebedev V (2003) Spectra of turbulence in dilute polymer solutions. *Phys Fluids* 15(7):2060–2072.
- Boffetta G, Celani A, Mazzino A (2005) Drag reduction in the turbulent Kolmogorov flow. *Phys Rev E Stat Nonlin Soft Matter Phys* 71(3 Pt 2B):036307.
- Watanabe T, Gotoh T (2010) Coil-stretch transition in an ensemble of polymers in isotropic turbulence. *Phys Rev E Stat Nonlin Soft Matter Phys* 81(6 Pt 2):066301.
- Hof B, de Lozar A, Avila M, Tu X, Schneider TM (2010) Eliminating turbulence in spatially intermittent flows. *Science* 327(5972):1491–1494.
- Hof B, Westerweel J, Schneider TM, Eckhardt B (2006) Finite lifetime of turbulence in shear flows. *Nature* 443(7107):59–62.
- Hof B, de Lozar A, Kuik DJ, Westerweel J (2008) Repeller or attractor? Selecting the dynamical model for the onset of Turbulence in Pipe flow. *Phys Rev Lett* 101(21):214501.
- Burghelera T, Segre E, Steinberg V (2004) Mixing by polymers: Experimental test of decay regime of mixing. *Phys Rev Lett* 92(16):164501.
- Jun Y, Steinberg V (2010) Mixing of passive tracers in the decay Batchelor regime of a channel flow. *Phys Fluids* 22(12):123101.
- Dubief Y, et al. (2005) New Answers on the Interaction Between Polymers and Vortices in Turbulent Flows. *Flow Turbulence and Combustion* 74(4):311–329.
- White CM, Dubief Y, Klewicki J (2012) Re-examining the logarithmic dependence of the mean velocity distribution in polymer drag reduced wall-bounded flow. *Phys Fluids* 24(2):021701.
- Chong MS, Perry AE, Cantwell BJ (1990) A general classification of three-dimensional flow fields. *Physics of Fluids A* 2(5):765–777.
- Warholic MD, Massah T, Hanratty TJ (1999) Influence of drag-reducing polymers on turbulence: Effects of Reynolds number, concentration and mixing. *Exp Fluids* 26(5):461–472.
- de Lozar A, Hof B (2009) An experimental study of the decay of turbulent puffs in pipe flow. *Philos Trans A Math Phys Eng Sci* 367(1888):589–599.
- Avila K, et al. (2011) The onset of turbulence in pipe flow. *Science* 333(6039):192–196.
- Housiadas KD, Beris AN (2006) Extensional behavior influence on viscoelastic turbulent channel flow. *J Nonnewton Fluid Mech* 140(1-3):41–56.
- Tamano S, Itoh M, Hotta S, Yokota K, Morinishi Y (2009) Effect of rheological properties on drag reduction in turbulent boundary layer flow. *Phys Fluids* 21(5):055101.
- Dallas V, Vassilicos JC, Hewitt GF (2010) Strong polymer-turbulence interactions in viscoelastic turbulent channel flow. *Phys Rev E Stat Nonlin Soft Matter Phys* 82(6 Pt 2):066303.

## Supporting Information

Samanta et al. 10.1073/pnas.1219666110

### SI Text

#### Sample Preparation and Characterization

The fluid was prepared by adding the required quantity of polymers to 30 L of distilled water. The solution was gently stirred for 48 h, and measurements were performed within a week. The solutions were characterized by means of a commercial rheometer (MARS II; Thermo Fisher Scientific) in controlled shear rate mode using a cone and plate geometry (diameter = 60 mm, cone angle = 0.5°). The instrument was set to a temperature of  $T = 20$  °C, which is the same temperature the pipe flow experiments were conducted at. The solutions were tested before and after the measurements in the pipe; in addition, we tested samples that were prepared in smaller quantities (250 mL) by means of the same protocol mentioned above. The results for the different solutions agreed within an experimental resolution of  $\pm 5\%$  and in agreement with former studies (1). Specifically, we did not observe any notable degradation of the polymer on the time scale of resident times in the tube experiments, in the rheological shear tests, or in the capillary breakup extensional rheometer (CaBER). The viscosity was measured at shear rates  $30 \text{ s}^{-1} < \dot{\gamma} < 2,500 \text{ s}^{-1}$  for polymer concentrations of 50 ppm, 100 ppm, 200 ppm, 300 ppm, 400 ppm, and 500 ppm. The effect of shear thinning is negligible [i.e., the respective power law coefficients were very small ( $< 0.026$ , compare Fig. S1)]. The (zero-)shear viscosity  $\eta$  increases with the polymer concentration  $c$  and from the dilution series, we can extract an overlap concentration of  $c^* \approx 1,280$  ppm (compare Fig. S2) via a quadratic fit satisfying  $[\eta] = \lim_{c \rightarrow 0} (\eta(c) - \eta_s) / \eta_s = 1/c^*$  (2).

In addition, the pressure drop in the pipe in the laminar case was calculated by means of the measured viscosity data and with the assumption of a parabolic flow profile. Again, the calculated values and the measured pressure drops agreed within  $\pm 5\%$ . The Reynolds number ( $Re$ ) was determined by means of the viscosity of the sample solution (i.e.,  $Re = \rho U D / \eta$ ).

The second rheological characterization was performed with a custom-built CaBER (3) at ambient temperature ( $T \approx 23$  °C). A droplet of the sample was placed between two steel plates, from which the upper one is displaced by a linear motor until the capillary bridge becomes unstable due to the Rayleigh–Plateau instability. In the following thinning process, a parallel filament is formed that shrinks exponentially in time. The characteristic time scale of the thinning process  $\lambda_C$  (compare Fig. S3) can be related to the polymer relaxation time  $\lambda$ . Simple models predict  $\lambda = 3\lambda_C$ , but it has been shown that the relation is much more complex in reality (1, 4). However, the CaBER is still most sensitive to the elasticity of diluted aqueous solutions, and the time scale  $\lambda_C$  is commonly used to define a Weissenberg number ( $Wi$ ) (5). The relaxation time  $\lambda_C$  depends on the concentration  $c$  according to a power law  $\lambda_C \propto c^{0.89 \pm 0.03}$  (1). The nonlinear fit was performed by direct weighting of the data to account for the increasing sparseness of filament data when decreasing the polymer concentrations and relaxation time, respectively. The error bars represent the SE of the measurement series of each concentration.

From the CaBER relaxation times, an estimate of the critical Weissenberg numbers ( $Wi_c$ ) can be made, and we found that the  $Wi_c$  were in the range of  $Wi_c = 3 - 15$ .

#### Velocity Measurements

Velocity measurements were carried out with particle image velocimetry in the  $D = 4$ -mm pipe. The flow was illuminated in the mid  $r$ - $z$  plane (with  $z$  being the axial direction and  $r$  being the

radial direction) using a laser light sheet for the experiments with polymer solution and a high-power light-emitting diode for the experiments with water, respectively. The fluid was seeded with 13- $\mu\text{m}$  spherical hollow glass spheres to obtain particle images. Sampling rates of the camera (Phantom V10; Vision Research) were 200 Hz for the polymer experiments and 50 Hz for the case of water. In Fig. S4, we show the  $z$  component of the velocity measured at the pipe centerline: In the case of water, the theoretical value of the centerline velocity for a laminar velocity profile for the given Reynolds number has been subtracted, and in the case of polymer, the average velocity has been subtracted. At  $Re = 527$ , the flow in the 500-ppm polyacrylamide solution is laminar. Once the  $Re$  is raised above 800, elasto-inertial turbulence (EIT) sets in and fluctuations start to increase with the  $Re$  (Fig. S4B). As shown in Fig. 4B for  $Re = 2,140$ , the flow is uniformly fluctuating. For a water flow with a similar  $Re = 2,080$  (Fig. S4C), however, flows show the intermittency distinctive of the transitional regime in Newtonian turbulence, with turbulent puffs (characterized by a strong dip of the centerline velocity) interspersed by more quiescent flow.

#### Initial Perturbations for Direct Numerical Simulations

The protocol for our simulation was designed to mimic the perturbed experimental setup within the limitation inherent to boundary conditions. For any flow, Newtonian or polymeric, the laminar solution is first obtained. Once the laminar flow is fully developed, a perturbation is introduced over a short duration, in the form of blowing and suction velocity on both walls, over which white noise of prescribed intensity is introduced. The velocity pattern is periodic in  $x$  and  $z$ :

$$v_w(x, z, t) = A \sin\left(\frac{8\pi x}{L_x}\right) \sin\left(\frac{8\pi z}{L_z}\right) + \varepsilon(t), \quad [\text{S1}]$$

where  $A$  is the amplitude,  $L_x$  and  $L_z$  are the horizontal domain dimensions, and  $\varepsilon(t)$  is the random noise. The amplitude is increased from zero over the first 10% of the duration of the perturbation and decreased to zero over the last 10%. Choosing  $A = 0.09U_b$  and the rms of  $\varepsilon$  at  $0.005U_b$  causes the Newtonian flow to transition at  $Re = 6,000$ . The total duration of the perturbation is  $0.5H/U_b$ .

#### Polymer Extension

Fig. S5 shows profiles of polymer extension, defined as

$$\frac{X}{L} = \frac{\sqrt{\text{tr}(\mathbf{C})}}{L}, \quad [\text{S2}]$$

across the channel half-height. The extension of polymers at the lowest  $Re$  is just shy of 20% of maximum polymer extension. At 17.4%, the wall polymer extension is higher than the analytical solution for a purely laminar channel flow (16.2%), due to the fluctuations of the velocity gradient tensor caused by EIT. Single-molecule experiments measured extension in shear flow, at  $Wi = 25$ , around 30% (6, 7). This discrepancy comes from the semiquantitative nature of the finitely extensible nonlinear elastic Peterlin (FENE-P) model. The choice of the polymer parameters is a compromise between capturing the key dynamical features of polymer–flow interactions and numerical stability. Among others, Li et al. (8), Housiadas and Beris (9), and Tamano et al. (10) studied the effects of rheological parameters and viscoelastic models. The conclusions of these studies are that (a)

elongational viscosity is the most important rheological property and (b) long polymers and a large  $Wi$  are more likely to reproduce the features of polymer drag reduction, especially maximum drag reduction. It is noteworthy that simulations with a smaller polymer  $L = 100$ , which yields a wall extension of 30%, were also found to produce EIT. Our choice of polymer length was motivated by the fact that using longer polymers emphasizes the elastic instability and facilitates the study of EIT while retaining the same dynamics as with  $L = 100$ .

#### Identification of the Structure of Elasto-inertial Instability

Fig. 4 shows an interesting pattern of flow instabilities in the form of quasi-2D patterns aligned in the streamwise direction. The identification of the flow structures is made possible by the visualization of isosurfaces of  $Q$ , the second invariant of the velocity gradient tensor  $\nabla\mathbf{u}$ . Defining the velocity gradient tensor as  $\nabla\mathbf{u} = \partial u_i / \partial x_j$ , the second and third  $R$  invariants are written as

$$Q = -\frac{1}{2} \frac{\partial u_i}{\partial x_j} \frac{\partial u_j}{\partial x_i}, \quad [\text{S3}]$$

$$R = -\frac{1}{3} \frac{\partial u_i}{\partial x_j} \frac{\partial u_j}{\partial x_k} \frac{\partial u_k}{\partial x_i}, \quad [\text{S4}]$$

where Einstein's index rule applies.  $Q$  and  $R$  are used to study the topology of turbulent flows (11) because their local values relate to the local topology of the streamlines. This is illustrated in Fig. S6 in the  $Q - R$  phase diagram that defines four quadrants delimited by  $R = 0$  and  $D = 0$ , where  $D$  is the discriminant of  $\nabla\mathbf{u}$ :

$$D = \frac{27}{4} R^2 + Q^3. \quad [\text{S5}]$$

It can also be shown that  $Q$  is the difference between the norm squared of the rotation and strain rate tensors, which suggests that positive regions of  $Q$  are regions where the local rotation rate overcomes the strain rate. This argument is the motivation for the widespread use of the positive  $Q$  criterion (12) for the identification of vortices. However, it is important to point out that the  $Q$ -vortex identification method is subjective, because the proper reduction of vortices requires that  $Q > Q_{\text{th}}$ , where  $Q_{\text{th}}$  is a positive threshold that depends on the flow intensity.

The local topology of the flow determines the stretching dynamics of the polymer field. Specifically, extensional flows cause the polymer to stretch, thereby increasing the local extensional viscosity, which is, for instance, the source of polymer drag reduction (13). At  $Re = 1,000$  (Fig. 4 and Fig. S7A), compact regions of positive  $Q$  do not define vortices because they fail to meet the criterion of spiraling streamlines (12). Nonetheless, the contours of  $D$  (Fig. S7A) clearly show that the isosurfaces of positive and negative  $Q$  are regions of weakly rotational and extensional flows in regions of large polymer extension, as shown by Fig. S7B. These fluctuations of extensional flow create, in turn, fluctuations of extensional viscosity that directly affect the flow. Note that the computational grid is displayed in Fig. 7A to demonstrate that the elastic instability is well resolved. In this particular case, the grid spacing in  $x$  is  $\approx 1l^+ = \nu/u_\tau$ .

- Zell A, Gier S, Rafai S, Wagner C (2010) Is there a relation between the relaxation time measured in CaBER experiments and the first normal stress coefficient? *J Nonnewton Fluid Mech* 165:1265–1274.
- Kozicki W, Kuang PQ (1996) An alternative method for evaluation of intrinsic viscosity. *Can J Chem Eng* 74:429–432.
- Anna SL, McKinley GH (2001) Elasto-capillary thinning and breakup of model elastic liquids. *J Rheol (N Y N Y)* 45:115–138.
- Clasen C, et al. (2006) How dilute are dilute solutions in extensional flows? *J Rheol (N Y N Y)* 50:849.
- Rodd LE, Scott TP, Boger DV, Cooper-White JJ, McKinley GH (2005) The inertio-elastic planar entry flow of low-viscosity elastic fluids in micro-fabricated geometries. *J Nonnewton Fluid Mech* 129:1–22.
- Smith DE, Babcock HP, Chu S (1999) Single-polymer dynamics in steady shear flow. *Science* 283:5408.
- Gerashchenko S, Steinberg V (2006) Statistics of tumbling of a single polymer molecule in shear flow. *Phys Rev Lett* 96(3):038304.
- Li C-F, Sureshkumar R, Khomami B (2006) Influence of rheological parameters on polymer induced turbulent drag reduction. *J Nonnewton Fluid Mech* 140:2340.
- Housiadas KD, Beris AN (2006) Extensional behavior influence on viscoelastic turbulent channel flow. *J Nonnewton Fluid Mech* 140(1-3):4156.
- Tamano S, Itoh M, Hotta S, Yokota K, Morinishi Y (2009) Effect of rheological properties on drag reduction in turbulent boundary layer flow. *Phys Fluids* 21:055101.
- Chong MS, et al. (1998) Turbulence structures of wall-bounded shear flows found using DNS data. *J Fluid Mech* 357:225–247.
- Dubief Y, Delcayre F (2000) On coherent-vortex identification in turbulence. *Journal of Turbulence* 1(1):11.
- Terrapon VE, Dubief Y, Moin P, Shaqfeh ESG, Lele SK (2004) Simulated polymer stretch in a turbulent flow using Brownian dynamics. *J Fluid Mech* 504:61–71.

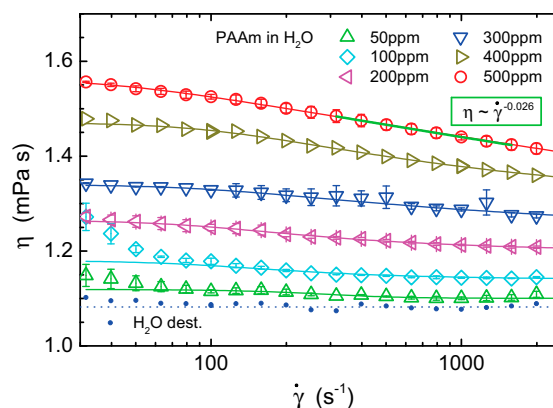


Fig. S1. Shear viscosities of the polymer solutions measured at shear rates between  $30 \text{ s}^{-1}$  and  $2,500 \text{ s}^{-1}$  for solutions of 50 ppm, 100 ppm, 200 ppm, 300 ppm, 400 ppm, and 500 ppm at  $T = 20^\circ \text{C}$ . Shear thinning is of little importance. Also shown is a reference measurement with pure water.

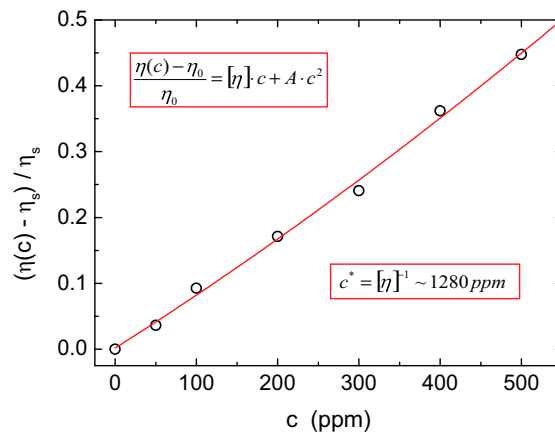


Fig. 52. Specific (zero)-shear viscosity of the polymer solutions for different concentrations. The overlap concentration is estimated to be  $c^* \approx 1,280$  ppm.

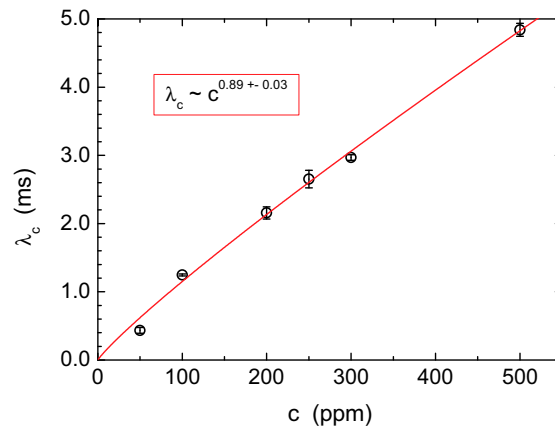


Fig. 53. Characteristic relaxation time  $\lambda_c$  of the polymer solutions in the CaBER experiments. It scales with the polymer concentration  $c$  with a power law with an exponent of  $0.89 \pm 0.03$ .

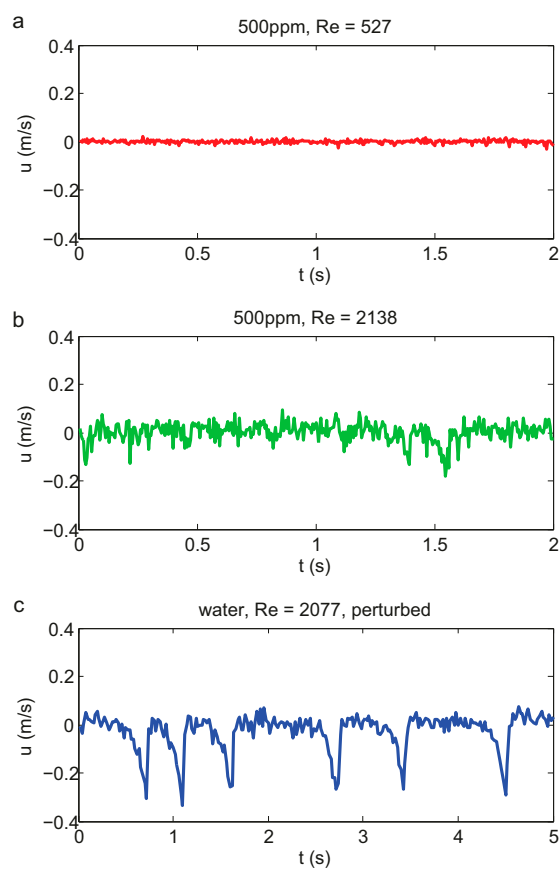


Fig. 54. Velocity time series. (A) Centerline velocity of laminar flow in a 500-ppm polymer solution at  $Re = 530$ . (B) Velocity time series in the elasto-inertial turbulent regime at  $Re = 2,140$ . (C) Velocity trace in a pure water flow at  $Re = 2,080$  shows the intermittent appearance of turbulent puffs typical of Newtonian turbulence.

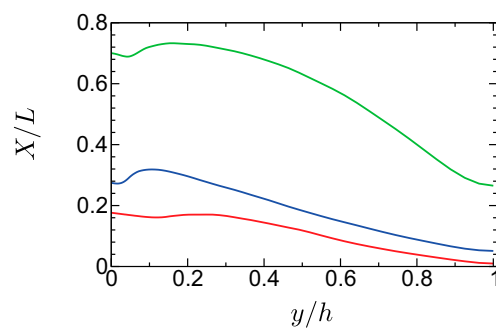


Fig. 55. Profiles of polymer extension defined by  $X/L = \sqrt{\text{tr}(\mathbf{C})}/L^2$  as a function of the distance from the wall normalized by the half-height of the channel  $y/h$ . Red line,  $Re = 1,000, Wi = 24$ ; blue line,  $Re = 6,000, Wi = 100$ ; green line,  $Re = 6,000, Wi = 700$ .

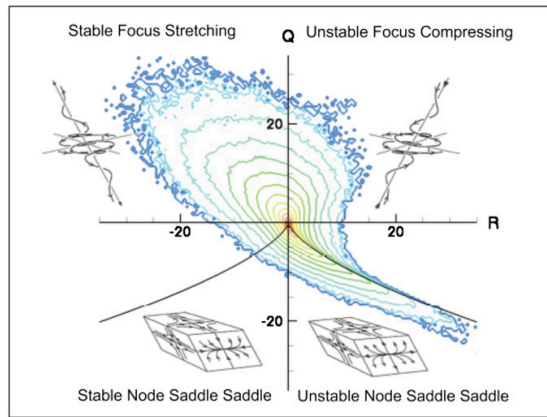


Fig. S6. Flow topology in the  $Q-R$  phase diagram [Reprinted with permission from the study by Chong et al. (13)], with the typical inverted teardrop shape of a joint-probability density function of a turbulent flow. The figure shows the four quadrants of flow topology delimited by  $R=0$  and  $D=0$  (Eq. S5), from ( $R>0, D>0$ ) counterclockwise: rotational flow under compression, rotational flow under extension, biaxial compressional flow, and biaxial extensional flow.

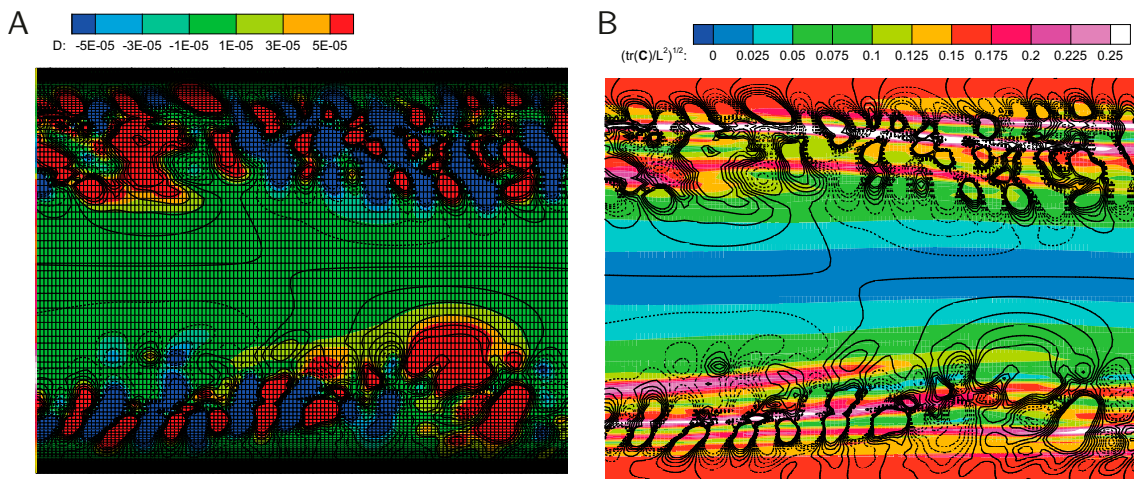


Fig. S7. Visualization of the instability observed in Fig. 4 in a cross-sectional plane of the flow (left to right) for about one-fourth of the length of the domain. The walls are the top and lower boundaries. (A) Contours of positive (solid black lines) and negative (dashed black lines)  $Q$  superimposed over the contours of positive (red) and negative (blue)  $D$  in a cross-sectional plane of the flow aligned with the streamwise and wall-normal directions. The grid is shown to demonstrate that the observed instability is fully resolved. (B) Contour lines are the same as in A, with contours of the polymer extension.

### C.3 Rheology of human blood plasma [Bru13]

Blood plasma is the aqueous solution which carries the blood cells, mainly red blood cells (erythrocytes, about 45 vol.%) and white blood cells (including platelets and leukocytes). Although it also contains proteins (aside from hormones, glucose and mineral ions), i.e. long-chained carbon molecules, it has been long considered to be Newtonian and consequently not contributing to the non-Newtonian rheology of whole blood neither in controlled experimental environment (in vitro) nor within a natural setting (in vivo). Indeed, so far, all experimentally observed deviations from the Newtonian flow behavior could be attributed to the surface activity of the plasma proteins and not to a real bulk effect.

In contrast to this common believe, the following study [Bru13] could prove that human blood plasma definitely behaves like a non-Newtonian fluid and exhibits viscoelastic bulk properties even when effectively avoiding surface activity. Viscoelastic flow behavior of blood plasma turned out to be most significant in extensional flow but negligible in steady shear flow in agreement with the literature and it particularly matches the viscoelastic flow behavior of a dilute polymer solution, namely an aqueous solution containing 15 % glycerol and 50 ppm of polyethylene oxide ( $M_w = 4 \times 10^6$  Da). A possible impact to physiological flow conditions (mimiced by microfluidic contraction flow) could be suggested, particularly in view of the recent findings of elasto-inertial turbulence in pipe flow.

The underlying extensive rheological characterization by means of capillary breakup extensional rheometry (CaBER) as well as steady shear rheometry constitutes the author's contribution to this project. In this context, great effort has been invested to find the perfect polymer match for the blood plasma.



## Rheology of Human Blood Plasma: Viscoelastic Versus Newtonian Behavior

M. Brust,<sup>1</sup> C. Schaefer,<sup>1</sup> R. Doerr,<sup>1</sup> L. Pan,<sup>2</sup> M. Garcia,<sup>2</sup> P.E. Arratia,<sup>2</sup> and C. Wagner<sup>1,\*</sup>

<sup>1</sup>*Experimentalphysik, Universität des Saarlandes, Postfach 151150, 66041 Saarbrücken, Germany*

<sup>2</sup>*Department of Mechanical Engineering and Applied Mechanics, University of Pennsylvania, Philadelphia, Pennsylvania 19104, USA*

(Received 16 August 2012; revised manuscript received 5 December 2012; published 15 February 2013)

We investigate the rheological characteristics of human blood plasma in shear and elongational flows. While we can confirm a Newtonian behavior in shear flow within experimental resolution, we find a viscoelastic behavior of blood plasma in the pure extensional flow of a capillary breakup rheometer. The influence of the viscoelasticity of blood plasma on capillary blood flow is tested in a microfluidic device with a contraction-expansion geometry. Differential pressure measurements revealed that the plasma has a pronounced flow resistance compared to that of pure water. Supplementary measurements indicate that the viscoelasticity of the plasma might even lead to viscoelastic instabilities under certain conditions. Our findings show that the viscoelastic properties of plasma should not be ignored in future studies on blood flow.

DOI: [10.1103/PhysRevLett.110.078305](https://doi.org/10.1103/PhysRevLett.110.078305)

PACS numbers: 83.50.Jf, 83.60.Wc, 87.19.U–

Blood is a complex fluid that consists of a suspension of blood cells in a liquid plasma which contains mostly water as well as proteins, mineral ions, hormones, and glucose. In humans, red blood cells (RBCs) are the most abundant type of cells in whole blood with a concentration of approximately 45% by volume. Because of this high RBC concentration, it is often believed that rheological behavior of whole blood is mostly determined by the presence of the RBCs. Blood exhibits shear thinning, and at low shear rates the red blood cells form reversible aggregates (rouleaux) that are broken up at high shear rates [1]. The rouleaux formation is caused by the plasma proteins (most likely due to a depletion effect), but the plasma solution, which is approximately 92% water, is currently believed to be Newtonian [1–3]. For example, experiments by Copley and King [4] and Jaishankar, Sharma, and McKinley [5] show that the non-Newtonian and viscoelastic effects found in plasma and bovine serum albumin (BSA) solutions in shear flows can be attributed to the surface layer of plasma proteins present at the liquid-air interface; that is, these non-Newtonian effects are surface rather than bulk effects. These surface effects can be suppressed by the addition of a small amount of surfactants to the protein solutions [5].

Much work has been devoted to the understanding of laminar blood flow as well as the appearance of flow instabilities that may appear under pathological conditions, e.g., near an aneurysm or blockage [6,7]. In general, one has to distinguish between inertia and viscoelastic driven instabilities. An elegant way to separate these two kinds of instabilities is the observation of vortices in a contraction flow device. Inertial effects lead to downstream vortices, whereas upstream vortices can be observed for viscoelastic fluids [8,9]. This approach has been used in a recent work by Sousa *et al.* [2], which gives an overview of the flow of two common blood analog solutions in contraction-expansion

microfluidic devices. The two investigated blood replacement solutions with the same shear but different elongational viscosity revealed a remarkably different flow behavior, which shows that it is not sufficient to consider only the shear viscosity in order to build a plasma analog solution. A pronounced viscoelastic behavior in elongational flow has been found in several other biofluids, too, e.g., for saliva [10,11] or DNA solutions.

In this Letter, we investigate the rheology and flow behavior of human blood plasma in both shear and extensional flows. We find that blood plasma shows significant viscoelastic effects in elongational flow in both (i) a capillary breakup extensional rheometer (CaBER, Fig. 1) and (ii) a microfluidic contraction-expansion device. In addition, a synthetic (polymeric) plasma replacement solution is identified that matches the shear and extensional rheology of human plasma.

*Sample solutions.*—Blood plasma used in the experiments was taken from three healthy donors and stored in test tubes using anticoagulants [Ethylenediaminetetraacetic acid or Citra]. Plasma is obtained by centrifuging the blood samples at 4000 rotations per minute for 5 min immediately after withdrawal. The separated transparent liquid phase is centrifuged again, and finally the pure plasma phase is extracted. All measurements are performed on the day of donation. Since the main protein in the plasma is albumin, an aqueous solution of 45 mg/ml albumin (BSA, Polysciences) is prepared for comparison. The plasma replacement solutions are prepared by adding small amounts of polyethylene oxide (PEO, Sigma Aldrich,  $M_w = 4 \times 10^6$  g/mol) to a Newtonian solvent. Three PEO solutions are prepared: (i) a 50 ppm PEO in 15/85 wt% glycerol-water solution (PEO50<sub>15/85</sub>), (ii) a 500 ppm PEO in 15/85 wt% glycerol-water solution (PEO500<sub>15/85</sub>), and (iii) a 50 ppm PEO in a 55/45 wt%

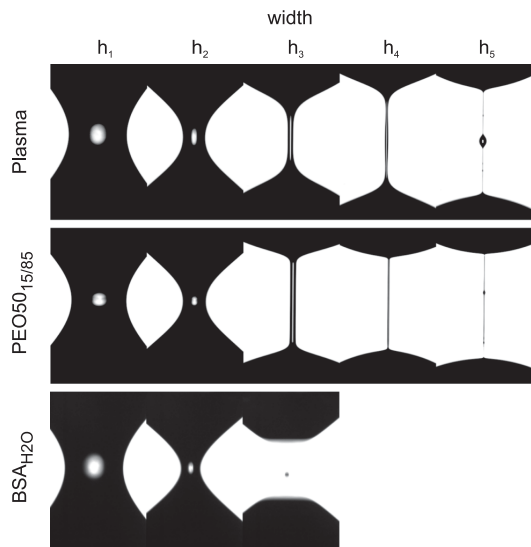


FIG. 1. Snapshots of the capillary bridges in the CaBER experiment. Images are  $833 \mu\text{m} \times 1344 \mu\text{m}$ .

glycerol-water solution (PEO50<sub>55/45</sub>). Two RBC suspensions at 50 vol% are also used, one in physiological buffer [phosphate buffered saline (PBS), Invitrogen] with 15 wt% glycerol (PBS<sub>15/85-Hct50</sub>) and the other under the same condition but with the addition of 50 ppm of PEO (PEO50<sub>15/85-Hct50</sub>). Finally, whole blood and distilled water are used as reference fluids.

Steady shear rheology is performed in a rheometer (Thermo Scientific, HAAKE MARS II) at shear rates ranging from  $\dot{\gamma} = 1$  to  $1000 \text{ s}^{-1}$  in rate controlled mode. A double-cone DC60/1° geometry is used in order to avoid the effect of surface viscoelasticity on the measured shear viscosity  $\eta(\dot{\gamma})$ . To reduce the instrumental noise, a special protocol is applied. For each shear rate, the torque signal is integrated over at least a full revolution of the cone. The minimal resolvable torque is  $\tau_{\text{min}} = 2 \mu\text{NM}$ , which limits the reliable minimal shear rate. Above, the accuracy is  $\Delta\eta = \pm 0.1 \text{ mPa}\cdot\text{s}$ . The temperature is kept constant at  $T = 20 \pm 1^\circ\text{C}$ .

Figure 2 shows the shear viscosity of blood plasma at room temperature ( $RT = 20^\circ\text{C}$ ), along with viscosity data of whole blood (average of three donors), two dilute PEO solutions, and a reference curve of pure water. Within the reliable data range (above the gray shaded area), the plasma sample as well as the 50 ppm PEO in 15 wt% glycerol-water solution show Newtonian behavior, that is, constant shear viscosity  $\eta$ . By contrast, the addition of a physiologic amount of RBCs (Hct50%) significantly increases the viscosity of the PEO solution. The solution exhibits shear thinning, and the flow curve can be fitted to the Carreau model [12]. The viscosity of full blood is

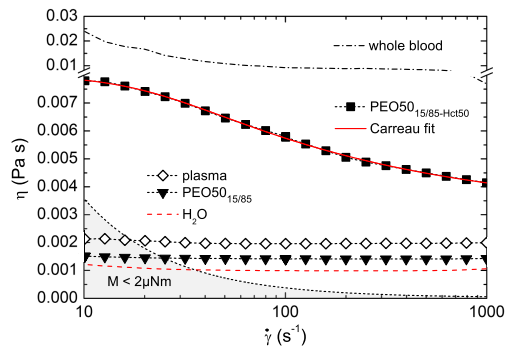


FIG. 2 (color online). Shear rate dependent viscosity  $\eta(\dot{\gamma})$  data at  $T = 20^\circ\text{C}$  obtained by the rotational shear measurements. The gray shaded area indicates the regime below the resolution of the rheometer.

higher than the viscosity of the PEO50<sub>15/85-Hct50</sub> solution. It is known that plasma proteins lead to a depletion-induced formation of aggregates of RBCs at low shear rates, and this effect might be less pronounced for the PEO solutions [1]. Table I summarizes the estimated zero shear viscosities  $\eta_0$ . We should mention that our determination of  $\eta_0$  for whole blood is of limited use only, because blood is a yield stress fluid (yield point was found to be approximately 5 mPa).

The relaxation time of the fluids is obtained by using a custom-made capillary breakup extensional rheometer (CaBER) setup [13,14]. The thinning of the capillary bridge is recorded by using a high speed camera and  $4\times$  magnification objective (Pentax, PLAN 4x/0.10, WD = 30). We find that the solutions have relatively short relaxation times, and a slow retraction method is used to allow for a quantitative evaluation of the data [15]. For a non-Newtonian fluid, the initial inertio-capillar thinning of the capillary bridge is followed by a formation of a straight filament, which thins exponentially in time. The relation  $h(t) = h_0 \exp[-(t - t_0)/\lambda_c]$  gives the characteristic CaBER relaxation time  $\lambda_c$ , where  $h(t)$  is the diameter of the filament at the time  $t$  during the exponential thinning process, which starts at time  $t_0$  and width  $h_0$ , respectively. According to the Oldroyd-B model, a simple approach leads to an estimate for the polymer relaxation time  $\lambda = \lambda_c/3$  [16,17].

Figure 1 shows a series of images of the thinning process of the capillary bridges of the plasma as well as the BSA and PEO50<sub>15/85</sub> solutions. The capillary bridge of the BSA solution shows the same dynamics as the distilled water (not shown), within experimental resolution. In this case, the capillary bridge breaks fast and leaves a well known satellite droplet. By contrast, the plasma and the PEO50<sub>15/85</sub> solution form a viscoelastic thread that thins exponentially in time (see Fig. 3). Both solutions also show the typical blistering instability at the very end of the

TABLE I. (Zero) shear viscosities  $\eta_0$  and CaBER relaxation times  $\lambda_C$  of the sample solutions.

Solution	Temperature $T$ (°C)	Shear viscosity $\eta_0$ (mPa s)	Relaxation time $\lambda_C$ (ms)
Whole blood	37	16.9	$7.8 \pm 0.6$
Plasma	20	1.95	$2.6 \pm 0.2$
Plasma	37	1.34	$1.5 \pm 0.2$
PEO500 <sub>15/85</sub>	20	2.47 <sup>a</sup>	$15.7 \pm 0.2$
PEO50 <sub>15/85</sub>	20	1.40	$2.6 \pm 0.1$
PEO50 <sub>55/45</sub>	20	7.88	$7.9 \pm 0.2$
PEO50 <sub>15/85-Hct50</sub>	20	8.03 <sup>a</sup>	$1.84 \pm 0.04$
BSA <sub>H<sub>2</sub>O</sub>	20	1.24	Newt.
PBS <sub>15/85-Hct50</sub>	37	7.6 <sup>a</sup>	Newt.
H <sub>2</sub> O	20	0.97	Newt.

<sup>a</sup>These values are obtained by a fit based upon the Carreau model [12].

thinning process characterized by the appearance of smaller droplets on the filament [18]. These results clearly demonstrate that plasma has viscoelastic properties.

Figure 3 shows the minimal width  $h(t)$  of the capillary bridge as a function of time  $t - t_{\text{final}}$ . Starting at a width of approximately  $h_1 \approx 0.5$  mm, all curves initially describe a uniform thinning down to an intermediate level of  $h_2 \approx 0.17$  mm. At this stage, polymers in the solution do not yet affect the flow, and the difference between the solutions can be seen only during further thinning of the filament. While the capillary bridge of the Newtonian sample breaks very rapidly (cf. width  $h_3$ ), the other samples form a filament which thins exponentially over characteristic time scales  $\lambda_C$ . Table I summarizes the corresponding relaxation times as averages over all performed measurements. Note that the BSA solution does not show any non-Newtonian behavior, and therefore we can exclude that the protein surface layer of the plasma is responsible for the elastic thinning behavior (in agreement with Ref. [19]), but some other plasma proteins in the bulk that have not yet been identified are responsible for the viscoelasticity. This result is also corroborated in a cone-plate geometry with a free surface layer: Adding

0.01 wt% of the soluble nonionic surfactant (Tween 20, critical micellar concentration  $cmc = 0.07$  wt%) to the plasma did indeed suppress the apparent shear thinning (data not shown) in agreement with the experiments described in Ref. [5]. Please note that in principle surfactants can lead to viscoelastic filaments themselves, but in our case the surfactant dissolved in pure water did not show any filament [20–28]. However, the addition of a surfactant to the plasma did *not* alter the thinning process in the CaBER, which again shows that the filament is not caused by a protein surface layer. We note that additional thinning experiments of the plasma solution were performed in which the surrounding air was replaced by silicon oil and a pronounced filament was as well observed (data not shown).

Again, we can compare our polymer solutions that should serve as model systems with the plasma samples. The data presented in Table I show that the PEO50<sub>15/85</sub> solution is a good plasma replacement solution, because it matches the plasma shear and elongational properties; by simply increasing the solvent viscosity of this solution, we get the PEO50<sub>55/45</sub> sample that matches the elongational properties of full blood, but it does not match its shear rheology very well. Therefore, we compared a PBS buffer solution with 50 vol% hematocrit without polymer (PBS<sub>15/85-Hct50</sub>), with polymer (PEO50<sub>15/85-Hct50</sub>), and with full blood. The polymeric hematocrit solutions reflects the elongational properties of blood to some extent. However, the PBS<sub>15/85-Hct50</sub> solution simply breaks up like a Newtonian liquid. This clearly shows that the non-Newtonian elongational viscosity (i.e., the elastic properties of the macromolecules) of the plasma contributes to the non-Newtonian elongational viscosity of blood. Again, an additional clustering of the RBCs in the whole blood due to the rouleaux formation might explain the remaining discrepancies.

Next, the effects of this apparent viscoelasticity of plasma flow are investigated in a microfluidic contraction-expansion device by measuring the pressure drop across the contraction part of the geometry [8,9]. This geometry has a

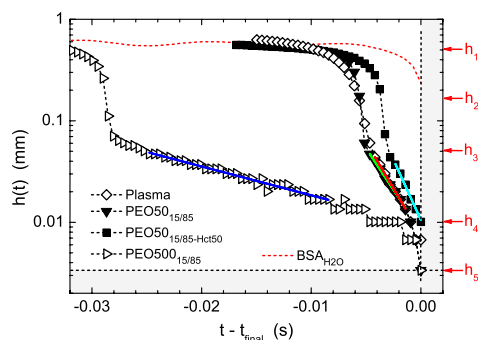


FIG. 3 (color online). Width  $h(t)$  of the capillary bridge as a function of time  $t - t_{\text{final}}$ . Markers on the right vertical axis refer to the images shown in Fig. 1. Straight lines are exponential fits.

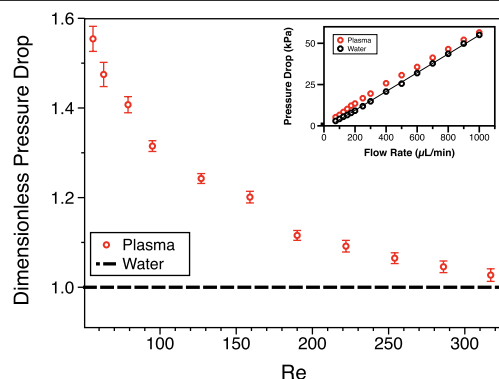


FIG. 4 (color online). Dimensionless pressure drop as a function of Reynolds number. The data show higher values of pressure drop for human plasma compared to water. Blood plasma shows a nonlinear, “thinning” behavior of pressure drop as a function of strain rate [29]. Inset: Pressure drop as a function of flow rate. Blood plasma shows nonlinear behavior.

significant elongation flow component, and it resembles flow restricted vessels or the flow at a branching from a larger to a smaller vessel. The microchannels are made of polydimethylsiloxane using standard soft lithography methods. Their length, width, and depth are  $L = 30$  mm,  $W = 400$   $\mu\text{m}$ , and  $h = 50$   $\mu\text{m}$ , respectively. These rectangular microchannels exhibit sharp contraction of reduced width  $w = 25$   $\mu\text{m}$  and length  $l = 100$   $\mu\text{m}$  in the middle. Note that the ratio of the expansion width to the contraction width is 1:16, which sets the (Hencky) elongation strain  $\epsilon = \ln(16) \approx 2.8$ . Pressure measurements are performed by directly incorporating two pressure taps (Honeywell 26PC) into the microchannel, both upstream and downstream of the contraction plane. The pressure sensors are used to cover a differential pressure range of  $0 < \Delta P < 56.5$  kPa. This type of measurement has been successfully applied to investigate the flow of viscoelastic fluids in expansion-contraction microfluidic devices [8].

Results for the pressure drop of both human plasma and water as a function of flow rate, or equivalently Reynolds number (Re), are shown in Fig. 4. Note that here  $\text{Re} = \rho V D_h / \eta_0$ , where  $V$  is the mean flow velocity,  $\rho$  the fluid density,  $\eta_0$  the zero shear rate viscosity, and  $D_h = 2wh/(w+h)$  the hydraulic diameter. For example, Fig. 4 (inset) shows that the water pressure drop increases linearly as the flow rate is increased. On the other hand, the blood plasma pressure drop shows a deviation from this linear trend. This nonlinear behavior can also be observed by normalizing the pressure drop at a given flow rate by the pressure drop of water at the same flow rate. Figure 4 shows that the dimensionless pressure drop of plasma decreases significantly as the Re increases. This indicates an extensional strain-rate thinning viscosity behavior that has been observed in other types of complex fluids such as

micellar solutions [29,30]. These measurements clearly show that blood plasma is a non-Newtonian fluid. We also checked by flow visualization that the increase in resistance is not caused by a viscoelastic instability, but we found that in principle the viscoelastic behavior of plasma could be responsible for viscoelastic instabilities, especially in complex flow situations and in the presence of red blood cells, i.e., 50% hematocrit [31].

In conclusion, we found a pronounced viscoelastic behavior of human blood plasma in a CaBER. Similar to dilute polymer solution, steady shear flow or small amplitude oscillatory shear does not indicate any elasticity of the plasma, because it stretches polymers less efficiently. There are several reports on viscoelasticity of plasma in shear flow, but they all could be attributed to the formation of a protein surface layer, which is not the case in our measurements. We could also show that the elongational properties of blood are to a large extent determined by elongational properties of the plasma proteins. In order to check the generality of our findings, we prepared a plasma replacement fluid with similar elongational and shear properties. Differential pressure measurements in a microfluidic contraction-expansion geometry confirmed the non-Newtonian character of plasma. Supplementary measurements with flow visualization indicate that this viscoelasticity might even lead to viscoelastic flow instabilities. Similarly, it is known that small amounts of polymers with elongational properties as our plasma replacement solution can lead to turbulent drag reduction; i.e., turbulent instabilities due to high inertia might be suppressed by the elongational properties of the plasma. Finally, recent numerical results indicate that a slight viscoelasticity of the solvent might lead to a pronounced cell depletion layer close to the vessel boundaries [32]. In view of these findings, it is expected that the viscoelasticity of plasma has to be taken into account in future studies.

This work was supported by the DFG Graduate college GRK1276 “Structure formation and transport in complex systems.” L. P. and P. E. A. are supported by NSF-CBET-0932449. We thank Anke Lindner and Alexander Morozov for carefully reading the manuscript.

\*c.wagner@mx.uni-saarland.de; <http://agwagner.physik.uni-saarland.de>

- [1] O. K. Baskurt and H. J. Meiselman, *Semin. Thromb. Hemostasis* **29**, 435 (2003).
- [2] P. C. Sousa, F. T. Pinho, M. S. N. Oliveira, and M. A. Alves, *Biomicrofluidics* **5**, 014108 (2011).
- [3] R. E. Wells and E. W. Merrill, *Science* **133**, 763 (1961).
- [4] A. L. Copley and R. G. King, *Thrombosis research* **1**, 1 (1972).
- [5] A. Jaishankar, V. Sharma, and G. H. McKinley, *Soft Matter* **7**, 7623 (2011).
- [6] D. M. Sforza, C. M. Putman, and J. R. Cebral, *Annu. Rev. Fluid Mech.* **41**, 91 (2009).

- [7] H. Baek, M. V. Jayaraman, P.D. Richardson, and G. E. Karniadakis, *J. R. Soc. Interface* **7**, 967 (2010).
- [8] L. E. Rodd, T.P. Scott, D. V. Boger, J.J. Cooper-White, and G. H. McKinley, *J. Non-Newtonian Fluid Mech.* **129**, 1 (2005).
- [9] L. E. Rodd, J.J. Cooper-White, D. V. Boger, and G. H. McKinley, *J. Non-Newtonian Fluid Mech.* **143**, 170 (2007).
- [10] P.P. Bhat, S. Appathurai, M. T. Harris, M. Pasquali, G. H. McKinley, and O. A. Basaran, *Nat. Phys.* **6**, 625 (2010).
- [11] S. J. Haward, V. Sharma, and J. A. Odell, *Soft Matter* **7**, 9908 (2011).
- [12] R. I. Tanner, *Engineering Rheology* (Oxford Science, New York, 1985).
- [13] A. Zell, S. Gier, S. Rafai, and C. Wagner, *J. Non-Newtonian Fluid Mech.* **165**, 1265 (2010).
- [14] R. Sattler, S. Gier, J. Eggers, and C. Wagner, *Phys. Fluids* **24**, 023101 (2012).
- [15] L. Campo-Deano and C. Clasen, *J. Non-Newtonian Fluid Mech.* **165**, 1688 (2010).
- [16] M. Stelter, G. Brenn, A. L. Yarin, R. P. Singh, and F. Durst, *J. Rheol.* **44**, 595 (2000).
- [17] S. L. Anna and G. H. McKinley, *J. Rheol.* **45**, 115 (2001).
- [18] R. Sattler, C. Wagner, and J. Eggers, *Phys. Rev. Lett.* **100**, 164502 (2008).
- [19] O. Regev, S. Vandebril, E. Zussman, and C. Clasen, *Polymer* **51**, 2611 (2010).
- [20] R. V. Craster, O. K. Matar, and D. T. Papageorgiou, *J. Fluid Mech.* **533**, 95 (2005).
- [21] R. V. Craster, O. K. Matar, and D. T. Papageorgiou, *J. Fluid Mech.* **629**, 195 (2009).
- [22] Y.-C. Liao, E. I. Franses, and O. A. Basaran, *Phys. Fluids* **18**, 022101 (2006).
- [23] Y.-C. Liao, H. J. Subramani, E. I. Franses, and O. A. Basaran, *Langmuir* **20**, 9926 (2004).
- [24] S. Kwak and C. Pozrikidis, *Int. J. Multiphase Flow* **27**, 1 (2001).
- [25] P. T. McGough and O. A. Basaran, *Phys. Rev. Lett.* **96**, 054502 (2006).
- [26] O. K. Matar, R. V. Craster, and M. R. E. Warner, *J. Fluid Mech.* **466**, 85 (2002).
- [27] F. Jin, N. R. Gupta, and K. J. Stebe, *Phys. Fluids* **18**, 022103 (2006).
- [28] S. Hansen, G. W. M. Peters, and H. E. H. Meijer, *J. Fluid Mech.* **382**, 331 (2000).
- [29] A. Bhardwaj, E. Miller, and J. P. Rothstein, *J. Rheol.* **51**, 693 (2007).
- [30] J. P. Rothstein, *J. Rheol.* **47**, 1227 (2003).
- [31] See Supplemental Material at <http://link.aps.org/supplemental/10.1103/PhysRevLett.110.078305> for viscoelastic instabilities of plasma, blood, and replacement solutions in a contraction-expansion device.
- [32] P. Pranay, Ph.D. thesis, University of Wisconsin, Madison, 2011.

---

## List of Figures

2.1	The unidirectional shear experiment . . . . .	5
2.2	Sketch of the Maxwell element . . . . .	7
2.3	Sketch of the Jeffreys element . . . . .	8
2.4	Representation of a polymer chain which is regarded as an elastic dumbbell . . . . .	12
2.5	Flow scenario of a Newtonian and viscoelastic fluid . . . . .	16
2.6	Change of conformation of polymer chains in shear flow . . . . .	17
2.7	Rod climbing effect . . . . .	18
2.8	Hoop stress and mechanism of amplification of perturbation . . . . .	18
2.9	Representative spectrum of eigenvalues . . . . .	20
3.1	Schematic and photography of the Haake MARS rotational shear rheometer . . . . .	24
3.2	Representative viscosity and normal stress data of P600 <sub>G80</sub> extracted from steady shear rotational rheometry . . . . .	25
3.3	Schematic representation of the Jeffreys model adapted to the experimental setup. . . . .	28
3.4	Representative shear rate relaxation data of the P600 <sub>G80</sub> solution . . . . .	29
3.5	Shear rate relaxation data of different Newtonian samples . . . . .	30
3.6	Characteristic relaxation time and viscosity extracted from shear rate relaxation data of P600 <sub>G80</sub> according to the Jeffreys model . . . . .	30
3.7	Small amplitude oscillatory data of P600 <sub>G80</sub> . . . . .	32
3.8	Complex viscosity of P600 <sub>G80</sub> from oscillatory data . . . . .	34
3.9	Sketch of the CaBER setup at different steps during the constriction process of the capillary bridge. . . . .	35
3.10	Evaluation of CaBER data of P600 <sub>G80</sub> . . . . .	36
3.11	Sequence of contour images of the capillary bridge of P600 <sub>G80</sub> during the CaBER experiment . . . . .	37
4.1	Pakdel-McKinley criterion versus (axisymmetric) linear stability analysis of the Oldroyd-B model in the small gap limit . . . . .	48
4.2	Summary of various results from linear stability analysis of the Oldroyd-B fluid . . . . .	49
5.1	Viscosities and relaxation times from the steady shear rheometry of the various polymer solutions plotted versus the polymer density number . . . . .	53
5.2	Rheological Weissenberg number of P600 <sub>G80</sub> as a function of the shear rate . . . . .	54
5.3	Estimation of the overlap concentration from the specific viscosity data . . . . .	56
5.4	Determination of the specific viscosity of the glycerol-based PAAm solutions at different shear rates . . . . .	58
5.5	Relaxation time $\lambda_0$ and viscosity $\eta_{1,0}$ from the shear rate relaxation measurements . . . . .	59
5.6	CaBER relaxation time $\lambda^C$ in dependence of the polymer number density $n$ . . . . .	60

5.7	Sequences of filament contour images of different polymer solutions in the CaBER experiment . . . . .	61
5.8	Rescaled filament width of the $M_w = (5-6) \times 10^6$ Da solutions plotted versus the rescaled time . . . . .	62
5.9	Comparison of filament width data of low and high molecular weight solutions . . . . .	62
6.1	Photography and sketch of the set of customized Taylor-Couette cells . . . . .	65
6.2	Torque contributions in the experimental Taylor-Couette setup . . . . .	66
6.3	Sketch of the visualization setup . . . . .	67
7.1	Experimental Taylor-Couette stress data of the P600 <sub>G80</sub> solution . . . . .	69
7.2	Sequence of images from the visualization of the Taylor-Couette flow . . . . .	70
7.3	Space-time plot of the flow patterns during the standard shear rate sweep measurement of P600 <sub>G80</sub> for $\varepsilon = 0.1$ . . . . .	71
7.4	Critical shear rates $\dot{\gamma}_c(\varepsilon)$ mapping the onset of elastic instability in the Taylor-Couette setups of different gap widths $\varepsilon$ . . . . .	72
7.5	Hysteresis of the flow curve in the Taylor-Couette experiment . . . . .	73
7.6	Representative images of the flow patterns at selected instants during the decaying part of the flow curve . . . . .	73
7.7	Evaluation of the experimental Taylor-Couette stress data of P600 <sub>G80</sub> beyond the onset of elastic instability . . . . .	75
7.8	Geometrical transition from the plane to the Taylor-Couette system . . . . .	75
7.9	Maximum of the differential stress data of the various polymer solutions plotted against the relative gap width . . . . .	76
8.1	Local shear rate at different positions within the annular gap of a Taylor-Couette cell . . . . .	80
8.2	Shortcoming of the small gap approximation at different positions within the annular gap of a Taylor-Couette cell . . . . .	81
8.3	Experimental onsets of elastic instability in terms of the modified rheological Weissenberg number plotted against the relative gap width . . . . .	82
8.4	Experimental evaluation of the rheometric scaling of elastic instability . . . . .	83
9.1	Illustration of the convergence of eigenvalues when increasing the number of collocation points $N$ . . . . .	92
9.2	Representative spectrum of maximum eigenvalues of an Oldroyd-B fluid ( $\beta = 0.79$ ) in the isothermal, purely elastic case, accounting for non-axisymmetric ( $m = 1$ ) perturbations . . . . .	92
9.3	Results of the linear stability analysis of the isothermal, purely elastic Taylor-Couette flow of a Maxwell and Oldroyd-B fluid ( $\beta = 0.79$ ) with respect to small axisymmetric perturbations . . . . .	93
9.4	Critical modified Weissenberg numbers of an Oldroyd-B fluid ( $\beta = 0.79$ ) accounting for different perturbation modes . . . . .	94
9.5	Minimal modified Weissenberg number (rescaled by $\sqrt{1-\beta}$ ) plotted against the relative gap width for different values of the relative viscosity $\beta = \eta_s/\eta_0$ . . . . .	95
9.6	Comparison of the different approaches for the rheological scaling of the onset of elastic instability in the small gap limit . . . . .	95
9.7	Linear stability analysis of the hybrid model as compared to the results from the analysis of the Oldroyd-B model . . . . .	99
9.8	Comparison of the different models predicting the onset of elastic instability for a $\beta = 0.55$ polymer solution . . . . .	99
9.9	Specific heat capacities $c_p$ of the various polymer solutions . . . . .	101

9.10	Estimation of the (rescaled) activation energies $\nu = \Delta E/k_B\vartheta_0$ for the different polymer solutions based on an Arrhenius-type viscosity law . . . . .	102
9.11	Interplay between the Nahme and the Péclet number . . . . .	103
9.12	Effect of viscous heating in combination with a fixed temperature difference between the inner and outer wall based on the hybrid model . . . . .	103
9.13	Eigenvalues of the most unstable perturbation mode for $\varepsilon = 0.3$ in different situations with or without incorporating viscous heating and a fixed difference of temperature $\Delta\vartheta = (Z - 1)\vartheta_0$ at the system's boundaries . . . . .	104
9.14	Eigenvalues $\Re(\max_{k_z}\{\mu(k_z, m)\})$ of perturbation modes $m = 0, 1, 2, 3$ of the hybrid model according to the parameters of the P600 <sub>G80</sub> solution . . . . .	105
10.1	Sketch of the protocols used within the degradation study . . . . .	109
10.2	Representative flow curves of fresh or pre-sheared P600 <sub>G80</sub> samples, acquired according to the standard and incomplete scanning protocol, respectively . . . . .	110
10.3	Representative CaBER measurements of a fresh and pre-sheared ( $\dot{\gamma}_{\max} = 80\text{ s}^{-1}$ ) P600 <sub>G80</sub> sample . . . . .	111
10.4	Excess areas of the flow curves from the Taylor-Couette measurements and corresponding CaBER relaxation times of differently pre-processed P600 <sub>G80</sub> samples, both normalized by the respective values of a fresh sample . . . . .	112
10.5	Stress signal of fresh P600 <sub>G80</sub> samples during the shearing at constant shear rate $\dot{\gamma}_{\text{ps}} = 80\text{ s}^{-1}$ . . . . .	112
10.6	Various scanning measurements of P600 <sub>G80</sub> , each performed after an initial pre-shearing at $\dot{\gamma}_{\text{ps}} = 80\text{ s}^{-1}$ for different periods $\Delta t = 600\text{ s}, 6000\text{ s}, 21600\text{ s}$ . . . . .	113
10.7	Temporal development of the stress signal of P600 <sub>G80</sub> during the preprocessing at different steady shear rates $\dot{\gamma}_{\text{ps}}$ . . . . .	113
10.8	Onset of elastic instability of the P600 <sub>G80</sub> solution in the TC-7.5-9.5 setup: the critical shear rates are plotted against the period of pre-shearing at various steady shear rates $\dot{\gamma}_{\text{ps}}$ . . . . .	114
10.9	Excess area $A$ of the Taylor-Couette flow curves of P600 <sub>G80</sub> for different values of shear rates $\dot{\gamma}_{\text{ps}}$ plotted against the period $\Delta t$ of initial pre-shearing . . . . .	114
10.10	Relative CaBER relaxation time $\lambda^C/\lambda_0^C$ of pre-sheared P600 <sub>G80</sub> samples . . . . .	115
10.11	Limiting values $\dot{\gamma}_c^{\text{lim}}$ , $A_{\text{lim}}$ and $\lambda_{\text{lim}}^C$ of P600 <sub>G80</sub> samples that were (infinitely long) sheared at various shear rates $\dot{\gamma}_{\text{ps}}$ . . . . .	115
10.12	Critical Weissenberg number $Wi_c^C = \lambda^C\dot{\gamma}_c$ calculated from the data of CaBER relaxation time and critical shear rate in the Taylor-Couette experiment . . . . .	117
10.13	Weissenberg number $Wi^C = \lambda^C(\dot{\gamma}_{\max})\dot{\gamma}_{\max}$ during a Taylor-Couette standard scanning measurement . . . . .	118
A.1	Steady shear apparent viscosity and normal stress data of the P150 <sub>G80</sub> solution . . . . .	128
A.2	Rheologic Weissenberg number of the P150 <sub>G80</sub> solution . . . . .	128
A.3	Relaxation of shear rate after sudden cessation of constant shear stress $\tau_0$ applied to the P150 <sub>G80</sub> solution . . . . .	129
A.4	Characteristic relaxation time $\lambda$ and viscosity $\eta_1$ of the P150 <sub>G80</sub> solution from the shear rate relaxation experiment . . . . .	129
A.5	Small amplitude oscillatory shear data of the P150 <sub>G80</sub> solution . . . . .	130
A.6	Comparison of small amplitude oscillatory and steady shear data of the P150 <sub>G80</sub> solution . . . . .	130
A.7	Minimal width $h(t)$ of the capillary bridge of various P150 <sub>G80</sub> samples during the constriction process in the CaBER experiment . . . . .	131
A.8	Integral stress data from the Taylor-Couette measurements of the P150 <sub>G80</sub> solution according to the standard scanning protocol . . . . .	131
A.9	Steady shear apparent viscosity and normal stress data of the P1200 <sub>G80</sub> solution . . . . .	132

A.10 Rheologic Weissenberg number of the P1200 <sub>G80</sub> solution . . . . .	132
A.11 Relaxation of shear rate after sudden cessation of constant shear stress $\tau_0$ applied to the P1200 <sub>G80</sub> solution . . . . .	133
A.12 Characteristic relaxation time $\lambda$ and viscosity $\eta_1$ of the P1200 <sub>G80</sub> solution from the shear rate relaxation experiment . . . . .	133
A.13 Small amplitude oscillatory shear data of the P1200 <sub>G80</sub> solution . . . . .	134
A.14 Comparison of small amplitude oscillatory and steady shear data of the P1200 <sub>G80</sub> solution . . . . .	134
A.15 Minimal width $h(t)$ of the capillary bridge of various P1200 <sub>G80</sub> samples during the constriction process in the CaBER experiment . . . . .	135
A.16 Integral stress data from the Taylor-Couette measurements of the P1200 <sub>G80</sub> solution according to the standard scanning protocol . . . . .	135
A.17 Steady shear apparent viscosity and normal stress data of the P500 <sub>S58</sub> solution . . . . .	136
A.18 Rheologic Weissenberg number of the P500 <sub>S58</sub> solution . . . . .	136
A.19 Relaxation of shear rate after sudden cessation of constant shear stress $\tau_0$ applied to the P500 <sub>S58</sub> solution . . . . .	137
A.20 Characteristic relaxation time $\lambda$ and viscosity $\eta_1$ of the P500 <sub>S58</sub> solution from the shear rate relaxation experiment . . . . .	137
A.21 Small amplitude oscillatory shear data of the P500 <sub>S58</sub> solution . . . . .	138
A.22 Comparison of small amplitude oscillatory and steady shear data of the P500 <sub>S58</sub> solution . . . . .	138
A.23 Minimal width $h(t)$ of the capillary bridge of various P500 <sub>S58</sub> samples during the constriction process in the CaBER experiment . . . . .	139
A.24 Integral stress data from the Taylor-Couette measurements of the P500 <sub>S58</sub> solution according to the standard scanning protocol . . . . .	139
A.25 Steady shear apparent viscosity and normal stress data of the P80 <sub>S64</sub> solution . . . . .	140
A.26 Rheologic Weissenberg number of the P80 <sub>S64</sub> solution . . . . .	140
A.27 Relaxation of shear rate after sudden cessation of constant shear stress $\tau_0$ applied to the P80 <sub>S64</sub> solution . . . . .	141
A.28 Characteristic relaxation time $\lambda$ and viscosity $\eta_1$ of the P80 <sub>S64</sub> solution from the shear rate relaxation experiment . . . . .	141
A.29 Small amplitude oscillatory shear data of the P80 <sub>S64</sub> solution . . . . .	142
A.30 Comparison of small amplitude oscillatory and steady shear data of the P80 <sub>S64</sub> solution . . . . .	142
A.31 Minimal width $h(t)$ of the capillary bridge of various P80 <sub>S64</sub> samples during the constriction process in the CaBER experiment . . . . .	143
A.32 Integral stress data from the Taylor-Couette measurements of the P80 <sub>S64</sub> solution according to the standard scanning protocol . . . . .	143
A.33 Steady shear apparent viscosity and normal stress data of the P150 <sub>S65.6</sub> solution . . . . .	144
A.34 Rheologic Weissenberg number of the P150 <sub>S65.6</sub> solution . . . . .	144
A.35 Relaxation of shear rate after sudden cessation of constant shear stress $\tau_0$ applied to the P150 <sub>S65.6</sub> solution . . . . .	145
A.36 Characteristic relaxation time $\lambda$ and viscosity $\eta_1$ of the P150 <sub>S65.6</sub> solution from the shear rate relaxation experiment . . . . .	145
A.37 Minimal width $h(t)$ of the capillary bridge of various P150 <sub>S65.6</sub> samples during the constriction process in the CaBER experiment . . . . .	146
A.38 Integral stress data from the Taylor-Couette measurements of the P150 <sub>S65.6</sub> solution according to the standard scanning protocol . . . . .	146
B.1 Plots of the Chebyshev polynomials $T_n(x)$ of the first kind for $n = 0, 1, \dots, 7$ . . . . .	149

---

## List of Tables

3.1	Parameters of the 2-component hybrid model fitted to the steady shear data of the P600 <sub>G80</sub> solution . . . . .	27
3.2	Parameters of the generalized Jeffreys model fitted to the oscillatory data of the P600 <sub>G80</sub> solution . . . . .	33
5.1	Listing of the various PAAm solutions that were investigated in the presented work	52
5.2	Intrinsic viscosity and overlap concentration (at zero shear rate) of the various polymer solutions . . . . .	57
5.3	Summary of rheometric properties of the different polymer solutions . . . . .	64
6.1	Summary of geometrical parameters of the various experimental Taylor-Couette cells . . . . .	66
7.1	Listing of transition points which give the onset of elastic instability of the different solutions in the various Taylor-Couette cells . . . . .	74
9.1	Summarized results of the linear stability analysis of the isothermal, purely elastic Taylor-Couette base flow of various Oldroyd-B fluids in terms of the critical Weissenberg numbers . . . . .	97
B.1	Chebyshev polynomials $T_n(x)$ of the first kind for $n = 0, 1, \dots, 7$ . . . . .	148

---

## Bibliography

- [Al-99] Al-Mubaiyedh U.A. et al., "*Influence of energetics on the stability of viscoelastic Taylor-Couette flow*", *Physics of Fluids*, **11**(11):3217–3226 (1999).
- [Al-00] Al-Mubaiyedh U.A. et al., "*Linear stability of viscoelastic Taylor-Couette flow: Influence of fluid rheology and energetics*", *Journal of Rheology*, **44**(5):1121–1138 (2000).
- [Alt10] Altmeyer S. and Hoffmann C., "*Secondary bifurcation of mixed-cross-spirals connecting travelling wave solutions*", *New Journal of Physics*, **12**(11):113035 (2010).
- [Alt11] Altmeyer S., "*Untersuchung von komplexen Wirbelströmungen mit newtonschem Fluid und Ferrofluiden im Taylor-Couette System*", Ph.D. thesis, Saarland University (2011).
- [And86] Andereck D.C. et al., "*Flow regimes in a circular Couette system with independently rotating cylinders*", *Journal of Fluid Mechanics*, **164**:155–183 (1986).
- [Ann01] Anna S.L. et al., "*An interlaboratory comparison of measurements from filament-stretching rheometers using common test fluids*", *Journal of Rheology*, **45**(1):83–114 (2001).
- [Asa05] Asadi M., "*Beet-Sugar Handbook*", Wiley (2005).
- [Avg93a] Avgousti M. and Beris A.N., "*Non-axisymmetric modes in viscoelastic Taylor-Couette flow*", *Journal of Non-Newtonian Fluid Mechanics*, **50**(2–3):225–251 (1993).
- [Avg93b] Avgousti M. and Beris A.N., "*Viscoelastic Taylor-Couette flow: Bifurcation analysis in the presence of symmetries*", *Proceedings of the Royal Society of London A - Mathematical and Physical Sciences*, **443**(1917):17–37 (1993).
- [Bal81] Ballauff M. and Wolf B.A., "*Degradation of chain molecules. 1. Exact solution of the kinetic equations*", *Macromolecules*, **14**(3):654–658 (1981).
- [Bal84] Ballauff M. and Wolf B.A., "*Degradation of chain molecules. 2. Thermodynamically induced shear degradation of dissolved polystyrene*", *Macromolecules*, **17**(2):209–216 (1984).
- [Bar98] Baravian C. and Quemada D., "*Using instrumental inertia in controlled stress rheometry*", *Rheologica Acta*, **37**(3):223–233 (1998).

- [Bau95] Baumert B.M. and Muller S.J., "*Flow visualization of the elastic Taylor-Couette instability in Boger fluids*", *Rheologica Acta*, **34**:147–159 (1995).
- [Bau99] Baumert B.M. and Muller S.J., "*Axisymmetric and non-axisymmetric elastic and inertio-elastic instabilities in Taylor-Couette flow*", *Journal of Non-Newtonian Fluid Mechanics*, **83**(1–2):33–69 (1999).
- [Bes54] Bestul A.B., "*Composition of apparent shearing forces during shear degradation of polymers*", *Journal of Applied Physics*, **25**(9):1069–1074 (1954).
- [Bes56] Bestul A.B., "*Kinetics of capillary shear degradation in concentrated polymer solutions*", *The Journal of Chemical Physics*, **24**(6):1196–1201 (1956).
- [Bes57] Bestul A.B., "*Evidence for mechanical shear degradation of high polymers*", *Journal of Physical Chemistry*, **61**(4):418–421 (1957).
- [Bes60] Bestul A.B., "*Energy requirements of mechanical shear degradation in concentrated polymer solutions*", *The Journal of Chemical Physics*, **32**(2):350–356 (1960).
- [Bir84] Bird R.B. and Curtiss C.F., "*Fascinating Polymeric Liquids*", *Physics Today*, **37**(1):36–43 (1984).
- [Bir87] Bird R.B. et al., "*Dynamics of polymeric liquids: Fluid mechanics*", John Wiley and Sons Inc., New York, NY, **1** (1987).
- [Bog85] Boger D., "*Model Polymer Fluid Systems*", *Pure and Applied Chemistry*, **57**(7):921–930 (1985).
- [Bou86] Bousfield D.W. et al., "*Nonlinear analysis of the surface tension driven breakup of viscoelastic filaments*", *Journal of Non-Newtonian Fluid Mechanics*, **21**(1):79–97 (1986).
- [Boy00] Boyd J.P., "*Chebyshev and Fourier Spectral Methods*", Dover Publications, Inc. (2000).
- [Bre73] Breitenbach J.W. et al., "*Abbau von Polystyrol in Cyclohexanlösung bei kleiner Schergeschwindigkeit*", *Macromolecular Chemistry and Physics*, **164**(1):353–355 (1973).
- [Bre97] Brenner M.P. et al., "*Breakdown of scaling in droplet fission at high Reynolds number*", *Physics of Fluids*, **9**(6):1573–1590 (1997).
- [Bro09] Broniarz-Press L. and Pralat K., "*Thermal conductivity of Newtonian and non-Newtonian liquids*", *International Journal of Heat and Mass Transfer*, **52**(21–22):4701–4710 (2009).
- [Bru13] Brust M. et al., "*Rheology of human blood plasma: Viscoelastic versus Newtonian behavior*", *Physical Review Letters*, **110**(7):078305 (2013).
- [Bur07] Burghlea T. et al., "*Elastic turbulence in von Karman swirling flow between two disks*", *Physics of Fluids*, **19**(5):053104 (2007).
- [Cam82] Campbell L. and Garnett W., "*The Life of James Maxwell*", MacMillan and Co. (1882).
- [Cha61] Chandrasekhar S., "*Hydrodynamic and Hydromagnetic Stability*", Oxford Clarendon Press (1961).

- [Cha83] Chang H.F.D. and Darby R., "*Effect of Shear Degradation on the Rheological Properties of Dilute Drag-Reducing Polymer Solutions*", *Journal of Rheology*, **27**(1):77–88 (1983).
- [Che70] Cheetham N.W.H. and Winzor D.J., "*Estimation of molecular weight distributions by gel chromatography*", *Journal of Chromatography A*, **48**:400–405 (1970).
- [Che08] Cheng N., "*Formula for the viscosity of a glycerol-water mixture*", *Industrial & Engineering Chemistry Research*, **47**(9):3285–3288 (2008).
- [Chh10] Chhabra R.P., "*Non-Newtonian fluids: An introduction*", Conference: SERC School-cum-Symposium on Rheology of Complex Fluids, pp.1–33 (2010).
- [Cla10] Clasen C., "*Capillary breakup extensional rheometry of semi-dilute polymer solutions*", *Korea-Australia Rheology Journal*, **22**(4):331–338 (2010).
- [Cou87] Couette M., "*Oscillations tournantes d'un solide de révolution en contact avec un fluide visqueux*", *Comptes Rendus des Séances de l'Académie des Sciences*, **105**:1064–1067 (1887).
- [Cox58] Cox W.P. and Merz E.H., "*Correlation of dynamic and steady flow viscosities*", *Journal of Polymer Science*, **28**(118):619–622 (1958).
- [Day98] Day R.F. et al., "*Self-similar capillary pinchoff of an inviscid fluid*", *Physical Review Letters*, **80**(4):704–707 (1998).
- [Den69] Denn M.M. and Roisman J.J., "*Rotational stability and measurement of normal stress functions in dilute polymer solutions*", *AIChE Journal*, **15**(3):454–459 (1969).
- [Deu11] Deuffhard P., "*Newton Methods for Nonlinear Problems*", Springer-Verlag Berlin Heidelberg (2011).
- [Dra02] Drazin P., "*Introduction to Hydrodynamic Stability*", Cambridge University Press (2002).
- [Dri95] Dris I.M. and Shaqfeh E.S.G., "*On Purely Elastic Instabilities in Eccentric Cylinder Flow*", *Journal of Non-Newtonian Fluid Mechanics*, **56**(3):349–360 (1995).
- [Dut07] Dutcher C.S. and Muller S.J., "*Explicit analytic formulas for Newtonian Taylor-Couette primary instabilities*", *Physical Review E*, **75**(4):047301 (2007).
- [Elb09] Elbing B.R. et al., "*Degradation of homogeneous polymer solutions in high shear turbulent pipe flow*", *Experiments in Fluids*, **47**(6):1033–1044 (2009).
- [Ent97] Entov V. and Hinch E., "*Effect of a spectrum of relaxation times on the capillary thinning of a filament of elastic liquid*", *Journal of Non-Newtonian Fluid Mechanics*, **72**(1):31–53 (1997).
- [Ess96] Esser A. and Grossmann S., "*Analytic expression for Taylor-Couette stability boundary*", *Physics of Fluids*, **8**(7):1814–1819 (1996).
- [Fai99] Faisst H., "*The transition from the Taylor-Couette system to the plane Couette system*", Diploma thesis, Philipps-Universität Magdeburg (1999).
- [Fai00] Faisst H. and Eckhardt B., "*Transition from the Couette-Taylor system to the plane Couette system*", *Physical Review E*, **61**(6):7227–7230 (2000).

- [Flo74] Flory P.J., "*Spatial configuration of macromolecular chains*", Stanford University, Department of Chemistry (1974).
- [Fou03] Fouxon A. and Lebedev V., "*Spectra of turbulence in dilute polymer solutions*", Physics of Fluids, **15**(7):2060–2072 (2003).
- [Gan64] Gandhi J.M., "*Stability of viscous flow between 2 co-axial rotating cylinders*", Applied Scientific Research, Section A: Mechanics, heat, chemical engineering, mathematical methods, **14**(1–2):138–146 (1964).
- [Ghe07] Gheorghiu C.I., "*Spectral Methods for Differential Problems*", "T. Popoviciu"-Institute of Numerical Analysis, Cluj-Napoca, Romania (2007).
- [Gie66] Giesekus H., "*Zur Stabilität von Strömungen viskoelastischer Flüssigkeiten*", Rheologica Acta, **5**(3):239–252 (1966).
- [Gie10] Gier S.E., "*Untersuchung der Bildung, des Wachstums und der Bewegung von Tropfen aus komplexen Flüssigkeiten*", Ph.D. thesis, Saarland University (2010).
- [Gin69] Ginn R.F. and Denn M.M., "*Rotational stability in viscoelastic liquids: Theory*", AIChE Journal, **15**(3):450–454 (1969).
- [Gra67] Granath K.A. and Kvist B.E., "*Molecular weight distribution analysis by gel chromatography on sephadex*", Journal of Chromatography A, **28**:69–81 (1967).
- [Gra74] Graessley W.W., "*The entanglement concept in polymer rheology*", Springer Berlin Heidelberg, **16** (1974).
- [Gra80] Graessley W.W., "*Polymer chain dimensions and the dependence of viscoelastic properties on concentration, molecular weight and solvent power*", Polymer, **21**(3):258–262 (1980).
- [Gro96] Groisman A. and Steinberg V., "*Couette-Taylor flow in a dilute polymer solution*", Physical Review Letters, **77**(8):1480–1483 (1996).
- [Gro97] Groisman A. and Steinberg V., "*Solitary vortex pairs in viscoelastic Couette flow*", Physical Review Letters, **78**(8):1460–1463 (1997).
- [Gro98a] Groisman A. and Steinberg V., "*Elastic vs. inertial instability in a polymer solution flow*", Europhysics Letters, **43**(2):165–170 (1998).
- [Gro98b] Groisman A. and Steinberg V., "*Mechanism of elastic instability in Couette flow of polymer solutions: Experiment*", Physics of Fluids, **10**(10):2451–2463 (1998).
- [Gro00] Groisman A. and Steinberg V., "*Elastic turbulence in a polymer solution flow*", Nature, **405**:53–55 (2000).
- [Gro01] Groisman A. and Steinberg V., "*Efficient mixing at low Reynolds numbers using polymer additives*", Nature, **410**:905–907 (2001).
- [Gro04] Groisman A. and Steinberg V., "*Elastic turbulence in curvilinear flow of polymer solutions*", New Journal of Physics, **6**(29):1–48 (2004).
- [Har65] Harrington R.E. and Zimm B.H., "*Degradation of polymers by controlled hydrodynamic shear*", Journal of Physical Chemistry, **69**(1):161–175 (1965).
- [Hof09] Hoffmann C. et al., "*Transitions between Taylor vortices and spirals via wavy Taylor vortices and wavy spirals*", New Journal of Physics, **11**(5):053002 (2009).

- [Hua10] Huang C.C. et al., “*Semidilute Polymer Solutions at Equilibrium and under Shear Flow*”, *Macromolecules*, **43**(23):10107–10116 (2010).
- [Hur01] Hur J.S. et al., “*Dynamics of dilute and semidilute DNA solutions in the start-up of shear flow*”, *Journal of Rheology*, **45**(2):421–450 (2001).
- [Joo94] Joo Y.L. and Shaqfeh E.S.G., “*Observations of purely elastic instabilities in the Taylor-Dean flow of a Boger fluid*”, *Journal of Fluid Mechanics*, **262**:27–73 (1994).
- [Koz96] Kozicki W. and Kuang P.Q., “*An alternative method for evaluation of intrinsic viscosity*”, *Canadian Journal of Chemical Engineering*, **74**(3):429–432 (1996).
- [Lar90] Larson R.G. et al., “*A purely elastic instability in Taylor-Couette flow*”, *Journal of Fluid Mechanics*, **218**:573–600 (1990).
- [Lar92] Larson R.G., “*Instabilities in viscoelastic flows*”, *Rheologica Acta*, **31**(3):213–263 (1992).
- [Lar94] Larson R.G. et al., “*The effect of fluid rheology on the elastic Taylor-Couette instability*”, *Journal of Non-Newtonian Fluid Mechanics*, **51**(2):195–225 (1994).
- [Lor94] Lorenz J., “*Die Navier–Stokes–Gleichungen für kompressible Flüssigkeiten*”, Institut für Geometrie und Praktische Mathematik, Lehrstuhl für Numerische Mathematik, RWTH-Aachen (1994).
- [Mac94] Macosko C.W., “*Rheology: Principles, Measurements, and Applications*”, Wiley-VCH (1994).
- [McK96] McKinley G.H. et al., “*Rheological and geometric scaling of purely elastic flow instabilities*”, *Journal of Non-Newtonian Fluid Mechanics*, **67**:19–47 (1996).
- [McK05] McKinley G.H., “*Visco-elasto-capillary thinning and break-up of complex fluids*”, *Rheology Reviews*:1–48 (2005).
- [Mir05] Mirzazadeh M. et al., “*Purely tangential flow of a PTT-viscoelastic fluid within a concentric annulus*”, *Journal of Non-Newtonian Fluid Mechanics*, **129**(2):88–97 (2005).
- [Moo67] Moore W.R., “*Viscosities of dilute polymer solutions*”, *Progress in Polymer Science*, **1**:1–43 (1967).
- [Mor07] Morozov A.N. and Saarloos W., “*An introductory essay on subcritical instabilities and the transition to turbulence in visco-elastic parallel shear flows*”, *Physics Reports*, **447**(3–6):112–143 (2007).
- [Mul89] Muller S.J. et al., “*A purely elastic transition in Taylor-Couette flow*”, *Rheologica Acta*, **28**(6):499–503 (1989).
- [Mul93] Muller S.J. et al., “*Experimental Studies of the Onset of Oscillatory Instability in Viscoelastic Taylor-Couette Flow*”, *Journal of Non-Newtonian Fluid Mechanics*, **46**(2-1):315–330 (1993).
- [Mul08] Muller S.J., “*Elastically-influenced instabilities in Taylor-Couette and other flows with curved streamlines: A review*”, *Korea-Australia Rheology Journal*, **20**(3):117–125 (2008).
- [Mus13] Mussler M. et al., “*Effective viscosity of non-gravitactic Chlamydomonas Reinhardtii microswimmer suspensions*”, *Europhysics Letters*, **101**:54004 (2013).

- [Pak96] Pakdel P. and McKinley G.H., "*Elastic Instability and Curved Streamlines*", Physical Review Letters, **77**(12):2459–2462 (1996).
- [Pak98] Pakdel P. and McKinley G.H., "*Cavity flows of elastic liquids: Purely elastic instabilities*", Physics of Fluids, **10**(5):1058-1070 (1998).
- [Pal05] Palmer A.S. and Phillips T.N., "*Numerical approximation of the spectra of Phan-Thien Tanner liquids*", Numerical Algorithms, **38**(1–3):133-153 (2005).
- [Pam08] Pamies R. et al., "*Determination of intrinsic viscosities of macromolecules and nanoparticles. Comparison of single-point and dilution procedures*", Colloid and Polymer Science, **286**(11):1223–1231 (2008).
- [Par11] Partal P. and Franco J.M., "*Non-Newtonian Fluids*", Rheology, vol. 1 (2011).
- [Per12] Pereira A.S. and Soares E.J., "*Polymer degradation of dilute solutions in turbulent drag reducing flows in a cylindrical double gap rheometer device*", Journal of Non-Newtonian Fluid Mechanics, **179–180**:9–22 (2012).
- [Pet67] Peters F.E., "*Greek Philosophical Terms: A Historical Lexicon*", New York University Press (1967).
- [Pet76] Petrie C.J.S. and Denn M.M., "*Instabilities in Polymer Processing*", AIChE Journal, **22**(2):209-236 (1976).
- [Pha77] Phan-Thien N. and Tanner R.I., "*A new constitutive equation derived from network theory*", Journal of Non-Newtonian Fluid Mechanics, **2**(4):353–365 (1977).
- [Ray17] Rayleigh L., "*On the Dynamics of Revolving Fluids*", Proceedings of the Royal Society of London A - Mathematical and Physical Sciences, **93**(648):148–154 (1917).
- [Rei64] Reiner M., "*The Deborah Number*", Physics Today, **17**(1):62 (1964).
- [Rod05] Rodd L.E. et al., "*Capillary Break-up Rheometry of Low-Viscosity Elastic Fluids*", Applied Rheology, **15**(1):12–27 (2005).
- [Sam13] Samanta D. et al., "*Elasto-inertial turbulence*", Proceedings of the National Academy of Sciences, **110**(26):10557–10562 (2013).
- [Sat09] Sattler R., "*Untersuchungen zum kapillaren Abriss von verdünnten und halbkonzentrierten Polymerlösungen*", Ph.D. thesis, Saarland University (2009).
- [Sch05] Schroeder C.M. et al., "*Characteristic periodic motion of polymers in shear flow*", Physical Review Letters, **95**(1):018301 (2005).
- [Sch13] Schäfer C. et al., "*Geometric scaling of purely elastic instability in the Taylor-Couette flow: A combined experimental, theoretical and numerical study*" (2013, in preparation).
- [Sha92] Shaqfeh E.S.G. et al., "*The effects of gap width and dilute solution properties on the viscoelastic Taylor-Couette instability*", Journal of Fluid Mechanics, **235**:285-317 (1992).
- [Sta32] Staudinger H., "*Die hochmolekularen organischen Verbindungen - Kautschuk und Cellulose*", Springer (1932).

- [Sun72] Sun Z.S. and Morton D.M., "*Stability of rotational couette flow of polymer solutions*", *AIChE Journal*, **18**(5):1010–1015 (1972).
- [Sun04] Sung J.H. et al., "*Mechanical degradation kinetics of poly(ethylene oxide) in a turbulent flow*", *Korea Australia Rheology Journal*, **16**(2):57–62 (2004).
- [Tag94] Tagg R., "*The Couette-Taylor problem*", *Nonlinear Science Today*, **4**(3):1–25 (1994).
- [Tay23] Taylor G.I., "*Stability of a Viscous Liquid Contained between Two Rotating Cylinders*", *Philosophical Transactions of the Royal Society of London. Series A, Containing Papers of a Mathematical or Physical Character*, **223**(605–615):289–343 (1923).
- [Too95] Toonder J.M.J. et al., "*Degradation effects of dilute polymer solutions on turbulent drag reduction in pipe flows*", *Applied Scientific Research*, **55**(1):63–82 (1995).
- [Van05] Vanapalli S.A. et al., "*Scission-induced bounds on maximum polymer drag reduction in turbulent flow*", *Physics of Fluids*, **17**(9):095108 (2005).
- [Van06] Vanapalli S.A. et al., "*Universal scaling for polymer chain scission in turbulence*", *Proceedings of the National Academy of Sciences of the United States of America*, **103**(45):16660–16665 (2006).
- [Vir75] Virk P.S., "*Drag Reduction Fundamentals*", *AIChE Journal*, **21**(4):625–656 (1975).
- [Von10] Vonlanthen R., "*The effects of fluid elasticity on grid turbulence*", Ph.D. thesis, École Polytechnique Fédérale de Lausanne (2010).
- [Wei47] Weissenberg K., "*A continuum theory of rheological phenomena*", *Nature*, **159**(4035):310–311 (1947).
- [Whi64] White J.L., "*Dynamics of viscoelastic fluids, melt fracture, and the rheology of fiber spinning*", *Journal of Applied Polymer Science*, **8**(5):2339–2357 (1964).
- [Whi00] White J.M. and Muller S.J., "*Viscous heating and the stability of Newtonian and viscoelastic Taylor-Couette flows*", *Physical Review Letters*, **84**(22):5130–5133 (2000).
- [Whi03] White J.M. and Muller S.J., "*Experimental studies on the effect of viscous heating on the hydrodynamic stability of viscoelastic Taylor-Couette flow*", *Journal of Rheology*, **47**(6):1467–1492 (2003).
- [Wil02] Willis A.P., "*The Hydromagnetic Stability of Taylor–Couette Flow*", Ph.D. thesis, University of Newcastle, Department of Mathematics (2002).
- [Yin87] Ying Q.C. and Chu B., "*Overlap concentration of macromolecules in solution*", *Macromolecules*, **20**(2):362–366 (1987).
- [Yu164] Yu Y.S. and Sun D.C., "*Stability of a viscous flow between two rotating coaxial cylinders*", *Journal of the Franklin Institute*, **277**(2):140–149 (1964).
- [Zel10] Zell A. et al., "*Is there a relation between the relaxation time measured in CaBER experiments and the first normal stress coefficient?*", *Journal of Non-Newtonian Fluid Mechanics*, **165**(19–20):1265–1274 (2010).
- [Zil12] Zilz J. et al., "*Geometric scaling of purely elastic flow instability in serpentine channels*", *Journal of Fluid Mechanics*, **712**:203–218 (2012).

- [Zil14] Zilz J. et al., "*Serpentine channels: micro-rheometers for fluid relaxation times*", Lab Chip, **14**:351-358 (2014).

---

## Danksagung / Acknowledgment

Mit den letzten Zeilen und Worten dieser Dissertation und damit dem vorläufigen Ende eines ganz speziellen Kapitels meines bisherigen Lebens ist die Zeit gekommen, Danke zu sagen. All jenen ganz herzlich zu danken, die, in welcher Form auch immer, maßgeblich dazu beigetragen haben, dass ich hier und jetzt diese Worte an sie richten kann. Leider wird es bei dem Versuch bleiben, euch alle gebührend auf dieser Seite zu erwähnen. Aber seid euch einer Sache gewiss: *ohne Euch gäbe es diese gedruckten Zeilen nich'!*

Unter den Menschen, die ich an dieser Stelle hervorheben möchte, steht mein Doktorvater Christian Wagner an vorderster Stelle. Ich möchte ihm an dieser Stelle nicht nur dafür danken, dass er es mir ermöglicht hat, unter seiner sehr menschlichen und zugleich professionellen Anleitung und großen Expertise, ausgestattet mit vielen Freiheiten doch stets mit dem Fokus für das Wesentliche, der Forschung in ihrer breiten Vielfalt nachzugehen und darauf aufbauend diese Arbeit anzufertigen. Auch und insbesondere sei ihm dafür gedankt, dass er mir während der letzten fünf Jahre auf seine verständnisvolle Art und Weise auch in den nicht seltenen, schwierigen Phasen der Promotion durch guten Zuspruch, Unterstützung und viel Geduld stets Vertrauen in die eigenen Fähigkeiten geschenkt und damit maßgeblich zum Gelingen dieser Arbeit beigetragen hat. Lieber Christian, ganz herzlichen Dank dafür, für viele Stunden spannender Diskussionen und für vieles mehr!

Very special thanks is dedicated to Alexander Morozov who has been an excellent teacher and friend during my stay in Edinburgh. The discussions with him were invaluable and his expertise significantly contributed to the content of this work. Alex, it has been a great pleasure to work under your excellent guidance. Thank you so much!

Here I'd like to thank all other collaborators for the fruitful cooperations and discussions, in particular Dr. Teo Burghilea, Dr. Rob Poole, Prof. Anke Lindner, Prof. Bruno Eckhardt, Prof. Björn Hof, Dr. Marc Fardin, Hannes Brauckmann and many more.

In ganz besonderem Maße möchte ich mich bei all den Menschen bedanken, die in den vergangenen fünf Jahren meinen Alltag an der Uni und zum Teil weit darüber hinaus geprägt haben und mir die Zeit so unvergesslich und angenehm wie möglich gestaltet haben. Angefangen bei Elke Huschens, die nicht nur bei all den administrativen Problemchen stets ein offenes Ohr für mich hatte und mit Rat und Tat zur Stelle war, sondern darüber hinaus mit ihrer herzlichen Art bei jedem "Wetter" gute Laune und ein Lächeln zu vermitteln wusste. Über Karin Kretsch, die mir mit ihrer Hilfsbereitschaft das (Über-)Leben im Labor durch ihre unschätzbare Zuarbeit und Kompetenz um so vieles einfacher gemacht hat. Hin zu Michael Schmidt, ohne dessen routinierte Federführung die Konzeption und präzise Umsetzung eines Großteils des experimentellen Aufbaus nicht möglich gewesen wäre. Ihm möchte ich stellvertretend für das gesamte Team der feinmechanischen Werkstatt danken. Bei unseren Elektronikern Stefan Loew und Jürgen Hoppe möchte ich mich bedanken für ihre Unterstützung bei allen Belangen

elektrotechnischer Natur. Ganz besonders möchte ich aber allen (ehemaligen) Mitgliedern der Arbeitsgruppe Wagner sowie allen übrigen Kommilitonen danken, die mich während der letzten Jahre auf all meinen Wegen auf dem Campus und darüber hinaus begleitet haben, mir stets mit Rat und Tat zur Seite gestanden haben und mit denen ich viele schöne Stunden verbringen durfte. Anke, Matthias, René, Simon, Volker, Ines, Max, Mona, Patrick und natürlich Matthias: euch möchte ich ganz herzlich danken.

Ein großer Dank geht nochmals an Max für die Stunden, die er sich Zeit genommen hat, um diese Arbeit Korrektur zu lesen. In diesem Zusammenhang auch herzlichen Dank für die vielen Denkanstöße!

Ein großes Dankeschön natürlich auch an meine Freunde und Familie abseits der Uni, die mir ein ums andere Mal zeigen mussten, dass es neben der Promotion auch noch andere, mitunter wesentlich wichtigere Dinge gibt. Eurer moralischen Unterstützung und eurem guten Zuspruch durfte ich mir stets sicher sein, hierfür und für eure Freundschaft kann ich euch nicht genug danken.

Auf der Liste der Personen, denen ich abschließend an dieser Stelle aus tiefstem Herzen danken möchte, stehen meine Eltern außer Konkurrenz. Ihre Bedeutung für mich vermag ich nicht in Worte zu fassen, ebenso das Ausmaß ihrer Unterstützung über all die Jahre.

Liebe Mama, lieber Papa, Danke für einfach alles!